

DISS. ETH NO. 29226

# **Three-dimensional Quantitative Perfusion and Scar Imaging for Experimental and Clinical Applications**

A thesis submitted to attain the degree of

**DOCTOR OF SCIENCES**  
(Dr. sc. ETH Zurich)

presented by

**Tobias Joachim Hoh**  
MSc, Technische Universität München

born on 09.09.1988

accepted on the recommendation of

Prof. Dr. Sebastian Kozerke  
Prof. Dr. Dominik von Elverfeldt

2023



# Abstract

Reduced perfusion of cardiac tissue is indicative of coronary artery disease, which is the most prevalent cardiovascular disease. At its onset, pathological alterations in the coronary vessel walls occur. While the consequences of these pathological changes are initially masked by autoregulation and outward remodeling of the vascular wall, sufficient blood flow and oxygen supply may no longer be ensured at increased demand i.e. during physical exercise or stress. Ultimately, these changes can result in acute myocardial infarction, followed by irreversible myocardial tissue damage if left untreated. Therefore, accurate and cost-effective quantification of myocardial perfusion and tissue viability is pivotal for diagnosis, treatment planning and individual prognosis.

Cardiovascular Magnetic Resonance (CMR) provides a powerful toolset to assess myocardial tissue perfusion and viability, without exposing the patient to ionizing radiation. Tissue perfusion can be quantified by dynamic contrast-enhanced perfusion imaging both under rest and stress. Late gadolinium enhancement (LGE) allows for tissue viability assessment and the identification of scars. However, in clinical practice, both perfusion and scar imaging have limitations in relation to anatomical coverage, patient compliance, accuracy and ease of use.

Clinically, perfusion imaging is performed in three short-axis slices, covering only parts of the left-ventricular myocardium. In the research setting, quantitative three-dimensional (3D) perfusion imaging methods require extended breathholds of the patient, which often limits their feasibility in practice. Improving patient comfort and compliance is therefore pivotal in translating quantitative 3D perfusion CMR into clinical routine.

In the first project of this thesis, a framework for improved 3D perfusion imaging, not requiring breathholds of the patient, is presented. The framework comprises motion-informed locally low-rank image reconstruction for Cartesian pseudo-spiral undersampled data acquisitions to enable robust free-breathing whole-heart quantitative perfusion imaging under rest and stress conditions. Using computer simulations, phantom and in-vivo data, it is shown that respiratory motion can be corrected under rest condition and under pharmacologically-induced stress. Furthermore, it is demonstrated that sector-wise quantitative perfusion maps can be derived reproducibly for varying heart rates and breathing patterns.

In a second project, hypercapnia as an alternative to pharmacological stressors for perfusion imaging is explored. An experimental setup and protocols to study hypercapnia-induced vasodilation via a controlled increase of the partial pressure of CO<sub>2</sub> in blood is presented. Hypercapnic stress is studied in a porcine model and changes of myocardial perfusion are assessed using free-breathing CMR perfusion methods.

While it is shown that reproducible control of partial pressure of CO<sub>2</sub> in blood is possible, no apparent changes of myocardial perfusion were detected. The results point to various open questions regarding biological mechanisms of autoregulation of vasodilation in experimental models and warrant further investigation.

Two-dimensional and three-dimensional LGE imaging methods are widespread in clinical practice, providing a large number of imaging slices and whole-heart coverage. The challenge with these methods lies with the labor-intensive and time-consuming processing of the data. Classical post-processing methods require manual annotation of healthy and/or scar tissue, which not only introduces observer-dependent bias and uncertainty but also adds to cost. Therefore, neural networks have been proposed to automatize the analysis.

The third contribution to this thesis is concerned with accuracy of neural network-based automatic scar assessment on LGE imaging data. While the use of neural networks allows for time-efficient processing of the data, variations in data acquisition and image reconstruction parameters may compromise network performance. To this end, network performance degradation due to mismatch of the point-spread functions in training and test data was investigated. High-resolution porcine model datasets with myocardial infarction were acquired ex-vivo and convolved with point-spread functions of increasing widths. It is shown that networks, which were trained on lower-resolution training data and deployed on higher-resolution test data, tend to be more robust against variation in test image resolution. On the contrary, networks trained at higher resolution lead to systematic overestimation of total and dense scar areas if deployed on low-resolution datasets. Accordingly, the study underlines the importance of taking the point-spread functions of data acquisition into account to ensure accurate scar detection.

In summary, current challenges in 3D perfusion imaging and scar quantification have been addressed. Following the methods developments, clinical studies are warranted to demonstrate the robustness and diagnostic yield in larger patient cohorts.

# Kurzfassung

Eine verminderte Durchblutung des Herzwes ist ein Hinweis auf eine Koronararterienkrankung, der am weitesten verbreiteten kardiovaskulären Erkrankung. Zu Beginn der koronaren Herzerkrankung treten pathologische Veränderungen der Herzkranzgefäßwände auf. Während die Folgen dieser pathologischen Veränderungen zunächst durch Autoregulation und Umbau der Gefäßwand kompensiert werden, kann bei körperlicher Belastung oder Stress eine ausreichende Durchblutung und Sauerstoffversorgung unter Umständen nicht mehr gewährleistet sein. Letztendlich können diese Einschränkungen zu einem akuten Myokardinfarkt führen, gefolgt von irreversiblen Myokardgewebeschäden. Daher ist eine genaue und kosteneffiziente Quantifizierung der myokardialen Durchblutung und der Gewebewitalität von entscheidender Bedeutung für die Diagnose, Behandlungsplanung und individueller Prognose.

Die kardiovaskuläre Magnetresonanztomographie (MRT) bietet ein leistungsfähiges Instrument zur Beurteilung der myokardialen Gewebedurchblutung und -vitalität, ohne den Patienten ionisierender Strahlung auszusetzen. Durch die dynamische kontrastmittelverstärkte Perfusionsbildgebung kann die Durchblutung des Gewebes sowohl im Ruhezustand als auch unter Stress quantifiziert werden. Die Methodik des Late-Gadolinium-Enhancements (LGE) erlaubt die Beurteilung der Vitalität des Gewebes sowie die Identifizierung von Narbengewebe. In der klinischen Praxis weisen jedoch sowohl die Perfusions- als auch die LGE-Bildgebung Limitationen in Bezug auf die anatomische Abdeckung, Genauigkeit, Zuverlässigkeit sowie Benutzerfreundlichkeit auf.

In der klinischen Praxis ermöglicht die Perfusions-MRT die Aufnahme von drei Schichtbildern, die nur Teile der Anatomie der linken Herzkammer abdecken. In der Forschung finden bereits Verfahren zur quantitative dreidimensionale (3D) Perfusions-MRT Verwendung; jedoch benötigen diese längere Atemstopps des Patienten, was die Durchführbarkeit erschwert und Zuverlässigkeit vermindert.

Im ersten Projekt dieser Arbeit wird eine Methodik für eine verbesserte 3D Perfusions-MRT, welche Aufnahmen ohne Atemstopp ermöglicht, vorgestellt. Unter Einbezug von Bewegungsinformation in der Bildrekonstruktion können unterabgetastete Daten, welche entlang einer pseudo-spiralförmigen, kartesischen Trajektorie aufgenommen werden, unter Ruhe- und Stressbedingung des Patienten robust rekonstruiert werden. Anhand von Computersimulationen, Phantom- und in-vivo-Daten wird gezeigt, dass die Atembewegung sowohl in Ruhe als auch unter pharmakologisch-induziertem Stress in der Bildgebung korrigiert werden kann. Darüber hinaus zeigt die quantitative Analyse der Perfusionsdaten, dass eine sektorbasierte Quantifizierung der Myokardperfusion, trotz unterschiedlicher Herzfrequenzen und Atemmuster, reproduzierbar berechnet werden kann.

In einem zweiten Projekt wird eine Alternative zu pharmakologischen Stressoren für die Perfusions-MRT erforscht. Hierzu werden ein Versuchsaufbau und Protokolle zur Untersuchung der hyperkapnie-induzierten Vasodilatation durch eine kontrollierte Erhöhung des CO<sub>2</sub>-Partialdrucks im Blut vorgestellt. Der hyperkapnische Stress wird an einem Schweinemodell untersucht und die Veränderungen der Myokardperfusion mittels Perfusions-MRT evaluiert. Es wird gezeigt, dass zwar eine reproduzierbare Kontrolle des CO<sub>2</sub>-Partialdrucks im Blut möglich ist, eine davon abhängige Veränderung der Myokardperfusion jedoch nicht eindeutig nachgewiesen werden kann. Die experimentellen Ergebnisse lassen einige Fragen zur biologischen Wirkweise der Gefäßautoregulation im experimentellen Tiermodell offen und bedürfen weiterer Untersuchungen.

Zwei- und dreidimensionale LGE-Bildgebungsverfahren sind in der klinischen Praxis weit verbreitet und bieten eine hohe Anzahl von Schichtbildern mit Abdeckung des gesamten Herzens. Diese Methoden bringen eine arbeitsintensive und zeitaufwändige Nachbearbeitung der Bilddaten mit sich. Etablierte Nachbearbeitungsmethoden erfordern eine manuelle Identifikation von gesundem beziehungsweise narbigem Gewebe, was nicht nur eine benutzerabhängige Unsicherheit in sich birgt, sondern auch die Kosten erhöht. Um die Nachbearbeitung zu automatisieren bietet sich die Verwendung neuronaler Netzwerke an.

Der dritte Beitrag dieser Arbeit befasst sich mit der Genauigkeit der automatischen Quantifizierung von LGE-Bildern mittels neuronaler Netzwerke. Die Verwendung neuronaler Netzwerke ermöglicht eine zeiteffiziente Verarbeitung der Bilddaten; jedoch können Unterschiede in der Bildaufnahme und in den verwendeten Bildrekonstruktionsparametern die Leistung der Netzwerke beeinträchtigen. Um diesen Aspekt genauer zu beleuchten, wurde die Genauigkeit netzwerkbasierter Segmentierung in Abhängigkeit von Unterschieden in der Punktausbreitungsfunktion in Trainings- und Testdaten systematisch untersucht. Hochaufgelöste LGE-Bilddaten von Schweinemodellen mit Myokardinfarkt kamen zur Anwendung, welche mit verschiedenen Punktausbreitungsfunktionen gefaltet wurden, um Kopien mit unterschiedlicher Auflösung zu erhalten. Dabei zeigt sich, dass Netzwerke, die auf Trainingsdaten mit geringerer Auflösung trainiert und auf Testdaten mit höherer Auflösung angewendet wurden, tendenziell robuster gegenüber Schwankungen in der Auflösung der Testbilder sind. Im Gegensatz dazu tendieren Netzwerke, die mit höherer Auflösung trainiert wurden und auf Daten mit geringer Auflösung angewendet werden, zu einer systematischen Überschätzung der Narbenfläche. Dementsprechend unterstreicht die Studie die Wichtigkeit, die der Bildaufnahme zugrundeliegende Punktausbreitungsfunktion zu berücksichtigen, um eine genaue Narbenerkennung zu gewährleisten.

Zusammenfassend ist festzuhalten, dass in der vorliegenden Arbeit Lösungen zu aktuellen Herausforderungen in der 3D Perfusion-MRT und der LGE-basierten Narbenquantifizierung entwickelt wurden. Im Anschluss an diese Methodenentwicklungen sind nun klinische Studien nötig, um die Robustheit und den diagnostischen Wert der Entwicklungen in grösseren Patientenkohorten unter Beweis zu stellen.

# Contents

<b>Abstract</b> .....	<b>iii</b>
<b>Kurzfassung</b> .....	<b>v</b>
<b>Contents</b> .....	<b>viii</b>
<b>Chapter 1 Introduction</b> .....	<b>1</b>
1.1 Motivation .....	2
1.2 Outline.....	4
1.3 Contributions.....	5
<b>Chapter 2 Physiological and Clinical Background</b> .....	<b>7</b>
2.1 Anatomy and Function .....	7
2.2 Physiology of Myocardial Perfusion and Stress .....	8
2.3 Coronary Artery Disease.....	10
2.4 Diagnostic Imaging .....	11
2.5 Cardiac and Respiratory Motion.....	12
<b>Chapter 3 CMR Perfusion Imaging</b> .....	<b>14</b>
3.1 Non-contrast Enhanced Perfusion Imaging.....	14
3.2 Contrast-enhanced Perfusion Imaging .....	15
3.2.1 Strategies for Whole-heart Perfusion Imaging.....	17
3.2.2 3D Cartesian k-Space Trajectories.....	20
3.2.3 Non-Cartesian k-Space Trajectories .....	21
3.2.4 Theoretical Acceleration Requirements.....	22
3.3 Accelerated Image Reconstruction.....	24
3.3.1 Image Reconstruction Formalism .....	24
3.3.2 Parallel Imaging.....	25
3.3.3 Spatio-temporal Parallel Imaging.....	25
3.3.4 Compressed Sensing .....	26
3.4 Motion Correction and Compensation Techniques.....	33



---

3.5	Perfusion Quantification .....	35
3.5.1	Semi-quantitative Estimation.....	35
3.5.2	Absolute Perfusion Quantification .....	36
<b>Chapter 4</b>	<b>Myocardial Fibrosis and Scar CMR .....</b>	<b>41</b>
4.1	Background .....	41
4.2	LGE Imaging Strategies.....	43
4.3	Myocardial Scar Analysis and Quantification .....	45
4.4	Machine Learning Segmentation .....	47
4.4.1	U-Net architecture.....	47
4.4.2	Neural Network Training.....	48
4.4.3	Overfitting Reduction.....	49
4.4.4	Test Time Augmentation.....	50
4.4.5	State of the Art Myocardial Scar Segmentations .....	52
<b>Chapter 5</b>	<b>Free-breathing Motion-informed Locally Low-rank Quantitative 3D Myocardial Perfusions Imaging.....</b>	<b>54</b>
5.1	Introduction .....	55
5.2	Methods.....	57
5.2.1	Image Acquisition .....	57
5.2.2	Image Reconstruction and Motion Compensation .....	59
5.2.3	Postprocessing And Myocardial Blood Flow Quantification .....	61
5.2.4	Simulation Studies .....	62
5.2.5	Phantom Studies.....	63
5.2.6	In-vivo Experiments .....	64
5.3	Results.....	64
5.3.1	Simulation Studies .....	64
5.3.2	Phantom Studies.....	67
5.3.3	In-vivo Studies.....	69
5.4	Discussion.....	72

---

5.5	Conclusion .....	75
<b>Chapter 6</b>	<b>Hypercapnic Myocardial Stress Perfusion in a Porcine Model – A Pilot Experiment .....</b>	<b>77</b>
6.1	Background .....	77
6.2	Methods .....	81
6.2.1	Hypercapnia Instrumentation .....	81
6.2.2	In-vivo Experiments.....	83
6.2.3	Animal Handling.....	84
6.2.4	Image Acquisition and Reconstruction.....	84
6.2.5	Image Post-processing and Analysis .....	85
6.3	Results .....	85
6.3.1	Hemodynamic Response to Hypercapnic Stimuli.....	85
6.3.2	MBF Response to Hypercapnic Stimulus.....	89
6.4	Discussion.....	91
<b>Chapter 7</b>	<b>Impact of Late Gadolinium Enhancement Image Resolution on Neural Network Based Automatic Scar Segmentation in Cardiovascular Magnetic Resonance Imaging .....</b>	<b>93</b>
7.1	Introduction .....	94
7.2	Methods .....	95
7.2.1	Animal Cohort and Handling .....	95
7.2.2	Image Acquisition.....	97
7.2.3	Image Post-processing .....	97
7.2.4	Reduction of Image Resolution .....	98
7.2.5	Network Training .....	98
7.2.6	Error Metrics.....	99
7.3	Results .....	100
7.3.1	Cohort Data Set.....	100
7.3.2	Segmentation Performance Dependency on Effective Resolution .....	100
7.4	Discussion.....	107
7.5	Conclusion .....	109

---

<b>Chapter 8</b>	<b>Summary .....</b>	<b>111</b>
8.1	Discussion.....	111
8.2	Outlook.....	113
<b>Bibliography.....</b>		<b>xi</b>
<b>Acknowledgements.....</b>		<b>xlii</b>
<b>List of Publications .....</b>		<b>xliv</b>
<b>Curriculum Vitae .....</b>	..... Error! Bookmark not defined.	



# Chapter 1

## Introduction

According to the World Health Organization, cardiovascular diseases (CVD) are the leading cause of death globally and approximately half of all CVDs are due to coronary artery disease (CAD) (1). In Switzerland, ~18 600 people per year suffer from acute myocardial infarction (MI), i.e. 0.2% of the population (2). While advances in diagnosis and timely interventions have reduced the morbidity and mortality in the western world, the aging population, lifestyle changes as well as economical constraints continue to exert strain on healthcare systems.

In the healthy human heart, a balance between oxygen demand and oxygenated blood, provided by the coronary arteries, is maintained. A decrease of the vascular lumen by a stenosis or alterations in microvascular structure can create an imbalance. Initially, the narrowing in the vascular lumen is compensated by arterial dilation. This is the onset of the ischemic cascade, which describes the progress of CAD and ischemic heart disease through build-up of atherosclerotic plaques to MI. Accumulation of atherosclerotic plaques progressively increases the degree of stenosis and deteriorates the vasodilator reserve to a point where autoregulation can no longer ensure sufficient oxygen supply under increased physical demand, i.e. physical stress. Impaired myocardial perfusion is then followed by abnormalities in contractility of the myocardium, changes in the electrocardiogram (ECG) and, eventually, chest pain occurs. If left untreated, irreversible myocardial tissue necrosis can be the result. To prevent fatal outcomes, an early diagnostic assessment of myocardial perfusion as well as the assessment of potential tissue necrosis or scar is pivotal for the optimal care and risk stratification of patients (3).

Cardiovascular Magnetic Resonance (CMR) imaging provides a toolbox to assess both perfusion and scar in a non-invasive fashion (4). Contrast-enhanced myocardial perfusion CMR allows to monitor myocardial signal changes in response to the passage of a contrast agent bolus injected intravenously (5). Differences in perfusion data, acquired during pharmacologically-induced stress and under rest of the patient, subsequently enable the detection of stress-induced tissue perfusion deficits (6–9). Following a pause of a couple minutes after contrast agent injection, Late Gadolinium Enhancement (LGE) imaging (10,11) offers imaging of myocardial scar and is considered the reference for tissue viability assessment (12).

## 1.1 Motivation

In clinical practice, CMR perfusion imaging is limited to the acquisition of three to four two-dimensional (2D) slices per heartbeat (13). So far, this has proven to be sufficient for diagnostic purposes. However, a continuous whole-heart coverage would ensure confidence that no defects of the myocardial tissue have been missed. Whole-heart imaging further allows to derive the myocardial ischemic burden, which provides a ratio of ischemic to total myocardial volume and can be linked to survival prognosis (14–16). Three-dimensional whole-heart perfusion imaging, however, requires substantial scan acceleration to accommodate data sampling into a sufficiently short acquisition window. In recent years, a variety of 3D whole-heart perfusion imaging and reconstruction approaches have been proposed (17).

A challenge with reconstruction from highly undersampled data is the requirement for sufficient spatio-temporal data correlations. Therefore, data acquisition is typically conducted in a breathhold, which has been particularly limiting during adenosine-induced stress. To increase patient comfort and compliance, initial research has been directed towards free-breathing 3D approaches with additional motion compensation (18–20). However, conventional motion correction techniques, e.g. navigator gating (21,22), do not comply with the required image acquisition in every heart-beat and application of retrospective motion binning is limited by the high acceleration factors (23). Intensity- and feature-based image registration methods are an option (24) but can be susceptible to dynamic changes in image contrast (25,26). Hence, a more sophisticated alternative is to incorporate additional motion information from a navigator or initial image registration into the reconstruction algorithm. For 3D perfusion imaging, this has been proposed for a highly undersampled Cartesian acquisition but has only been tested in shallow breathing and in conjunction with semi-quantitative analysis (18). Employing latest advances in compressed sensing (CS) based low-rank reconstruction with patch-based decomposition (27) might allow to enhance the conditioning of iterative image reconstruction towards fully quantitative free-breathing perfusion imaging.

Another limitation in clinical practice is that myocardial perfusion is mainly assessed visually. Hypo-perfused regions are identified by delayed signal enhancement or its absence for several imaging time frames. Experienced observers are required to diagnose perfusion defects. To this end, semi- and fully-quantitative evaluation of perfusion is desirable as it promotes objective diagnosis, simplifies analysis (e.g. helps to distinguish types of diseases (28,29)) and may advance diagnostics of microvascular diseases (30). However, as stated in current guidelines of the Society for Cardiovascular Magnetic Resonance (SCMR) (31), perfusion quantification is currently only considered a complementary diagnostic analysis tool. Missing standardization of perfusion models and their evaluation, as well as missing normal values, are still a barrier for more widespread use.

Conventional stressor agents, such as adenosine, can cause side effects such as chest pressure, pain and shortness of breath (4). In addition, the physiological response can vary among patients depending on age and sex, and can be modulated by substances such as caffeine (32,33). For some patients, pharmacological stressors can be generally contraindicated (4). Therefore, alternatives to pharmacological stressors should be explored.

Myocardial scar mass is of prognostic value in patients with ischemic cardiomyopathies (34–37). In clinical practice, manual segmentation of the left ventricle (LV) is required. Manual user interaction is time-consuming and observer dependent. Hence, it is an obstacle for the successful clinical integration of LGE imaging methods. Lately, automatic segmentation methods using convolutional neural networks (CNN) have been proposed as a promising alternative (38). However, available datasets often lack details on data acquisition and reconstruction as well as post-processing parameters. This can potentially produce biased results as it has been shown for CNN-based image reconstruction methods (39). The impact of similar effects in myocardial scar segmentation should thus be studied to elucidate the utility of these methods.

## 1.2 Outline

In Chapter 2 the basic anatomy and function of the human heart is summarized. The physiology of myocardial perfusion and its response under stress is outlined. Coronary artery disease in context of the ischemic cascade from reduced perfusion to myocardial scar formation is introduced. Furthermore, an overview on other clinically relevant imaging methodologies is given. Cardiac and respiratory motion is explained.

In Chapter 3 methods for myocardial perfusion CMR are reviewed. Background information on non-contrast enhanced perfusion is provided. For contrast-enhanced perfusion, the use of contrast agents and imaging requirements in myocardial perfusion imaging are detailed. A closer look at acquisition strategies and accelerated image reconstruction for whole-heart coverage is provided. Relevant motion correction techniques, dedicated to free-breathing perfusion imaging, are also reviewed. Finally, the basics of semi- and fully-quantitative myocardial perfusion estimation are introduced.

Chapter 4 deals with myocardial fibrosis and scar imaging. Basic imaging requirements and imaging strategies are reviewed. Moreover, standard clinical scar and fibrosis analysis is outlined before state-of-the-art methods for myocardial scar quantification are introduced. Furthermore, network-based automatic scar quantification and their latest advancements are summarized.

In Chapter 5 an implementation of motion-informed iterative reconstruction, combined with Cartesian pseudo-spiral undersampling for free-breathing three-dimensional quantitative perfusion CMR under rest and stress is given.

In Chapter 6 an explorative study to assess the response of myocardial blood flow to controlled hypercapnic stress in a porcine model is provided.

In Chapter 7 a systematic investigation of network performance due to mismatch of effective image resolution, i.e. the image point-spread function, in training and testing data for network-based myocardial scar quantification is presented.

The findings of this thesis are summarized and complemented by an outlook for future research in Chapter 8.



---

## 1.3 Contributions

Improved patient compliance and optimization of post-processing methods are indispensable to translate advances in myocardial perfusion and quantitative scar imaging to a wider clinical community.

Highly-accelerated dynamic 3D perfusion imaging relies on spatio-temporal data correlation, which is compromised for image acquisition in free-breathing in particular. It is shown that additional motion conditioning of the reconstruction problem can improve image reconstruction. Building up on improved data correlation characteristics from locally low-rank image reconstruction methods, data inconsistencies are addressed by incorporation of motion information from a transformation displacement field for each time frame. Using motion-informed locally low-rank reconstruction in conjunction with pseudo-spiral in-out Cartesian data undersampling, improved quantitative 3D perfusion can be acquired in free-breathing under rest and stress.

Hypercapnic stress induced by target end tidal  $P_{ETCO_2}$  was explored as an alternative vasodilator. It is shown that by optimization of an automatic gas-blending setup to local requirements, hypercapnia can be initiated in mechanically ventilated porcine models. While it is shown that reproducible control of blood  $pCO_2$  is possible, conclusive changes of myocardial perfusion by means of the quantitative free-breathing 3D framework are not detectable.

To advance diagnostics of LGE based viability assessment after MI, a testing framework for current network-based automatic scar segmentation is implemented. Forty-five high-resolution 3D LGE datasets were acquired from post mortem porcine models. Semi-automatic scar segmentation in  $\sim 2500$  slices allow systematical assessment of U-net based network segmentation degradation due to mismatch of effective resolution in training and testing data. It is shown that networks, which were trained on lower-resolution training data and deployed on higher-resolution test data, tend to be more robust against variation in test image resolution. On the contrary, networks trained at higher resolution lead to systematic overestimation of total and dense scar areas. Accordingly, the work underlines the importance of taking the point-spread functions of data acquisition into account in order to ensure accurate scar detection. It is further shown that, within the clinically relevant spectrum of image resolutions, automatic network-based segmentation can provide robust segmentation with reduced temporal burden if it is properly trained and applied.



# Chapter 2

## Physiological and Clinical Background

### 2.1 Anatomy and Function

The human heart (**Figure 2.1**) is the muscular organ responsible for the distribution of blood and oxygen throughout the human body. Located in the inferior mediastinum, it receives deoxygenated venous blood from the systemic circulation through the venae cavae. Blood from the lower extremities, the pelvis and the abdomen is pumped to the right atrium via the inferior vena cava. Concurrently, blood from the upper extremities and the head arrives via the superior vena cava to the right atrium. The blood is then pumped through the tricuspid valve into the right ventricle (RV). The function of the RV is to transfer the blood through the pulmonary valve and the pulmonary artery into the lungs for oxygenation. Oxygenated blood is then transported back through the pulmonary vein into the left atrium and passes the mitral valve to arrive at the left ventricle (LV). From there, it is finally pumped through the aortic valve into the aorta and distributed back into the circulatory system. Governed by the autonomous conduction system, this pumping process involves alternating contraction (i.e. systole) and relaxation of the heart muscle (i.e. diastole). The muscle tissue of RV and LV is called the myocardium. The interface at the inner border of the myocardial wall is called endocardium, while the myocardium at the outer border is called epicardium. The myocardium is supplied with oxygen via the coronary arteries (**Figure 2.1 B**). The coronary arteries include the right coronary artery and the left coronary artery, the latter consisting of the circumflex and the left anterior descending arteries. The coronary arteries are rooted in the aortic sinus just downstream of the aortic valve.

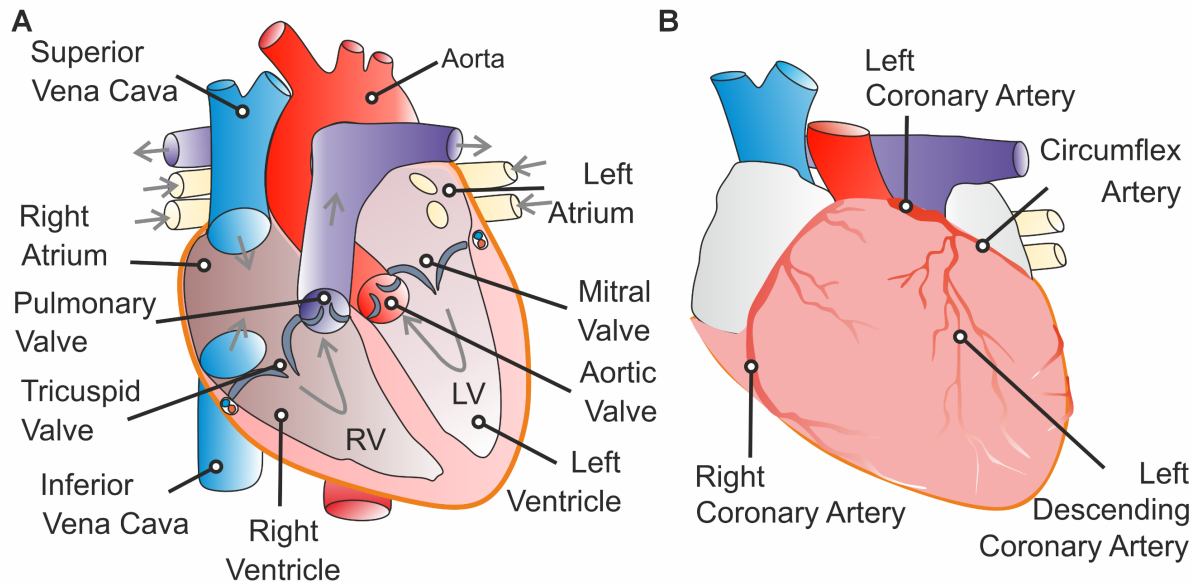


**Figure 2.1:** The human heart from the inside (A) and with the main coronary arteries from the outside (B). Figure adapted and recreated from (40).

Redistribution of the deoxygenated blood from the myocardium is conducted by coronary veins, which drain into the so-called coronary sinus in the right atrium. The distinctive feature of myocardial perfusion is that the filling of the coronary arteries happens mostly during the diastolic phase of the heart cycle. During the contractile, systolic phase, myocardial tissue and its vessels are compressed with decreased perfusion.

## 2.2 Physiology of Myocardial Perfusion and Stress

The following review closely follows the textbook on Human Physiology by Pape et al. (41). Myocardial perfusion is pivotal to provide the heart muscle with oxygen ( $O_2$ ) and relevant metabolic substances, such as adenosine triphosphate (ATP), to provide energy to the myocardial muscle cells (i.e. myocytes). Vice versa, the removal of metabolic waste products and carbon dioxide ( $CO_2$ ) is required. An increase in physical activity requires more oxygen supply to the body and thus increased cardiac work. At the same time, the demand in oxygen in the myocardium rises. It can either be satisfied by increased oxygen uptake from the blood or by increasing the myocardial blood flow (MBF). The MBF is 0.7-0.8 ml/g tissue/min at resting state, which corresponds to 5% of the total cardiac output per minute (i.e. heart minute volume). The unique feature of the coronary system is its remarkably high oxygen extraction rate from blood of 10-11 ml  $O_2$ /min/100g tissue at resting state. Under exercise, MBF increases 4-5 times the normal MBF. The ratio of coronary blood flow under stress and at rest is referred to as the coronary flow reserve (CFR). Under exercise, myocardial oxygen consumption increases 4-5 times. In theory, the higher demand can be met with an increase of blood flow or oxygen extraction. As the rate of oxygen extraction is already

quite high, adaptation to exercise is delivered almost exclusively through increased blood flow. MBF can be increased 4-5 times the resting rate at maximum. The ratio of coronary blood flow under stress to flow at rest is referred to as the coronary flow reserve (CFR).

The MBF is regulated by complex physiological mechanisms which are governed by physical, neuro-hormonal, metabolic and endothelial factors. Coronary flow is directly affected by physical factors like pressure in the aorta, the left ventricle and the right ventricle. Neuro-hormonal regulation is imposed by the vegetative nervous system with its main biochemical neurotransmitters epinephrine and norepinephrine (i.e. catecholamines). While norepinephrine mainly acts on alpha-1-adrenergic receptors with a systemic vasoconstrictive effect, it also acts on beta-1-adrenergic receptors in the heart (although less potent than epinephrine). Increased cardiac output is induced through the following effects of beta-1-adrenergic receptor activation: increased contractility (i.e. positive inotropic effect), increased heart rate (i.e. positive chronotropic effect), increased electric conduction rate (i.e. positive dromotropic effect) and increased relaxation during the diastolic phase (i.e. positive lusitropic effect). This increases the oxygen demand, which in turn triggers a metabolic response for a net vasodilation of the coronary vessels, to combat the systemic vasoconstriction caused by catecholamines. The endothelial part of the vessel wall can be stimulated by norepinephrine, acetylcholine, histamine and ATP to produce nitric oxide (NO), which prompts the relaxation of the smooth muscle cells surrounding the vessel walls. Furthermore, endothelial cells can produce prostaglandins, adenosine and other factors which also act as vasodilators. Including vasoconstrictive endothelial factors, endothelial factors are crucial due to their direct proximity and close interaction with the myocytes.

Diagnostic coronary vasodilation can be induced by physical exercise or by pharmacological stress. Pharmacological interventions target either adrenergic or adenosine receptors. Dobutamine primarily acts on beta-1-adrenergic receptors in the heart which leads to increased heart work and thus a demand-meeting increase in myocardial perfusion. Its vasoconstrictive (alpha-1-adrenergic receptors) and vasodilating (beta-2-adrenergic receptors) effects mostly cancel each other out, making dobutamine an excellent emergency drug in cardiac shock (i.e. failure of adequate pumping function).

Vasodilators such as adenosine, regadenoson and dipyridamole act on endothelial adenosine receptors ( $A_{2A}$ ) in the coronary vessels, forcing vascular smooth muscle cells to relax. Adenosine acts on all  $A_1$ ,  $A_{2A}$ ,  $A_{2B}$  and  $A_3$  adenosine receptors. It has a very short half-life time of less than 10 seconds, which requires continuous administration to induce vasodilation on a minute timescale. In comparison, regadenoson acts selectively on  $A_{2A}$  adenosine receptors and has a half-life time of 20 minutes. Dipyridamole indirectly increases the adenosine concentration in vascular cells by inhibiting the reuptake of endothelial-produced adenosine.

While being established drugs for diagnostic coronary vasodilation, adenosine, regadenoson and dipyridamole cause common side-effects such as chest pressure/pain, shortness of breath, headache, dizziness, nausea or flushing. Of note, adenosine prolongs and/or blocks the transmission of electrical signals between the atrium and the ventricle, especially when administered as a bolus. In rare cases, the continuous administration during stress examination can lead to an atrioventricular (AV) block i.e. a partial to complete interruption of the electrical transmission between atrium and ventricle (4). It is hence contraindicated in patients with higher degrees of AV blocks (2<sup>nd</sup> or 3<sup>rd</sup>) or “sick sinus syndrome”.

## 2.3 Coronary Artery Disease

In coronary heart disease (CAD) the lumen of coronary vessels is reduced as a result of the formation of atherosclerotic plaques in the arterial walls, leading to reduced coronary flow  $Q$  given reduced vessel  $r$  as given by the Hagen-Poiseuille’s law:

$$Q = \frac{\pi \cdot r^4 \cdot \Delta p}{8 \cdot l \cdot \eta} \quad (2.1)$$

with  $\eta$  being the dynamic blood viscosity and  $\Delta p$  the pressure gradient over the length of the vessel  $l$ .

Under stress, the narrowing of the vascular lumen can prevent an appropriate increase of blood flow, which results in a mismatch between oxygen demand and tissue supply, i.e. ischemia. In acute myocardial ischemia, symptoms such as chest pain and dyspnea can occur. If plaques rupture, thrombus formation may lead to a total occlusion of the affected vessel. If left untreated, this can result in acute damage of myocardial tissue and, consequently, in myocardial infarction (MI). Chronic undersupply of myocytes eventually leads to the formation of a scar, starting in the subendocardial tissue, where, due to the high myocardial wall stress, the highest amount of energy and thus oxygen is consumed.

Viability is the ability of dysfunctional tissue to recover either after a short-term ischemia that only occurs during stress or after revascularization, i.e. the interventional opening of occluded coronary vessel segments. These two phenomena are referred to as stunning or hibernation, respectively. After an occlusion of more than 6 hours, however, tissue damage must be considered irreversible.

Besides the macrovascular or epicardial coronary lesions, pathological changes of the microvasculature can occur, leading to microvascular disease (MVD). However, both entities may express themselves with similar symptoms and the measurement of the extent of stenosis does have no accurate implication for the treatment. Only perfusion assessment under stress can reveal the exact pathological implications (6). Relative to catheter-based fractional flow reserve (FFR) measurements (42), which serve as a reference method, CMR perfusion imaging has been shown to be adequate for detecting epicardial coronary disease (6) without using ionizing radiation.

## 2.4 Diagnostic Imaging

Following the guidelines of the European Society of Cardiology (43), patients with suspected CAD are recommended to undergo stress testing (44). For a low pretest probability, an anatomical assessment of stenoses and calcium scoring using computed tomography (CT) can be sufficient to diagnose. To assess tissue perfusion, nuclear imaging techniques such as single-photon emission tomography (SPECT) and positron emission tomography (PET) can be utilized, which, however, provide limited spatial resolution, are not always available and involve radioactive tracer materials to be injected into the patient. Among the nuclear imaging techniques, diagnostic accuracy and image quality of PET have been shown to be superior as compared to SPECT (45).

CMR is a non-ionizing technique that provides morphological anatomical information in addition to function, viability and perfusion assessment. Generally, CMR offers more detail on anatomical information. Its higher spatial resolution compared to nuclear imaging methods allows to resolve the transmural extent of perfusion gradients across the myocardium. Moreover, CMR perfusion showed higher sensitivity and superiority for the non-invasive detection of CAD than SPECT (46,47). Because of its high reproducibility, non-ionizing radiation and good image quality, CMR has emerged as equally rated with echocardiography and PET for the non-invasive assessment in patients with suspected CAD (48). While before PET has been the gold-standard for perfusion imaging, also allowing to measure viability and function, CMR offers significantly higher spatial resolution (45). Another disadvantage of PET is that stress perfusion and viability assessment require administration of two different contrast agents, i.e.  $^{13}\text{N}$  ammonia and  $^{18}\text{F}$  FDG, respectively (49) adding to the burden of ionizing contrast agent exposure and patient compliance. However, a disadvantage of CMR perfusion relative to PET is that image acquisition is distorted by respiratory motion. While PET imaging is conducted in shallow breathing, for CMR, breath holds are the clinically established motion compensation strategy for visual grading and quantification of the first-pass perfusion.

More advanced quantification models meanwhile offer additional kinetic parameters, but require uncorrupted signal-time information beyond the first-pass, i.e. over more than 30 seconds, and thus require free-breathing acquisitions with additional motion compensation (50). Even more important than improved quantitative perfusion modelling, acquisition in breathhold has been limiting, in particular, during adenosine-induced stress. In order to increase patient comfort and compliance CMR perfusion ultimately aims for free-breathing acquisition.

## 2.5 Cardiac and Respiratory Motion

Under physical or pharmacologically-induced stress, heart rates reach up to 100 bpm or higher. The duration of systole is mainly unaffected ( $\sim 350$  ms) while the duration of diastole shortens (51). In order to avoid organ motion induced blurring and motion artefacts, data acquisition needs to be restricted to a window where the heart is in relative stasis, i.e. in the end-systolic or mid-diastolic phase. In end-systole, the heart is contracted along its long and short axis, leading to a thickened myocardium. This state supports whole-heart coverage and the assessment of the transmural perfusion deficits, although systolic pressure compresses arteries and leads to relative cessation of flow (52). Of note, the contractile motion during systole is not solely radial. Due to the helical alignment of myocytes, a component of torsion is added over the LV myocardium from apex to base (51). The quiescent phase in end-systole is very short ( $\sim 50$  ms) as compared to mid-diastole ( $>250$  ms). However, while the duration of the end-systole is comparatively constant, the diastasis phase is highly heart rate dependent and varies between  $>250$  ms and  $<50$  ms for heart rates between rest and stress, respectively (53,54). In comparison, the maximal difference of end-systolic phase under stress is  $\sim 10\%$  (55). At rest, 3D perfusion imaging with conventional acquisition windows of 190 ms to 250 ms (17) is advantageous in mid-diastole because of the long quiescent phase. Nevertheless, end-systolic and diastolic imaging have been shown to be comparable for a 3D acquisition window of 145 ms (56). The duration of one respiratory cycle is 4-5 seconds at rest and may shorten under stress, as shown in Figure 2.2 A for one volunteer, but are generally highly subject specific (57). The main direction of respiratory-induced translation and deformation of cardiac structures caused by the diaphragm is in the superior-inferior direction, i.e. head-feet, while the chest wall moves in the anterior-posterior direction (58). The diaphragm movement can be regarded as a linearly translated motion of the heart with hysteresis (51,59). While this linearity suggests a mainly rigid-deformation of the heart during breathing, 3D deformation studies showed residual non-rigid deformation with high inter-subject variability (60). While the diaphragm movement is often considered as rigid translational deformation of the heart during breathing (51,59), 3D deformation studies showed non-rigid deformation with high inter-subject variability (60). Respiratory organ motion modeling in the context of motion compensation further indicated that heart breathing motion can be highly intra- and inter-breathing-cycle variant (61). Exemplary displacement fields for non-rigid deformation due to respiratory motion are shown for one volunteer in Figure 2.2 B.



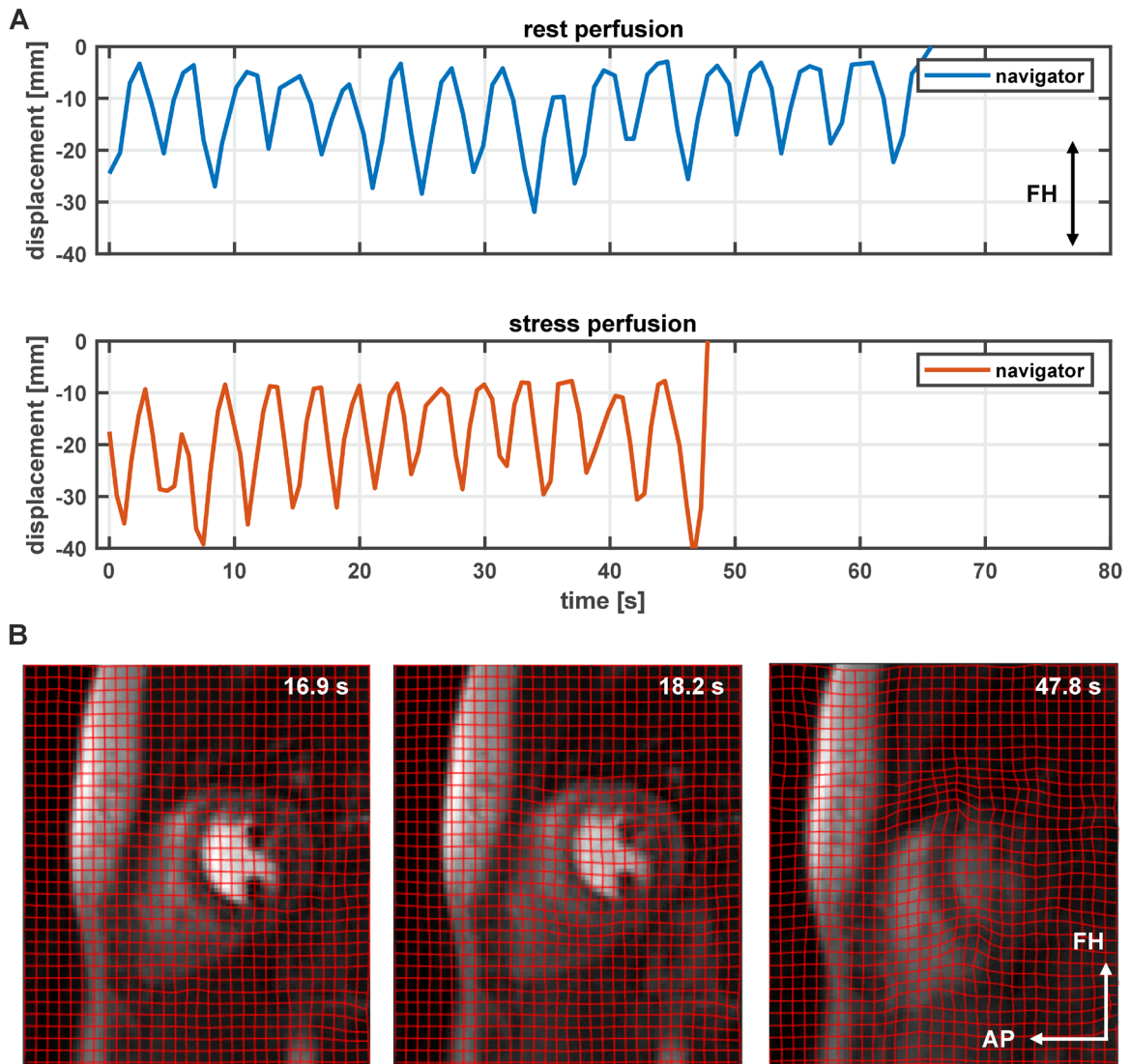


**Figure 2.2:** Breathing patterns in feet-head direction as determined by diaphragm navigator in feet-head (FH) direction (A) in a volunteer under rest and pharmacological stress. Average heart rates at rest and stress were 72 bpm and 100 bpm, respectively. (B) Displacement fields obtained from non-rigid registration at stress. The chest wall moves in the anterior-posterior (AP) direction. Relative timings are indicated by triangular markers in (A).

# Chapter 3

## CMR Perfusion Imaging

### 3.1 Non-contrast Enhanced Perfusion Imaging

Arterial spin labeling (ASL) is an endogenous contrast technique to map the perfusion of water. In ASL, blood is magnetically labeled (62) and subsequently imaged with a delay to ensure that the labeled blood has extravasated into myocardial tissue. A 'control' experiment without the 'label' pulse is performed in addition. The resulting difference image is perfusion-weighted and can be quantified using dedicated perfusion labeling and modeling (63–65). A disadvantage of ASL is that the perfusion-weighted signal is comparatively low due to low concentration of labeled spins in the imaged tissue and T1 effects (66). Moreover, ASL is inherently sensitive to motion and physiological noise (67).

Native T1 mapping (68,69) is another technique to indirectly probe perfusion differences between ischemic and normal tissue. In theory, coronary vasodilation is concomitant with an increasing amount of myocardial water and thus results in increased T1 values. This can be referred to as changes in myocardial blood volume during ischemia (70). In a proof-of-concept study T1 mapping under rest and adenosine stress was used to differentiate ischemic tissue (71), and further works have aimed at contextualizing these findings (72–76). It is yet to be seen whether clinical relevance can be established (77).

Another alternative is to use oxygenation-sensitive CMR by exploiting blood oxygenation level dependent (BOLD) contrast. Using BOLD, differences between diamagnetic deoxygenated and paramagnetic oxygenated hemoglobin are imaged using T2\*-sensitive sequences (78). Given the low contrast-to-noise ratio of BOLD CMR, long scan durations are required, which in turn prevent using pharmacological stressors. Instead, the mixture of the air inhaled by the patient has been modified to manipulate the partial CO<sub>2</sub> pressure in the blood to induce vasodilation or vasoconstriction of the myocardial capillaries, respectively (79). Alternatively, hyperventilation may be used to reduce blood CO<sub>2</sub>, which induces vasoconstriction and thus reduces oxygen supply along with increased amount of deoxygenated blood (80,81). The technique has been shown to detect changes in oxygenation in patients with heart failure

and stenoses (82). However, the methodology requires further validation in larger cohort studies to elucidate its potential for diagnosis (83).

## 3.2 Contrast-enhanced Perfusion Imaging

Contrast-enhanced CMR perfusion imaging uses paramagnetic contrast agents, which alter T1 relaxation times. The apparent relaxation time  $T_1(t)$  is dependent on the administered Gadolinium concentration  $c(t)$  for a specific relaxivity  $r_1$  according to (84):

$$\frac{1}{T_i(t)} = \frac{1}{T_{i,0}} + r_i \cdot c(t) \quad (3.1)$$

where  $i = 1,2$  correspond to the longitudinal and transverse relaxation times, respectively.  $T_{i,0}$  refers to the relaxation time before enhancement. In order to achieve high T1 contrast, saturation-recovery (SR) sequences are employed, where a  $90^\circ$  RF saturation pulse (i.e. adiabatic, single  $90^\circ$  or composite  $90^\circ$ ) is applied as magnetization preparation according to (85)

$$S_{SR} \propto 1 - \exp(-t_{SAT}/T1). \quad (3.2)$$

The choice of saturation delay time ( $t_{SAT}$ ) is a trade-off between good SNR after long recovery of longitudinal magnetization (>400 ms) and acceptable contrast (~100 ms) (86). **Figure 3.1** depicts exemplary CMR perfusion images and signal intensity curves in a patient with ischemia. Regions-of-interest labeled as ischemic show reduced signal intensities as compared to healthy tissue.

Contrast-enhanced CMR perfusion imaging has been widely adopted in the research and clinical settings (7,9,28,86–91). In the landmark CE-MARC study (7) the diagnostic performance of the technique has been documented relative to SPECT imaging. Following this trial, MR-INFORM provided the evidence that CMR imaging is a valid tool to stratify patients (90). The more recent GadaCAD studies established the sensitivity and specificity of Gadolinium for detection of CAD by assessing myocardial perfusion and LGE imaging and showed the diagnostic accuracy (9). While Gadolinium was previously only approved for off-label use in the U.S., this study led to the FDA approval of Gadolinium enhanced CMR to assess myocardial perfusion and LGE for this indication (9). Investigation of long term prognostic value of stress perfusion CMR in a large patient cohort showed that stress CMR is well tolerable and inducible ischemia is a valid predictor for higher incidence of major adverse cardiovascular events (91).

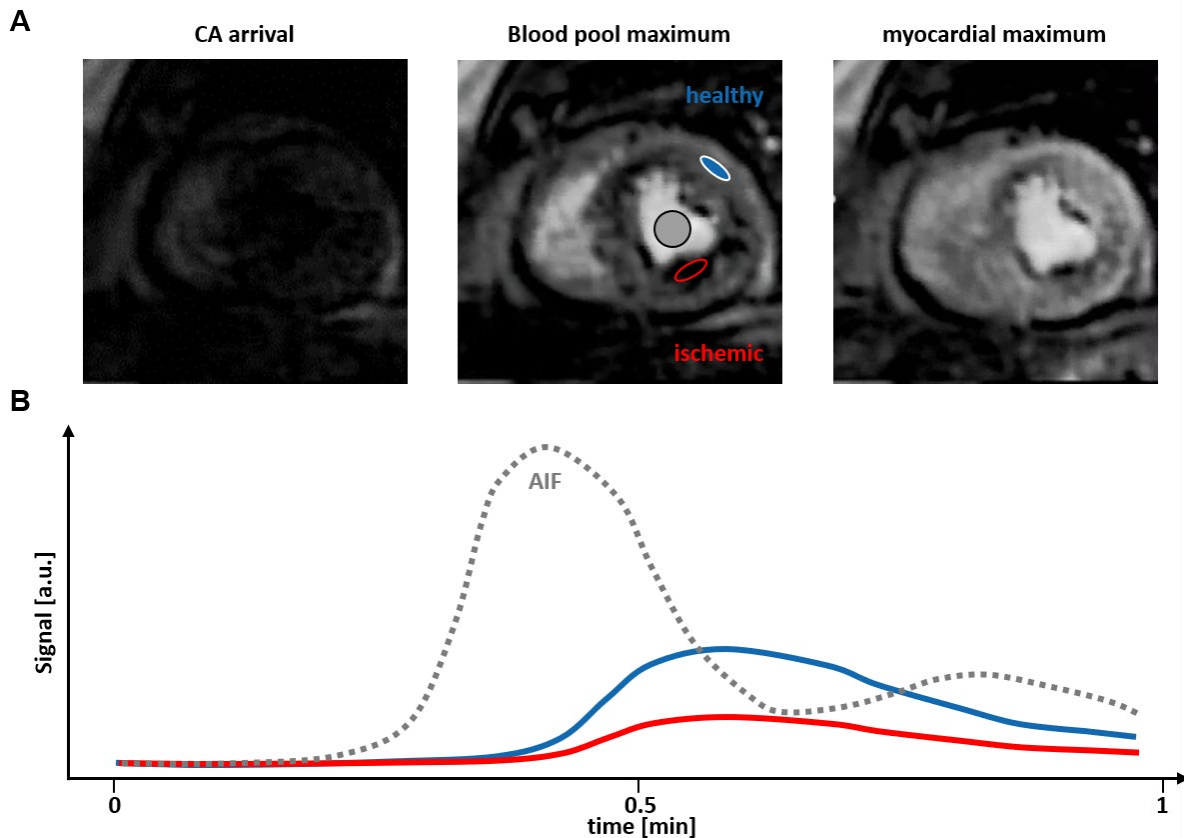


**Figure 3.1:** First-pass perfusion image time series in a patient with ischemia (red circle). (A) Perfusion images from time frames at (left to right) contrast agent (CA) arrival in the RV, maximum left ventricular blood pool (grey circle) enhancement and at myocardial maximum. (B) Corresponding signal time curves for blood pool (i.e. arterial input function (AIF)), healthy myocardium and ischemia in dotted grey, blue and red, respectively.

Although DCE CMR can be categorized as being a non-invasive method as e.g. compared to cardiac catheterization, the administration of an extrinsic contrast agent is still necessary. Among paramagnetic contrast agents, Gadolinium (i.e. Gadobutrol) is effective due to its molecular structure (92). As free Gadolinium is highly toxic, it is shielded by either linear or macrocyclic chelates. However, Gadolinium might detach from the protecting chelate, especially in less stable linear chelates. In the past, two problematic side effects have been identified in the context of exposure with Gadolinium. Nephrogenic systemic fibrosis (NSF) has been reported and associated with the injection of Gadolinium in patients with severe renal impairment or dialysis (93,94). After investigation by several agencies, including EMA and FDA, the use of macrocyclic instead of linear Gadolinium chelates has been recommended. As reported by Ramalho et al. (95), no new cases of NSF have been reported since 2009, which the authors associate with the use of macrocyclic agents, smaller doses and restricted use in patients with renal failure. Another concern has been the dose-dependent retention of Gadolinium in several organs (i.e. primarily in the brain and bones) also in patients with normal renal function (96–98). This finding has been associated with

limited kinetic inertness of linear agents (99,100). While the EMA consequently suspended sales of four linear Gadolinium contrast agents (101), the FDA issued a safety announcement and recommended a consideration of the retention characteristics of each agent especially for patients with higher risk of Gadolinium deposition (102). Efforts are made to further investigate potential Gadolinium deposition as well as better characterization of symptoms associated with Gadolinium exposure (103,104). General considerations regarding the use of contrast material in cardiovascular imaging were reviewed by Paiman et al. (105).

### 3.2.1 Strategies for Whole-heart Perfusion Imaging

First-pass perfusion imaging has basic requirements (17,106) and protocol recommendations (4). A low temporal footprint is decisive to mitigate image artefacts due to intra-cardiac motion; a quiescent cardiac phase between mid- and end-diastole is commonly used, which, however, limits the duration of acquisition window. Spatial in-plane resolution is recommended to be  $<2.5$  mm, allowing visual assessment of sub-endocardial ischemia and its transmural extent. Slice thickness should be  $<8$  mm. The LV has to be covered with a minimum of three slices in short-axis orientation. This allows for left-ventricular segmentation as proposed by the American Heart Association (AHA) (107). Ideally, a linear relationship between administered bolus concentration and signal intensity as indicated in Equation (3.1) is ensured, or correction methods need to be applied. Quantitative perfusion analysis (106,108) requires an accurate measurement of the arterial input function (AIF).

For image readout, spoiled gradient echo (SPGRE) (109) sequences with low flip angles are used for repeated excitation of the slice volume. Every excitation is succeeded by the acquisition of a single line in k-space. In balanced steady state free precession (bSSFP) (110), dephased transverse magnetization is refocused to keep the gradient moment constant at zero phase in all gradient directions. The SNR thus tends to be higher as compared to SPGRE. Especially for static magnetic fields at 3 T, bSSFP imaging can result in high SAR values and sensitivity to off-resonances. While reduced SAR limits lead to imaging speed deceleration, frequency shifts due to off-resonances can cause band and ringing artefacts (106,111,112).

In Figure 3.2 a summary of multiple strategies for perfusion imaging sequences aiming for full heart coverage is shown. In 2D, three to four slice readouts with individual SR magnetization preparation pulses can be covered per heart cycle. For absolute perfusion quantification the fourth slice may comprise the acquisition of the AIF at the root of the ascending aorta or in the LV base. Signal saturation of the AIF can be prevented by reduced  $t_{SAT} < 20$  ms. The AIF acquisition window can be reduced to  $\sim 50$  ms and allows acquisition in end-diastole. Interleaving of imaging and quantification acquisition using one contrast agent administration is referred to as dual-sequence single-bolus acquisition scheme (113). The order of

perfusion imaging and AIF acquisition can be inverted. Total duration for 3 slices plus AIF of ~500 ms allows acquisition for heart rates of ~120 bpm.

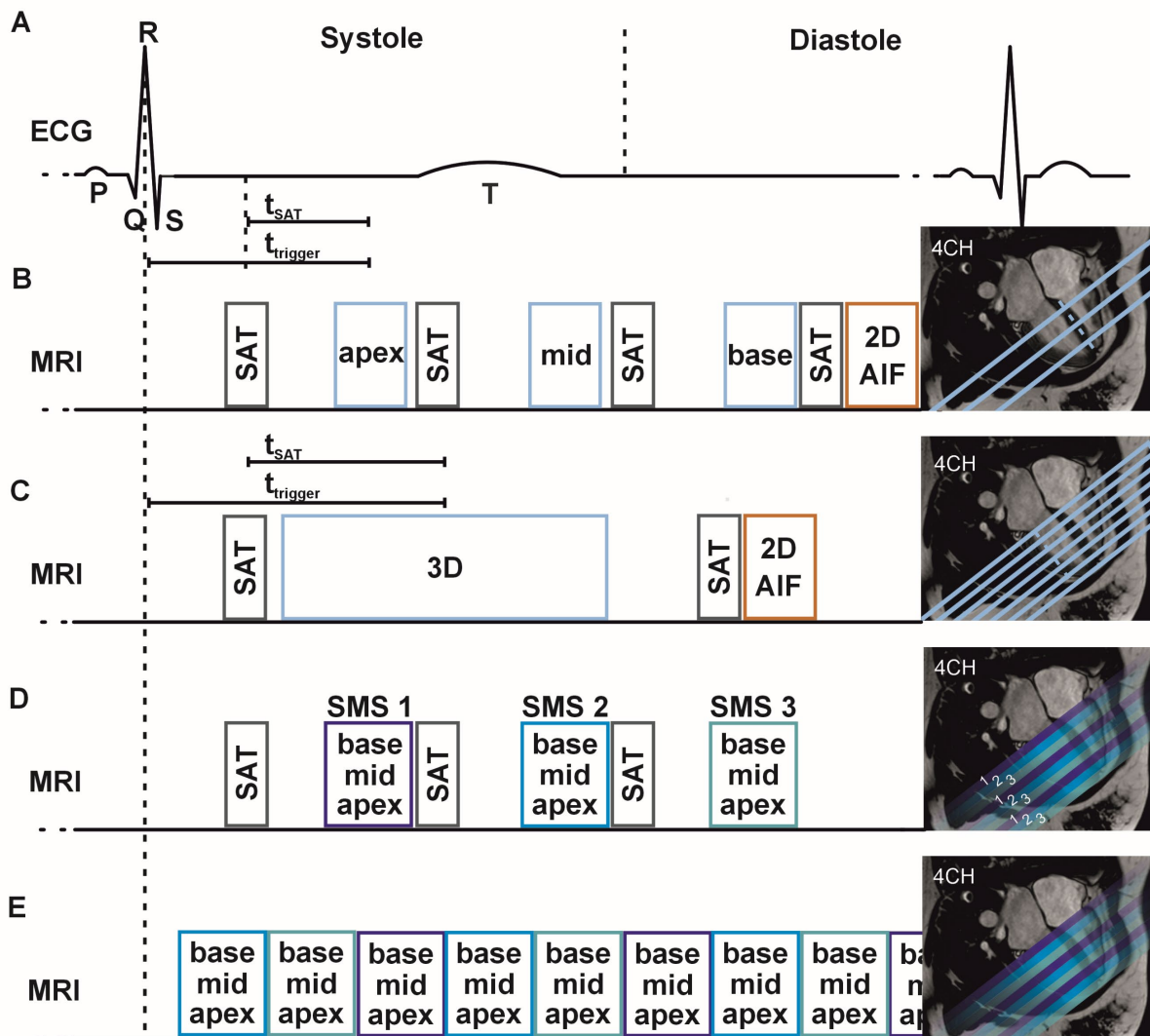


**Figure 3.2:** Summary of acquisition schemes. (A) Electrocardiogram (ECG) to estimate the relative temporal heart cycle dimensions. (B) Conventional clinical acquisition of an apical (apex), a midventricular (mid) and a basal (base) 2D slice as indicated in the inset of cine image in 4 chamber view. The 90° saturation pulse is followed by 2D readout after saturation delay ( $t_{SAT}$ ). Readout per slice is triggered to R wave by trigger delay time ( $t_{trigger}$ ). For absolute perfusion quantification a 2D slice for the acquisition of the arterial input function (AIF) is interleaved. (C) Temporal positioning of 3D first-pass perfusion sequence with acquisition in systole, acquisition window ( $t_{ACQ}$ ) and AIF acquisition in diastole. (D) Simultaneous multi-slice (SMS) acquisition for whole-heart coverage in three slice groups. (E) SMS sequence for continuous acquisition without ECG gating. Times of acquisition from boxes are not to scale.

Most 3D perfusion CMR is based on a similar acquisition scheme as shown in Figure 3.2 C. Following saturation recovery magnetization preparation, a 3D volume covering the LV from apex to base is acquired. Non-quantitative works using Cartesian acquisition schemes have been reported in the past for

CMR perfusion imaging (14–16,114–118) with an acquisition window ranging from 190 ms to 250 ms (17). Quantitative 3D Cartesian dual-sequence single-bolus acquisition has been reported by Wissmann et al. (119) with a 3D acquisition window of  $\sim 250$  ms and  $t_{SAT} = 150$  ms. Temporal footprint of AIF acquisition was  $\sim 60$  ms at  $t_{SAT} = 30$  ms. In similar fashion 3D perfusion has been reported for radial trajectories with an acquisition window of 310 ms (120). Fair et al. (19) leveraged stack-of-radials with variable density to achieve an acquisition window of 188 ms. Mendes et al. (20) further optimized radial SOS and minimized the acquisition window to 150 ms with an interleaved AIF acquisition for interleaved MBF quantification. Images were acquired in free-breathing and under stress. Shin et al. (121) reported 3D perfusion CMR based on a stack-of-spirals with an acquisition window of 230 ms. Wang et al. (122) reported centric and reversed centric 3D stack-of-spirals to be comparable in terms of image quality (250 ms acquisition window and  $t_{SAT} = 150$  ms). Both 3D radial works did not interleave AIF acquisition and required dual bolus administration for perfusion quantification.

Another group of acquisition schemes that can achieve whole-heart coverage are 2D simultaneous multi-slice acquisitions (SMS) (123). In SMS, also referred to as multiband imaging, multiple slice-selective RF pulses are used simultaneously and combined with phase modulation as well as parallel imaging allow the concurrent acquisition of multiple image slices (124–128). Compared to conventional sequential 2D CMR perfusion imaging, multiple slices are acquired in the same duration as a single slice without reduction in resolution. As shown in Figure 3.2 D, CMR perfusion using multiple slice groups for whole-heart coverage in three cardiac phases can be obtained as first proposed by Nazir et al. (129). The acquisition window per Cartesian slice was 175 ms. A similar, also non-quantitative approach, using spiral trajectories perfusion was proposed by Yang et al. with temporal footprints of  $\sim 50$  ms (130). Tian et al. (131) used radial-based SMS with comparable image quality. Absolute perfusion quantification from SMS using a dual-bolus approach has been reported (132). Quantification using dual-sequence, single-bolus has been shown with alternating heart-cycle acquisition (133).

For continuous acquisition, SR radial SMS ungated perfusion as shown in Figure 3.2 E (134) can be used. This has been extended towards motion resolved quantitative perfusion from dual sequence acquisition by Tian et al. (135). The continuous acquisition required a dual bolus approach for perfusion quantification.

However, for SMS imaging, banding artefacts especially at higher field strength as well as reduced SNR can be a problem (136). In that regard, 3D acquisitions are advantageous as relative SNR for 3D compares to 2D as (17,137):

$$\text{SNR}_{3D} \propto \text{SNR}_{2D} \cdot \sqrt{N_z} \quad (3.3)$$

where  $N_z$  is the number of partitions along the longitudinal direction of the heart.

### 3.2.2 3D Cartesian k-Space Trajectories

Regular undersampling along a sheared k-space can readily be applied to 3D volumes and has been successfully deployed for 3D FPP as k-t undersampling (114,138).

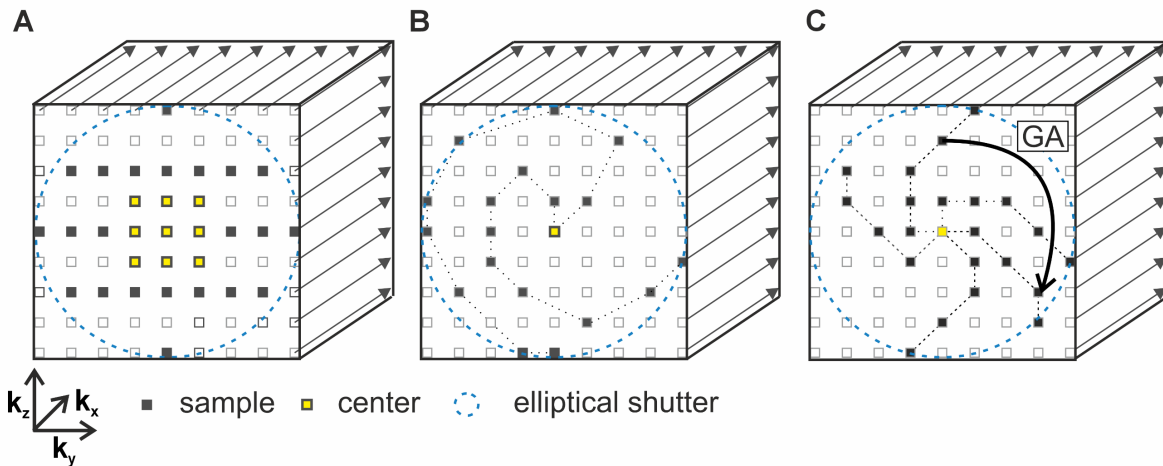


**Figure 3.3:** 3D Cartesian k-space trajectories for a single time frame. (A) Outline of basic k-t sampling pattern with undersampling on a sheared grid. (B) Cartesian pseudo-spiral out-in golden-angle (GA) trajectory. (C) Pseudo radial out-in sampling trajectory.

In **Figure 3.3 A**, a 3D Cartesian acquisition pattern often used for parallel imaging is shown. It consists of a regular undersampling sheared grid, which is shifted over adjacent temporal time frames. The k-space center (indicated in yellow) is acquired continuously. More samples can be omitted when Hermitian symmetry of k-space is assumed or approximated (139,140). This concept is called Partial Fourier (PF) (141). However, due to the occurrence of phase variations in MR images, Hermitian symmetry is not guaranteed and cannot always be recovered.

In **Figure 3.3 B**, a pseudo-spiral profile ordering scheme is outlined. Consecutive k-space rotation steps are according to the golden angle (GA) (142), which was first deployed for temporal 3D CMR acquisitions as CASPR (143,144). Similarly, pseudo-radial spokes can be prescribed and rotated following the GA, which was introduced as VDRad (**Figure 3.3 C**) (144).



### 3.2.3 Non-Cartesian k-Space Trajectories

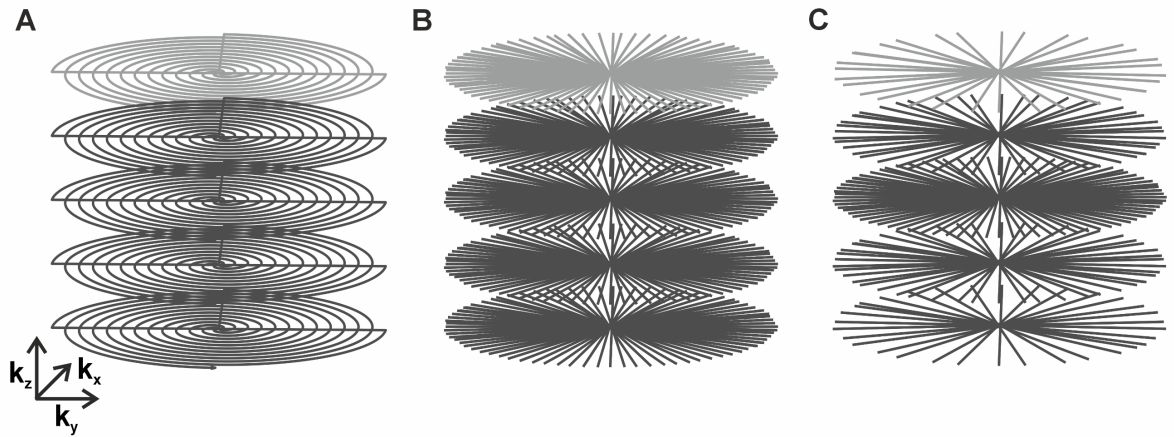


**Figure 3.4:** Arbitrary k-space trajectories. (A) Stack of spirals. (B) Radial stack of stars. (C) Radial stack of stars with variable density along  $k_z$ -dimension and tiny golden angle distribution  $\Delta\phi = 23.6^\circ$ . For all trajectories, partial Fourier acquisition along the  $k_z$ -dimension is indicated by light grey trajectories.

The spiral trajectory can cover the full k-space in a single shot with either continuous or variable density. If the temporal interval is limited, multiple successive interleaves ( $N_{INT}$ ), i.e. spiral arms, can be implemented. As well as for Cartesian EPI, spiral acquisition with long readout train suffers from off-resonance effects (145). Hence, a saturation pulse followed by multiple interleaves is favorable. FPP imaging can benefit from variable density sampling (146). Spatial coverage can be achieved by either 3D spherical or elliptical trajectories. For 3D FPP, stack of spirals (see **Figure 3.4 A**) has been successfully applied (121,122,147).

Radial sampling trajectories refer to a set of projections, i.e. spokes, which cross the k-space center in a star like pattern. In the simplest case, the angle between adjacent spokes  $\phi$  is equiangular and varies between  $0 < \phi < \pi$  for projections traversing the k-space center. The k-space center is subject to oversampling if the k-space at the end of the spokes is sampled in a Nyquist fashion. The Nyquist criterion is fulfilled at the edge of the spokes if the distance between spokes is limited by (85)

$$k_{max} \Delta\phi \leq \frac{1}{FOV}. \quad (3.4)$$

For sampling as  $\phi \in [0, \pi]$ , the number of spokes  $N_S$  that fulfill the Nyquist criterion at the outskirts of k-space is:

$$N_S = \frac{\pi}{\Delta\phi} = k_{max} \pi FOV. \quad (3.5)$$

Due to the multiple k-space center sampling, a continuous motion-averaging operation is applied. Although radial trajectories are inherently slower than other techniques when the Nyquist criterion is fulfilled at the edges, the trajectories are versatile and flexible in terms of ordering. Similarly, as in Cartesian sampling, Partial Echo and Partial Fourier sampling can be implemented. Further undersampling can be achieved by omitting single spokes in the azimuthal direction. GA sampling is used for optimal profile distribution and tiny GA (TGA) sampling (148) keeps eddy-current artefacts caused by high gradient steps at bay. 3D cylindrical coverage is performed by a stack of 2D radials, depicted in **Figure 3.4 B** and **C** as stack of stars (SOS) and variable density SOS, respectively. SOS sampling has been successfully applied to 3D FPP as undersampled SOS (149) and using variable density SOS in free-breathing (19,20).

### 3.2.4 Theoretical Acceleration Requirements

For 3D FPP sequences reported in literature, the acquisition windows vary between 190 ms and 380 ms (17). Following the conservative approximation of Fair et al. (17), an acquisition window of 150 ms is considered herein and allows the estimation of acceleration needed for sequences based on standard, fully sampled Cartesian, spiral and radial acquisition schemes. Based on the assumption that for Cartesian sampling the Nyquist criterion is fulfilled for

$$N_Y = 2k_{max}FOV. \quad (3.6)$$

Radial projections are Fourier sampled at the outskirts for a number of spokes

$$N_S = \frac{\pi}{2} N_Y. \quad (3.7)$$

Potential scan acceleration can then be calculated based on the following imaging geometry: FOV: 300 x 300 mm<sup>2</sup>, in-plane resolution: 2.5 x 2.5 mm<sup>2</sup>, number of phase encodes  $N_Y = 120$  and number of partitions to cover 100 mm at a resolution of 10 mm is  $N_Z = 10$ . Total acquisition times  $t_{ACQ}$ , referring to the specific parameters obtained from a 1.5 T Philips Achieva MR system, are summarized in **Table 3.1**. In order to compare the relative readout time per profile, the readout durations are given as  $t_{profile}$  (Cartesian/radial) and  $t_{interleave}$  (spiral). Of note, for the fully sampled radial acquisition, the number of required profiles as calculated by the vendor software is not by a factor of  $\pi/2$  higher as suggested by Equation (3.17). Arguably, this is a more realistic scenario since Nyquist sampling at the outskirts of radial profiles results in massive oversampling at the center of k-space. Although being only a rough estimation, it shows that, dependent on the employed trajectory, scan acceleration of  $R>10$  is required. Image reconstruction methods for the highly undersampled data are introduced in the following sections.

	<b>Cartesian</b>	<b>Spiral</b>	<b>Radial</b>
TR/TE [ms]	2.1/1.0 ( $t_{\text{profile}} = 0.45$ ms)	7.7/0.62 ( $t_{\text{interleave}} = 4.75$ ms)	2.5/1.72 ( $t_{\text{profile}} = 0.45$ ms)
$t_{\text{ACQ}} =$	$\text{TR} \cdot N_Y \cdot N_Z$	$\text{TR} \cdot N_Z \cdot N_{\text{INT}}$ ( $N_{\text{INT}} = 14$ )	$\text{TR} \cdot N_S \cdot N_Z$
$t_{\text{ACQ}}$ [ms]	2400 ( $A_{\text{shutter}} / A_{\text{FOV}} = 1920$ )	1079	2980
$R = t_{\text{ACQ}} / t_{\text{ACQ-WINDOW}}$	<b>~16</b> <b>(Shutter: ~13)</b>	<b>~8</b>	<b>~20</b>
Relative acquisition duration per profile [%]	$t_{\text{profile}} / \text{TR} =$ 21.4	$t_{\text{interleave}} / \text{TR} =$ 58.5	$t_{\text{profile}} / \text{TR} =$ 18.0
Total relative acquisition duration [ms]	513 (Shutter: 412)	630	536

**Table 3.1:** Timings of 3D FPP sequences and required undersampling factor  $R$  for acquisition window  $t_{\text{ACQ}} = 150$  ms. For every trajectory, TR, number of profiles in plane ( $N_Y$ ) and/or numbers of partitions along z-dimension ( $N_Z$ ), number of interleaves  $N_{\text{INT}}$  and acquisition duration per interleave  $t_{\text{interleave}}$  (spiral) are from a 1.5 T Philips Achieva MR system. For Cartesian acquisition, reduction in number of profiles by an elliptical shutter is considered by a geometrical reduction factor  $A_{\text{shutter}} / A_{\text{FOV}}$ . The bottom rows refer to the relative acquisition duration per individual readout and its extrapolation to the acquisition duration of the 3D volume.

## 3.3 Accelerated Image Reconstruction

### 3.3.1 Image Reconstruction Formalism

The standard model for MR image encoding can be described as

$$\mathbf{d}(\mathbf{k}) = \int_V \rho(\mathbf{x}) e^{-j\mathbf{k}\mathbf{x}} d\mathbf{x}, \quad (3.8)$$

where  $\mathbf{d}$  is the data and  $\rho(\mathbf{x})$  the continuous distribution of transverse magnetization in the excited imaging volume  $V$ . In the k-space formalism, the k-space vector  $\mathbf{k}$  is the time integral of the gradient vector  $\mathbf{G}(t)$ :

$$\mathbf{k} = \gamma \int_0^\tau \mathbf{G}(t) dt, \quad (3.9)$$

where  $\tau$  refers to the time during which the gradient is switched on. If the distribution of magnetization  $\rho(\mathbf{x})$  is assumed to be rasterized, the MR signal can be written as a discrete Fourier transform:

$$\mathbf{d}(\mathbf{k}) = \sum \rho(\mathbf{x}) e^{-j\mathbf{k}\mathbf{x}}. \quad (3.10)$$

In vector matrix notation, the acquired complex valued k-space data  $\mathbf{d}(\mathbf{k})$  is given as:

$$\mathbf{d} = \mathbf{E}\boldsymbol{\rho} + \boldsymbol{\eta}, \quad (3.11)$$

where  $\boldsymbol{\rho}$  is the discretized image object,  $\mathbf{E}$  is the corresponding encoding matrix and  $\boldsymbol{\eta}$  is the acquisition noise vector. For zero-mean Gaussian noise  $\boldsymbol{\eta} \sim \mathcal{N}(0, \sigma_d^2 \text{Id.})$  the linear model can be solved in the least squares sense to obtain an estimate  $\hat{\mathbf{i}}$  of the object  $\boldsymbol{\rho}$  as:

$$\hat{\mathbf{i}} = \underset{\mathbf{i}}{\operatorname{argmin}} \|\mathbf{E}\mathbf{i} - \mathbf{d}\|_2^2. \quad (3.12)$$

The  $\ell_2$ -norm is given by  $\|\cdot\|_2 = (\sum_i |x_i|^2)^{1/2}$  and enforces data consistency. Using the normal equation, one obtains:

$$\hat{\mathbf{i}} = (\mathbf{E}^H \mathbf{E})^{-1} \mathbf{E}^H \mathbf{d} = \mathbf{E}^\dagger \mathbf{d}, \quad (3.13)$$

where  $\mathbf{E}^\dagger$  is the pseudo-inverse of  $\mathbf{E}$ .

### 3.3.2 Parallel Imaging

By utilizing the spatial information of multiple receiver coils, acceleration can be achieved using parallel imaging (PI) methods. In standard SENSE PI (150), uniform undersampling using sampling mask  $\mathbf{\Omega} \in \{0,1\}^{N_s N_c \times N_s N_c}$  leads to equidistant fold-over artefacts, i.e. aliasing artefacts in the image domain. To resolve the artefact, the coil sensitivities of  $N_c$  coils need to be calculated for all voxels  $N_v$  to obtain  $\mathbf{C} \in \mathbb{C}^{N_c N_v \times N_v}$ . The reconstructed image  $\hat{\mathbf{i}} \in \mathbb{C}^{N_v}$  from k-space data  $\mathbf{d} \in \mathbb{C}^{N_s N_c}$ , containing  $N_s$  k-space samples each can be obtained as (151):

$$\hat{\mathbf{i}} = \underset{\mathbf{i}}{\operatorname{argmin}} g(\mathbf{i}) + h(\mathbf{i}) = \underset{\mathbf{i}}{\operatorname{argmin}} \|\mathbf{E}\mathbf{i} - \mathbf{d}\|_2^2 + \lambda \mathcal{R}(\mathbf{i}), \quad (3.14)$$

where  $g(\mathbf{i})$  and  $h(\mathbf{i})$  are the data fidelity and the regularization term, respectively. The encoding operator is given as  $\mathbf{E} = \mathbf{\Omega} \mathcal{F} \mathbf{C}$ , with the Fourier transform  $\mathcal{F} \in \mathbb{C}^{N_s N_c \times N_v N_c}$ . The regularizer  $\mathcal{R}(\mathbf{i})$  together with regularization coefficient  $\lambda$  allows incorporating appropriate prior knowledge or assumptions about the image. If the reconstruction is applied to non-Cartesian k-space trajectories, the encoding matrix operator  $\mathbf{E}$  additionally incorporates a gridding operator  $\mathbf{G}^\dagger$  that resamples the acquired data onto a rectilinear grid.

For all regularized imaging problems, the optimal regularization parameter  $\lambda$  has to be chosen. It can be selected by minimizing the mean reconstruction error between a fully sampled reference and the reconstruction in case a reference is available. Alternatively, the optimization problem can be constrained if the ideal noise level  $\varepsilon$  is known, i.e. by using a grid search, a  $\lambda$  can be found for which  $\|\mathbf{E}\mathbf{i} - \mathbf{d}\|_2^2 \approx \varepsilon$ . Furthermore, using the L-curve method (152),  $\lambda$  can be chosen based on a trade-off between the data fidelity  $g(\mathbf{i})$  and the regularization term  $h(\mathbf{i})$ .

### 3.3.3 Spatio-temporal Parallel Imaging

The conventional frame-by-frame reconstruction problem can be extended by exploiting spatio-temporal redundancy present in dynamic data. In k-t SENSE (138), prior knowledge is incorporated as a set of low-resolution dynamic training images. A weighted least-squares approach is used to solve for the dynamic image series  $\hat{\mathbf{I}}_{k-t \text{ SENSE}}$  with  $T$  dynamic frames  $\mathbf{I} = [\mathbf{i}_1, \dots, \mathbf{i}_T]$ , where  ${}^{x-f} \mathbf{M}$  denotes the training data in the spatial-temporal frequency domain:

$$\hat{\mathbf{I}}_{k-t \text{ SENSE}} = \underset{\mathbf{I}}{\operatorname{argmin}} \|\mathbf{E}\mathbf{I} - \mathbf{d}\|_2^2 + \lambda \left\| \left( {}^{x-f} \mathbf{M} \right)^{-1} \mathbf{F}_{t \rightarrow f} \mathbf{I} \right\|_2^2. \quad (3.15)$$

Operator  $\mathbf{F}_{t \rightarrow f}$  denotes the Fourier transform to convert from time  $t$  to temporal frequency  $f$ . This reconstruction concept was deployed to CMR perfusion imaging (153,154). A limitation of the approach,

however, is its sensitivity to breathing motion where  $\mathbf{F}_{t-f}$  is the Fourier transform in the temporal domain. After the application of adaptive filtering in x-f space, this process allows for an artefact free repopulation of the k-t space.

To improve the robustness of the approach low-rank properties of the spatio-temporal data were included using principal component analysis (PCA) leading to k-t PCA (155). In k-t PCA, temporal basis functions are derived from the training data by applying a PCA basis transformation  $\mathbf{B}_{f \rightarrow pc}$ . With the training data coefficients  ${}^{x-pc}\mathbf{M}$  the dynamic image series is reconstructed as:

$$\hat{\mathbf{I}}_{kt-PCA} = \underset{\mathbf{I}}{\operatorname{argmin}} \|\mathbf{E}\mathbf{I} - \mathbf{d}\|_2^2 + \lambda \left\| \left( {}^{x-pc}\mathbf{M} \right)^{-1} \mathbf{B}_{f \rightarrow pc} \mathbf{F}_{t \rightarrow f} \mathbf{I} \right\|_2^2. \quad (3.16)$$

k-t PCA has extensively been used for CMR perfusion imaging (14–16,114–118). Schmidt et al. (18) further extended the scheme to include non-rigid motion correction (see section 3.4). While primarily used in conjunction with undersampled Cartesian trajectories, all k-t approaches are applicable to non-Cartesian trajectories as well (156).

### 3.3.4 Compressed Sensing

The theory of Compressed Sensing (CS) was introduced by Candès and Donoho in 2004 (157,158). Its application to MRI can be considered as an extension of iterative PI methods and requires three conditions (158):

- i) Sparsity of signal or transforms thereof.
- ii) Incoherence of undersampling artefacts: Artefacts are of random nature to allow the distinction between undersampling, fold-over artefacts and unfolded signal. Undersampling masks have to be incoherent in time.
- iii) Non-linear image reconstruction (159):

$$\hat{\mathbf{I}}_{CS} = \underset{\mathbf{i}}{\operatorname{argmin}} \|\mathbf{E}\mathbf{i} - \mathbf{d}\|_2^2 + \lambda \|\mathbf{F}_{sp}\mathbf{i}\|_1, \quad (3.17)$$

with  $\mathbf{F}_{sp}$  the sparsifying, e.g. Daubechies-wavelet, transform.  $\|\cdot\|_1$  the  $\ell_1$ -norm given by  $\|\cdot\|_1 = \sum_i |\mathbf{i}_i|$ . The balance between data consistency and the sparsity is controlled by the regularization weight  $\lambda$ .

## Joint Temporal and Spatial Regularization

3D FPP inherently entails sparsity mainly in the spatio-temporal domain and makes it an ideal candidate for the application of CS. The 4D dataset enables a higher compressibility of the dataset as the extra dimension allows for the application of several sparsifying transforms. In practice, the various CS CMR reconstruction methods differ in their application of the sparsified regularization term.

Besides the discrete wavelet transform, total variation (TV) (160) can be employed, which penalizes variation of the signal, favoring piece-wise constant representations. TV can either be applied in the temporal or spatial domain for pixels  $p$  in dimensions  $d$  as  $\text{TV}(\mathbf{I})_t = \|\nabla_t \mathbf{I}\|_1$  and  $\text{TV}(\mathbf{I})_x = \sum_{p \in \text{pixels}} \sqrt{\sum_{d \in \text{dimensions}} |\nabla_d \mathbf{I}|_p^2}$ , respectively. Application in both domains has been deployed as spatio-temporal constrained reconstruction (STCR) for 3D radial SOS FPP (149,161) as

$$\hat{\mathbf{I}}_{\text{STCR}} = \underset{\mathbf{I}}{\text{argmin}} \|\mathbf{E}\mathbf{I} - \mathbf{d}\|_2^2 + \lambda_1 \text{TV}(\mathbf{I})_{\text{spatial}} + \lambda_2 \text{TV}(\mathbf{I})_{\text{temporal}}. \quad (3.18)$$

By Fair et al. (162), this reconstruction was employed to explore free-breathing 3D FPP (see section 3.4). At this point it shall be mentioned that the spatio-temporal redundancies in dynamic data are also exploited for CS in k-t SPARSE (163) for only one coil, in k-t SPARSE-SENSE (164) for multiple coils, thereby reducing blurring, and in k-t FOCUSS (165). Wissmann et al. showed feasibility of kt-PCA, k-t Sparse and k-t SPARSE-SENSE in work on spatio-temporal fidelity in highly-undersampled 3D FPP (166).

A combination of low-rank and sparsity approaches has been proposed for dynamic CMR and perfusion by Lingala et al. as k-t SLR (167,168) for radially undersampled data in 2D. The image reconstruction is posed as a spectrally regularized matrix recovery problem. Temporal image time frames are sorted in a Casorati matrix representation of k-space data, where data per time frame form a column vector  $\mathbf{I} \in \mathbb{C}^{N_x N_y \times N_t}$ , with  $N_x N_y$  k-space samples and  $N_t$  dynamics. Posed in the Casorati form, data can be represented as a combination of spatial ( $\mathbf{U}$ ) and temporal ( $\mathbf{V}$ ) basis functions and a diagonal weighting matrix  $\mathbf{B}$  as  $\mathbf{I} = \mathbf{U}^T \mathbf{B} \mathbf{V}$ . The rank of  $\mathbf{I}$  is defined by the number of non-zero elements in  $\mathbf{B}$ . The spectral and sparsity penalized image reconstruction is then posed as (167,168):

$$\hat{\mathbf{I}}_{\text{kt-SLR}} = \underset{\mathbf{I}}{\text{argmin}} \|\mathbf{E}\mathbf{I} - \mathbf{d}\|_2^2 + \lambda_1 (\|\mathbf{I}\|_{\wp})^{\wp} + \lambda_2 (\text{TV}(\mathbf{I})_{x-t}), \quad (3.19)$$

where the Hessian-Schatten  $\wp$ -norm (169) is used as surrogate for the rank  $(\|\mathbf{I}\|_{\wp})^{\wp} = \sum_{p \in \text{pixels}} \text{SV}(\mathbf{I})_p^{\wp}$  for  $\wp < 1$  and the singular values (SV) of  $\mathbf{I}$ . TV regularization is imposed by  $\text{TV}(\mathbf{I})_{x-t} = \sum_{p \in \text{pixels}} \sqrt{|\nabla_x \mathbf{I}|_p^2 + |\nabla_y \mathbf{I}|_p^2} + \alpha |\nabla_t \mathbf{I}|_p^2$ , where  $\alpha$  controls the relative weight of the temporal TV regularization. Accordingly, kt-SLR is similar to the previously mentioned STCR when  $\lambda_1 = 0$ . Especially in

presence of motion, temporal TV is preferable over Tikhonov regularization as it maintains the non-smoothness of motion. For DCE FPP, temporal TV regularization can introduce staircase artefacts in the signal-intensity time curves as TV promotes piecewise-constant signals.

A related reconstruction concept to kt-SLR was deployed as Low-Rank PLUS Sparse (L+S) matrix decomposition reconstruction (170) based on work by Candès et al. (171). It was proposed as being specifically suitable for DCE CMR. While the relatively static background information can be modeled by a low-rank matrix component, the varying contrast enhancement in the myocardium is modeled by a sparse matrix component (172). The matrix decomposition is a PCA based technique which is able to recover contaminated data from undersampled CMR acquisitions. Accordingly, the low-rank (L) and sparse (S) component have to be found. Image reconstruction is posed as convex optimization with  $\|\cdot\|_*$  being the nuclear norm, i.e. the sum of singular values of  $\mathbf{L}$ , and is identical to the Hessian Schatten  $\wp$ -norm for  $\wp = 1$ . For time-series data,  $\mathbf{d}$  is again reorganized into the Casorati matrix and the problem posed as:

$$\begin{aligned} \hat{\mathbf{i}}_{L+S} = \underset{\mathbf{i}}{\operatorname{argmin}} & \|\mathbf{E}\mathbf{i} - \mathbf{d}\|_2^2 + \lambda_L \|\mathbf{L}\|_* + \lambda_S \|\mathbf{F}^t \mathbf{S}\|_1 \\ \text{s. t. } & \mathbf{i} = \mathbf{L} + \mathbf{S} \end{aligned} \quad (3.20)$$

Among other examples for successful application to CMR purposes, L+S performed well in 8-fold FPP (170). Aliasing artefact reduction without degradation of temporal fidelity as compared to conventional CS has been reported with potential for free-breathing applications in abdominal perfusion.

### Optimization for Compressed-sense Reconstruction

While linear reconstruction problems in PI can be solved iteratively using conjugate gradient descent (173) or gradient descent, non-linear CS require algorithms such as the proximal gradient descent (PGD) method (174) or the alternating direction method of multipliers (ADMM) (175,176). Following work by Boyd et al. (175) and Liu et al. (177), PGD can be used when the reconstruction problem is posed in the synthesis form:

$$\hat{\mathbf{i}} = \underset{\mathbf{i}}{\operatorname{argmin}} \|\mathbf{E}\mathbf{i} - \mathbf{d}\|_2^2 + \lambda \|\mathbf{P}\mathbf{i}\|_1, \quad (3.21)$$

where the operator  $\mathbf{P}$  is invertible. The problem can then be transformed into

$$\hat{\mathbf{i}} = \underset{\mathbf{i}}{\operatorname{argmin}} \|\mathbf{E}\mathbf{P}^{-1}\mathbf{i} - \mathbf{d}\|_2^2 + \lambda \|\mathbf{i}\|_1, \quad (3.22)$$

with  $f(\mathbf{i}) = \|\mathbf{E}\mathbf{P}^{-1}\mathbf{i} - \mathbf{d}\|_2^2$ . The approximation sub problem that has to be solved per iteration is then posed as



$$\operatorname{argmin}_{\mathbf{i}} \frac{1}{2\alpha} \|\mathbf{i} - (\mathbf{i}_0 - \alpha \nabla f(\mathbf{i}_0))\|_2^2 + \lambda \|\mathbf{i}\|_1, \quad (3.23)$$

with  $\alpha$  being the step length. The proximal mapping operator is then defined as

$$\operatorname{prox}_{\lambda, h}(\mathbf{z}) = \operatorname{argmin}_{\mathbf{i}} \frac{1}{2} \|\mathbf{i} - \mathbf{z}\|_2^2 + \lambda h(\mathbf{i}), \quad (3.24)$$

for iteration  $k$  and with  $\mathbf{z}_k = \mathbf{i}_k - \alpha \nabla f(\mathbf{i}_k)$ . The reconstruction problem per iteration step is then posed as

$$\mathbf{z}^{(\kappa+1)} = \mathbf{i}^{(\kappa)} - \alpha \mathbf{E}^T (\mathbf{E} \mathbf{i}^{(\kappa-1)} - \mathbf{d}) \quad (3.25)$$

and

$$\mathbf{i}^{(\kappa+1)} = \operatorname{argmin}_{\mathbf{i}} \frac{1}{2} \|\mathbf{i} - \mathbf{z}_k\|_2^2 + \alpha \lambda R(\mathbf{i}) \hat{=} \operatorname{prox}_{\alpha, \lambda, R}(\mathbf{z}_k). \quad (3.26)$$

Of note, the convergence rate of standard proximal gradient descent is linear ( $O(1/\kappa)$ ) but can be accelerated to  $O(1/\kappa^2)$  by inclusion of Nesterov-acceleration into the proximal gradient method (178).

ADMM optimization is required when  $\mathbf{P}$  in Equation (3.14) is not invertible, e.g. in case of TV regularization, where  $\mathbf{P} = \nabla$ ). The major idea of ADMM is to perform variable splitting and decompose optimization of the data and penalty terms, imposing constraints on the splitted variables:

$$\begin{aligned} \operatorname{argmin}_{\mathbf{z}, \mathbf{i}} g(\mathbf{i}) + h(\mathbf{z}) + \frac{\upsilon}{2} \|\nabla \mathbf{i} - \mathbf{z}\|_2^2 \\ \text{s. t. } \nabla \mathbf{i} = \mathbf{z}, \end{aligned} \quad (3.27)$$

with  $g(\mathbf{i}) = \frac{1}{2} \|\mathbf{E} \mathbf{i} - \mathbf{d}\|_2^2$ ,  $h(\mathbf{z}) = \lambda \|\mathbf{z}\|_1$  and the augmentation parameter  $\upsilon > 0$ . This equivalent augmented constrained optimization problem can be solved using the dual ascent method, yielding ADMM iterations with scaled dual variables:

$$\mathbf{i}^{(\kappa+1)} = \operatorname{argmin}_{\mathbf{i}} \frac{1}{2} \|\mathbf{E} \mathbf{i} - \mathbf{d}\|_2^2 + \frac{\upsilon}{2} \|\nabla \mathbf{i} - \mathbf{z}^\kappa + \mathbf{u}^\kappa\|_2^2, \quad (3.28)$$

$$\mathbf{z}^{(\kappa+1)} = \operatorname{argmin}_{\mathbf{z}} \lambda \|\mathbf{z}\|_1 + \frac{\upsilon}{2} \|\nabla \mathbf{i}^{(\kappa+1)} - \mathbf{z} + \mathbf{u}^\kappa\|_2^2, \quad (3.29)$$

and the dual step:

$$\mathbf{u}^{(\kappa+1)} = \mathbf{u}^{(\kappa)} + \nabla \mathbf{i}^{(\kappa+1)} - \mathbf{z}^{(\kappa+1)}. \quad (3.30)$$

Theoretically, ADMM convergence is similar to PGD ( $O(1/\kappa)$ ) but can be slower when compared to Nesterov-accelerated PGD. However, for both ADMM and PGD, acceleration methods are available (173). Most importantly, ADMM depends on the augmentation parameter  $\nu$  which has to be tuned in addition to the regularization  $\lambda$ . This is also the case for PGD, where the step length  $\alpha$  also has to be chosen. However, an  $\alpha$  for the convergence of proximal gradient steps should be in the order of magnitude of the operator  $\mathbf{E}$  norm for which efficient line search methods exist.  $\nu$  on the other hand can be very difficult to determine in practice (173). While the final image reconstruction is not affected, the convergence rate is highly dependent on proper tuning, which poses a significant disadvantage for reconstruction problems which are posed in the analysis form and thus require ADMM optimization (173).

### Local Low-rank Regularization

Instead of treating dynamic variations by the sparsity regularization term, the low-rank model renders itself sufficient if locally low-rank models are employed (27). Dynamic signal variations have a better chance to be correlated locally if the nuclear norm of distinct local patches (i.e. 3D blocks) is regularized. Thus, spatio-temporal correlation of imaging data is leveraged by penalizing the nuclear norms of patch matrices stacked along time. For zero-filled k-space data, the Casorati matrix is of shape  $\mathbf{d} \in \mathbb{C}^{N_s N_c \times T}$  with  $T$  dynamics,  $N_c$  coils, containing  $N_s$  k-space samples. Locally low-rank (LLR) reconstructed image data  $\mathbf{I}_{\text{LLR}} \in \mathbb{C}^{N_v \times T}$  of  $N_v$  voxels is obtained by solving the following convex optimization problem (27):

$$\hat{\mathbf{I}}_{\text{LLR}} = \underset{\mathbf{I}}{\operatorname{argmin}} \|\mathbf{E}\mathbf{I} - \mathbf{d}\|_2^2 + \lambda_{\text{LLR}} \sum_{b \in U} \|\mathbf{P}_b \mathbf{I}\|_*, \quad (3.31)$$

with the undersampling operator  $\mathbf{\Omega} \in \{0,1\}^{N_s N_c \times N_s N_c}$ , Fourier transform  $\mathcal{F} \in \mathbb{C}^{N_s N_c \times N_v N_c}$ , coil sensitivities  $\mathbf{C} \in \mathbb{C}^{N_c N_v \times N_v}$  and regularization weight  $\lambda_{\text{LLR}}$ . The distinct patch extraction operator  $\mathbf{P}_b \in \{0,1\}^{n_x n_y n_z \times N_v}$  refers to the  $b$ -th patch, where  $U$  is a set of patch indices, with patch size of  $n_x \times n_y \times n_z$  voxels. The patch extraction is a linear operation that can be computed efficiently. The image reconstruction is thus decomposed for each patch and allows to apply PGD optimization to solve the problem. In **Figure 3.5 B** the local rankedness for varying patch sizes is depicted. Compared to the global patch over the entire image, smaller patches are of lower rank. While for global and larger patches (**Figure 3.5 C and D**) images are blurred, with smaller patches (**Figure 3.5 E**), local correlation can reduce blurring. However, with smaller patches motion characteristics are masked, as motion introduces variance in the penalty term, which is effectively averaged over all timeframes when the reconstruction problem is solved. Similarly, if  $\lambda_{\text{LLR}}$  is chosen too high, motion characteristics are suppressed. For larger distinct patches, motion characteristics are preserved but can result in blocking artefacts at the coherent edges of the patches.

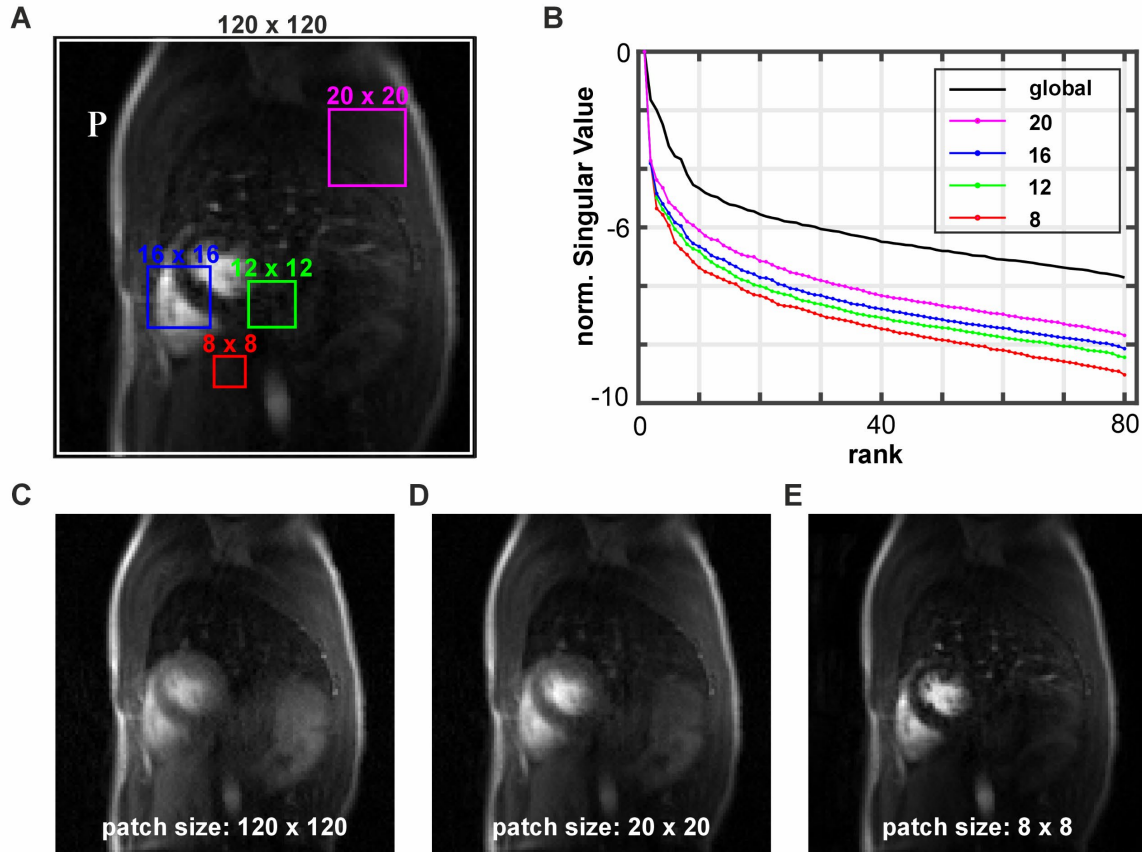


**Figure 3.5:** Patch based locally low-rank (LLR) reconstruction (A) Varying sizes of patches P. (B) Corresponding rankedness for reconstructions with patch size from  $120 \times 120$  (global) to  $8 \times 8$ . (C-E) Corresponding LLR images with varying patch sizes.

Blocking artefacts can be mitigated using overlapping patches. Again, the temporal patch projections are then considered separately. In a final step, overlapping boundary areas are averaged. However, using overlapping patches is computationally expensive. E.g., for a matrix size of  $120 \times 120 \times 10$  and patches of  $8 \times 8 \times 8$ , 144 000 SVDs have to be computed per iteration as compared to 144 for distinct patches. Proximal gradient descent cannot be directly applied as the patch extraction operator for overlapping patches is not invertible. The reconstruction is then no longer posed in the synthesis form, as it is for distinct patches and alternatives such as ADMM (175,176) have to be used. In the given reconstruction problem in Equation (3.31), blocking artefacts are alleviated by randomly selecting a set of patch indices  $U$  to introduce incoherence to the border regions of the patches. The computational burden of the distinct patch extraction operation can be reduced by randomly shifting the image over the grid of the given patch size instead of randomly changing the geometry of the patch. Note that adding random patch shifts in PGD iterations approximates overlapping patch geometry by computing proximal maps of distinct patches. Although this approach is effective and widely employed in medical image reconstruction methods (27), it should be mentioned that no rigorous proofs on the approximation quality are known to

the author. As a general remark, SVD is faster on CPU than on GPU. Acceleration of the reconstruction on GPU is faster, as Fourier transforms can be computed more efficiently. Computational efficiency can further be improved by neglecting the calculation of SVD for patches over a certain upper bound. For patches above the threshold, SVD is zero. Non-convergence of the LLR reconstruction problem to global minima results in intensity flickering in the temporal domain as well as residual aliasing artefacts.

In conclusion, the choice of hyperparameters is very important for CS (especially regarding quantitative analysis) and poses a problem for 3D DCE FPP imaging. Dynamic frame by frame imaging and the required high acceleration factors render fully-sampled GT image acquisition infeasible. In addition, every consecutive image acquisition lacks comparability as CNR characteristics differ due to residual contrast agents in blood and tissue. Furthermore, CS alters the noise statistics and can lead to reduced contrast. It is thus difficult to find solutions that match conventional noise characteristics known from e.g. fully-sampled SENSE acquisition reconstructions. As observed in LLR reconstruction, intensity flickering indicates the non-convergence of CS image reconstruction problems. Additional hyperparameters that keep the standard deviation of background intensity variation to a certain value can be defined. As an alternative, grid search can be applied to empirically select parameters that generalize well for various given datasets by image quality rating from experienced users.

Typical CS artefacts are blurring, lack in contrast, blocking artefacts (e.g. especially for LLR). Compared to PI methods, CS can be considered as an extension with a dedicated undersampling pattern that allows higher scan acceleration  $R$  and hence requires more sophisticated methods to solve the optimization problem. Conventional PI is unbiased, i.e. without regularization, and reconstruction accuracy is reduced as compared to CS methods. PI is commonly faster and easier to solve. However, PI is limited in high scan acceleration and is susceptible to noise in the data.

## 3.4 Motion Correction and Compensation Techniques

The most prevalent motion correction and compensation techniques applied to first-pass perfusion imaging are summarized in the following.

Image domain registration in its basic form is an image warping technique (179). Application of inverse transformation results in a registered image, where transformation models can either be rigid, global (i.e. affine) or non-rigid. Respiratory-induced organ motion is often considered a rigid translation and thus locally rigid models are applied for registration of CMR perfusion data (180,181). Zhou et al. (182) successfully applied linear phase shifts in k-space according to motion information from a rigid registration step. Assuming 3D translations only, the application of phase ramps is also feasible for 3D imaging.

Motion correction using non-rigid motion models to account for local variations can be achieved by application of displacement fields. The series of moving images  $\mathbf{I}_m = [\mathbf{i}_1, \dots, \mathbf{i}_T]$  are registered to a fixed target image  $\mathbf{I}_f$  by the displacement fields  $\mathbf{D}_{fm} = [\mathbf{D}_1^T, \dots, \mathbf{D}_T^T]^T$  for  $\mathbf{D} \in \mathbb{R}^{N_v \times T}$  according to:

$$\mathbf{I}_f \approx \mathbf{I}_m \circ \mathbf{D}_{fm}. \quad (3.32)$$

While a benchmark study (183) did not show benefits of non-rigid over rigid motion correction, later work by Scannel et al. (25) motivated non-rigid registration by the need to distinguish between bulk motion and signal intensity changes. First, bulk motion compensation is applied where the image series  $\mathbf{I}$  is decomposed into a low-rank component  $\mathbf{L}$  and a sparse component  $\mathbf{S}$  according to:

$$\begin{aligned} & \underset{\mathbf{L}, \mathbf{S}}{\operatorname{argmin}} \|\mathbf{L}\|_* + \lambda \|\mathbf{S}\|_1 \\ & \text{s. t. } \mathbf{L} + \mathbf{S} = \mathbf{I} \end{aligned} \quad (3.33)$$

Deformation fields derived from  $\mathbf{L}$  are then used to compensate for bulk motion. In a second step, motion correction refinement using increasing values of  $\lambda$  and finer grids is applied. In a similar fashion, in a work by Xue et al. (184), perfusion contrast changes are decoupled from respiratory motion by iterating between non-rigid motion correction and perfusion transform-based model image estimation.

For 3D perfusion imaging, the displacement field vector is defined as  $\mathbf{D} = [\mathbf{D}_1^T, \dots, \mathbf{D}_T^T]^T$  for  $\mathbf{D} \in \mathbb{R}^{N_v \times T}$ . It can be obtained by solving the optimization problem (185):

$$\hat{\mathbf{D}} = \underset{\mathbf{D}}{\operatorname{argmin}} E_D(\mathbf{D}; \mathbf{I}_f, \mathbf{I}_m) + \lambda E_R(\mathbf{D}), \quad (3.34)$$

where  $E_D$  is an image dissimilarity metric and  $E_R$  is a spatial displacement regularization term. While sum of squared intensity differences are often used as dissimilarity metric, PCA based similarity measures are advantageous (186) and thus the nuclear norm is employed.

$$\hat{\mathbf{D}} = \underset{\mathbf{d} \in \{\mathbf{D}_1, \dots, \mathbf{D}_T\}}{\operatorname{argmin}} \|[\mathbf{i}_1 \circ \mathbf{D}_1, \dots, \mathbf{i}_T \circ \mathbf{D}_T]\|_* + \lambda \sum_{pt} \sqrt{\sum_{jk} (\nabla_k \mathbf{D}_j)_{pt}^2}. \quad (3.35)$$

As regularization term vectorial total variation (VTV) (187) for each spatio-temporal voxel location  $(p, t)$  can be used. Furthermore, such a non-rigid registration can be isotropic if the displacement field is parametrized as  $\mathbf{D}_t = \mathbf{D}_t(\mathbf{D}'_t)$  with B-spline coefficients  $\mathbf{D}'_t$  over isotropic number of voxels in each spatial dimension. For quantitative 3D perfusion, non-rigid image domain registration was used by Mendes et al. (20) to align images.

Another type of motion compensation technique includes radial self-gating and motion binning. Since radial sampling repeatedly traverses the k-space center (23,135,188,189), the acquired radial interleaves can be sorted into cardiac and respiratory phases. For perfusion imaging, these methods are feasible with moderate undersampling factors (135,190). Retrospective binning has also been proposed for multiband excitation to achieve whole-heart phase-resolved quantitative perfusion imaging by Tian et al. (135).

For 3D perfusion CMR, dual-step motion compensation approaches, which use initially obtained image information to improve the conditioning of iterative image reconstruction methods, can be beneficial. In an extension of 3D k-t PCA by Schmidt et al. (18), at first, motion is extracted from the low-resolution training and the undersampled k-t dataset by non-rigid image registration. The x-pc domain can then be motion corrected by translation of single time frames to a specific respiratory state.

In a similar fashion, Chen et al. (191) proposed the block low-rank sparsity with motion-guidance (BLOSM) motion correction method for 2D perfusion CMR. Motion information is first deduced by registration of initial low-resolution reconstruction. Data is then divided into blocks or patches to exploit local sparsity. These blocks are then tracked over time using the registration displacement fields. While this method has not been applied to 3D perfusion acquisition, it has been extended to reconstruct from continuously acquired radial, simultaneous multi-slice data by Tian et al. (135).

## 3.5 Perfusion Quantification

Perfusion quantification requires segmentation of epi- and endocardial contours as well as a region of interest in either the left-ventricular blood pool or, preferably, in the aortic root. Conventionally, the myocardium is segmented into circumferential sectors in every slice according to the AHA segment model (107). The segmental summation of pixel intensities results in sector-wise and arterial, i.e. AIF, signal intensity-time profiles.

### 3.5.1 Semi-quantitative Estimation

Several semi quantitative measures can be derived from signal intensity time (SI-t) curves of contrast enhancement as summarized in **Figure 3.6**. As signal intensities are given in arbitrary units, measured signal-time profile characteristics are most suitable for relative comparisons.

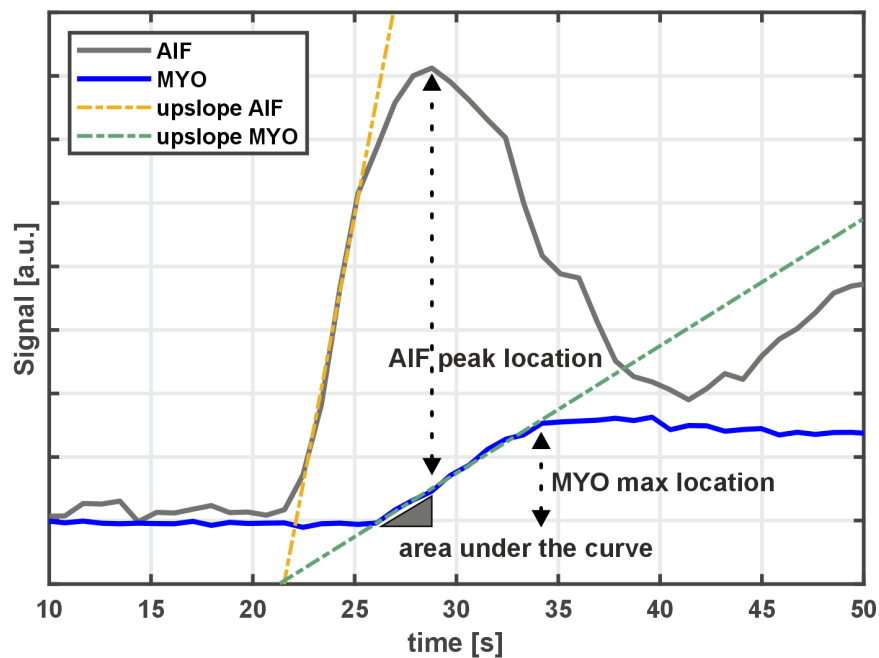


**Figure 3.6:** Characteristic signal intensity-time curve for myocardial contrast enhancement from left-ventricular myocardium (MYO) and the arterial input function (AIF). Semi-quantitative perfusion estimates can be deduced from linear models of the MYO and AIF upslope. Figure adapted from (108) using own data.

The *myocardial upslope* (192) can be derived from a linear regression over the initial myocardial signal enhancement. The *area under the myocardial SI-t curve* is the signal curve time integral from the beginning of the upslope to the time of peak AIF signal (193). *Peak SI* refers to the maximum of the myocardial SI-t curve. Reduction of this peak value can be linked to coronary artery stenosis (87). Another parameter is the *time to peak*. It denotes the time between contrast arrival and the maximum of

myocardial signal (194). In general, all semi-quantitative measures are prone to AIF variability between rest and stress. Especially under pharmacological stress, semi-quantitative measures reportedly underestimate an increase in perfusion (195). Furthermore, the presented semi-quantitative measures do not allow for inter-subject comparison, which limits their diagnostic value.

### 3.5.2 Absolute Perfusion Quantification

Absolute myocardial perfusion quantification relies on either the model-independent central volume principle (196) or the compartment models describing the kinetics of contrast agent distribution in the tissue of interest (108,197). Prior to application of the models, prerequisites must be met. First, the AIF has to be acquired with high fidelity. Furthermore, the relationship between signal and contrast agent concentration needs to be established. To achieve these goals, a dual sequence approach is used (113,198,199), which involves two separate imaging modules with different saturation delay times.

#### Signal to Concentration Conversion

Independent of the underlying kinetic assumption, the acquired signal has to be converted. Given the signal model of the saturation recovery Cartesian sequence,  $T_1(t)$  translates to signal  $I(t)$  as (197,200)

$$I(t) = I_0 \cdot \left[ \left(1 - \exp\left(-\frac{t_{\text{sat}}}{T_1(t)}\right)\right) \cdot a(t)^{n-1} + \left(1 - \exp\left(-\frac{TR}{T_1(t)}\right)\right) \cdot \frac{1-a(t)^{n-1}}{1-a(t)} \right], \quad (3.36)$$

with

$$a(t) = \exp\left(-\frac{TR}{T_1(t)}\right) \cos \alpha, \quad (3.37)$$

the baseline signal for fully relaxed magnetization  $I_0$ , saturation delay  $t_{\text{sat}}$ , repetition time  $TR$ , flip angle  $\alpha$ , and the number of profiles sampled until k-space centre  $n$ . Only by keeping track of  $n$ , the correct signal weighting according to the effective saturation delay of the current profile is considered. The AIF is acquired with a short saturation delay and for both the tissue and the AIF signal the linear relation between signal intensity  $I(t)$  and contrast agent concentration can be obtained from Equation (3.1) as

$$c(t) = \frac{1}{r_1} \cdot \left( \frac{1}{T_1(t)} - \frac{1}{T_{1,0}} \right), \quad (3.38)$$

where  $T_{1,0}$  refers to the normal relaxation time of the tissue without contrast enhancement. It can either be used based on literature values or from acquisition of a T1 MOLLI scan (201).  $I_0$  can then either be fitted or taken from a pre-pulse scan, acquired without saturation pre-pulse (202,203).



## Model-free Quantification

Model-independent central volume principle (196) implies that no functional kinetic model is considered. Instead, one volume of perfusion  $v_d$  with a single in- and outlet is considered **Figure 3.7 A**. The rate of blood accumulation in the tissue is driven by the concentration differences of the contrast agent flowing into and out of the region multiplied by the rate of blood flow  $F$  (108,204).

For absolute perfusion quantification the relation between concentration in the myocardial tissue, the AIF and the MBF can be established as a mathematical deconvolution problem. The impulse response function (IRF) relates to the contrast dynamics as (197)

$$c_{\text{MYO}}(t) = \text{IRF}_{\text{Fermi}}(t) * c_{\text{AIF}}(t), \quad (3.39)$$

with  $c_{\text{MYO}}(t)$  and  $c_{\text{AIF}}(t)$  referring to the myocardial tissue and AIF concentrations, respectively. The deconvolution of Equation (3.39) can then be conducted with the Fermi deconvolution model, which applies only for the first-pass of the contrast agents, with the corresponding IRF (197,205):

$$\text{IRF}_{\text{Fermi}}(t) = F \cdot \frac{1 - v}{1 - v \cdot \exp(-\mu t)} \cdot \Theta(t - t_{\text{shift}}) \quad (3.40)$$

The fitting parameters  $\mu$  and  $v$  do not entail any physiological meaning. The time difference between AIF and myocardial signal  $t_{\text{shift}}$  is reflected by the Heaviside step function  $\Theta$ . However, for  $t = 0$ , the amplitude of  $\text{IRF}_{\text{Fermi}}$  corresponds to the MBF. Convolution of  $\text{IRF}_{\text{Fermi}}(t)$  with the  $c_{\text{AIF}}(t)$  of AIF leads to an estimated model tissue curve. This curve is then fitted to the actual sector- or pixel-wise measured tissue curve. The least-squares fitting routine optimizes the model parameters in order to obtain the impulse response function with the desired MBF value.

As the central volume principle does not entail any information about the physiological kinetics, it is limited to the MBF parameter. Only the first-pass of perfusion can be reflected by the  $\text{IRF}_{\text{Fermi}}$  and primarily relates to the vascular transit of contrast with accurate estimation yield. If more than the first-pass is considered, the MBF is underestimated. More complex physiological models are required to consider kinetics beyond the first-pass.

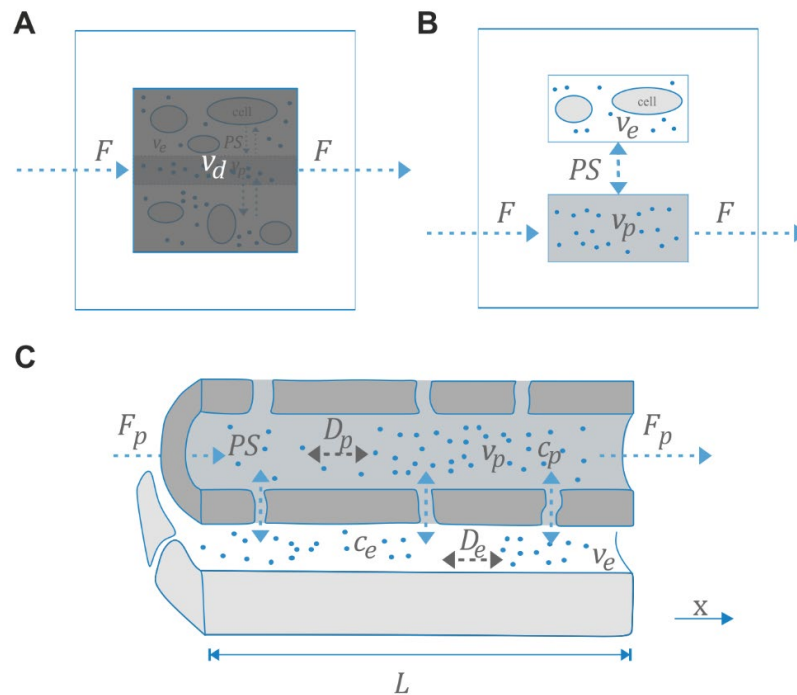


**Figure 3.7:** Summary of kinetic models. (A) Single distribution volume  $v_d$ , where only the rate of blood flow  $F$  at in- and outlet is considered i.e. independent of the underlying physiology ('black box'). (B) Two-compartment model with exchange of extracellular contrast agent (blue dots) between plasma  $v_p$  (grey) and extracellular space  $v_e$ , described by the permeability-surface area product  $PS$ . (C) Multi-compartment distributed parameter model, referred to as Blood tissue exchange model (BTEX), where spatio-temporal kinetics are considered. (A,B) adapted from (206–208). (E) adapted from Bassingthwaite et al. (209).

## Model-based Quantification

In theory, model-based perfusion quantification should encompass as much of the involved physiological kinetics as possible. An overview on models is given in (206). The contrast agent is diluted in the plasma and the extravascular extracellular space while a single inlet and outlet are assumed. The flowrate  $F$  corresponds to the MBF. The exchange between the plasma and extracellular space is governed by the permeability surface area product  $PS$  while  $v_p$  and  $v_e$  describe the relative intravascular and extracellular spaces.

The two-compartment model (**Figure 3.7 B**) describes the bi-directional exchange between plasma and extracellular space (210). The model is referred to as lumped two-compartment model, where a uniform distribution of contrast agent concentration is assumed (108). Similar to the Fermi deconvolution, the lumped compartment model can be condensed into a time dependent IRF. The solution of the time dependent differential equation describing the tracer kinetics in the model is given as (206):

$$\text{IRF}_{2-\text{COMP}}(t) = F \cdot \exp\left(-\frac{F}{v_p}t\right) + PS \cdot \exp\left(-\frac{PS}{v_e}t\right), \quad (3.41)$$

which can then be fitted to the measured concentration time-curve. In that case, the fitting parameters do not only entail shape describing character but are related to the physiological parameters described in the tracer kinetic model by  $v_p$ ,  $v_e$ ,  $PS$  and  $F$ . Of note, the physiological meaning of the additional parameters is only relevant if myocardial concentration curves beyond the first-pass are considered.

As not considering spatial concentration variations may result in underestimation of  $v_p$  and  $v_e$  (108), distributed parameter models, where a higher contrast agent concentration at the inlet as compared to the outlet are considered, are preferable (**Figure 3.7 E**). Hence, in addition to the compartmentation between plasma and extracellular space spatial variation of the concentration is considered in the longitudinal direction of the vascular space. Originally developed as blood tissue exchange model (BTEX) by Bassingthwaite et al. (209), Kellman et al. (198) applied such a distributed parameter model to estimate MBF. It assumes no exchange into the intercellular space and neglects metabolic consumption. The spatial variation of contrast concentration is considered and described by a system of partial differential equations (PDE):

$$\frac{\partial c_p(x, t)}{\partial t} = \frac{-F_p L}{v_p} \frac{\partial c_p(x, t)}{\partial x} + \frac{PS}{v_p} \cdot (c_e(x, t) - c_p(x, t)) + D_p \frac{\partial^2 c_p(x, t)}{\partial x^2} \quad (3.42)$$

$$\frac{\partial c_e(x, t)}{\partial t} = -\frac{PS}{v_e} \cdot (c_e(x, t) - c_p(x, t)) + D_e \frac{\partial^2 c_e(x, t)}{\partial x^2} \quad (3.43)$$

Again, subscripts  $p$  and  $e$  correspond to the plasma and extracellular space, respectively.  $D$  is the axial Diffusion coefficient,  $L$  denotes the length of the capillary and  $x$  is the direction along the capillary. Boundary conditions are a fixed range of capillary length from 0 to  $L$ , which can be set to 1 mm (209), with a fixed number of spatial steps. Blood plasma concentrations  $c_p(t)$  relate to the AIF concentration  $c_b(t)$  and the blood hematocrit (HCT), according to  $c_p(t) = \frac{c_b(t)}{1-\text{HCT}}$ . For healthy subjects, blood HCT = 0.42 (198) is assumed. Blood volume and flow are then derived as  $F_b = \frac{F_p}{1-\text{HCT}}$  and  $V_b = \frac{V_p}{1-\text{HCT}}$ , respectively. Plasma and extravascular diffusion coefficients for Gadobutrol contrast agents can be considered as:  $D_p = 1e - 5 \text{ cm}^2/\text{s}$  and  $D_e = 1e - 6 \text{ cm}^2/\text{s}$  (211). As the PDEs cannot be solved as a simple set of exponentials, an iterative fitting algorithm (L2-norm) procedure can be used to yield  $v_p$ ,  $v_e$ ,  $PS$  and  $F$ , i.e. the MBF.

While this dilution model offers increased details regarding the underlying physiological complexity it comes with the drawback that the differential equation problem is an overdetermined system and a contrast time curve can result from more than one sets of parameters. An explanatory equivalent time curve is shown in Figure 3.8.

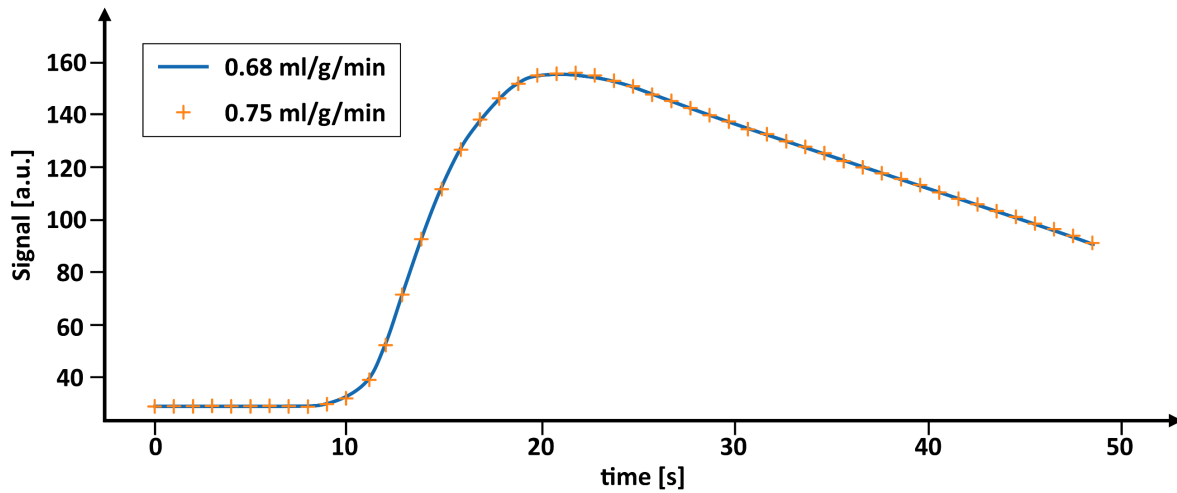


**Figure 3.8:** Signal-time equivalent curves derived from simulating the blood tissue exchange model (BTEX). Blood flow  $F_b = 0.68$  ml/g/min (blue line) corresponds to  $PS = 1.32$  ml/g/min,  $V_p = 9.7$  ml/100 mg and  $v_e = 20.8$  ml/100mg. Blood flow  $F_b = 0.75$  ml/g/min (markers) corresponds to  $PS = 1.45$  ml/g/min,  $V_p = 10.67$  ml/100 mg and  $v_e = 22.88$  ml/100mg. Adapted from (212).

Another downside of the complexity is the increased vulnerability to noise when applying conventional least-squares fitting. CNNs can be used to predict perfusion parameters fast and accurately. In absence of sufficient amounts of quantified perfusion data, training can be performed with synthetically generated data simulated with the BTEX model. However, while CNN prediction is considerably faster, only using training data from BTEX modelling can be prone to overfitting (213). A more promising approach is automatic MBF quantification using physics informed CNNs as recently proposed by van Herten et al. (214).

# Chapter 4

## Myocardial Fibrosis and Scar CMR

### 4.1 Background

Myocardial scar imaging by LGE imaging (11) is considered the reference standard for myocardial viability assessment (12) in the context of acute and chronic MI (215,216). Myocardial scar mass is also of prognostic value in patients with ischemic cardiomyopathies (34–37).

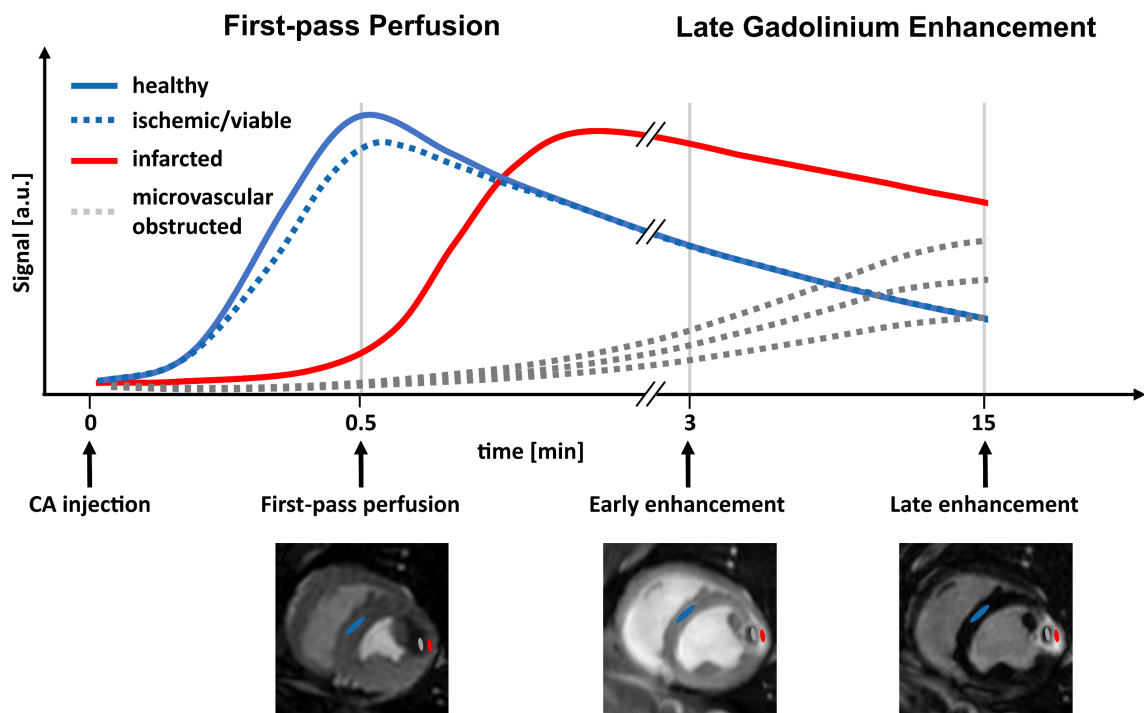


**Figure 4.1:** Signal-time curves of contrast enhancement in first-pass perfusion and late Gadolinium enhancement in a porcine model with acute myocardial infarction. Figure adapted from (11).

LGE relies on contrast enhancement using Gadolinium contrast agent material temporarily trapped in tissue (**Figure 4.1**). Accordingly, LGE imaging is performed 10 to 20 minutes post injection (10).

Differences in contrast agent uptake can already be seen after 3 to 5 minutes in the early enhancement images. While contrast agent concentrations are significantly reduced in healthy myocardium, infarcted tissue remains enhanced. Zones of tissue with microvascular obstruction remains dark in LGE imaging. After 10-20 minutes, the contrast agent concentration in healthy myocardium is further reduced while contrast material remains trapped in tissue with compromised cell membranes, which translates into high contrast between scar (hyperenhanced) and healthy tissue. The recommended contrast agent dose for LGE imaging is 0.1 to 0.2 mmol/kg body weight (b.w.), which matches the administered concentrations after a stress and rest perfusion protocol.

To further illustrate contrast agent concentration in myocardial tissue over time, T1 values in a porcine animal model after a single and repeated contrast agent injection are shown in **Figure 4.2**.

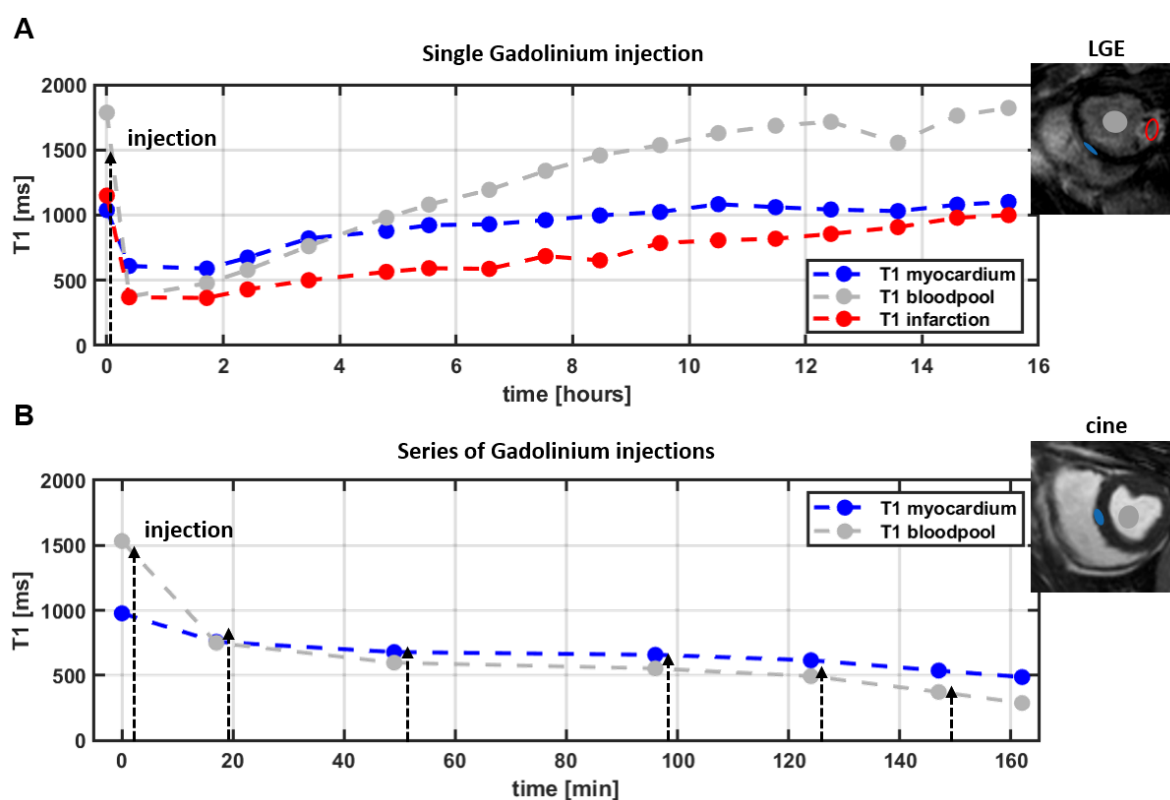


**Figure 4.2:** Change in T1 in healthy myocardial tissue, left-ventricular blood pool and infarcted tissue after Gadolinium contrast agent injection. (A) Single contrast agent injection (0.2 mmol/kg b.w.) in a porcine model with acute inferior myocardial infarction. The inset shows the corresponding regions of interest (ROIs) in a midventricular late Gadolinium enhancement (LGE) image. The infarct is discernible in the inferior myocardium. (B) Series of six contrast agent injections (dose: 0.075 mmol/kg b.w. each) in a healthy porcine model. The inset on the right shows the ROIs in a midventricular cine short-axis view image. All T1 values were obtained using a T1 MOLLI scan (201).

After a single injection of 0.2 mmol/kg b.w., blood T1 decreases from 1750 ms to 375 ms after 23 minutes. T1 values in healthy and infarcted myocardium are reduced from 1039 ms to 610 ms and from 1150 ms

to 686 ms, respectively. Over the course of 15 hours, T1 in blood slowly recovers to the original value. Healthy and infarcted tissue also recover, but at a slower rate and not to their initial values. Of note, the renal clearance in porcine models decreases over the course of experiment under general anesthesia. For comparison, in humans, the mean half-life time of Gadobutrol contrast agent is 1.8 hours in blood (217). The T1 evolution for repeated contrast agent administrations of 0.075 mmol/kg b.w. is shown in **Figure 4.2 B**. After the third injection and a waiting period of 46 minutes, washout almost compensates the third contrast agent injection. After a total of 6 injections, the T1 values are reduced to 487 ms and 287 ms, respectively.

## 4.2 LGE Imaging Strategies

Inversion recovery (IR)-based imaging is employed in LGE. The corresponding simplified signal model, assuming ideal inversion pulses, reads:

$$S_{\text{IR}}(\text{TI}) = M_0 \frac{1 + \exp\left(-\frac{\text{TR}}{\text{T}_1}\right) - 2 \exp\left(-\frac{\text{TI}}{\text{T}_1}\right)}{1 + \cos(\alpha) \exp\left(-\frac{\text{TR}}{\text{T}_1}\right)} \cdot \sin(\alpha) \exp\left(-\frac{\text{TE}}{\text{T}_2^*}\right), \quad (4.1)$$

where TI, TR, TE and  $\alpha$  denote inversion time, repetition time, echo time and imaging flip angle, respectively. Assuming small imaging flip angles (i.e.  $\cos(\alpha) \approx 1$ ) and  $\text{TE} \ll \text{T}_2^*$  the model can be simplified to:

$$S_{\text{IR}}(\text{TI}) \propto M_0 \frac{1 + \exp\left(-\frac{\text{TR}}{\text{T}_1}\right) - 2 \exp\left(-\frac{\text{TI}}{\text{T}_1}\right)}{1 + \exp\left(-\frac{\text{TR}}{\text{T}_1}\right)}, \quad (4.2)$$

and if  $\text{TR} \gg \text{T}_1$  reduces to:

$$S_{\text{IR}}(\text{TI}) \propto M_0 \left(1 - 2 \exp\left(-\frac{\text{TI}}{\text{T}_1}\right)\right). \quad (4.3)$$

To maximize contrast between scar and healthy myocardium in LGE imaging, the inversion time TI has to be set to the value at which the magnetization of healthy myocardium crosses zero during readout (**Figure 4.3 A**). The optimal TI is manually identified from a Look-Locker scan (218) that acquires a set of images with varying TI.

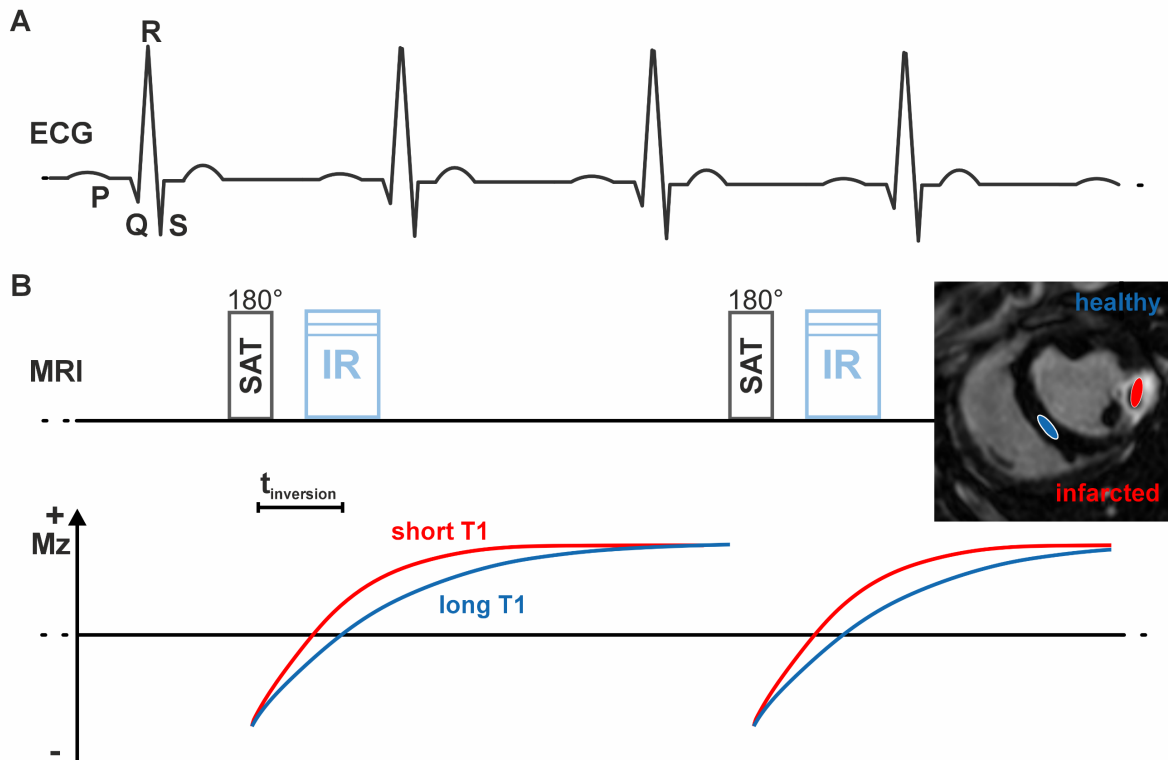


**Figure 4.3:** Late Gadolinium enhancement imaging sequence. (A) Electrocardiogram (ECG) to trigger image acquisition. (B) Inversion recovery (IR) sequence and longitudinal magnetization (Mz). The inversion time delay (TI) is set to a value at which Mz of the healthy myocardium (inset) equals zero.

Following the review on LGE by Kellman et al. (11) and SCMR recommendations (4,12), the spatial in-plane resolution is recommended to be between 1.4 mm and 1.8 mm; higher resolutions of up to 1.0 mm are beneficial to assess small scars in thinned myocardial walls. Slice thickness should be 6 to 8 mm with slice gaps of 1 to 2 mm. A temporal footprint between 150 ms to 200 ms is recommended to mitigate cardiac motion artifacts in mid- to end-diastole but should be further reduced in tachycardia (>100 bpm). Three-dimensional acquisition methods allow for whole-heart coverage. For in-plane resolutions comparable to 2D methods, the volumetric data has to be acquired in every heartbeat (219–222). Accordingly, the condition for the simplified signal model no longer holds and the signal model according to Equation (4.1) is to be used. 3D LGE imaging is especially advantageous in combination with motion compensation techniques including navigator gating (223–226), which allow for free-breathing acquisitions. Thereby, high and isotropic resolution can be achieved (227). Of note, a study by Bustin et al. (228) showed that 3D high-resolution free-breathing LGE was able to detect more LGE areas in patients with a history of COVID-19 when compared to conventional 2D LGE.



### 4.3 Myocardial Scar Analysis and Quantification

In clinical practice, the visual assessment of LGE images is sufficient for many indications (31). After image intensity windowing to obtain dark myocardium, occurrence of LGE is assessed. Scar localization is then compared to other acquired views to identify matching structures. CAD and non-CAD (e.g. myocarditis) type hyperenhancement is mainly distinguished by the presence of subendocardial hyperenhancement. For precise characterization of ischemia and viability, the location and transmural extent of LGE should then be compared with cine and perfusion images using the AHA 17-segment model (229).

Scar mass quantification requires the segmentation of the myocardium and the hyperenhanced tissue in every imaging slice. Scar mass is calculated from the sum of slice thickness and interslice gap, which is then multiplied by the hyperenhanced area and the density of tissue. It is typically presented in percent of total LV mass (%LV).

Manual LV and scar segmentation is time-consuming and requires well-trained operators. With limited contrast, precise delineation of myocardial and scar borders can be challenging, even when anatomical information from cine imaging is at hand. This can introduce significant interobserver variation hampering the diagnostic quality.

To improve consistency and reduce the manual workload, semi-automatic approaches have been developed. Using the full-width-at-half-maximum (FWHM) method, a threshold  $\tau_{FWHM}$  is defined at 50% of the maximum hyperenhanced myocardial signal intensity in a scar region identified by the operator (230,231):

$$\tau_{FWHM} = \frac{\max_{\text{myocardium}}}{2}. \quad (4.4)$$

Another approach uses thresholding at  $n$  times the standard deviation ( $n$ -SD) add to the mean of healthy myocardial signal, which requires the manual segmentation of a healthy (remote) region within the myocardium (**Figure 4.4**). The threshold  $\tau_{n-SD}$  is defined as:

$$\tau_{n-SD} = \mu_{\text{remote}} + n \cdot \sigma_{\text{remote}}, \quad (4.5)$$

where  $\mu_{\text{remote}}$  and  $\sigma_{\text{remote}}$  denote the mean signal amplitude and the SD in the remote healthy tissue, respectively. While earlier SCMR guidelines proposed  $n=2$  and  $n=5$  for non-ischemic scar and MI, respectively (12,232), there is no consensus for non-ischemic scar in the latest recommendations (31). The selection of extent and location of the healthy remote myocardium can hamper the reproducibility and can cause high variability, especially when no surface coil sensitivity normalization is applied (233,234).

Depending on the definition of the threshold by either the FWHM or n-SD thresholding method, LGE within the myocardium is then segmented automatically. Hyperenhancement artefacts due to noise or partial voluming effects, as well as zones of MVO, can require manual observer interaction, which increases subjectivity and adds workload. Variations in coil sensitivities over the myocardium affect the underlying signal statistics used for either of the thresholding methods, thereby introducing potential bias.

While comparisons of manual and semi-automatic approaches suggest no significant difference in segmented scar volumes and reproducibility (37,230,235–237), there is no consensus which method should be preferred (31,238). Most recent work on data from a multi-center and multi-vendor study concluded that n-SD thresholding can be unreliable (233). However, when body-coil sensitivity normalization was used, identification of MI using the FWHM method was comparable to n-SD thresholding at 5 SDs (233).

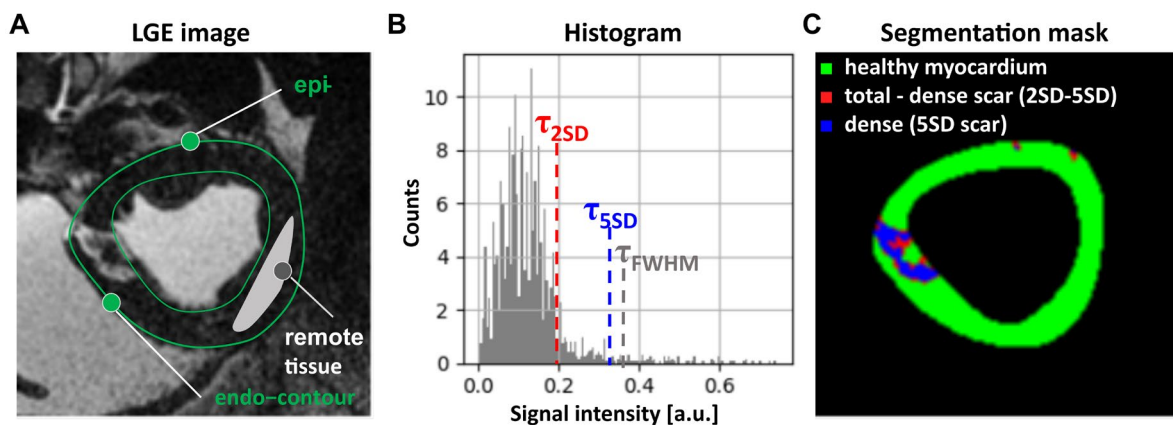


**Figure 4.4:** Scar segmentation using the  $n$  times the standard deviation ( $n$ -SD) method. (A) Late Gadolinium enhancement (LGE) image with manually drawn epi- and endocardial borders and the remote healthy tissue segmentation ( $\mu = 0.109$ ). (B) Signal intensity histogram of myocardial intensities with thresholds  $\tau_{2SD} = 0.199$  and  $\tau_{5SD} = 0.334$ . For comparison, the threshold for the FWHM method is  $\tau_{FWHM} = 0.372$  is shown. (C) Resulting  $n$ -SD thresholding segmentation mask.

Other algorithms that require LV segmentation but do not require further user interaction have been proposed to segment myocardial scar by means of level set, expectation maximization or Gaussian mixture model algorithms (237,239,240). Several approaches to mitigate the burden of manual LV segmentation have been proposed. Semi-automatic and fully automatic methods, either combining co-registration of cine and LGE images (241,242) or only LGE images in combination with prior knowledge on physiological constraints and inter-slice smoothness have been proposed (235,243). An overview automatic scar segmentation algorithms is given by Karim et al. (235).

## 4.4 Machine Learning Segmentation

Deep learning algorithms, and more specifically U-Net type convolutional neural networks (CNNs) (244,245), have led to efficient automatization of medical image segmentation tasks. In the following sections, the fundamentals of U-net based myocardial scar segmentation are outlined by referring to the review work by Chen et al. (38).

### 4.4.1 U-Net architecture

Generally, CNNs for image segmentation tasks consist of an encoder and decoder pathway. The encoder captures local information from the input image (i.e. input layer) by convolving the input with learned filters followed by spatial down-sampling, while the decoder path performs spatial up-sampling to obtain an output of the input image size (i.e. output layer). Due to the condensation of information in the encoder, spatial information can be lost. This motivates the direct propagation of features from the encoder to the decoder by so-called skip connections as proposed by Ronneberger et al. (244,245). An example U-Net is shown in **Figure 4.5**.

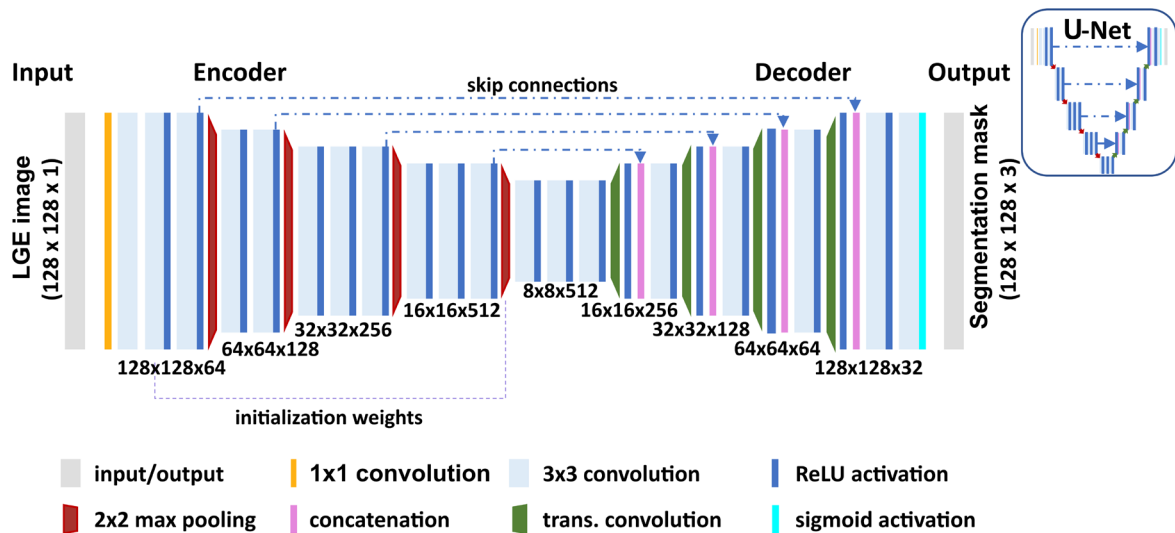


**Figure 4.5:** Exemplary U-Net type convolutional neural network architecture for image segmentation. The input layer is an image (matrix size:  $128 \times 128 \times 1$ ). The output layer consists of resulting segmentation masks with three channels (matrix size:  $128 \times 128 \times 3$ ) for three different tissue classes. The number of filters are  $k_l \in 64, 128, 256, 512$ . Quadratic convolutional kernels are of size  $n_{kernel}^2 \in 1 \times 1, 3 \times 3$ .

The encoder and decoder pathways are connected by convolutional layers. Convolutional layers apply  $k_l$  convolutional kernels of size  $n_{kernel} \times n_{kernel}$  (e.g. size  $3 \times 3$ ) to extract  $k_l$  feature maps. The number of parameters in a convolutional layer is given as:

$$k_l \cdot (n_{kernel}^2 \cdot l_{input} + 1), \quad (4.6)$$

where  $l_{input}$  is the number of channels of the input image. For the first convolutional layer the number of parameters is  $64 \cdot (3^2 \cdot 1 + 1) = 640$ . Convolution operations are often followed by a non-linear transformation such as the rectifier linear unit (ReLU) activation function, defined as  $\hat{\rho}(x) = \max(0, x)$ . After the first three convolutions, a  $2 \times 2$  max pooling kernel is applied to further down-sample the spatial dimensions. In **Figure 4.5**, in total four down-sampling steps are applied in the encoder resulting in a low spatial resolution and high-level feature representation ( $8 \times 8 \times 512$ ). Further convolution steps would increase the detection of features and thus the depths of the network but can lead to over-fitting (see below). The depth of the network increases with the receptive field of a network which defines the area in the input image that contributes to the feature aggregation after a given number of down-sampling steps. In **Figure 4.5**, after four down-sampling steps, the maximal local extent in information in one element of a  $8 \times 8$  matrix corresponds to the receptive field of  $16 \times 16$  pixels in the original image. From the deepest point of feature detection, the decoder reinterprets the feature maps to up-sample the data back towards the original input dimensions of high-spatial resolution and low features. The most commonly used up sampling strategy is the learnable transposed convolutions followed by ReLU activation. Resulting feature maps are then concatenated with the feature maps that are fed in from the encoder pathway via the skip connections to promote a multiscale analysis of the available data. After another convolution and activation layer, the next up-sampling step is performed. After four up-sampling steps, the feature maps are transformed using sigmoid activation function defined as  $\rho(x) = \frac{1}{1+e^{-x}}$  in order to threshold the classification features to either 0 or 1.

## 4.4.2 Neural Network Training

Successful CNN based segmentation methods require training of the network weights. The most common approach is supervised training that requires sets of images and feature or class label pairs (for semi- and unsupervised learning refer to the end of this chapter). In the training process, the total number of these feature label pairs is split into a training, a validation (i.e. 10% to 20%) and an ‘unseen’ test set. In the forward evaluation, the training sets are used to train the network weights. The current weights are then tested on the independent validation set to track the model performance. An optimizer and an evaluation metric (i.e. loss function) are required to update the trained weights in every iteration over all training data (i.e. epoch) and to stochastically minimize the segmentation loss function using backpropagation. Using the independent test set, the generalization accuracy in comparison to the prediction performance on the validation set can be estimated.

At the beginning of network training, weights need to be initialized. Improper choice of initial weights can lead to vanishing or exploding gradients in the backpropagation and have an impact on the generalization of the final classification model. In the U-net architecture shown in **Figure 4.5**, transfer learning techniques (see below) using pretrained weights from another classification network e.g. ResNet34 (246) are employed to accelerate the training process. In the illustrated implementation, the ResNet34 expects a three-channel image and thus a single convolutional layer of three 1 x 1 kernels was prepended to the exemplary network architecture.

The two most commonly used optimizers for the iterative training process are mini batch gradient descent and adaptive-moment-estimation (Adam). For Adam, the learning rate as well as the corresponding moment estimation smoothing parameters  $\beta_1$  and  $\beta_2$  have to be chosen manually but do not require specific hyperparameter tuning.

Several loss functions which evaluate the current state of the training model during the training process can be defined. For segmentation problems, pixel-wise comparison functions such as cross-entropy or Dice loss are the methods of choice. Cross-entropy minimizes the Kullback–Leibler (KL) divergence between the probability of the output over all label classes and the training label per pixel. For a given target segmentation mask  $\mathbf{y}_i^c$  and the predicted probabilistic mask  $\hat{\mathbf{p}}_i^c$  from  $c$  classes of labels, the cross-entropy loss can be defined as (38):

$$\mathcal{L}_{\text{cross-entropy}} = -\frac{1}{n} \sum_{i=1}^n \sum_{c=1}^n \mathbf{y}_i^c \log(\hat{\mathbf{p}}_i^c) \quad (4.7)$$

The Dice-loss function captures the spatial correspondence between the target and predicted segmentation mask and is computed from the area of overlap divided by the total number of pixels in both masks:

$$\mathcal{L}_{\text{Dice}} = 1 - \frac{2 \sum_{i=1}^n \sum_{c=1}^C \hat{\mathbf{y}}_i^c \hat{\mathbf{p}}_i^c}{\sum_{i=1}^n \sum_{c=1}^C (\hat{\mathbf{y}}_i^c + \hat{\mathbf{p}}_i^c)} \quad (4.8)$$

Focal loss is another method that has been proposed for segmentation tasks with imbalances among classes (247). To this end, the cross-entropy loss is extended by an additional focus factor that weighs pixels with high positive classification accuracy less than securely wrong classified pixels and those with high ambiguity.

### 4.4.3 Overfitting Reduction

A general challenge is to avoid overfitting of the network weights to the features of the training data sets. While the determined weights may result in minimal loss on the training dataset, generalization accuracy to ‘unseen’ test images can be reduced. During the training process overfitting is detected if the training

and validation losses continuously diverge and/or differ by orders of magnitude. In practice, various strategies exist to avoid overfitting. However, these strategies cannot be applied interchangeably and only monitoring and evaluation of training and validation losses can help to obtain the best combination of strategies. A main factor for overfitting is the network architecture itself. Overfitting is promoted when the number of optimizable parameters is too high for the size and diversity of the training dataset. On the other hand, it is also desirable to increase the representational capacity of networks by adding more convolutional layers and hence free parameters to capture all relevant data features. Thus, the architecture should be chosen so that a sufficient complexity, which can be trained reliably on the given amount of data, is achieved. Estimation of the optimal network depth requires practical experience supported by evaluation of the loss metrics. If the validation error does not follow the training error, overfitting is likely to have occurred. If either training or validation error does not converge, *early stopping* of the training process may reduce the chances of overfitting. *Kernel weight regularization* adds a penalty term (e.g.  $\ell_1$ -,  $\ell_2$ -norm or Tikhonov regularization) to the loss function to promote aggregation of only relevant features by penalizing large weights. In addition to  $\ell_2$ -norm regularization,  $\ell_1$ -norm penalizes the accumulation of several mid-size weights in order to promote a sparser representation of the learned weights. *Transfer learning* uses prior knowledge from a different segmentation task by utilizing suitable weight initialization. While it helps to lower the generalization error and thus overfitting, it also reduces the necessary training time. *Ensemble learning* combines several trained models to increase the total segmentation accuracy. The chances of overfitting are reduced if one model is biased. The *Dropout* technique (248) is a strategy that randomly sets a fraction of the network weights per batch evaluation to zero. This helps to avoid encoding of one image by just a single parameter which would result in in overfitting. *Data augmentation* is used to enlarge the number and diversity of training data sets by various transformations of the original data and thus reduces the generalization error. Opposite to over-fitting, under-fitting is the result of insufficient representational complexity leading to insufficient inference accuracy. Under-fitting can be a problem if fundamental network or training parameters are chosen wrongly and consequently prevent the model from converging. In practice, under-fitting can be revealed immediately if inferred segmentation on the validation images does not represent the training class labels (i.e. the segmentation masks).

#### 4.4.4 Test Time Augmentation

In addition to extending the training set, data augmentation can be used to improve segmentation accuracy for an already trained model by exposing the network to various augmentations of the input image, resulting in a set of predictions. This process is referred to as test time augmentation (TTA) (249). The average over all predictions yields a probabilistic description of the pixel classification. In order to obtain classification, a majority vote (e.g. thresholding at 0.5) is required to determine the unique class

membership of individual pixels. In **Figure 4.6**, the 8-fold TTA consisting of four 90° rotations and four reflections is shown.

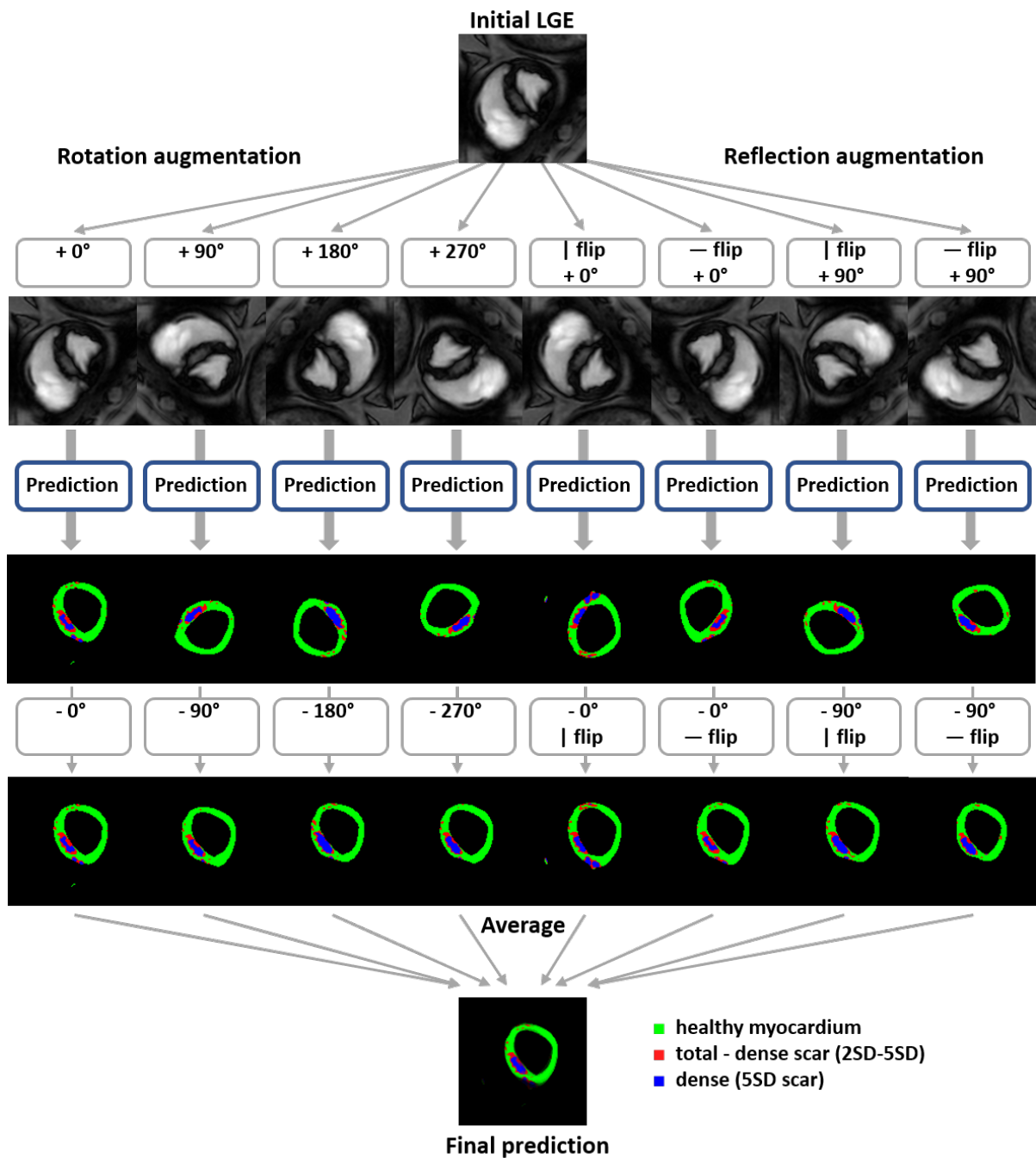


**Figure 4.6:** Test time augmentation (TTA) for myocardial scar segmentation. In the augmentation phase, the input is rotated and reflected. | and — refer to reflections along the vertical and horizontal axes, respectively. The augmented images are then segmented individually. Augmentation operations are inversely applied to the resulting segmentation masks. The final prediction mask is obtained as an average of the augmented predictions. Majority vote results in final classification.

## 4.4.5 State of the Art Myocardial Scar Segmentations

Due to the limited availability of annotated LGE datasets, the deployment of network-based myocardial scar segmentation algorithms is relatively limited when compared to other segmentation tasks. In order to compare network performance for segmentation tasks, several metrics have been used in segmentation challenges (250). The Dice score (Equation (4.8)) is well established as measure for local correspondence. Surface distance-based metrics as e.g. the Hausdorff distance (251) measure the distance between two surfaces. Clinical diagnostic parameters, e.g. %LV for myocardial scar mass, are of value to compare segmentation performance. Notably, comparison of several metrics should be investigated to corroborate the segmentation performance of a method. However, often only the Dice score is reported in publications. To contextualize myocardial scar segmentation performance, an overview of recent work using U-Net implementations (e.g. EMIDEC (252)) and peer-reviewed publications (38) is given in the following section.

Early on, work proposed by Fahmy et al. (253) successfully increased the robustness of U-Net based scar segmentation by additional input of aligned or fused short-axis cine images to the LGE images in the training dataset. Only clinical metrics and no Dice scores were evaluated, but segmentation accuracy and variability were similar to manual segmentation. In a study by Moccia et al. (254), a fully connected CNN was used for scar segmentation in 30 patients with LGE images as sole input. Assessment using leave-one-patient out cross validation led to Dice scores of 0.88. In a multicenter, multivendor study by Fahmy et al. (255) U-Net type CNNs, with LGE images as their only input, were used to segment scars in patients with hypertrophic cardiomyopathy. The reported Dice scores were  $\sim 0.5$ . Work proposed by Zabihollahy et al. (256) used 3D LGE datasets to train a U-Net based scar segmentation. Cascading two U-Nets for myocardial and scar segmentation yielded Dice scores of 0.85. Another U-Net implementation by Brahim et al. (257) also cascaded an anatomical net and a pathology net for additional pathological constraints, which were trained separately. Their performance assessment showed Dices scores for myocardium and scar tissues of 0.88 and 0.74, respectively, thereby improving on most methods reported in the EMIDEC challenge (252). In another study by Popescu et al. (258), which had access to 155 patients datasets, augmented training data was used to complement training of the U-Net. Based on cine data, artificial images with myocardial scars matching LGE histograms were generated. Inclusion of additional anatomical information allowed to deploy so-called anatomically-informed segmentation with direct output of clinical features and scar burden. Segmentation Dice scores for LV and scar segmentation were 0.93 and 0.57, respectively.

While U-Net type architectures, trained using supervised learning, represent the current state of the art for myocardial scar segmentation, unsupervised learning should be explored too. Also, other network topologies could be considered as reviewed elsewhere (38).





# Chapter 5

## Free-breathing Motion-informed Locally Low-rank Quantitative 3D Myocardial Perfusions Imaging

---

\*Published as: **T. Hoh**, V. Vishnevskiy, M. Polacin, R. Manka, M. Fuetterer and S. Kozerke, Free-breathing motion-informed locally low-rank quantitative 3D myocardial perfusion imaging, Magn Reson Med, 2022, 1-17

---

## 5.1 Introduction

The clinical utility and value of dynamic contrast-enhanced myocardial first-pass perfusion imaging has been demonstrated in a number of landmark trials (7,8,259). While in today's clinical use image data is mostly assessed visually or semi-quantitatively to identify ischemia, quantitative approaches (260) have gained momentum with recent technical advances in data acquisition, reconstruction and processing (184,261–263).

In contrast to conventional dynamic multi-slice 2D imaging sequences, 3D approaches with whole-heart coverage allow data acquisition in a single time window per cardiac cycle (17). The potential clinical value of robust 3D myocardial perfusion imaging relates, in particular, to the ability to quantify the relative ischemic myocardial volume (14,16). In view of the increasing utilization of ischemic burden as a marker for decision making for revascularization in stable coronary artery disease (48), added value has been indicated. Moreover, the importance of quantification of myocardial blood flow and related parameters has been emphasized in the context of triple vessel coronary artery disease (29,264), microvascular disease (28,265) and other conditions (266).

Dynamic 3D perfusion methods require substantial scan acceleration in order to accommodate data sampling into a sufficiently short acquisition window per cardiac cycle. To this end, k-t undersampling in conjunction with k-t BLAST, k-t SENSE (138,267,268) and k-t PCA (114,155) has initially been deployed and demonstrated in the clinical setting for various applications and compared against reference standards in single (14–16,115,116) and multi-centre trials (117,118). Dedicated advances to improve the reconstruction accuracy from undersampled multi-slice 2D or 3D Cartesian (18,119,269), radial (19,149,270–273) and spiral (121,122,146,147) k-space trajectories have been proposed. Work on 3D Cartesian (114), radial stack-of-stars (20,135) and spirals (123) has demonstrated improvements with impact on quantitative perfusion parameters. The ramification of spatio-temporal fidelity on quantitative perfusion indices has been investigated and quantified (166).

A challenge with k-t reconstruction, however, relates to the requirement to ensure sufficient spatio-temporal data correlations. Therefore, data acquisition is typically conducted in a breathhold, which has been limiting, in particular, during adenosine-induced stress. In order to increase patient comfort and compliance, initial research has been directed to enable free-breathing 3D data acquisition based on Cartesian (18) and stack-of-stars undersampling (19).

To address respiratory motion of free-breathing data acquisition, approaches applying global or local registration in the image domain have been described. To address challenges due to the dynamic contrast enhancement, image signal separation into low-rank and sparse components followed by model-based

registration has been proposed (25). It is noted, however, that 2D registration-based methods can inherently only correct for in-plane and not continuous through-slice motion.

Besides image-domain registrations, radial self-gating and respiratory motion binning have been used (23,135,188,189) to restrict or sort data to different respiratory states. However, retrospective binning of spokes into breathing and heart phases is only applicable for moderate undersampling or continuous acquisition schemes (135,190).

In general, non-rigid motion, corrupting the data, can be corrected for using an approximate solution given by an estimated motion field (274). If rigid motion is assumed, it can be compensated for by application of linear phase shifts in k-space as demonstrated for perfusion imaging (182).

Motion correction has become an important step to improve the conditioning of iterative image reconstruction methods (18,191,275). Block low-rank sparsity tracking (BLOSM) has proved beneficial (191), and has been extended to reconstruct from continuously acquired radial, simultaneous multi-slice, heart-phase resolved data (135). Similar methods have also been used in computed tomography perfusion imaging (276) and in other MR applications such as MR parameter mapping (27) and MR fingerprinting (277).

For quantification of perfusion data, a dual-sequence, single-bolus approach is desirable (20,113,119). The arterial input function (AIF) is preferably recorded in the ascending aorta in an interleaved fashion (278).

The present study proposes and validates a 3D motion correction approach for locally low-rank (LLR) image reconstruction of Cartesian pseudo-spiral in-out k-t undersampled single bolus first-pass perfusion data. The method is referred to as respiratory motion-informed locally low-rank reconstruction (MI-LLR). It is shown that, by incorporating a transformation displacement field for each dynamic frame, MI-LLR is able to correct for non-rigid in- and through-plane organ motion during rest and stress. Numerical simulations and phantom experiments are used to demonstrate the robustness of the MI-LLR approach with respect to cardiac and breathing motion in comparison to LLR (27) and frame-by-frame compressed sensing (CS) using wavelets as sparsifying transform ( $\ell_1$ -wavelet) (279,280) reconstructions. In-vivo feasibility of the proposed method is assessed in subjects during rest and stress condition.

---

## 5.2 Methods

### 5.2.1 Image Acquisition

A dynamically interleaved 2D/3D dual-sequence, single-bolus scheme was implemented on a clinical 1.5T MR system based on an electrocardiogram (ECG) triggered saturation-recovery spoiled gradient echo sequences with  $T_1$ - and  $B_1$ -insensitive saturation preparation pulses (281) as described previously (119).

As shown in **Figure 5.1 A**, the 3D perfusion scan is triggered to end systole. The 2D arterial input function (AIF) images are acquired in the ascending aorta during diastole. A pseudo-spiral Cartesian undersampling pattern was implemented as illustrated in **Figure 5.1 B,C**. The sampling distribution was defined by a variable density function (159) with an elliptical k-space shutter as depicted in **Figure 5.1 B**. For each dynamic imaging frame, k-space profiles were chosen according to the density distribution while avoiding profile duplication. At the k-space centre, a  $2 \times 4$   $k_z$ - $k_y$  area was fully sampled. The temporal order of profiles was according to a spiral-in – spiral-out scheme, placing the k-space centre and the nominal saturation delay at half the acquisition time (Figure 1C). Imaging parameters were: TR/TE = 2.0/1.0 ms, spatial resolution:  $2.5 \times 2.5 \times 10 \text{ mm}^3$ , FOV:  $300 \times 300 \times 100 \text{ mm}^3$ , covering the full ventricle from apex to base, flip angle:  $15^\circ$ , acquisition window: 240 ms, saturation delay: 135 ms, undersampling factor  $R = 10$ .

For the interleaved acquisition of the AIF, a fully sampled centre-out Cartesian pattern was used with spatial resolution:  $10 \times 10 \text{ mm}^2$ , slice thickness: 15 mm, flip angle:  $15^\circ$ , acquisition window: 56-64 ms, saturation delay: 30 ms. TR and TE were set equal to the corresponding 3D sequence to avoid different  $T_1$  and  $T_2^*$  weightings.

All images were acquired on a 1.5 T Philips Achieva MR system (Philips Healthcare, Best, The Netherlands) using a 5-element cardiac receive coil array. Gadobutrol (Gadovist, Bayer Schering Pharma, Germany) was used as contrast agent (CA).

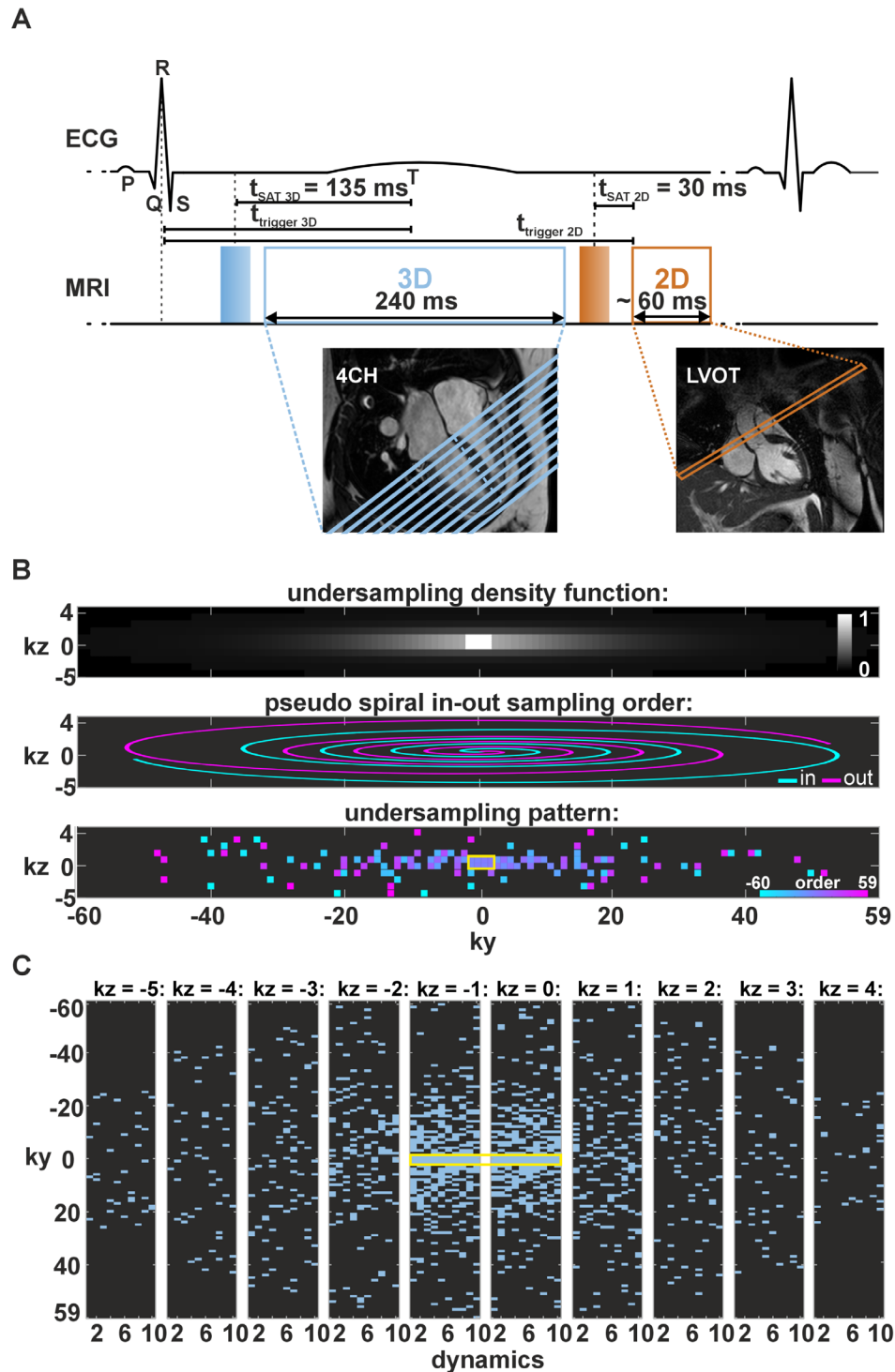


**Figure 5.1:** Data acquisition. (A) Dual-sequence diagram with corresponding ECG trace and typical planning of the 3D and 2D stacks. The 3D perfusion scan is triggered to end systole, the 2D AIF images to diastole. The 3D volume is sampled by the proposed undersampled pseudo-spiral in-out Cartesian trajectory, while linear centre-out Cartesian sampling is used for the 2D AIF slice. (B) 3D data acquisition scheme. Data are sampled using a volumetric pseudo-spiral Cartesian sampling pattern. Undersampling density function (top), idealised spiral-in-out trajectory (middle), exemplary 10-fold undersampling pattern (bottom). (C) Resulting  $ky$ - $kz$  sampling pattern after ten dynamics. The yellow rectangle highlights the densely sampled k-space centre.

## 5.2.2 Image Reconstruction and Motion Compensation

Conventional LLR reconstruction (27) leverages spatio-temporal correlation of imaging data by penalizing the nuclear norms of patch matrices stacked along time. For zero-filled k-space data  $\mathbf{S} \in \mathbb{C}^{N_s N_c \times T}$  with  $T$  dynamics,  $N_c$  coils, containing  $N_s$  k-space samples each, locally low-rank (LLR) reconstructed image data  $\mathbf{I}_{\text{LLR}} \in \mathbb{C}^{N_v \times T}$  of  $N_v$  voxels is achieved by solving the following convex optimization problem (27):

$$\mathbf{I}_{\text{LLR}} = \underset{\mathbf{I}}{\operatorname{argmin}} \|\mathbf{\Omega} \mathcal{F} \mathbf{C} \mathbf{I} - \mathbf{S}\|_2^2 + \lambda_{\text{LLR}} \sum_{b \in U} \|\mathbf{P}_b \mathbf{I}\|_* \quad (5.1)$$

with the undersampling operator  $\mathbf{\Omega} \in \{0,1\}^{N_s N_c \times N_s N_c}$ , Fourier transform  $\mathcal{F} \in \mathbb{C}^{N_s N_c \times N_v N_c}$ , coil sensitivities  $\mathbf{C} \in \mathbb{C}^{N_c N_v \times N_v}$  and regularization weight  $\lambda_{\text{LLR}}$ . The patch extraction operator  $\mathbf{P}_b \in \{0,1\}^{n_x n_y n_z \times N_v}$  refers to the  $b$ -th patch, where  $U$  is a set of patch indices, with patch size of  $n_x \times n_y \times n_z$  voxels. In each iteration, patches are selected randomly to avoid blocking artefacts. The optimization problem (Equation (5.1)) is posed in the synthesis form (282) and, therefore, solved with Nesterov-accelerated proximal gradient descent (178).

For the first stage of MI-LLR reconstruction, approximate displacement fields are derived to feed a motion-compensated reference system to a second reconstruction stage, allowing to reduce the rank of the inverse problem. Therefore, the initial reconstruction  $\mathbf{I}_{\text{LLR}} = [\mathbf{i}_1, \dots, \mathbf{i}_T]$  is then registered across  $T$  dynamics using the pTV registration toolbox (185). Group-wise image registration is achieved by minimizing the nuclear image dissimilarity metric of warped images  $\mathbf{i}_t \circ \mathbf{d}_t$  stacked over time  $\|[\mathbf{i}_1 \circ \mathbf{d}_1, \dots, \mathbf{i}_T \circ \mathbf{d}_T]\|_*$  (186), where displacement fields  $\mathbf{d}_t = \mathbf{d}_t(\mathbf{d}'_t)$  are parametrized by 1<sup>st</sup>-order B-spline coefficients  $\mathbf{d}'_t$  with a cell width of 5 voxels in each spatial dimension:

$$[\mathbf{d}'_1, \dots, \mathbf{d}'_T] = \underset{[\mathbf{d}'_1, \dots, \mathbf{d}'_T]}{\operatorname{argmin}} \|[\mathbf{i}_1 \circ \mathbf{d}_1, \dots, \mathbf{i}_T \circ \mathbf{d}_T]\|_* + \lambda_{\text{VTV}} \sum_{pt} \sqrt{\sum_{jk} (\nabla_k \mathbf{d}'_j)_{pt}^2}. \quad (5.2)$$

The regularization weight  $\lambda_{\text{VTV}}$  penalizes the vectorial total variation (VTV) (187), which imposes group sparsity over displacement component  $j$  in direction  $k$  for each spatio-temporal voxel location  $(p, t)$ .

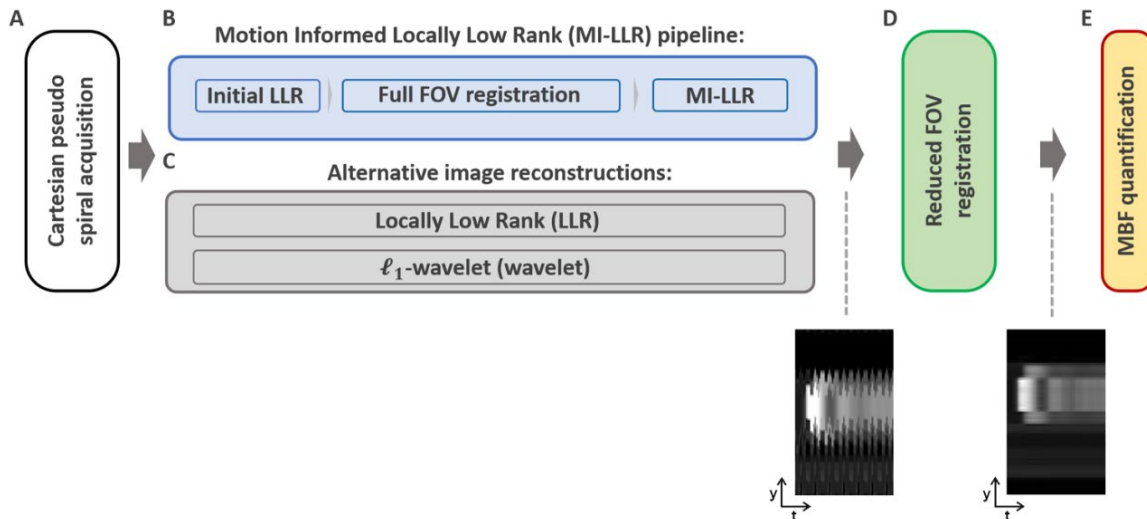


**Figure 5.2:** 3D data acquisition and reconstruction steps. (A) Data acquisition using the Cartesian 10-fold accelerated spiral-in – spiral-out acquisition pattern. (B) Motion-informed locally low-rank (MI-LLR) reconstruction pipeline: Patch-based initial local low-rank reconstruction (LLR) followed by full field of view (FOV) registration. Resulting deformation field allows to regularize over motion states for MI-LLR. (C) Alternative image reconstructions using LLR and a frame by frame  $\ell_1$ -wavelet (wavelet) reconstruction. After step B and D, 3D image series still contain motion as indicated by the intensity-time profiles and require registration in the reduced FOV around the heart (D) in order to perform myocardial blood flow (MBF) quantification (E). Please note: The MI-LLR reconstruction pipeline is also further detailed in Supporting Information Figure S1.

Displacements fields  $\mathbf{d}_j$ , estimated by image registration, map acquired images into a common reference frame. To pose the second stage of the MI-LLR reconstruction problem in the synthesis form (282), the displacement fields are inverted using linear interpolation:  $\mathbf{q}_t \approx \mathbf{d}_t^{-1}$ . Hence, corresponding linear operators  $\mathbf{Q}_t \mathbf{i}_t = \mathbf{Q}_t(\mathbf{q}_t) \mathbf{i}_t = \mathbf{i}_t \circ \mathbf{q}_t$  were used to map a fixed reference frame to the target configuration  $t$ :

$$\mathbf{I}_{\text{MI-LLR}} = \underset{\mathbf{I}}{\operatorname{argmin}} \|\Omega \mathcal{F}[\mathbf{Q}_1 \mathbf{i}_1, \dots, \mathbf{Q}_T \mathbf{i}_T] - \mathbf{S}\|_2^2 + \lambda_{\text{MI-LLR}} \sum_{b \in \mathbf{U}} \|\mathbf{P}_b \mathbf{I}\|_{*}. \quad (5.3)$$

Here,  $\lambda_{\text{MI-LLR}}$  weights LLR regularization in the motion-compensated configuration, while  $\mathbf{Q}_t \mathbf{i}_t$  for  $t = 1, \dots, T$  represents the original image sequence defined by the k-spaces  $\mathbf{S}$ . Since image warping operators  $\mathbf{Q}_t$  are applied in the data term, this optimization problem is convex and formulated in the synthesis form allowing to use the Nesterov-accelerated proximal gradient descent (178). The algorithm was implemented in Matlab (Mathworks, Natick, MA) on GPUs.

Sensitivity maps for coil calibration were estimated from reference scans using the ESPIRiT method (283). Imaging data from the scanner was extracted and pre-processed using MRecon (Gyro Tools LLC, Zurich, Switzerland).



The entire framework is schematically outlined in **Figure 5.2** A-E. At first, data is acquired using the Cartesian pseudo spiral acquisition and put into the MI-LLR reconstruction, which encompasses two stages. In the first stage (**Figure 5.2** B), images are reconstructed using LLR (Equation 1) with a patch size of  $n_x = n_y = n_z = 12$  and underregularization to capture spatio-temporal image variations ( $\lambda_{\text{LLR}} = 0.05$ ). While the images show residual undersampling artefacts, motion patterns are not suppressed and visible. These images are registered using Equation (5.2) with regularization weight  $\lambda_{\text{TV}} = 0.001$  on the displacements to suppress the impact of residual aliasing artefacts in the initial LLR reconstruction. Thereafter, estimated displacement fields are used to perform the second stage of the MI-LLR reconstruction according to Equation (5.3), thereby allowing to reduce the regularization weight. The MI-LLR pipeline is illustrated for a representative case in Supporting Information Figure S1\*.

For alternative reconstructions (**Figure 5.2** C), LLR and  $\ell_1$ -wavelet (wavelet), referring to CS reconstruction using wavelets as sparsifying transform and sensitivity encoding (i.e. SPARSE-SENSE) (159,279,280,284,285), were used. Image data  $\mathbf{I}_{\text{wavelet}} \in \mathbb{C}^{N_v \times T}$  of  $N_v$  voxels was obtained by solving:

$$\mathbf{I}_{\text{wavelet}} = \underset{\mathbf{I}}{\text{argmin}} \|\mathbf{\Omega} \mathcal{F} \mathbf{C} \mathbf{I} - \mathbf{S}\|_2^2 + \lambda_{\text{wavelet}} \|\mathbf{D} \mathbf{I}\|_1, \quad (5.4)$$

where  $\mathbf{D}$  is the discrete Daubechies wavelet transform. Equation (5.4) was solved using the Berkeley advanced reconstruction toolbox (BART) (286).

For in-vivo image reconstructions, the minimum values of the regularization parameters  $\lambda_{\text{MI-LLR}}$  and  $\lambda_{\text{LLR}}$ , which suppress background signal variation to 0.05 % of the maximum image intensity, were chosen using a grid search approach and were  $\lambda_{\text{MI-LLR}} \sim 0.30$  and  $\lambda_{\text{LLR}} \sim 0.40$ . The regularization parameter of the  $\ell_1$ -wavelet reconstruction  $\lambda_{\text{wavelet}}$  was set to 0.01. For synthetic experiments, optimal regularization parameters, yielding the lowest reconstruction error, were found using a grid search and were  $\lambda_{\text{MI-LLR}} \sim 0.25$ ,  $\lambda_{\text{LLR}} \sim 0.30$  and  $\lambda_{\text{wavelet}} \sim 0.01$ .

### 5.2.3 Postprocessing And Myocardial Blood Flow Quantification

Reconstructed 3D data was zero-filled to  $1.25 \times 1.25 \times 5 \text{ mm}^3$  and 2D-AIF images were zero-filled to  $2.5 \times 2.5 \text{ mm}^2$ . All image series were registered to compensate for residual motion prior to signal post-processing. Signal post-processing and perfusion quantification were conducted in Matlab (Mathworks, Natick, MA). For local myocardial perfusion mapping, the images were convolved using the following kernel:  $\frac{1}{5} [0,1,0; 1,1,1; 0,1,0]$  to reduce noise at the cost of resolution.

\*Supporting Information is available online: <https://pubmed.ncbi.nlm.nih.gov/35713206/>

The myocardium was segmented across the 10 slices and divided into six circumferential sectors per slice. Local and sector-wise myocardial signal time curves were derived along with the AIF.

Given the signal model of the saturation recovery Cartesian sequence,  $T_1(t)$  translates to signal  $I(t)$  as (197,200):

$$I(t) = I_0 \cdot \left[ \left(1 - \exp\left(-\frac{T_{\text{sat}}}{T_1(t)}\right)\right) \cdot a(t)^{n-1} + \left(1 - \exp\left(-\frac{\text{TR}}{T_1(t)}\right)\right) \cdot \frac{1 - a(t)^{n-1}}{1 - a(t)} \right]$$

with

$$a(t) = \exp\left(-\frac{\text{TR}}{T_1(t)}\right) \cos \alpha$$
(5.5)

with the baseline signal for fully relaxed magnetization  $I_0$ , saturation delay  $T_{\text{sat}}$ , repetition time TR, flip angle  $\alpha$ , the number of profiles sampled until k-space centre  $n$ . Accordingly,  $T_1(t)$  was calculated for every dynamic  $t$  and for myocardium as well as in the ascending aorta. Concentration-time curves  $c(t)$  were derived using:

$$c(t) = \frac{T_{1,0} - T_1(t)}{T_1(t) \cdot T_{1,0} \cdot r},$$
(5.6)

where  $T_{1,0}$  refers to the native  $T_1$  relaxation time and  $r$  to the specific contrast agent relaxivity (Gadobutrol:  $r = 5.2 \text{ L/mmol} \cdot \text{s}$ ). Accordingly, MBF was quantified using  $c_{\text{MYO}}(t)$  and  $c_{\text{AIF}}(t)$  based on a Fermi model (197):

$$c_{\text{MYO}}(t) = \text{IRF}_{\text{Fermi}}(t) * c_{\text{AIF}}(t),$$

with

$$\text{IRF}_{\text{Fermi}}(t) = \text{MBF} \cdot \frac{1 - v}{1 - v \cdot \exp(-\mu t)} \cdot \Theta(t - t_{\text{shift}})$$
(5.7)

with fitting parameters  $v$ ,  $\mu$  that entail no physiological meaning and the Heaviside step function  $\Theta$ , with the time difference between AIF and myocardial signal given by  $t_{\text{shift}}$ . The parameters of interest were fitted in the least square sense. To determine the global myocardial and blood  $T_{1,0}$  a MOLLI scan (201) was used. Further details of the implementation of the deconvolution and estimation process are outlined in (119).

## 5.2.4 Simulation Studies

Numerical simulations were performed to validate the MI-LLR framework. A fully sampled free-breathing 3D perfusion numerical phantom was created using the signal model given in Equation (5.5) based on the MRXCAT simulation framework (287). Spatial resolution of the ground truth (GT) phantom was  $1.25 \times 1.25 \text{ mm}^2$ , slice thickness: 5 mm, 20 slices. To introduce partial volume effects, the GT object was subsequently

downsampled to yield the final phantom parameters: 2.5x2.5x10 mm<sup>3</sup>, 10 slices, TR/TE: 2.0/1.0 ms, flip angle: 15°, contrast agent dose: 0.075 mmol/kg body weight (b.w.), 5 receive coils, myocardial blood flow (MBF): 3.5 mL/g/min, 70 simulated heart beats, R=10. The numerical phantom was further modified to include cardiac and respiratory motion during readout to investigate the effects of motion on reconstruction and MBF estimation. Heart rates between 60 and 120 bpm and respiratory motion based on in-vivo navigator data with maximum amplitudes of 25 and 40 mm as provided in the supporting material (Supporting Information Figure S2) were simulated.

In order to analyze the simulation results, the normalized root mean square error (nRMSE) of reconstructed magnitude images with respect to GT images in the masked myocardial region of interest (respective masks are indicated in **Figure 5.3 A**) were calculated according to:

$$\text{nRMSE} = \sqrt{\frac{\sum_{\tilde{p} \in \text{mask}} |\mathbf{I}(\tilde{p}) - \mathbf{I}_{\text{GT}}(\tilde{p})|^2}{N_{\text{mask}} * \max(\mathbf{I}_{\text{GT}}(\tilde{p})^2)}}, \quad (5.8)$$

where  $N_{\text{mask}}$  corresponds to the number of pixels  $\tilde{p}$  in the myocardial mask.

MBF data derived from reconstructed images was compared to MBF values from GT. Reconstructed image data was registered using the displacement fields obtained from registration of the GT image series to avoid confounding effects of the final registration step on MBF accuracy. Quantification errors were evaluated as mean absolute error (MAE)  $\pm$  one standard deviation of the absolute error (SD) over all myocardial pixels from 10 slices of the 3D volume, calculated according to:

$$\text{MAE} = \frac{\sum_{\tilde{p} \in \text{mask}} |\mathbf{MBF}(\tilde{p}) - \mathbf{MBF}_{\text{GT}}(\tilde{p})|}{N_{\text{mask}}}, \quad (5.9)$$

where  $N_{\text{mask}}$  corresponds to the number of myocardial pixels  $\tilde{p}$  in the masked 3D volume. To investigate the effects of signal-to-noise ratio (SNR) on MBF quantification accuracy, different noise levels were added to simulated data at resting heart-rate, i.e. 60 bpm, and 25mm respiratory motion amplitude.

Statistical differences were assessed using the two tailed paired Student's t-test;  $p < 0.05$  was considered significant.

## 5.2.5 Phantom Studies

To verify the signal to concentration conversion after image acquisition and reconstruction, tubes were filled with purified water and doped with different concentrations of Gadobutrol (from 0 to 2.25 mmol/L). The detailed setup of the phantom validation is summarized in Figure 5.5. The tubes were inserted into a cylindrical Agar phantom. Concentrations were sequentially varied to mimic the contrast agent dynamics in the left ventricle (LV) and in myocardium by manually replacing tubes in between subsequent

measurements. Concurrently, the phantom was displaced laterally to four positions with a maximum displacement of 30 mm to mimic in-vivo breathing motion dynamics.

## 5.2.6 In-vivo Experiments

Twelve healthy volunteers (7 male) with an average age  $25.2 \pm 2.4$  years underwent first-pass rest perfusion examinations; 7 underwent a rest and stress protocol. All volunteers were scanned upon written informed consent according to local ethics regulations. Two contrast-enhanced dual-sequence imaging experiments were run using contrast agent boluses at doses of 0.075 mmol/kg b.w. to compare imaging at rest and stress. contrast agent was injected at 4 mL/s and followed by a 30 mL saline flush at the same rate using a power injector (Medrad, Indianola, PA, USA). Fifteen minutes were allowed for contrast agent washout in-between the two bolus injections; stress imaging was always performed first. Adenosine (Kantonsapotheke, University Hospital Zurich, Switzerland) was injected for at least 3 minutes at doses of 140  $\mu\text{g}/\text{kg}$  b.w./min under continuous monitoring of heart rate and blood pressure in accordance with standard clinical practice. Image acquisition covered 80 heartbeats during free breathing of the subject. MI-LLR images, intensity-time profiles, concentration-time curves and resulting MBF maps were compared to LLR and  $\ell_1$ -wavelet reconstructions for reference.

## 5.3 Results

### 5.3.1 Simulation Studies

Comparing MI-LLR to LLR and  $\ell_1$ -wavelet reconstructions, image error was found to be reduced as shown by images at left-ventricular (LV) and myocardial (Myo) peak signal (Figure 5.3) with reconstruction nRMSEs for MI-LLR of 14.7% (LV) and 8.7% (Myo) versus LLR (26.2% and 9.6%) and  $\ell_1$ -wavelet (37.9 % and 13.8 %). Intensity-time profiles indicate improved motion compensation with MI-LLR relative to LLR as indicated by yellow markers (Figure 5.3 B,C). Concentration-time curves of the six sectors reflect improved motion compensation of the myocardium. In particular septal sectors show reduced signal variance with MI-LLR when compared to LLR and  $\ell_1$ -wavelet. For MI-LLR, local and sector-wise MBF maps reveal more uniform values of  $3.53 \pm 1.01$  mL/g/min with MI-LLR when compared to  $3.82 \pm 1.33$  mL/g/min with LLR and  $4.38 \pm 1.75$  mL/g/min with  $\ell_1$ -wavelet. MBF maps generally show MBF overestimation which is, however, reduced with MI-LLR when compared to LLR and  $\ell_1$ -wavelet.

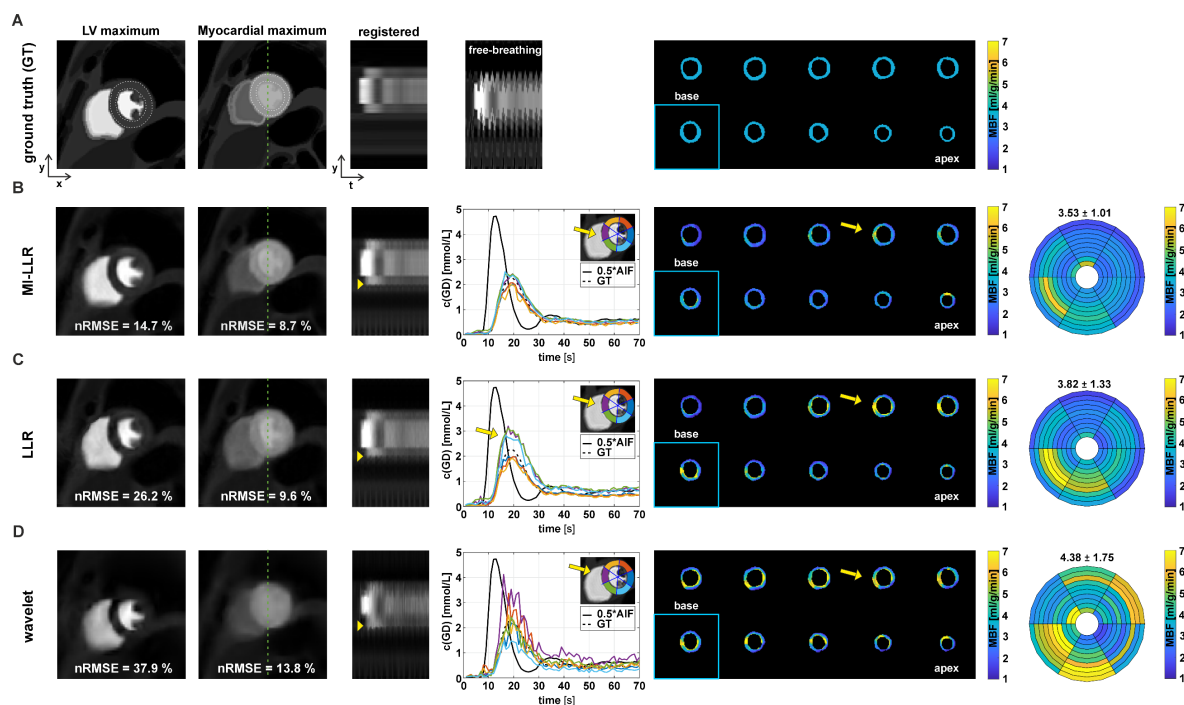


**Figure 5.3:** Simulation results for synthetic stress data at a heart rate of 60 bpm and 25 mm respiratory amplitude. Ground truth (GT) (A) and the proposed motion-informed locally low-rank reconstruction (MI-LLR) (B), LLR (C) and  $\ell_1$ -wavelet (wavelet) (D). The panels show (horizontal order), for a midventricular slice, reconstruction results and errors (nRMSEs) at peak left-ventricular (LV) and peak myocardial signal in the myocardial region as indicated by white dashed masks, intensity-time profiles upon motion correction with displacement fields obtained from registration of GT image series (for reference, GT profiles are shown for the registered and the free-breathing case), concentration-time curves, for all slices, myocardial blood flow (MBF) maps, and regional means with  $MBF \pm SD$ , respectively.

In **Figure 5.4** reconstruction nRMSE and mean absolute error (MAE) of MBF as a function of heart rate, respiratory amplitude and SNR are reduced with MI-LLR when compared to LLR and  $\ell_1$ -wavelet. Heart rate dependencies for 25 mm and 44 mm peak respiratory amplitude show a reduced reconstruction nRMSEs and MBF MAEs of MI-LLR when compared to LLR (**Figure 5.4** A,B,D,E). With a peak respiratory amplitude of 25 mm, median reconstruction nRMSEs for MI-LLR varied from 7.9% to 8.5%, while LLR shows higher median reconstruction nRMSEs (8.8% to 9.5%), as does  $\ell_1$ -wavelet (13.5% to 13.4%). Reduced MBF MAEs resulted with MI-LLR (1.25 – 1.44) as compared to LLR (1.55 – 1.61) and  $\ell_1$ -wavelet (2.39 – 2.86) up to a heart rate of 120 bpm. As summarized in **Table 5.1**, regional MBF showed significantly reduced variation with MI-LLR ( $\pm 30\%$ ) as compared to LLR ( $\pm 38\%$ ) and  $\ell_1$ -wavelet ( $\pm 45\%$ ). With a peak respiratory amplitude of 40 mm, MI-LLR yielded reduced median nRMSEs of 8.7% to 8.9% when compared to 8.8% to 9.3% for LLR and 13.1% to 13.2% for  $\ell_1$ -wavelet; reduced MBF MAEs are seen with MI-LLR (1.25 – 1.44) when compared to LLR (1.89 – 2.03) and  $\ell_1$ -wavelet (3.05 – 3.14). Regional MBF showed significantly reduced variation for MI-LLR ( $\pm 38\%$ ) when compared to LLR ( $\pm 44\%$ ) and  $\ell_1$ -wavelet ( $\pm 44\%$ ).

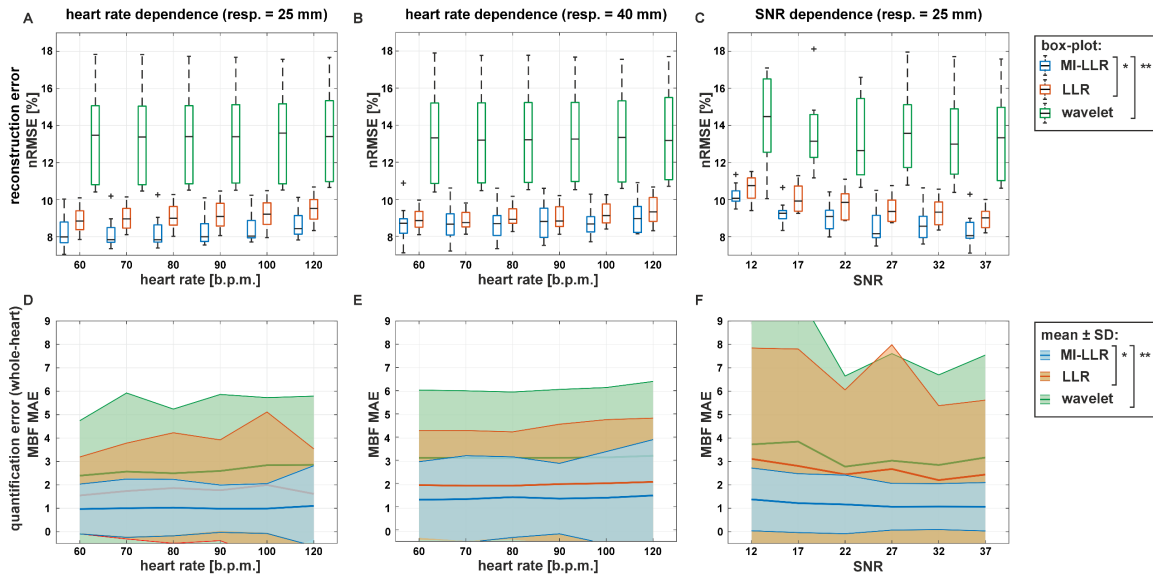


**Figure 5.4:** Simulation results comparing reconstruction nRMSE (A-C) and MBF MAE (D-E) for MI-LLR versus LLR and  $\ell_1$ -wavelet (wavelet) for heart rates from 60 to 120 bpm for respiration amplitudes of 25 mm (A,D) and 40 mm (B,E), and as a function of SNR (C,F). The boxplots summarize reconstruction RMSE over ten slices at myocardial peak signal. Shaded areas in (D-F) indicate one standard deviation (SD) of MBF over all pixels from all ten slices. To enhance representation, shaded areas are not shown for MAE < 0.5. Significant differences ( $p < 0.05$ ) are marked by asterisks: \* refers to significant reduction when motion-informed locally low-rank (MI-LLR) is compared relative to LLR. \*\* refers to significant reduction when MI-LLR or LLR are compared relative to  $\ell_1$ -wavelet (wavelet). For amplitudes of 25 mm, 40 mm and SNR all  $p^* < 0.001$ ,  $p^{**} < 0.001$ .

The SNR dependence demonstrates improved performance of MI-LLR when compared to LLR; median reconstruction nRMSEs decreased from 10.1% to 8.1% for MI-LLR when compared to 10.8% to 9.0% for LLR, and 14.5% to 13.4% for  $\ell_1$ -wavelet when increasing SNR from 12 to 37 (Figure 5.4 C); likewise reduced MBF MAE is seen with MI-LLR (1.38 – 1.07) when compared to LLR (3.11 – 2.44) and  $\ell_1$ -wavelet (3.73 – 3.17) with reduced regional MBF variation for MI-LLR ( $\pm 34\%$ ) as compared to LLR ( $\pm 53\%$ ) and  $\ell_1$ -wavelet ( $\pm 52\%$ ).

The average motion accuracy after the final registration step was 1.96 mm and 2.18 mm for 25 mm and 40 mm breathing amplitude, respectively. After registration, differences in motion accuracy between MI-LLR and LLR were insignificant.th

MBF Quantification Metrics			Motion-informed locally low-rank (MI-LLR)	Locally low rank (LLR)	$\ell_1$ -wavelet (wavelet)
Simulation	mean MBF $\pm$ SD [mL/g/min] (SD[%]) (ground truth = 3.5 mL/g/min)	Resp. amplitude: 25 mm, HR: 60 – 120 bpm	3.44 $\pm$ 1.03 (30%) **	3.77 $\pm$ 1.43 (38%) **	4.04 $\pm$ 1.82 (45%)
		Resp. amplitude: 40 mm, HR: 60 – 120 bpm	3.74 $\pm$ 1.42 (38%) **	3.67 $\pm$ 1.62 (44%) **	4.59 $\pm$ 2.02 (44%)
		Resp. amplitude: 25 mm, SNR: 12 – 37	3.43 $\pm$ 1.17 (34%) **	3.96 $\pm$ 2.10 (53%) **	4.44 $\pm$ 2.31 (52%)
In-vivo	$\pm$ mean intra-volunteer SD [mL/g/min] (SD[%])	Stress: Mean resp. amplitude $\pm$ SD: 24.9 $\pm$ 7.4 mm Mean HR $\pm$ SD: 87 $\pm$ 9 bpm	$\pm$ 1.07 (33%) **	$\pm$ 1.22 (36%) **	$\pm$ 6.87 (115%)
		Rest: Mean resp. amplitude $\pm$ STD: 16.3 $\pm$ 9.3 mm Mean HR $\pm$ SD: 67 $\pm$ 7 bpm	$\pm$ 0.17 (26%) **	$\pm$ 0.19 (28%) **	$\pm$ 1.17 (113%)

**Table 5.1:** MBF quantification metrics for simulation and in-vivo data. Significant differences ( $p < 0.05$ ) of absolute and relative myocardial blood flow (MBF) standard deviation (SD, SD[%]) are marked by asterisks: \* refers to significant differences when MBF SDs of motion-informed locally low-rank (MI-LLR) are compared relative to LLR; \*\* refers to significant differences when MBF SDs of MI-LLR or LLR are compared relative to  $\ell_1$ -wavelet (wavelet). In-vivo SDs were normalized by the means (SD[%]).

### 5.3.2 Phantom Studies

Reconstruction results for the proposed method are shown in **Figure 5.5**. Exact signal to concentration conversion is examined by comparison of reference to measured concentration with a linear regression model. **Figure 5.5 D** shows the contrast agent concentrations derived from  $T_1$  values measured with the proposed 3D acquisition and reconstruction. Data are in agreement up to Gadolinium concentrations of 2.4 mmol/L as indicated by the slope of linear regression of 1.08 (offset = 0.07).

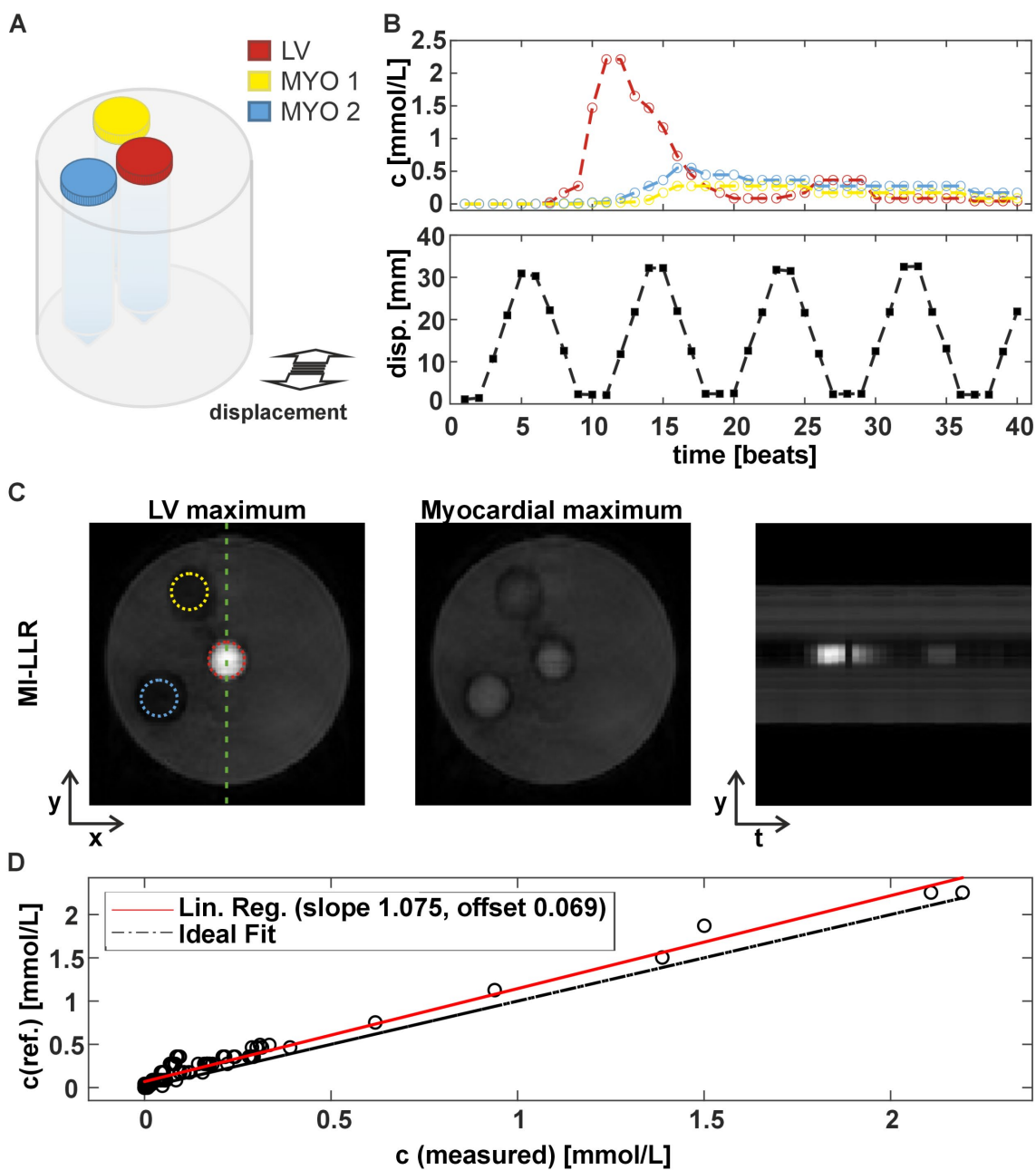


**Figure 5.5:** Phantom sequence validation. (A) Agar phantom holds three sites for falcon tubes filled with saline, doped with various concentrations of Gadobutrol. (B) The respective concentrations are varied concomitant with a displacement of the phantom, measured with a navigator, in order to reflect the perfusion and breathing dynamics, respectively. (C) Resulting motion informed locally low-rank (MI-LLR) reconstructions at concentrations corresponding to left-ventricular (LV) and myocardial maximum with respective temporal intensity profile plot. (D) Comparison of reference Gadolinium concentrations, verified by  $T_1$  mapping, and the measured concentrations obtained with the 3D acquisition scheme.



### 5.3.3 In-vivo Studies

In **Figure 5.6** and **Figure 5.7**, example reconstruction results for rest and stress acquisitions of a healthy male volunteer (average heart rate 70 bpm (rest) and 81 bpm (stress), navigator displacement 20 mm (rest) and 24 mm (stress) are reported at peak left-ventricular and myocardial contrast maximum, and intensity profiles. At rest, MI-LLR images appear less blurred than LLR at myocardial intensity maximum. Intensity profiles indicate sharper borders between myocardium and blood pool for MI-LLR when compared to LLR. At stress, MI-LLR images appear less blurred than LLR;  $\ell_1$ -wavelet images show pronounced artefacts. Intensity profiles indicate sharper borders between myocardium and blood pool for MI-LLR as compared to LLR images, with more residual motion seen in the LLR profile, while  $\ell_1$ -wavelet intensity profiles are dominated by pronounced signal intensity artefacts.

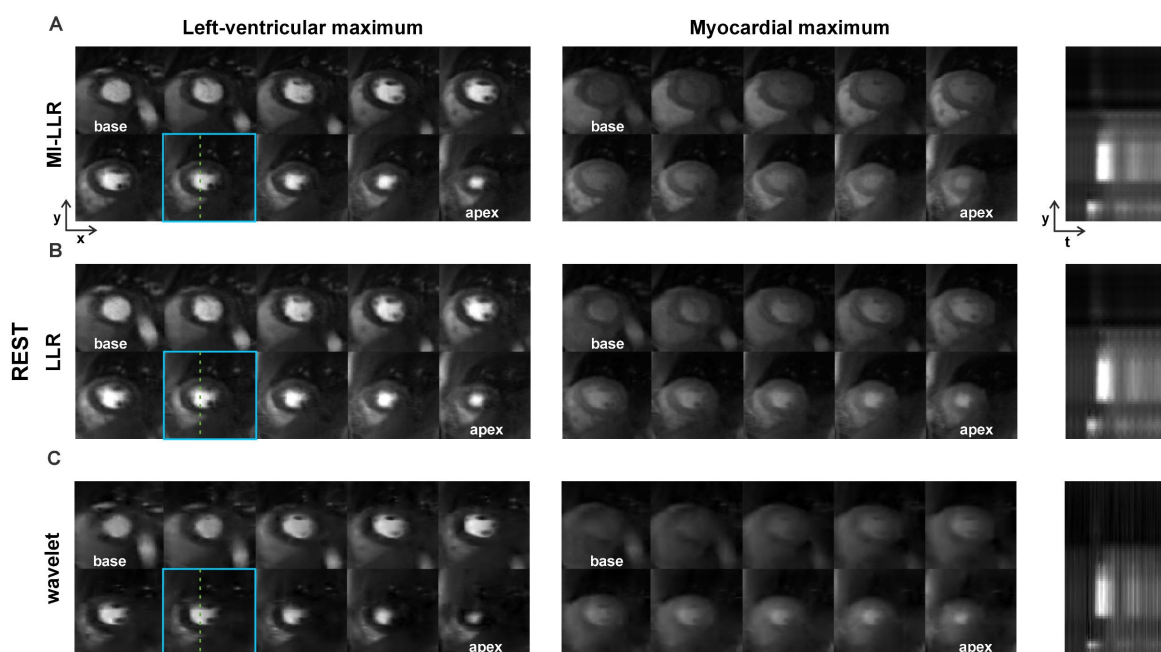


**Figure 5.6:** In-vivo results for motion-informed locally low-rank (MI-LLR) (A), LLR (B) and  $\ell_1$ -wavelet (wavelet) (C) during rest condition. Imaging results are shown (horizontal order) over ten slices at left-ventricular myocardial signal maximum and as a temporal intensity profile at a midventricular slice, indicated by blue frame and dashed line. Average heart rate and maximum displacement were 70 bpm and 20 mm, respectively.

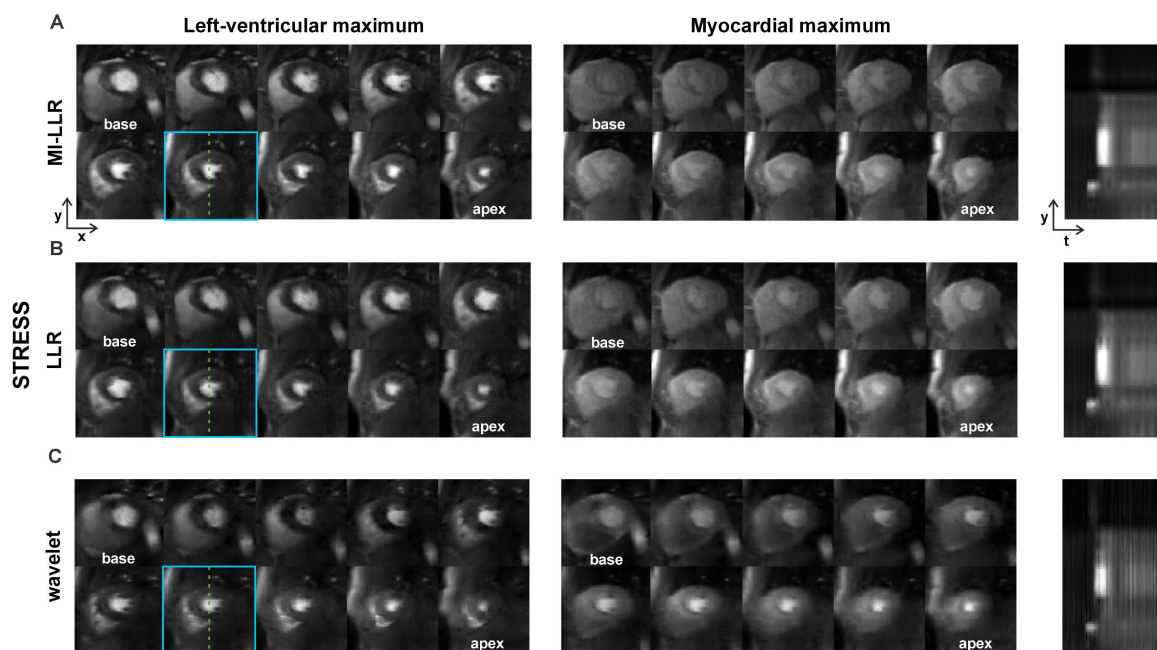


**Figure 5.7:** In-vivo results for motion-informed locally low-rank (MI-LLR) (A), LLR (B) and  $\ell_1$ -wavelet (wavelet) (C) during stress condition. Imaging results are shown (horizontal order) over ten slices at left-ventricular, myocardial signal maximum and as a temporal intensity profile at a midventricular slice, indicated by blue frame and dashed line. Average stress heart rate and maximum displacement were 81 bpm and 24 mm, respectively.

At stress (Figure 5.9), concentration-time curves show residual artefacts induced by motion for both MI-LLR and LLR. Signal maxima are lower for MI-LLR (at 0.69 mmol/L with  $0.65 \pm 0.05$  mmol/L) as compared to LLR (at 0.80 mmol/L with  $0.69 \pm 0.08$  mmol/L). MBF maps show uniform MBF values but signal spilling in the basal slices. Apical locations show reduced local MBFs as compared to basal locations. Bulls eye plots indicate that regional means are compromised less with MI-LLR; MBF variation is seen to be significantly reduced ( $p < 0.05$ ) using MI-LLR ( $\pm 0.70$  mL/g/min) vs. LLR ( $\pm 0.79$  mL/g/min) versus  $\ell_1$ -wavelet ( $\pm 3.36$  mL/g/min).

Spatial variation of contrast agent concentration across the myocardium at peak myocardial enhancement for all volunteers is compared in Supporting Information Table S1. MBF quantification results for all subjects are summarized in **Table 5.1** and Supporting Information Figure S3. One subject showed a high response to adenosine stress resulting in heart rates exceeding 130 bpm. Failing ECG gating resulted in triggering of only every second heartbeat. The stress scan was thus excluded from analysis. For MI-LLR reconstruction, at an average resting heart rate of  $67 \pm 7$  bpm, the average inter-volunteer MBF was  $0.65 \pm 0.22$  mL/g/min, while, under stress and an average stress heart rate of  $87 \pm 9$  bpm, the average MBF was  $3.23 \pm 0.61$  mL/g/min compared to  $0.68 \pm 0.23$  mL/g/min (rest) and  $3.39 \pm 0.34$  mL/g/min (stress) for LLR versus  $1.03 \pm 0.75$  mL/g/min (rest) and  $5.94 \pm 3.98$  mL/g/min (stress) for  $\ell_1$ -wavelet.

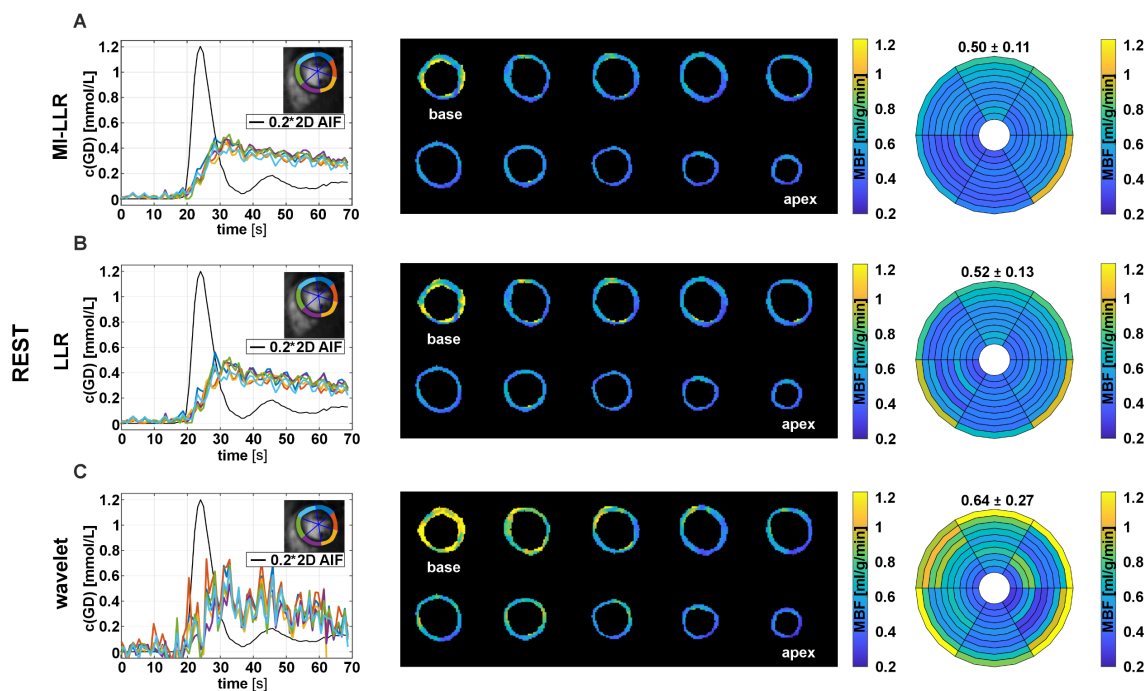


**Figure 5.8:** Quantification of in-vivo results during rest resulting from motion-informed locally low-rank (MI-LLR) (A), LLR (B) and  $\ell_1$ -wavelet (wavelet) (C) data of the volunteer presented in **Figure 5.6**. The results in panels show (horizontal order) mean concentration time curves over myocardial sectors from midventricular slice (indicated by blue frame in **Figure 5.6**) with the 2D arterial input function (AIF) myocardial blood flow (MBF) maps and regional means with  $\text{MBF} \pm \text{SD}$ . Average resting heart rate and maximum displacements were 70 bpm and 20 mm, respectively.

Intra-volunteer variation of absolute and relative MBF was lower in MI-LLR ( $\pm 0.17$  mL/g/min (26%) and  $\pm 1.07$  ml/g/min (33%)) versus LLR ( $\pm 0.19$  mL/g/min (28%) and  $\pm 1.22$  mL/g/min (36%)) and versus  $\ell_1$ -wavelet ( $\pm 1.17$  mL/g/min (113%) and  $\pm 6.87$  mL/g/min (115%)), for rest and stress, combined. At rest, the reduction in regional MBF variation between MI-LLR and LLR was significant ( $p = 0.0073$ ); at stress it was insignificant. SDs of MBF values derived from MI-LLR and LLR were significantly reduced when compared to  $\ell_1$ -wavelet at rest and stress.

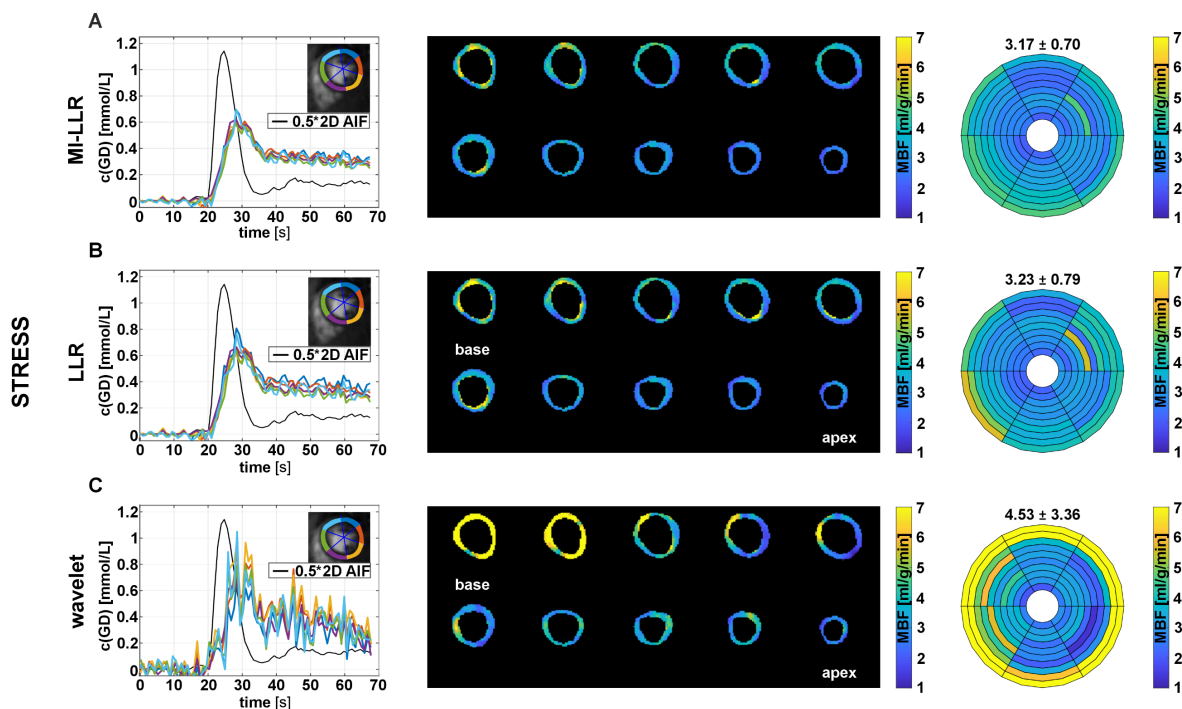


**Figure 5.9:** Quantification of in-vivo results during stress resulting from motion-informed locally low-rank (MI-LLR) (A), LLR (B) and  $\ell_1$ -wavelet (wavelet) (C) data of the volunteer presented in Figure 5.7. The results in panels show (horizontal order) mean concentration time curves over myocardial sectors from midventricular slice (indicated by blue frame in Figure 5.7) with the 2D arterial input function (AIF), myocardial blood flow (MBF) maps and regional means with  $\text{MBF} \pm \text{SD}$ . Average stress heart rate and maximum displacements were 81 bpm at 24 mm, respectively.

## 5.4 Discussion

In this study, a 3D motion-informed locally low-rank image reconstruction framework, combined with Cartesian pseudo-spiral k-t undersampling, was developed and the suitability for robust free-breathing whole-heart quantitative perfusion imaging has been demonstrated under rest and stress conditions in volunteers.

The proposed MI-LLR approach yields qualitative and quantitative improvement compared to LLR reconstruction for free-breathing imaging. In-vivo MBF values derived from both 3D MI-LLR and LLR agree with the range of values reported for quantitative 2D perfusion CMR methods (17). Reduced variation of regional MBF values was found for MI-LLR when compared to LLR and  $\ell_1$ -wavelet in simulation and for in-vivo data at rest. Average rest and stress values and their variations compare well to data from other 3D studies (119,135,166). Differences between MI-LLR and LLR depend on individual subjects' breathing pattern and heart rates (example cases shown in Supporting Information Figures S5-S8; Supporting Information Video S3, S4).

Especially in simulation, MI-LLR reduces signal elevations in the septal region as caused by high contrast signal from the right- and left-ventricular blood pools. The visually apparent trend for underestimation in the infero-lateral regions is relative to the sites of increased signal which are observed predominantly in basal slices.

In order to relate MI-LLR and LLR to methods commercially available on clinical MR systems, frame-by-frame  $\ell_1$  compressed sensing with wavelets as sparsifying transform and coil encoding was used, which resulted in significant image distortions and erroneous MBF quantification. The Cartesian pseudo spiral in-out sampling pattern used in the present work ensured that the central k-space was always covered halfway during the acquisition window. This differs from other works which promote motion robustness by means of radial sampling strategies (20,135,288), where the central k-space is traversed by every profile and as such is susceptible to variations in motion state throughout the acquisition, unless this is accounted for by e.g. retrospective binning. Of note, 3D stack-of-stars acquisition schemes inherently demand higher undersampling factors, i.e.  $\pi/2$  more data is required in order to fulfil the Nyquist criterion when compared to Cartesian sampling (17,20). Possible reduction of the acquisition window by means of partial echo and partial Fourier sampling as used in other studies (20,119) was avoided as the approximated Hermitian symmetry is potentially violated by the local modulation of signal phase due to the contrast agent (289). However, cardiac motion during the acquisition could have contributed to Gibbs ringing, i.e. dark-rim artefacts (290), which were observed in some cases in this study (e.g. Supporting Information Video S2).

Conversion of signal intensities to concentrations requires a signal model. Phantom validation (**Figure 5.5**) of MI-LLR signal intensity to concentration conversion showed good agreement within precision of experiment in the range of expected myocardial Gadobutrol concentrations from 0.1 to 2.3 mmol/L and motion amplitudes of 30 mm.

Simulation studies using the MRXCAT framework confirmed sufficient robustness of MI-LLR at higher heart rates and breathing amplitudes and was shown to outperform LLR and  $\ell_1$ -wavelet over a realistic SNR range. MBF quantification from MI-LLR reconstruction showed reduced variability in apical and basal sectors, as well as reduced overestimation of midventricular, infero- and anteroseptal regions. The investigated respiratory amplitudes of 25 mm and 40 mm in feet-head direction were taken from recorded in-vivo respiratory motion amplitudes as shown in Supporting Information Figure S2; other works only considered amplitudes of 1.7 mm and  $\sim 8$  mm (18,135). In the simulation studies sinusoidal breathing patterns of 4.5 s cycle duration were assumed; especially under stress, more irregular and abrupt breathing patterns might occur. In these cases, the exact implications of sudden motion on quantification accuracy remain to be quantified.

It is noted that the perfusion model (Equation (5.7)) fitting problem is reasonably well posed, i.e. three model parameters are fitted considering approximately 40 time points per pixel (the exact value depends on the time span of the first-pass and thus the shape of the curve). Therefore, no clear trend in MBF accuracy vs. heartrate or SNR could be detected, contrary to reconstruction nRMSEs (Figure 4A-C). However, systematic bias is intrinsic to each of the considered methods, therefore a significant improvement of MI-LLR compared to LLR in terms of MBF accuracy was seen in the simulation studies. In the future, a blood tissue exchange model (BTEX) with four free parameters modelled as partial differential equations should be tried as proposed in (209,291). In that case, superiority of MI-LLR motion compensation is expected to improve quantification robustness more profoundly than shown for the Fermi-based fitting.

In image reconstruction, the patch size as well as the range of regularization parameters  $\lambda$  were determined empirically and found to be generalizable to all datasets. A reference ground truth image could alternatively be used to optimize  $\lambda$ s (292), the acquisition of which is, however, hampered by the residual contrast agent in the tissue and the resulting change in contrast. The effects of regularization and employed image registration on net spatio-temporal resolution are yet to be determined. Although simulation and in-vivo results show motion robustness of the proposed reconstruction, maximum scan acceleration factors to reduce the influence of intra-shot cardiac motion contributions remain to be investigated. Previous work exploiting motion information for 3D perfusion imaging utilized uniform Cartesian k-t undersampling (18) in conjunction with  $\ell_2$  based regularization, as opposed to non-uniform k-t undersampling and nuclear norm regularization used here. As a result of  $\ell_2$ -regularization, temporal blurring was observed compromising MBF quantification (18). A comparison of different quantitative free-breathing perfusion approaches (i.e. data acquisition, reconstruction and MBF quantification) for uniform Cartesian, random Cartesian, radial and spiral undersampling based on synthetic data could be beneficial and will be subject of future work.

Relating to previous work that uses motion correction with LLR, the BLOSM approach is similar to the proposed MI-LLR strategy but was only applied in the context of 2D data (191); through-plane motion from true 3D acquisitions was not investigated. Continuous Radial Interleaved simultaneous Multi-slice acquisition at sPoiled steady-state (CRIMP) achieves whole-heart coverage combining self-gating and patch tracking in a continuous multiband acquisition, which uses dual bolus injections for MBF quantification (135).

Computation times for the entire reconstruction were on the order of  $\sim 15$  min per scan using a hybrid CPU-GPU implementation. Processing times are mainly determined by the cost of the 3D image registration steps. Furthermore, currently a 5-channel coil is used. For larger numbers of receiver channels, the proposed method could be adapted using coil compression methods (293).

A limitation of our study is the small number of subjects included. In order to allow for more generalizable statistical results, future studies should enroll larger numbers of subjects without and with suspected coronary artery disease. Diagnostic accuracy should then be addressed in simulation and the in-vivo evaluation. Reader assessment regarding image quality should be investigated. The method was implemented at 1.5 T but is applicable to other field strengths.

## 5.5 Conclusion

The combination of 3D Cartesian spiral in-out undersampling in conjunction with motion-informed low-rank reconstruction improves single-bolus free-breathing quantitative 3D myocardial perfusion imaging under rest and stress condition.





# Chapter 6

## Hypercapnic Myocardial Stress Perfusion in a Porcine Model – A Pilot Experiment

### 6.1 Background

Among the main objectives of myocardial perfusion imaging is the detection of ischemia. Detection of tissue associated with ischemia at early stages is only possible after induction of pharmacological induced stress to reach a regime of vasodilation beyond the physiological autoregulation (294). Autoregulation of vascular impedance or tone supports coronary flow over a wide range of pressure to satisfy the oxygen demand of myocardial tissue (**Figure 6.1**). Accordingly, compromised coronary vessel integrity may be masked and hence cannot be detected by perfusion imaging at normal, resting condition. Therefore, autoregulation needs to be suppressed by inducing a state of maximum vasodilatation, which is referred to as a stress state. While unobstructed vessels would show minimum pressure loss and hence maximum flow (**Figure 6.1**, black dashed arrow), an epicardial stenosis would induce progressive pressure loss with resulting reduction of coronary flow (**Figure 6.1**, grey dashed arrows), potentially causing ischemia (294).

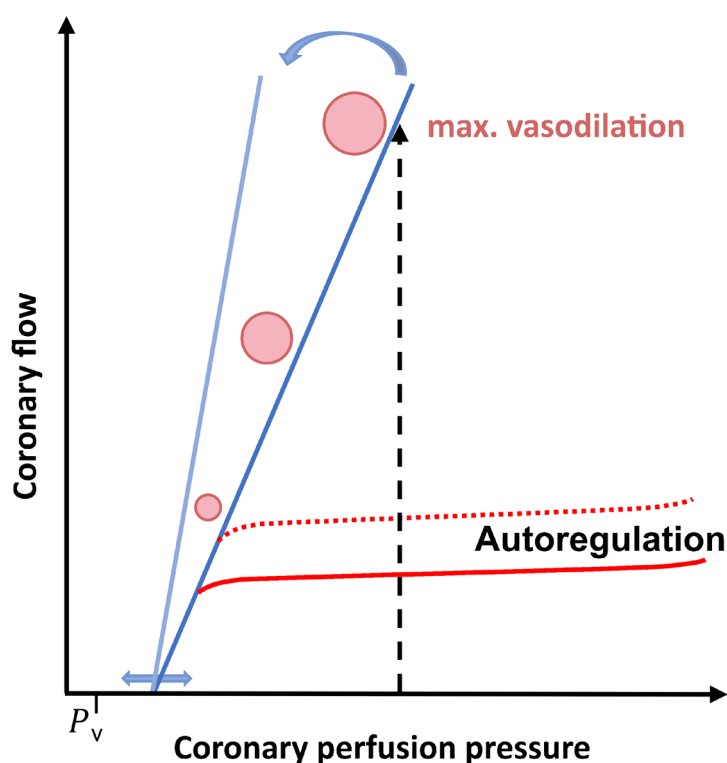


**Figure 6.1:** Coronary pressure to flow relationship (dark blue).  $P_v$  is the venous pressure. Vascular tone is indicated by red circles. Variation in cardiac function results in change of position (blue horizontal arrow) and change of slope (light blue). Figure adapted from Siebes et al. (294).

In a clinical setting, pharmacological stress agents, such as adenosine, are used to suppress vascular autoregulation. Adenosine induces coronary vasodilation by acting on endothelial receptors ( $A_{2A}$ ) in coronary vessels, forcing vascular smooth muscle cells to relax (295). Systemic vasodilation results in lowered blood pressure and tachycardia. In practice, adenosine stress is induced for 2-3 minutes, which is a sufficient time span to perform contrast-enhanced myocardial perfusion imaging.

However, besides the elevation of heart rate and MBF, current stress agents can cause side effects such as chest pain or discomfort, shortness of breath, headache, dizziness, nausea or flushing. In rare cases, this can lead to an atrioventricular block (4). Also, the short half-time of adenosine requires continuous infusion during the required imaging time window along with monitoring of blood pressure by medical personal.

Besides pharmacologically induced vasodilation, the vasodilatory effect of  $CO_2$  in blood has been explored (296,297). It has been found that an increase in arterial  $CO_2$  partial pressure, which is equivalent to the end-tidal partial  $CO_2$  pressure ( $P_{ET}CO_2$ ), results in an increase of cerebral and myocardial perfusion (296,297). An elevation of  $P_{ET}CO_2$  above the normal range in humans, i.e. 35-45 mmHg, has various physiological effects. It causes a shift in body acid-base balance towards lower blood pH, changes in

metabolism and respiratory compensation. The effect of vasodilation is associated with activation of  $K^+_{ATP}$  channels and/or stimulation of nitric oxide (NO) production in the vessel walls, resulting in relaxation of smooth muscle cells. Similar to the effects of adenosine-induced vasodilation, increased MBF can be expected. Systemically, an increase in respiratory rate and heart rate is induced.

In the literature, the effect of hypercapnia on MBF has been reported early on (298). Numerous authors have tried to establish relations between hypercapnia and MBF in experimental preclinical and clinical settings using a variety of invasive and non-invasive methodologies. While the majority of preclinical studies could report elevated blood flow as a response of hypercapnia in animal models (297,299–304), other studies could not show such relation (305,306). In humans, elevated blood flow in large coronary vessels was measured using Doppler ultrasound and velocity encoded CMR (307), using transthoracic Doppler echocardiography (308) and invasive catheter Kety-Schmidt MBF estimation (309). In a PET investigation, elevated blood flow in the heart was detected during hypercapnia (310). In contrast, a Doppler ultrasound study could not show significantly elevated coronary blood flow induced by hypercapnia (311). The authors related the inconclusive and contradictory results to differences in study design and limited standardisation of animal species, blood flow probing methodology and especially hypercapnia protocols (312).

These problems were mitigated in more recent works which are based on a setup with automatically controlled  $P_{ET}CO_2$  and  $P_{ET}O_2$ . The dependency between an increase in  $P_{ET}CO_2$  (at a constant level of  $P_{ET}O_2$  i.e. normal blood  $O_2$  pressure or euoxia) and hypercapnia with an elevation of blood flow in the myocardium could be established using multiple methodologies: MR blood oxygen level dependent (BOLD) myocardial imaging has been studied, where myocardial oxygenation is used as a surrogate for myocardial perfusion (79,313). In a study by Yang et al. (79), the response between targeted  $P_{ET}CO_2$  and blood  $PCO_2$  was validated in a canine model for a range of 20 to 60 mmHg. Hypercapnia was induced twice in plateaus of  $P_{ET}CO_2$  at 10 mmHg above the subject's normal  $P_{ET}CO_2$  for 4 minutes with waiting periods of 5 minutes in between. In the same study, hypercapnia was induced in healthy young men twice in plateaus of  $P_{ET}CO_2$  at 5 and 10 mmHg above the subject's normal  $P_{ET}CO_2$  for 4 minutes. Imaging was performed 1 minute after  $P_{ET}CO_2$  stabilized. Controlled hypercapnia was shown to invoke stimuli similar to adenosine. In a second study (313), hypercapnia was induced in canines four times in plateaus of  $P_{ET}CO_2$  at 60 mmHg (i.e. 25 mmHg above normal) for 5 minutes with waiting periods of 5 minutes in between while euoxia was maintained at  $P_{ET}O_2$  at 130 mmHg. The BOLD response to hypercapnia could be established and showed the potential to non-invasively assess ischaemic heart disease. Noteworthy, in studies on oxygen sensitive CMR (82,314), it was shown that vasoactive breathing exercises, i.e. hyperventilation and long breathholds, induce changes in blood  $CO_2$ , which trigger hypercapnia-induced vasodilation in a similar manner as pharmacological vasodilators. Yang et al. went on to study hypercapnia

and the myocardial perfusion response using MBF quantification in a PET study in canines (315). Hypercapnia was induced once during a plateau of  $P_{ET}CO_2$  at 60 mmHg (i.e. 25 mmHg above normal while euoxia was maintained at  $P_{ET}O_2 = 125$  mmHg). At rest  $P_{ET}CO_2 = 35$  mmHg was targeted. The effect of hypercapnia on MBF was compared with adenosine and showed elevated MBF comparable to standard dose adenosine (315). In a PET study by Pelletier et al. (312), these results were replicated in young healthy men and could show a  $P_{ET}CO_2$  dose-dependent increase in MBF. Hypercapnia was induced four times in plateaus of  $P_{ET}CO_2 = 50, 55$  and two times 60 mmHg for 6 minutes each, while euoxia was maintained at  $P_{ET}O_2$  of 100 mmHg. The first three plateaus with steps were used to investigate dose response with resting periods of 4 minutes in between. The last two plateaus were used to test repeatability and were separated by a waiting period  $> 10$  minutes to allow the return of  $P_{ET}CO_2$  to normal. PET imaging was started after 3 minutes in the plateau. At rest  $P_{ET}CO_2$  was targeted to the respective subject's normal value (35-43 mmHg). For stress stimuli at 60 mmHg, MBF doubled but was not higher when compared to adenosine. Generally, stress hypercapnia above  $P_{ET}CO_2$  of 60 mmHg increases the risk for acidosis and is not sustainable in an experiment with repetitive hypercapnia, especially in anesthetized animal models.

Given these previous works, inducing hypercapnia by controlled modulation of  $P_{ET}CO_2$  is of interest for contrast-enhanced MBF perfusion imaging. While canine models have been studied in detail, little is known about the effects of hypercapnia in porcine models. Previous work conducted by our group has revealed that induction of pharmacological stress is difficult in the porcine model, i.e. adenosine has proven itself to be difficult because of a non-specific systemic response with severe loss of blood pressure. Similarly, Elias et al. (316) also observed loss in systolic, diastolic and mean arterial blood pressure and found that heart rate and cardiac output did not increase upon adenosine infusion. Husso et al. (317) showed the expected hemodynamic (i.e. blood pressures, cardiac output and heart rate) and blood flow response using co-administered phenylephrine to maintain blood pressure.

The pilot study described in the following aimed at investigating the feasibility of myocardial stress perfusion induced by hypercapnia in a porcine animal model. To this end, induction of hypercapnia by modulating end tidal partial pressure was tested and optimized. The response of MBF to hypercapnia was measured using quantitative free-breathing 2D and 3D perfusion CMR.

---

## 6.2 Methods

### 6.2.1 Hypercapnia Instrumentation

The experimental setup for mechanical ventilation is depicted in Figure 6.2. In order to control  $P_{ET}CO_2$ , a computer-controlled gas blender was used (RespirAct RA-MR, Thornhill research, Toronto, Canada) (318,319). The active control unit remained in the MR control room and the gas blending unit was placed close to the subject's head. The respiratory ventilation was provided by a standard clinical ventilator with external  $O_2$  and air input. In the first setup for pilot experiment #1, the ventilator was placed in the control room, which required long hoses (~10 m as compared to 1.5 to 2.0 m in clinical setting) for ventilation and did not allow to maintain the required ventilation response (please refer to **Figure 6.4**). For the second and third set of pilot experiments, the ventilation was placed behind the back wall of the scanner room in order to keep the distance between ventilator and subject's head as short as possible (~2.0 m). A camera allowed monitoring of the ventilator from the control room. Expiratory and inspiratory hoses were inserted into the scanner room via waveguides in the RF cage. The inspiratory tube ran from the ventilator into the blending unit. From there, the gas mixture was fed into the animal. There, inspiration and expiration hoses were connected to the intubation tube by a fork junction. A valve ensured one-directional air flow. For gas sensing, a small hose was attached right at the end of the junction to feed air back to the blending unit. The sensory information was sent to the control unit in the MR control room. Cables and hoses which provide  $O_2$ ,  $CO_2$  and a calibration gas were fed through a waveguide to link the control with the blending unit. The calibration gas was a dedicated mixture of 10%  $O_2$  and  $N_2$ . It allowed to perform autocalibration prior to the experiments. The required  $P_{ET}CO_2$  pressures for rest and hypercapnia stress were set in the interface of the RespirAct before the control was activated.  $P_{ET}O_2$  was also preset but are adapted by the algorithm to maintain euoxia. During the experiment the target pressures and corresponding measurement as well as breathing were monitored as shown in the inset of Figure 6.2.

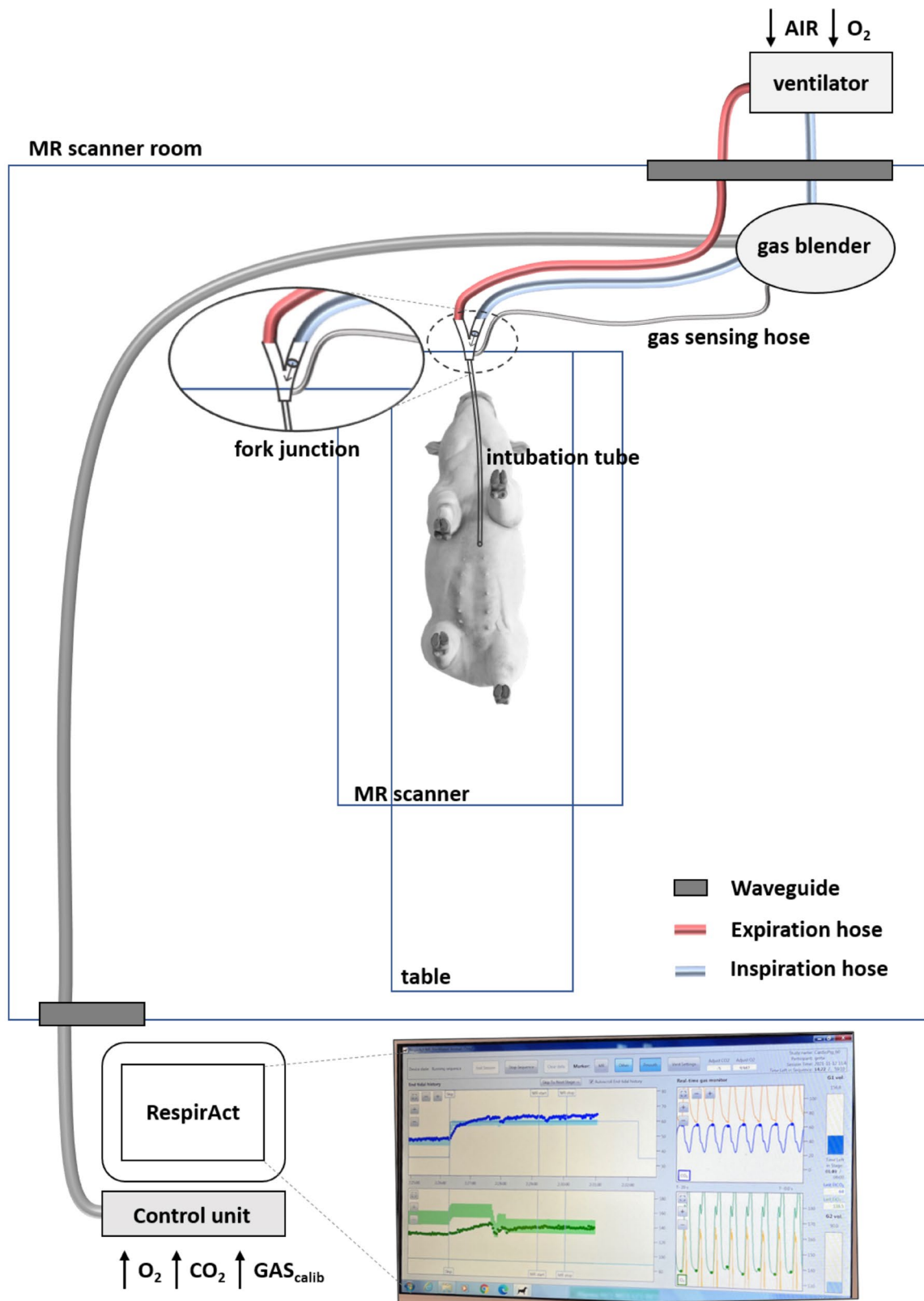


**Figure 6.2:** Experimental setup for the hypercapnia experiments in the anesthetized porcine model using the RespirAct device in conjunction with a clinical ventilator. The inset in the bottom right shows a screenshot of the RespirAct's interface during a hypercapnia stress experiment. The schematic is not to scale.

## 6.2.2 In-vivo Experiments

The porcine model experiments follow procedures adapted from hypercapnia canine and human studies by Yang et al. (79,313,315) and the human study by Pelletier et al. (312).

The first goal of the experiment was to establish the feasibility of the experimental setup. The second goal was to test the MBF response to hypercapnia and to investigate the repeatability as well as the dose response relationship.

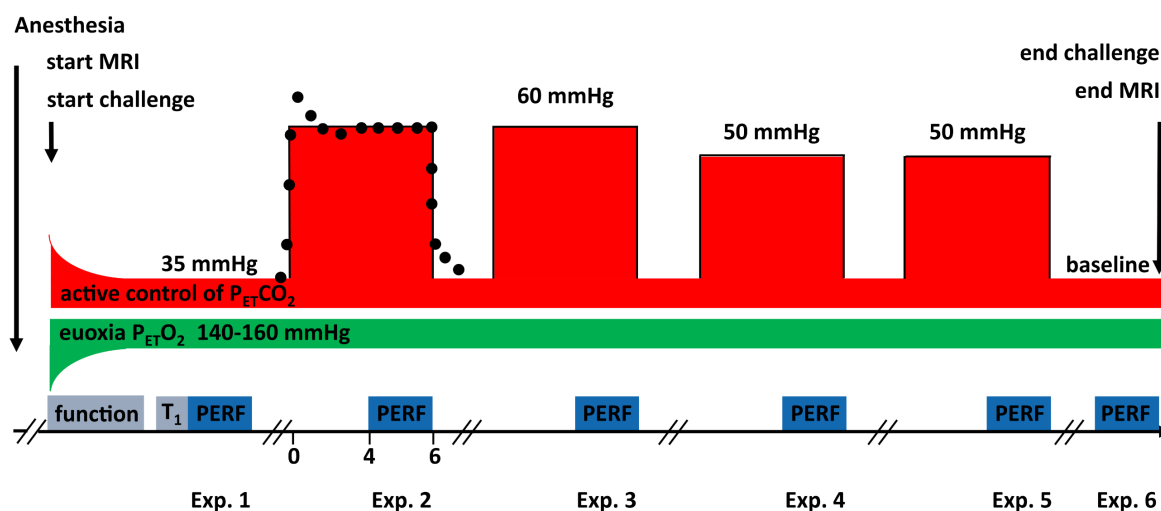


**Figure 6.3:** Protocol of the hypercapnia challenge. The active  $P_{ET}CO_2$  controlled by the gas blender is indicated in red. The  $P_{ET}O_2$  level for euoxia is indicated in green. The expected time for the system and the ventilated subject to adapt to the control is indicated by the down- and up-slope for  $P_{ET}CO_2$  and  $P_{ET}O_2$ , respectively. The expected  $P_{ET}CO_2$  response to the stress plateau at 60 mmHg is indicated by black markers. In the bottom line the timeline with the corresponding MRI experiments is given.

In pilot #1, the system's ability to reach controlled  $PCO_2$  and a targeted plateau of  $P_{ET}CO_2$  at 60 mmHg for 6 minutes was tested. In pilot study #2, the response of MBF to change in  $P_{ET}CO_2$  was measured for a protocol as shown in the overview **Figure 6.3**. At the start of the protocol, the  $P_{ET}CO_2$  control is activated and the targeted baseline is set to  $P_{ET}CO_2$  at 35 mmHg, while  $P_{ET}O_2$  euoxia was maintained by the gas blender. According to the previous studies (79,313,315), the expected range for  $P_{ET}O_2$  was 140 to 160 mmHg. Depending on the animal's physiological normal state, a couple of minutes of delay was expected before the targeted values at baseline were achieved. Functional imaging for planning as well as a MOLLI T1 scan were acquired in the meantime. Initial 3D perfusion imaging at baseline (i.e.  $P_{ET}CO_2 = 35$  mmHg) was performed to establish the normal MBF value at rest. It was followed by pairs of plateaus at 60 mmHg (for repeatability) and 50 mmHg (dose dependent response and repeatability), respectively. The duration of the hypercapnia plateau was set to 6 minutes to account for the initial  $P_{ET}CO_2$  overshoot that is settled within 1 to 2 minutes (79,313,315). Perfusion experiments were performed in the last two minutes of the

plateaus. In order to allow for return to baseline  $\text{PCO}_2$  at euoxia, which requires several breathing cycles in anesthesia, and sufficient contrast agent washout from tissue, the waiting time between experiments was >10 minutes. A final perfusion experiment was obtained at baseline during rest.

For pilot #3, the protocol of pilot #2 was repeated. In order to differentiate and consider different levels of myocardial perfusion in the different heart phases, 2D perfusion experiments with imaging of three slices triggered to peak systole, early diastole and diastole, were used.

The direct conversion of targeted  $\text{P}_{\text{ETCO}_2}$  into arterial  $\text{PCO}_2$  is considered the independent variable for vasoreactivity (79,320). As the RespirAct is not intended for use in anaesthetised animals, this relationship had to be validated (79). For the pilot studies #2 and #3, the collected arterial and venous blood gases (see animal handling) were measured before and during the stress plateaus and compared against the values sensed by the RespirAct blending unit.

For perfusion experiments, a contrast-enhanced 2D/3D dual-sequence single-bolus scheme was used. Contrast agent boluses at doses of 0.075 mmol/kg b.w. and 0.1 mmol/kg b.w. were injected at 4 mL/s and followed by a 30 mL saline flush at the same rate using a power injector (Medrad, Indianola, PA, USA). Image acquisition covered 60 heartbeats during continuous respiratory ventilation of the animals.

### 6.2.3 Animal Handling

Three domestic healthy female swine (*Sus scrofa domestica*, breed: Swiss large white, body weights 45 kg) were used for the experiments. All swine were premedicated and intubated. The animal for pilot #1 was positioned laterally. For pilot #2 and #3, animals were positioned supine. General anesthesia was maintained with isoflurane (2 to 3%) by positive pressure ventilation. In the standard CMR anesthesia setup, ventilation is conducted with 100%  $\text{O}_2$ . However, when the ventilation runs in series with the RespirAct, the ventilator  $\text{O}_2$  is set to 0%, while the peak end expiratory pressure (PEEP) is increased from 3.8 to 15.0 mmHg. Heart rate and ECG, inspiratory and expiratory gas partial pressures, urine output, arterial and venous blood gases were monitored continuously throughout the procedure. Arterial blood pressure was measured before and during every hypercapnic stress measurement. All animal handling, procedures and protocols were approved by the Cantonal Veterinary Office (Zurich, Switzerland).

### 6.2.4 Image Acquisition and Reconstruction

MR imaging was conducted on a clinical 1.5 T Philips Achieva MR system (Philips Healthcare, Best, The Netherlands) with a 40 mT/m at 200 T/m/s gradient system, equipped with a five-channel cardiac receiver array. Gadobutrol (Gadovist, Bayer Schering Pharma, Germany) contrast agent was used.

For the 3D perfusion dual-sequence scheme, imaging parameters were: TR/TE = 2.0/1.0 ms, spatial resolution:  $2.5 \times 2.5 \times 10 \text{ mm}^3$ , FOV:  $300 \times 300 \times 100 \text{ mm}^3$ , covering the full ventricle from apex to base,



flip angle: 15°, acquisition window: 240 ms, saturation delay: 135 ms, undersampling factor  $R = 10$ . The 3D perfusion scan was triggered to end systole.

For the interleaved acquisition of the AIF, a fully sampled centre-out Cartesian pattern was used with spatial resolution:  $10 \times 10 \text{ mm}^2$ , slice thickness: 15 mm, flip angle: 15°, acquisition window: 56-64 ms, saturation delay: 30 ms. TR and TE were set equal to the corresponding 3D sequence to avoid different  $T_1$  and  $T_2^*$  weightings. The 2D AIF images were acquired in the ascending aorta during diastole.

The 3D perfusion images were reconstructed using the motion informed locally low-rank pipeline detailed in (321). 2D perfusion data were reconstructed on the scanner using the product SENSE implementation.

## 6.2.5 Image Post-processing and Analysis

Post-processing and perfusion quantification were conducted in MATLAB (Mathworks, Natick, MA). The 2D perfusion data was registered prior to quantification (185). Semi-quantitative analysis of signal time curve upslopes was performed in 6 circumferential myocardial sectors and the left ventricular AIF (108). Myocardial upslopes were normalized by the upslope of the AIF. Full MBF quantification was performed using Fermi model deconvolution (9). Values per experiment are given as the sectorial mean of the mid-ventricular slice.

## 6.3 Results

### 6.3.1 Hemodynamic Response to Hypercapnic Stimuli

The  $P_{\text{ETCO}_2}$  data for pilot #1 is shown in **Figure 6.4**. During the first ten minutes, end-tidal pressure was subject to variation during initialization of the system. When the  $P_{\text{ETCO}_2}$  control was turned off during switching of the system sequence, the lack in active control led to a spike in  $P_{\text{ETCO}_2}$  and a rapid negative drop in  $P_{\text{ETCO}_2}$  (also shown in **Figure 6.5** for pilot #2 and #3).  $P_{\text{ETCO}_2}$  reached a baseline of 39 mmHg after 15 minutes, 5 mmHg higher than the set value of 35 mmHg. During baseline,  $P_{\text{ETCO}_2}$  varied between 135-138 mmHg. At the onset of the target plateau level of 60 mmHg (in the following referred to as stress-60),  $P_{\text{ETCO}_2}$  rose to 56 mmHg over the course of 2 minutes, followed by a sharp decline down to 41 mmHg. Just before the end of the stress-60 plateau,  $P_{\text{ETCO}_2}$  peaked at 53 mm and thus failed to reach the intended value of 60 mmHg. At onset of the stress-60 plateau,  $P_{\text{ETCO}_2}$  sharply rose to 163 mmHg and steadily decreased during the stress experiment.

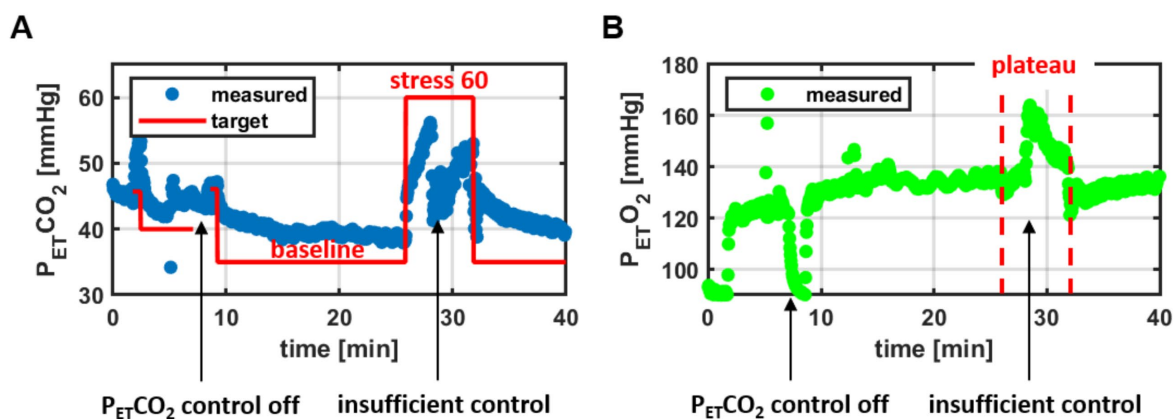


**Figure 6.4:** End-tidal pressure pilot #1. (A) Curve of target  $P_{ET}CO_2$  as produced by the gas blender (red line) and measured  $P_{ET}CO_2$  (blue dots). The intended plateau at  $P_{ET}CO_2 = 60$  mmHg is labelled as stress 60. (B) Corresponding measured  $P_{ET}O_2$  (green markers). Red, dashed lines indicate the stress 60 plateau.

**Figure 6.5** shows the  $P_{ET}CO_2$  tracing for pilot #2 and #3 with the short ventilation tube setup. In pilot #2, during the first ten minutes, end-tidal pressure was again subject to variations during initiation of active  $P_{ET}CO_2$  control.  $P_{ET}CO_2$  reached the baseline after 60 minutes. Similarly,  $P_{ET}O_2$  rose to euoxia at 160 mmHg. At the onset of stress-60,  $P_{ET}CO_2$  steadily increased to 60 mmHg over the course of 3.5 minutes (as also shown in the inset). The level was maintained as scheduled for the remaining 2.5 minutes. At the onset of stress,  $P_{ET}O_2$  briefly increased and slightly decreased during stress to 157 mmHg. At the end of the plateau,  $P_{ET}O_2$  decreased, while the system had to regulate in response to the sudden drop in  $P_{ET}CO_2$ . Baseline was again reached after 20 minutes. For the second stress-60, the plateau was reached even swifter. For the following two stress-50 plateaus, data showed an instantaneous increase with the expected brief overshoot of the plateau (see second inset). The plateau was maintained for 5 out of 6 minutes.

For pilot #3, the baseline of  $P_{ET}CO_2$  was reached after 25 minutes. At baseline,  $P_{ET}O_2$  reached 155 mmHg. For the stress-60 experiments, the response was quicker than that seen for pilot #2, also indicated by the short overshoot. For stress-50, the plateau was reached but was subject to a sudden drop down to 40 mmHg. Gaps in the traces of target  $P_{ET}CO_2$  marked the end of one experiment as assigned by the gas blender. Before the system transitioned again into a controlled state of  $P_{ET}CO_2$  it briefly reset. During this period active gas control was off causing a sudden downslope in  $P_{ET}O_2$  along with a spike in  $P_{ET}CO_2$ .

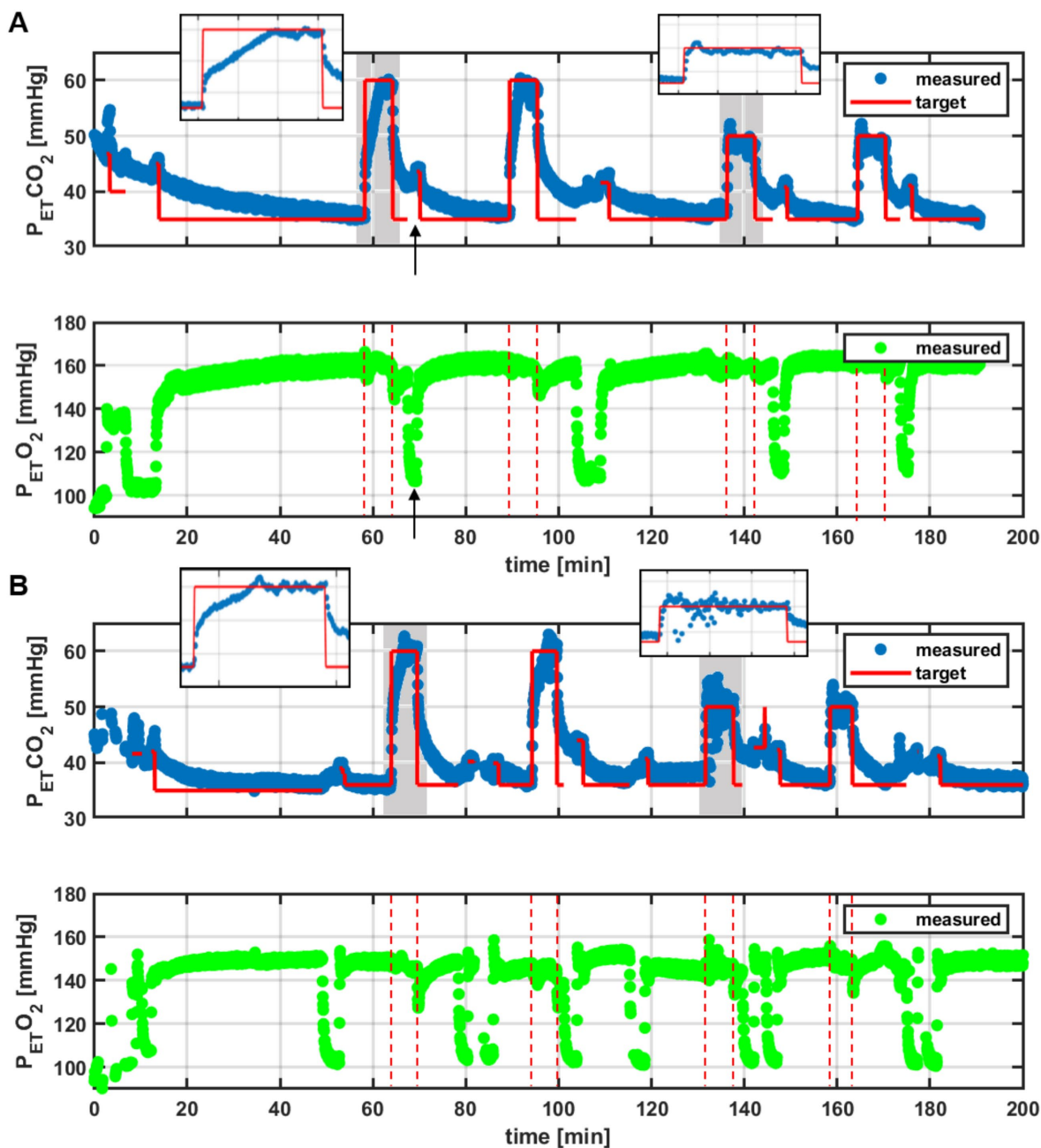


**Figure 6.5:** End-tidal history at different levels of hypercapnia for pilot #2 and #3 in A and B, respectively. Respective top panels show curve of target  $P_{ET}CO_2$  as produced by the gas blender (red line) and measured  $P_{ET}CO_2$  (blue markers). The insets show enlarged plot of 6 minute plateaus. Bottom panel shows corresponding measured  $P_{ET}O_2$  (green markers). Red, dashed lines indicate corresponding stress plateaus.

Results on  $P_{ET}CO_2$  and  $P_{ET}O_2$  as measured by the gas blender as well as from arterial blood samples ( $PCO_2$  and  $PO_2$ ) as measure for vasoreactivity are summarized in **Figure 6.6**. For pilot #2 and #3, comparison of arterial blood  $CO_2$  pressure against  $P_{ET}CO_2$  as measured by the sensor in the blending unit shows a linear correlation ( $R=0.96$ ,  $p<0.0001$ ). Comparison of arterial blood  $O_2$  against  $P_{ET}O_2$  showed no linear correlation. A detailed summary is given in Table 1 and 2 for pilot #2 and #3, respectively.

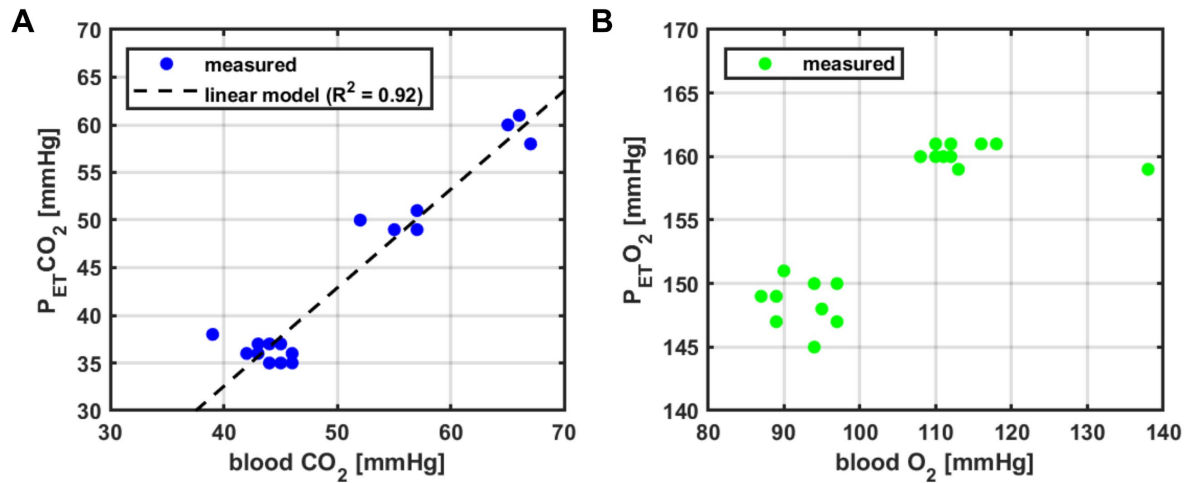


**Figure 6.6:** Relationship between blood partial and end-tidal pressures for CO<sub>2</sub> (A) and O<sub>2</sub> (B) in pilot experiments #2 and #3. For the relationship of blood CO<sub>2</sub> and P<sub>ET</sub>CO<sub>2</sub>, a linear correlation is shown ( $R^2 = 0.92$ , two tailed Student's t-test  $p < 0.00001$ ). Full data is summarized in Table 1 and 2.

Comparing of heart rate before onset of the P<sub>ET</sub>CO<sub>2</sub> stress plateau and at the plateau shows no increase in heart rate (variation of < 1 bpm) as shown in Table 1 and 2.

### 6.3.2 MBF Response to Hypercapnic Stimulus

The results for the investigation of the response of MBF to hypercapnia stimuli in pilot study #2 are shown in the MBF maps in **Figure 6.7**. In the two baseline experiments, median MBFs were 0.77 ml/g/min and 0.97 ml/g/min for the final and initial experiment, respectively. At the two 60 mmHg targets, MBF was 0.71 ml/g/min and 0.77 ml/g/min as compared to 0.76 ml/g/min and 0.78 ml/g/min at the two 50 mmHg targets, respectively. Accordingly, no response of MBF to different levels of hypercapnia is seen (for full data see **Table 6.1**). For pilot study #3, results of semi-quantitative perfusion estimation are shown in **Table 6.2**. Upslope values for myocardium and LV AIF, as well as normalized myocardium do not show a consistent response to the hypercapnic stimulus.

Pilot 2 Experiment #: (type) Parameter:		1 (baseline)	2 (60 mmHg)	3 (60 mmHg)	4 (50 mmHg)	5 (50 mmHg)	6 (baseline)
P <sub>ET</sub> CO <sub>2</sub> (sensor) [mmHg]	rest	36	35	35	35	35	35
	stress	37	59	58	49	49	35
PCO <sub>2</sub> (blood) [mmHg]	rest	46	46	44	45	44	45
	stress	45	N/A	67	57	55	N/A
P <sub>ET</sub> O <sub>2</sub> (sensor) [mmHg]	rest	161	160	160	160	161	161
	stress	160	160	159	159	161	161
PO <sub>2</sub> (blood) [mmHg]	rest	110	110	111	108	112	116
	stress	112	N/A	138	113	118	N/A
HR [bpm]	rest	90	90	80	79	82	82
	stress	95	91	80	79	82	82
MBF (relative change) [ml/g/min]		0.77±0.14	0.71±0.07 (-7.8%)	0.77±0.07 (0%)	0.76±0.05 (-1.4%)	0.78±0.05 (+1.4%)	0.97±0.05 (+25%)
norm. Upslope MYO* (relative change)		0.04±0.01	0.07±0.02 (+61%)	0.06±0.02 (+52%)	0.04±0.01 (-2.7%)	0.05±0.01 (+13%)	0.04±0.01 (-1%)

**Table 6.1:** Summary of results for pilot #2. Quantitative perfusion estimates are given as their median±SD. Semi-quantitative perfusion estimates are given as mean±SD in arbitrary units (a.u.).

Pilot 3 Experiment #: (type) Parameter:		1 (baseline)	2 (60 mmHg)	3 (60 mmHg)	4 (50 mmHg)	5 (50 mmHg)	6 (baseline)
P <sub>ET</sub> CO <sub>2</sub> (sensor) [mmHg]	rest	36	36	37	38	36	37
	stress	36	60	61	51	50	37
PCO <sub>2</sub> (blood) [mmHg]	rest	N/A	42	44	39	43	43
	stress	N/A	65	66	57	52	N/A
P <sub>ET</sub> O <sub>2</sub> (sensor) [mmHg]	rest	149	149	147	145	151	149
	stress	149	150	148	147	150	149
PO <sub>2</sub> (blood) [mmHg]	rest	N/A	89	89	94	90	87
	stress	N/A	97	95	97	94	N/A
HR [bpm]	rest	69	67	69	71	71	72
	stress	69	67	69	71	71	72
MBF (relative change) [ml/g/min]		N/A	N/A	N/A	N/A	N/A	N/A
norm. Upslope MYO* (relative change)		0.04±0.01	0.05±0.01 (+19%)	0.08±0.01 (+8%)	0.07±0.02 (+56%)	0.08±0.02 (+90%)	0.09±0.01 (+97%)

**Table 6.2:** Summary of results for pilot #3. Fully quantitative could not be obtained. Semi-quantitative perfusion estimates are given as mean±SD in arbitrary units (a.u.).

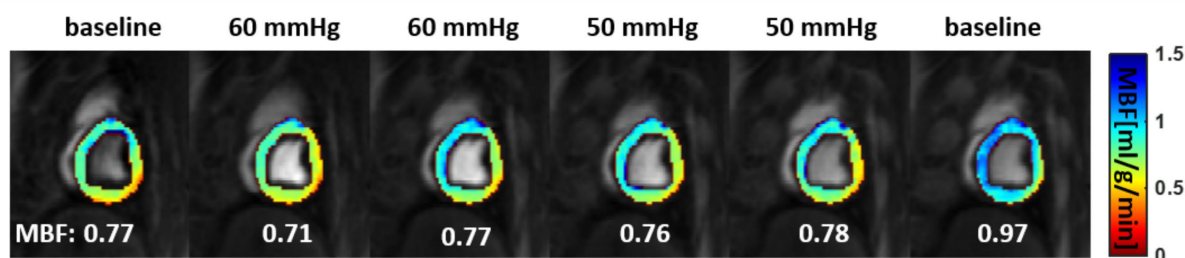


**Figure 6.7:** Myocardial blood flow (MBF) results for pilot #2. From left to right, myocardial MBF maps superimposed to the perfusion images in a midventricular slice are shown for experiment 1 to 6 with their P<sub>ET</sub>CO<sub>2</sub> targets and median myocardial MBF given in ml/g/min.

## 6.4 Discussion

This work documents inconclusive hemodynamic responses to hypercapnia in an anaesthetized porcine model. While delivery of hypercapnic stimuli was successful, once the distance between the mechanical respirator and the animal was kept as short as possible and the animal was positioned in supine position, myocardial perfusion did not show the expected increase in response to hypercapnia. Also, monitored heart rates remained constant and showed no response to hypercapnic stimuli.

The absence of a hemodynamic response in our studies may be linked to several factors. In previous human studies, increases in cardiac work due to hypercapnia were noted (309,311) and hypercapnia induced increases in MBF are considered to be partially induced by increased heart work as hemodynamic response. Corrections were made to separate the effect of hypercapnia on MBF from heart rate and blood pressure. The corrected MBF ( $MBF_{cor}$ ) was normalized by heart rate and systolic blood pressure (SBP) as combined in the Rate Pressure Product (RPP). Correction is then  $MBF_{cor} = (MBF \cdot \text{mean}(RPP_{rest, population}) / RPP_{stress, subject})$ : Considering the corrected MBF is arguably relevant, as especially microvascular vasodilation can occur independent of increased cardiac work (294). In the PET study by Pelletier et al. (312), average corrected MBF increased for  $P_{ET}CO_2$  at 60 mmHG from  $0.44 \pm 0.045$  ml/g/min to  $0.59 \pm 0.15$  ml/g/min. This reduced MBF response in ‘absence’ of heart rate elevation.

Second, in light of the corrected MBF response of 34% in the human PET study, the inconsistent MBF results in the conducted measurements, the precision and accuracy of the CMR quantitative perfusion measures have to be contextualized. For the 3D quantitative methods in pilot #2, mean $\pm$ SD of coefficients of variance (COV) for pixel-wise MBF mapping in the healthy myocardium were  $13 \pm 7\%$ . For 2D, semi-quantitative normalized upslope sector-wise COVs (mean $\pm$ SD) over all measurements were  $26 \pm 13\%$  and  $18 \pm 8\%$  for pilot #2 and pilot #3, respectively. In addition, reduced precision after the initial contrast agent administration has to be considered for insufficient washout times. Nevertheless, the contrast to noise ratio after the first administration of contrast agent, can be considered to be sufficient for quantitative perfusion measurements (108). For the 3D perfusion method, MBF accuracy can be as low as  $\sim 25\%$  (321).

In light of these findings, a limitation of the pilot studies is the lack of blood pressure data. While blood pressure was monitored throughout the experiments, continuous data was not stored. Although general anaesthesia was maintained using Isoflurane, it was initiated using Propofol which is a known vasodilator (322). However, Husso et al. (316) used Propofol combined with Fentanyl to maintain anesthesia in a porcine adenosine stress study and argue that both substances together do not affect blood pressure (323).

To test whether euoxic- end-tidal  $P_{ET}CO_2$ -targeted hypercapnia invokes any hemodynamic response, invasively obtained blood pressure in the coronary arteries during hypercapnia could be obtained. In

addition, stroke volume obtained from cine imaging in conjunction with MBF measurements should be monitored.

As the utility of the porcine model to investigate MBF changes in response to hypercapnia remains inconclusive as has been reported in previous studies (316), future work should either consider the use of canines as the preferable animal model or rather focus entirely on the application in humans. The application of hypercapnia in humans is considered clinically safe (324,325).

In conclusion, the here investigated hypercapnia stress setup and protocol was able to induce controlled euoxic-hypercapnia in a porcine model. Vasodilation and MBF response were found non-existent within the limited sensitivity of the employed 2D and 3D free-breathing myocardial perfusion CMR, which is also a consequence of negligible hemodynamic response in animal model. To validate the relevance of hypercapnia induced vasodilation for DCE CMR, a pilot study in healthy young human volunteers should be conducted. Dose dependent hypercapnic stress response should be investigated and compared to adenosine induced stress.



# **Chapter 7**

## **Impact of Late Gadolinium**

## **Enhancement Image Resolution on**

## **Neural Network Based Automatic**

## **Scar Segmentation in**

## **Cardiovascular Magnetic**

## **Resonance Imaging**

---

\*Submitted as: T. Hoh, J. Weine, T. Joyce, R. Manka, M. Weisskopf, N. Cesarovic, M. Fuetterer, S. Kozerke, Impact of Late Gadolinium Enhancement Image Resolution on Neural Network Based Automatic Scar Segmentation in Cardiovascular Magnetic Resonance Imaging, JCMR

## 7.1 Introduction

Myocardial scar mass derived from cardiovascular magnetic resonance (CMR) late Gadolinium enhancement (LGE) imaging (11) is considered the gold-standard for non-invasive myocardial viability assessment (12) in the context of acute and chronic myocardial infarction (MI) (215,216). LGE imaging can identify reversible myocardial dysfunction before coronary revascularization (326). Myocardial scar mass is of prognostic value in patients with ischemic and non-ischemic cardiomyopathies (34–37,236,255,327–330).

In clinical practice, myocardial scar mass quantification requires segmentation of epicardial and endocardial contours (epi- and endo-contours) of the left ventricle (LV) in LGE short-axis view images. With limited contrast, precise delineation of myocardial borders can be challenging, even when anatomical information from aligned functional cine imaging is at hand.

Scar tissue segmentation is either conducted manually or using semi-automatic thresholding methods. For the latter, the two recommended methods are thresholding at 50% of the maximum hyperenhanced myocardial signal intensity, referred to as full-width-at-half-maximum (FWHM), and thresholding at  $n$  times the standard deviation ( $n$ -SD) of mean healthy myocardial signal (12,31). Both thresholding methods require manual segmentation of epi- and endo-contours followed by delineation of hyperintense or remote tissue, respectively (31,230). Comparisons of the manual and the two semi-automatic approaches suggest no significant difference in segmented scar volumes and reproducibility (37,230,234–236). Generally, the manual segmentation is time-consuming and requires well-trained observers as well as standardized criteria to account for varying CMR sequences and hardware. In a multi-center study, significant interobserver differences in %LV mass were reported (331), indicating limited generalization of the classification of scar data.

Several attempts to mitigate the limitations of human interactions in scar segmentation have been proposed. Semi-automatic and fully automatic methods, either combining co-registration of CINE and LGE images (241,242), or only LGE images in combination with prior knowledge on constraints and inter-slice smoothness, have been reported (235,243). More recently, deep learning algorithms and more specifically convolutional neural networks (CNN) have been proposed for myocardial scar segmentation (38), especially as contributions to segmentation challenges (252). These machine learning techniques either rely on fusion of CINE and LGE images (253), or take LGE images as their only input (254–257). Other work incorporates augmented training data to deploy anatomically informed segmentation (258).

The standard data processing approach for CNN based segmentation includes resampling or interpolation of image data to obtain training and test data with constant field-of-view (FOV) and matrix size, i.e. constant in-plane resolution, as well as normalized contrast (253–255,257,258). This is especially

---

necessary when training data from publicly available CMR datasets is used, e.g. from segmentation challenges. For CNN based image reconstruction, varying data and processing have shown to produce biased results (39,332). For myocardial scar mass quantification, the impact of image resolution changes (e.g. artefacts introduced by partial volume effects) remains to be studied.

In general, the achievable in-vivo image resolution is constrained by motion and especially limited by inconsistent contrast during lengthy image acquisition durations. In absence of in-vivo ground-truth data, post-mortem high-resolution data has been used in animal models to study accuracy of LGE imaging and scar segmentation methods (231,333).

The objective of the present study is to investigate the impact of varying image resolutions on automatic LGE myocardial scar quantification using a representative U-Net type network. To generate reference segmentations for LGE data of MI, high-resolution post-mortem porcine MI models (n=45) are used; training and test data of different in-plane resolutions are derived from the reference data. The network is trained at in-plane image resolutions of  $\Delta x = 0.7, 1.2,$  and  $1.7$  mm, and tested on resolutions ranging from  $\Delta x = 0.7$  to  $1.8$  mm. The network predictions are compared against n-SD thresholding using manual observer LV and remote region annotations, based on signed fractional errors of scar mass and Dice score.

## 7.2 Methods

### 7.2.1 Animal Cohort and Handling

Forty-five domestic healthy female swine (*Sus scrofa domestica*, breed: Swiss large white, body weights (BW) 60–85 kg) were used for the experiments. All swine were fully anesthetized and intubated for positive pressure ventilation. General anesthesia was maintained with isoflurane (2% - 3%) in 100% oxygen. Heparin was administered intravenously and repeated every hour to maintain an activated clotting time of >250s.

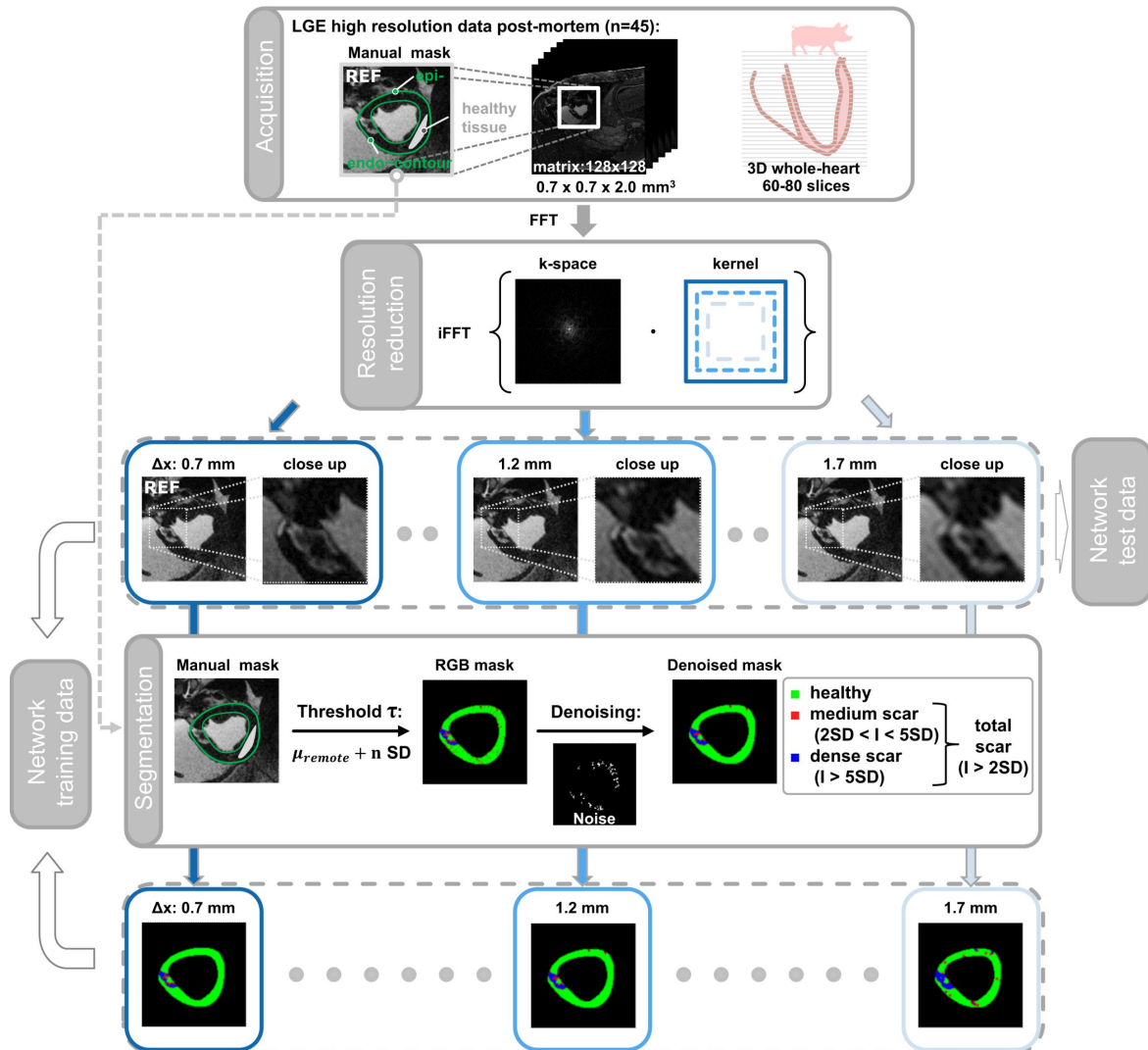


**Figure 7.1:** Processing of images and reference (REF) segmentation. From top to bottom: Late Gadolinium enhancement (LGE) image acquisition with crop to final matrix size and manual expert observer segmentation of epi- and endocontours and healthy myocardium. Resolution reduction by multiplication of k-space signal with low-pass filter-kernel at constant field-of-view. Examples of resulting images with in-plane resolutions  $\Delta x = 0.7$  mm, 1.2 mm and 1.7 mm, respectively. Semiautomatic scar segmentation using n-SD thresholding at respective resolutions with REF myocardial masks followed by morphologic denoising of scar masks. Healthy myocardium in green, medium scar with intensity  $I > 2SD$ ,  $< 5SD$  in red and dense scar ( $I > 5SD$ ) in blue. Total scar ( $I > 2SD$ ) is the sum of red and blue regions. Bottom row shows resulting segmentation masks at respective image resolutions. Corresponding image feature pairs serve as training data.

Acute MI and microvascular obstruction in the apical septum, or basal inferior and lateral wall was induced by 90 minutes occlusion of the left anterior descending coronary artery (LAD) or the left circumflex artery, respectively. After the procedure and subsequent imaging, performed in the acute phase of MI (6h after reperfusion), all animals were euthanized in deep anesthesia by lethal injection of pentobarbital. All

animal handling, procedures and protocols were approved by the Cantonal Veterinary Office (Zurich, Switzerland). The full data curation pipeline is illustrated in **Figure 7.1**.

## 7.2.2 Image Acquisition

Imaging was conducted on a clinical 1.5 T Philips Achieva MR system (Philips Healthcare, Best, The Netherlands), delivering 40 mT/m at 200 T/m/s, and a five- or 32-channel cardiac receiver array. Functional as well as Gadolinium-enhanced imaging was performed as part of a standard ischemic heart disease protocol (4).

A Gadobutrol contrast agent (Gadovist, Bayer Schering Pharma, Germany) was injected (0.2 mmol/kg BW). The animal was euthanized 20 min after contrast administration and LGE imaging was immediately performed post-mortem. High-resolution images were acquired using a sequence consisting of a 3D inversion-recovery gradient-echo sequence with the following parameters: TE/TR 2.3/4.7 ms, acquisition resolution 0.7x0.7x2.0 mm<sup>3</sup>, parallel imaging (SENSE) reduction factor: 2.2, and flip angle: 15°. The optimal inversion delay was estimated using an inversion delay scout sequence, maximizing signal contrast between affected and remote myocardium (~290 ms). Total image acquisition time of one 3D dataset was 25 min.

The 3D whole-heart image data was resliced in short-axis orientation yielding 2D slices (~60-80 per dataset) covering the LV from apex to base.

## 7.2.3 Image Post-processing

The high-resolution images were analyzed using GTVolume (GyroTools LLC, Zurich, Switzerland). Apical and basal slices were omitted when endocardial borders were not distinguishable without referring to functional imaging, or the extent of muscle around the blood pool was smaller than 100%. In all other slices, epi- and endocardial borders were manually delineated. Healthy remote tissue regions were labelled by drawing of b-spline contours around myocardium that showed no hyperenhancement. The papillary muscles were excluded for the analysis. Images and segmentation masks were exported and further processed using Python (version 3.8).

Masks for myocardial- and scar-tissue were generated using the n-SD approach, i.e. by assigning the thresholds according to

$$\tau = \mu_{remote} + n \cdot \sigma_{remote} \quad (7.1)$$

where  $\mu_{remote}$  and  $\sigma_{remote}$  denote the mean signal amplitude and its SD in the remote healthy tissue, respectively. Two values of n (i.e. 2 and 5) were used to differentiate total and dense scar, i.e. >2SD and >5SD scar, respectively. Class associations are presented as RGB images where color channels correspond

to healthy myocardium in green, medium scar ( $2SD < I < 5SD$ ) in red, and dense ( $I > 5SD$ ) scar in blue. The sum of red and blue regions refers to total scar ( $I > 2SD$ ).

To avoid mislabeling of single pixels as scar in the high-resolution data, the reference (REF) masks were denoised by applying morphological opening to the binary total scar mask (red + blue). To ensure consideration of individual pixels in the vicinity adjacent to the clusters red and blue, a dilation operation was performed to the total scar mask before it was multiplied with both original red and blue channels. An example case of this filtering process with the original mask, the filtered mask and their difference is shown in **Figure 7.1**.

## 7.2.4 Reduction of Image Resolution

To test the dependence on image resolution for training and prediction, the high-resolution data was projected to resolutions of  $\Delta x \in \{0.7, \dots, 1.8\}$  mm, with the highest resolution corresponding to the original acquisition resolution of  $\Delta x_{orig} \sim 0.7$  mm. To this end, the image data was Fourier transformed to k-space data, multiplied with a rectangular low-pass filter and inverse Fourier transformed back to image space. Accordingly, a constant matrix size of (128x128) at a constant FOV was kept throughout. An outline of the resolution reduction is shown in **Figure 7.1**.

## 7.2.5 Network Training

A five-fold cross-validation scheme was applied to increase statistical meaning of the reported errors. In each cross-validation pass the total dataset of 45 subsets was split into training ( $n=36$ ; 1970 - 2036 slices) and test data ( $n=9$ ; 461 - 527 slices). For each of the three in-plane resolutions:  $\Delta x = 0.7$  mm, 1.2 mm, and 1.7 mm, a U-net style architecture network (Ternaus-Net (334)) was trained using the ‘Segmentation Models for PyTorch’ library (335). For the encoder path, a ResNet34 (246) with pretrained weights from the ImageNet dataset ([www.image-net.org](http://www.image-net.org)) was used to accelerate convergence and increase accuracy (334,336,337). The number of down-sampling steps in the encoder path was set to 5, and the number of convolutional channels in the decoder path were (256, 128, 64, 32, 16). In the decoder path, batch norm operations were used after every convolution and the final layer used a sigmoid activation. As optimizer, Adam with an initial learning rate of  $1e^{-3}$ ,  $\beta_1 = 0.9$  and  $\beta_2 = 0.999$  was used. The training batch size was set to 32 and as loss function the multi-class Dice loss was used. Three-hundred epochs were used to train the network.

Before passing the LGE images to the network, the images were cropped to a  $128 \times 128$  matrix centered at the LV. This process matches the procedure of other work (253,257,258). Furthermore, the test image intensity was normalized to [0, 1] per image. Test time augmentation was used i.e. training data was augmented 8-fold using multiple 90-degree rotations combined with horizontal or vertical flipping. At

test/validation time, the mask prediction for each test image was obtained by applying the same 8 image augmentation operations and by computing the mean of all predictions after reversing the augmentation.

## 7.2.6 Error Metrics

Predictions of each network (trained at  $\Delta x = 0.7, 1.2$  and  $1.7$  mm) were evaluated on the test data with resolutions ranging from  $\Delta x = 0.7$  to  $1.7$  mm. The resulting estimation of myocardium, total and dense scar tissue area was compared pair-wise against n-SD thresholding.

For all resolutions  $\Delta x$ , the areas (in  $\text{mm}^2$ ) of the tissue segmentations ( $T \in \{\text{MYO}, \text{SD2}, \text{SD5}\}$ ) per slice with pixels  $\tilde{p}$  of mask  $M$  is given as:

$$A_P(T) = \Delta x^2 \sum_{\tilde{p} \in M} (P(\tilde{p}) \wedge T). \quad (7.2)$$

where  $P$  is the segmentation derived from either network prediction or n-SD thresholding of the data using myocardial epi- and endocontours at the highest resolution image.

The signed relative fractional error in percent for myocardial tissue is then derived to compare network performance against n-SD thresholding as:

$$\Delta \text{MYO} = \frac{A_{\text{network}}(\text{MYO}) - A_{\text{nSD}}(\text{MYO})}{A_{\text{nSD}}(\text{MYO})}. \quad (7.3)$$

For scar tissues ( $T \in \{\text{SD2}, \text{SD5}\}$ ), the signed pairwise fractional error in percent points (p.p.) is derived as:

$$\Delta T = \frac{A_{\text{network}}(T)}{A_{\text{network}}(\text{MYO})} - \frac{A_{\text{nSD}}(T)}{A_{\text{nSD}}(\text{MYO})}. \quad (7.4)$$

To provide full descriptive statistics, resulting marginal distributions of fractional errors with their medians and interquartile range (IQR) minima and maxima as well as their means and SDs are reported.

To capture the spatial correspondence of network segmentation and thresholding the Sorensen-Dice coefficient was calculated between tissue masks as area of overlap divided by the total number of pixels in both masks (338):

$$\text{Dice score}(T) = 2 \cdot \frac{\sum_{\tilde{p}} \{\text{network}(\tilde{p}) \wedge T \cdot \text{nSD}(\tilde{p}) \wedge T\}}{\sum_{\tilde{p}} \{\text{network}(\tilde{p}) \wedge T + \text{nSD}(\tilde{p}) \wedge T\}}. \quad (7.5)$$

Dice score marginal distributions with their medians and IQR minima and maxima, as well as their means and SDs are derived. For all three training resolutions, Dice score histograms at the training resolutions are derived, respectively. To enhance readability, Dice score histograms are visualized as their kernel density estimations for all investigated test image resolutions.

---

## 7.3 Results

### 7.3.1 Cohort Data Set

Over the 45 subjects (1497 slices), mean ( $\pm$ SD) myocardial area is  $1150 \text{ mm}^2$  ( $\pm 335 \text{ mm}^2$ ) on REF. The relative area of total scar (i.e. SD2) is 10% ( $\pm 12\%$ ) and dense scar (i.e. SD5) relative area is 5% ( $\pm 8\%$ ) of the myocardial area. Total scar can extend to up to 40% of the myocardial area, while the extent of dense scar is  $<10\%$  for  $\sim 92\%$  of the investigated slices.

### 7.3.2 Segmentation Performance Dependency on Effective Resolution

#### Representative Case

**Figure 7.2** shows a representative LGE test case, which features an infarct in the antero- and inferoseptal myocardial wall. Resolution reduction leads to partial voluming and change of noise level in the images, as also shown in the corresponding close ups of the identical case in Figure 7.1.

For the network prediction from high-resolution training (Figure 7.2 B), all segmented areas remain relatively constant for  $\Delta x \leq 1.1 \text{ mm}$ . For test images with lower resolution  $\Delta x > 1.2 \text{ mm}$ , total and dense scar is overestimated, especially at the antero-septal border.



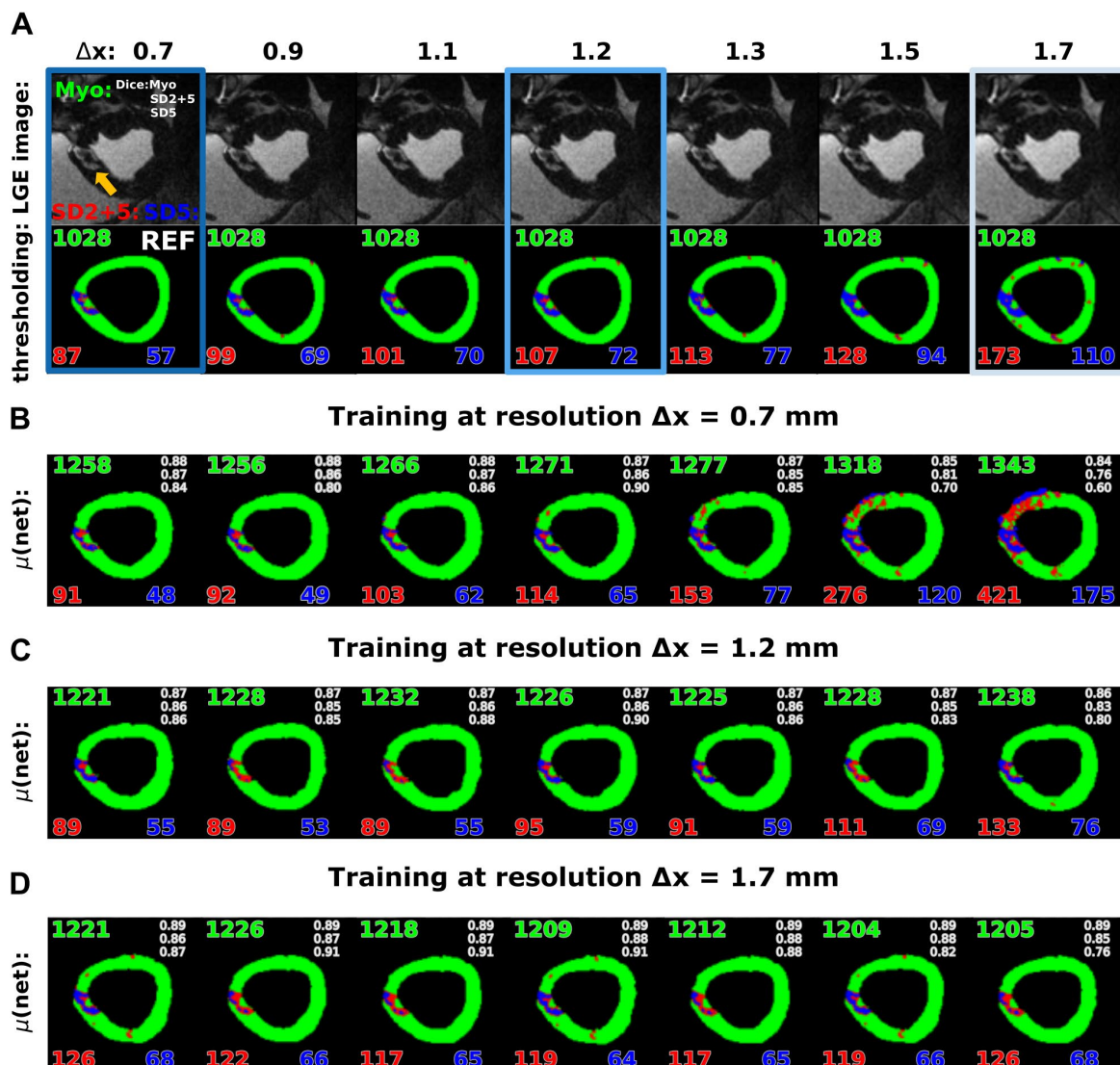


**Figure 7.2:** Representative example dataset. Late Gadolinium enhancement (LGE) images with reduction in in-plane resolution  $\Delta x$  and n-SD thresholding segmentation masks are shown in (a). Corresponding network segmentation predictions for the networks trained at these resolutions are shown in (b-d), respectively. Healthy myocardium in green, medium scar with intensity  $I > 2SD$ ,  $< 5SD$  in red and dense scar ( $I > 5SD$ ) in blue. Total scar ( $I > 2SD$ ) is the sum of red and blue regions. Regional areas in mm for myocardium, total scar and dense scar are given as numbers in green, red and blue, respectively. Blue frames highlight the resolutions  $\Delta x = 0.7$  mm, 1.2 mm and 1.7 mm of image label pairs used for network training. Dice scores relative to n-SD thresholding on REF are given in the top right corner of the shown frames.

At test image resolution  $\Delta x = 1.7$  mm, SD2 and SD5 scar area prediction fails. Myocardial area prediction is biased with overestimations of 22.4% to 30.6% at the highest and lowest resolutions, respectively. For the two lower training resolutions, myocardial area prediction bias remains constant at  $\sim 20\%$ .

---

At training resolution,  $\Delta x = 1.2$  mm (**Figure 7.2 C**), predicted areas for myocardial, SD2 and SD5 are subject to a more moderated increase over the full range of investigated resolutions. Of note, classification between SD2 and SD5 scar varies.

At lowest training resolution,  $\Delta x = 1.7$  mm (**Figure 7.2 D**), predicted areas for myocardial, SD2 and SD5 are the most constant. Prediction masks show residual artefacts.

### Fractional Scar Area Investigation

Results for fractional scar area investigation are shown in Figure 7.3. As for the example case, marginal distributions of fractional errors indicate that for networks trained at high resolution, masks are prone to changes for varying test resolutions.

For the network prediction from high-resolution training (Figure 7.3 A), mean  $\Delta MYO$  remains on the order of 3% ( $\pm 13\%$ ) for resolutions  $\Delta x \leq 1.1$  mm. For resolutions  $\Delta x \geq 1.2$  mm, mean errors remain constant but exhibit increased variance ( $\pm 19\%$ ). Over the span of investigated resolutions, a trend towards inaccurate SD2 and SD5 scar prediction is visible with a pronounced increase of up to  $\sim 25$ p.p. ( $\pm 25$ p.p.) and  $\sim 10$ p.p. ( $\pm 13$ p.p.), respectively.

For training at  $\Delta x = 1.2$  mm (Figure 7.3 B),  $\Delta MYO$  results indicate an approximately constant bias  $< 1\%$ . A trend towards underestimation in pairwise comparisons of SD2 scar prediction is indicated.  $\Delta SD5$  shows moderate variation over the span of investigated resolutions. Again, data suggests that accuracy benefits from increased test image resolution, as also indicated by decreased IQRs.

For training at  $\Delta x = 1.7$  mm (Figure 7.3 C),  $\Delta SD2$  indicates a trend from 3.8p.p. overestimation at high resolution to -4.3p.p. underestimation at low resolution.  $\Delta SD5$  shows a similar, but more moderate trend. SDs remain constant at  $\sim 5$ p.p.

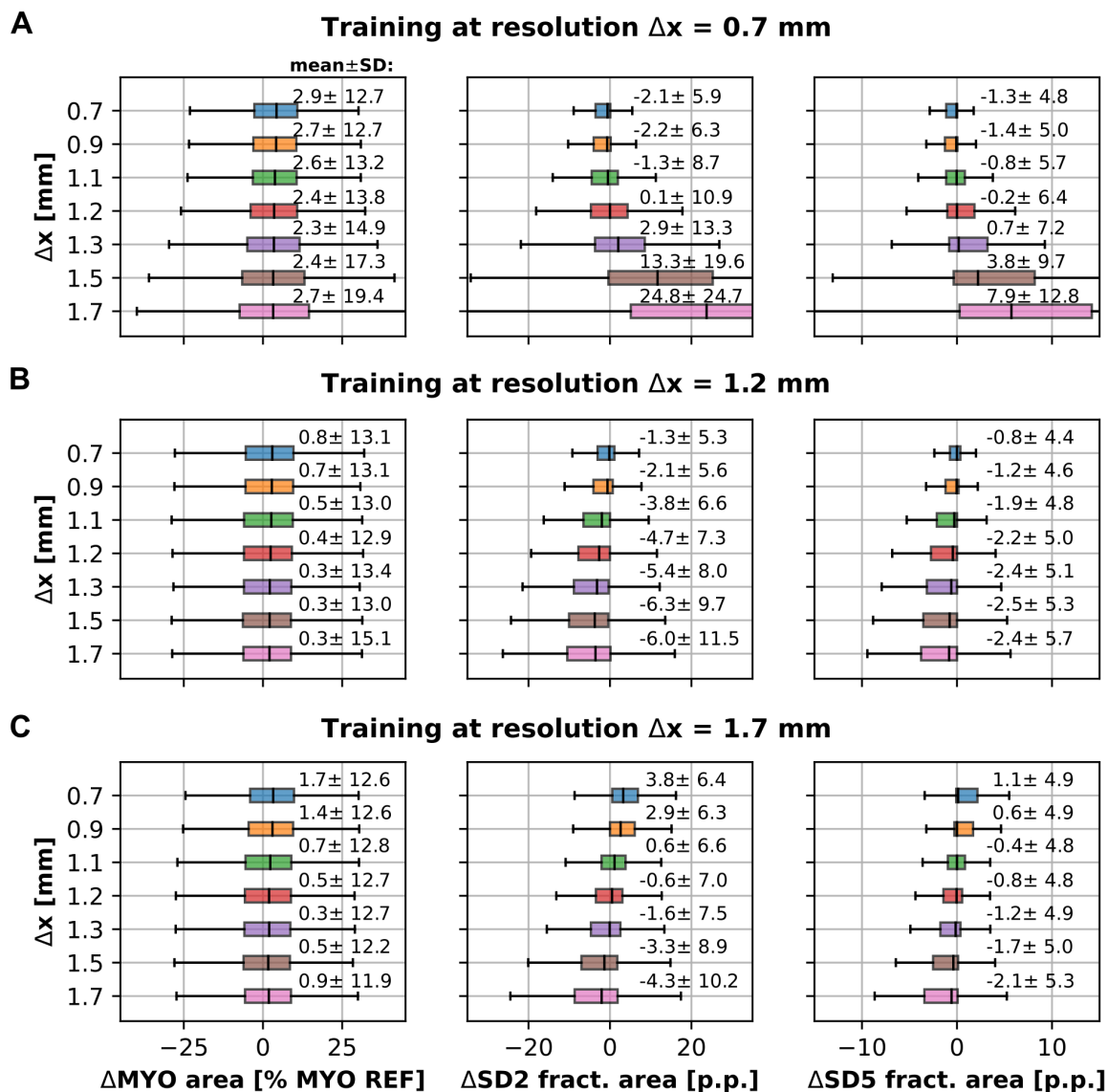


**Figure 7.3:** Boxplot analysis of signed errors between network predictions and n-SD thresholding as function of in-plane resolutions  $\Delta x$  from 0.7 mm to 1.7 mm are shown for networks trained at  $\Delta x = 0.7$  mm (A), 1.2 mm (B) and 1.7 mm (C). From left to right, panels show box-plots for signed errors  $\Delta MYO$  relative to myocardial area at reference (REF), signed fractional differences for total (SD2) and dense (SD5) scar, respectively. Mean  $\pm$  SD are given in the legend.

## Spatial Correspondence

**Figure 7.4** illustrates the results of network performance by means of Dice score comparison (for mean  $\pm$  SD see Table 7.1).

For high-resolution training (**Figure 7.4** A) and high-resolution test images ( $\Delta x < 1.2$  mm), mean myocardium Dice scores are 0.88 ( $\pm 0.05$ ). For test resolutions  $\Delta x \geq 1.2$  mm, Dice

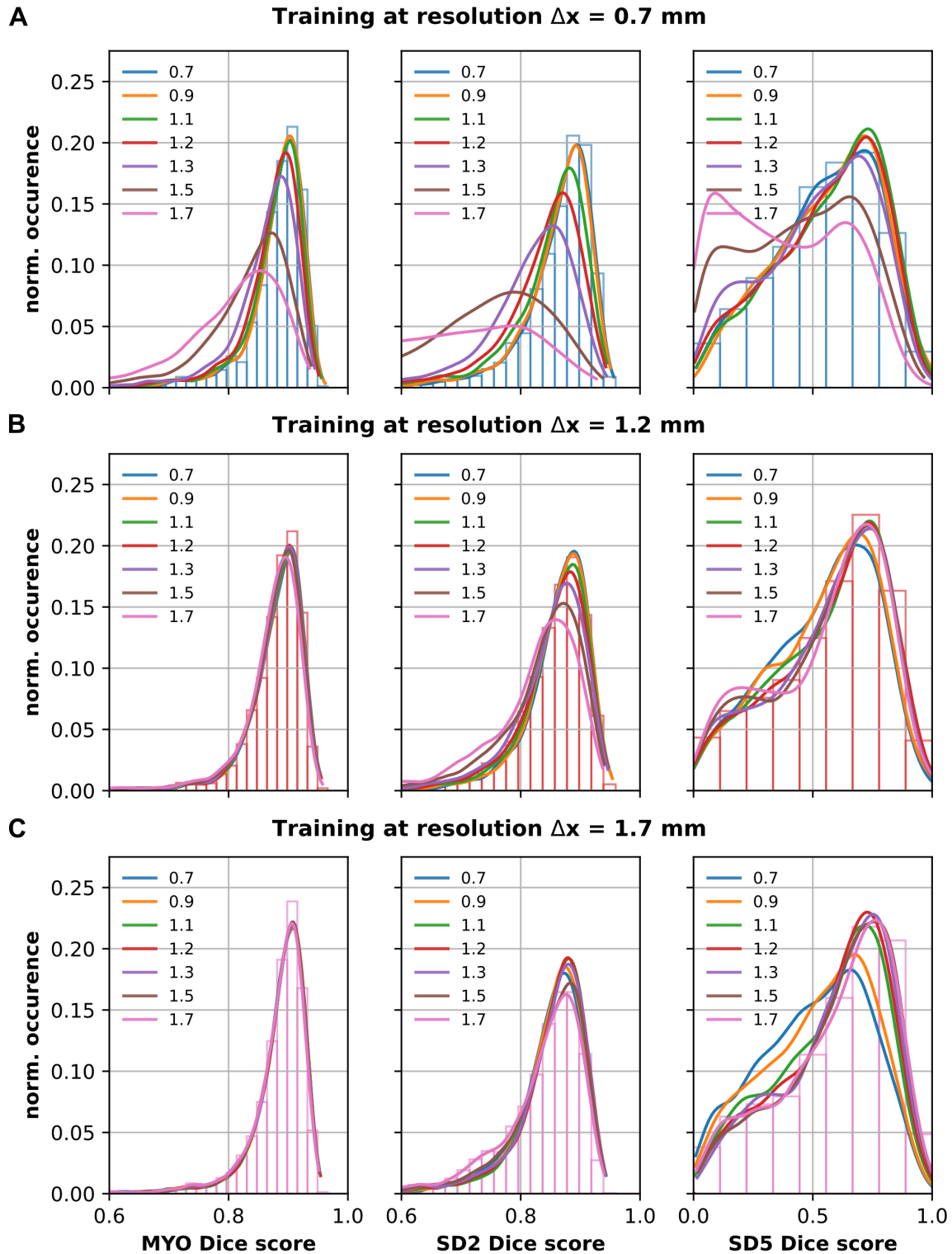


**Figure 7.4:** Dice score marginal distributions between network predictions and n-SD thresholding as function of in-plane resolutions  $\Delta x$  from 0.7 mm to 1.7 mm are shown for networks trained at  $\Delta x = 0.7$  mm (A), 1.2 mm (B) and 1.7 mm (C). From left to right, panels show Dice scores as kernel density estimations of histograms for myocardium, total (SD2) and dense (SD5) scar, respectively. Actual histogram reflects distribution of Dice scores at training data resolution. Corresponding mean  $\pm$ SD are given in Table 7.1.

---

scores decrease, and the shape of distributions varies. Specifically, for the lowest resolution test images ( $\Delta x = 1.7$  mm), the mean Dice score is  $0.80 (\pm 0.10)$ . SD2 Dice score for resolutions  $\Delta x \leq 1.2$  mm vary from  $0.86 (\pm 0.06)$  to  $0.83 (\pm 0.08)$ ; for  $\Delta x > 1.2$  mm, mean Dice scores further decrease from  $0.81 (\pm 0.07)$  to  $0.65 (\pm 0.16)$ . Distributions of SD5 Dice scores show pronounced variation over the span of test resolutions.

For training at  $\Delta x = 1.2$  mm (**Figure 7.4 B**), variations of distributions are more moderate. Mean myocardium Dice scores remain in the range of  $0.88 (\pm 0.05)$  to  $0.87 (\pm 0.06)$ . SD2 Dice scores for test resolutions  $\Delta x \leq 1.2$  mm, vary from  $0.86 (\pm 0.06)$  to  $0.85 (\pm 0.07)$ . For  $\Delta x > 1.2$  mm, mean Dice scores decrease from  $0.85 (\pm 0.07)$  to  $0.82 (\pm 0.08)$ . Distributions of SD5 Dice score are broadened with less pronounced peaks as for the highest resolution training but only show subtle variations over the span of test resolutions.

For training at  $\Delta x = 1.7$  mm (**Figure 7.4 C**), myocardial Dice score distributions show no variation. Their means remain in the range of  $0.89$  to  $0.88$  at constant SDs ( $\pm 0.05$ ). Compared to data for network training resolution  $\Delta x = 1.2$  mm, SD2 Dice score distributions are more homogeneous. SD5 Dice score distributions are again broadened with less pronounced peaks as seen for the highest training resolution. Biggest variations are seen for distributions for test data at  $\Delta x = 0.7$  and  $0.9$  mm. As for the fractional errors, for both networks at lower resolution, Dice score investigation suggests that variability benefits from increased image resolution.

Results for fractional scar area investigation and spatial correspondence are further summarized in **Figure 7.5**. Medians and IQRs of signed fractional errors over all investigated test image resolutions are shown in **Figure 7.5 A**. For training resolutions  $\Delta x = 0.7, 1.2$  and  $1.7$  mm, median (IQR) compares as  $0.0\%$  ( $9.7\%$ ),  $-1.9\%$  ( $6.9\%$ ) and  $0.9\%$  ( $7.1\%$ )

**Table 7.1** Dice score results

Res. $\Delta x$	Training at resolution $\Delta x = 0.7$ mm			Training at resolution $\Delta x = 1.2$ mm			Training at resolution $\Delta x = 1.7$ mm		
	Myocardium Dice score	SD2 Dice score	SD5 Dice score	Myocardium Dice score	SD2 Dice score	SD5 scar Dice score	Myocardium Dice score	SD2 Dice score	SD5 scar Dice score
<b>0.7</b>	$0.88 \pm 0.05$	$0.86 \pm 0.06$	$0.55 \pm 0.22$	$0.88 \pm 0.05$	$0.86 \pm 0.06$	$0.54 \pm 0.22$	$0.89 \pm 0.05$	$0.85 \pm 0.06$	$0.51 \pm 0.23$
<b>0.9</b>	$0.88 \pm 0.05$	$0.86 \pm 0.06$	$0.56 \pm 0.22$	$0.88 \pm 0.05$	$0.86 \pm 0.06$	$0.55 \pm 0.22$	$0.89 \pm 0.05$	$0.85 \pm 0.06$	$0.53 \pm 0.23$
<b>1.1</b>	$0.88 \pm 0.05$	$0.85 \pm 0.07$	$0.57 \pm 0.22$	$0.88 \pm 0.05$	$0.85 \pm 0.06$	$0.57 \pm 0.23$	$0.89 \pm 0.05$	$0.85 \pm 0.06$	$0.57 \pm 0.23$
<b>1.2</b>	$0.87 \pm 0.05$	$0.83 \pm 0.08$	$0.55 \pm 0.23$	$0.88 \pm 0.05$	$0.85 \pm 0.07$	$0.57 \pm 0.23$	$0.89 \pm 0.05$	$0.85 \pm 0.06$	$0.58 \pm 0.22$
<b>1.3</b>	$0.86 \pm 0.06$	$0.81 \pm 0.09$	$0.52 \pm 0.23$	$0.88 \pm 0.05$	$0.85 \pm 0.07$	$0.56 \pm 0.24$	$0.89 \pm 0.05$	$0.85 \pm 0.06$	$0.59 \pm 0.22$
<b>1.5</b>	$0.83 \pm 0.07$	$0.73 \pm 0.12$	$0.45 \pm 0.24$	$0.88 \pm 0.06$	$0.83 \pm 0.07$	$0.56 \pm 0.24$	$0.88 \pm 0.05$	$0.84 \pm 0.07$	$0.60 \pm 0.23$
<b>1.7</b>	$0.80 \pm 0.10$	$0.65 \pm 0.16$	$0.39 \pm 0.25$	$0.87 \pm 0.06$	$0.82 \pm 0.08$	$0.56 \pm 0.24$	$0.88 \pm 0.05$	$0.83 \pm 0.07$	$0.59 \pm 0.23$

Dice score mean  $\pm$  SD between network predictions and n-SD thresholding for in-plane resolutions  $\Delta x$  from 0.7 mm to 1.7 mm are shown for networks trained at  $\Delta x = 0.7$  mm, 1.2 mm, and 1.7 mm. Corresponding Dice score marginal distributions are shown in Fig. 7.4.

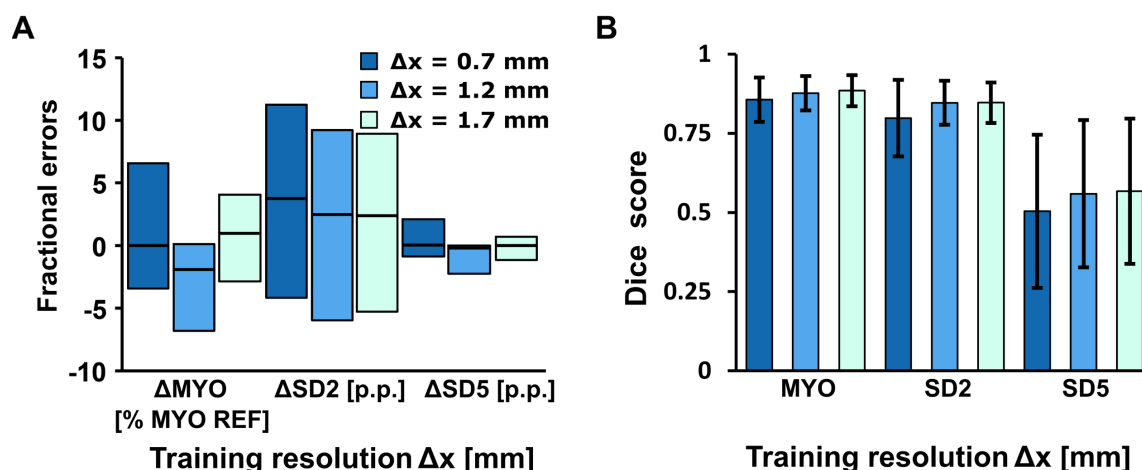


**Figure 7.5:** Segmentation performance summary. (A) Signed errors median and inter quartile ranges (IQRs) over all investigated in-plane resolutions  $\Delta x$  from 0.7 mm to 1.8 mm are shown for networks trained at  $\Delta x = 0.7$  mm, = 1.2 mm and = 1.7 mm. Boxes refer to median (IQR) signed errors  $\Delta$ MYO relative to myocardial area at reference (REF), signed fractional errors for total (SD2) and dense (SD5) scar, respectively. Legend refers to panel (A) and (B). (B) Dice score mean  $\pm$  SD between network predictions and n-SD thresholding over all investigated in-plane resolutions  $\Delta x$  are shown for same network trainings as in (A).

for myocardium, as 3.8p.p. (15.6p.p.), 2.5p.p. (15.1p.p.) and 2.3p.p. (14.3p.p.) for SD2 scar, and as 0.0p.p. (3.0p.p.), -0.3p.p. (2.3p.p.) and 0p.p. (1.9p.p.) for SD5 scar, respectively.

In **Figure 7.5 B**, mean  $\pm$  SD of Dice scores over all test image resolutions for training resolutions  $\Delta x = 0.7$ , 1.2 and 1.7 mm compare as 0.86 ( $\pm 0.07$ ), 0.88 ( $\pm 0.05$ ) and 0.89 ( $\pm 0.05$ ) for myocardium, as 0.80 ( $\pm 0.12$ ), 0.85 ( $\pm 0.07$ ) and 0.85 ( $\pm 0.05$ ) for SD2 scar, and as 0.50 ( $\pm 0.24$ ), 0.56 ( $\pm 0.23$ ) and 0.57 ( $\pm 0.23$ ) for SD5 scar, respectively. As for the fractional errors, this suggests that networks trained at lower resolution images show higher local correspondence.

## 7.4 Discussion

In this chapter, the impact of image resolution on scar segmentation using neural networks has been evaluated. Our high-resolution post-mortem dataset allowed to train networks at three different effective resolutions i.e. enabled a change of the image point-spread function (PSF) while keeping matrix size and field-of-view constant.

Networks trained on high-resolution images were found to be less robust to changes in test image resolutions, when compared to networks trained at lower resolutions. This was reflected in the marginal distributions of signed fractional area errors and Dice scores and was further highlighted in the segmentation performance summary (**Figure 7.5**).

---

Reduced resolution corresponds to a wider PSF, which leads to a spatial information being smeared out over neighboring pixel i.e. spatial signal variations occur on a larger scale and are smoother. Accordingly, when used in the training, the network becomes insensitive to changes on fine scales. To this end, a network, which was trained on low-resolution data, shows a tendency towards overestimating scar areas with increasing resolution in the test data as it is less sensitive to sharper transitions in the image.

On the contrary, networks trained on high-resolution images can represent features and variations on a fine scale. When trained on the highest resolution and deployed on successively lower resolution test data, significant overestimation of scar areas occurs. We associate this finding with the inability of the network to represent increasing partial volume effects in the test data.

Given the recommended range for LGE image acquisition resolutions of approximately  $\sim 1.4$ - $1.8$  mm (4) and potentially higher resolutions used in clinical trials (34), the results shown in **Figure 7.3. B** for a network trained at  $\Delta x = 1.2$  mm reflect a practical scenario. Considering a test data resolution ranging from  $\Delta x = 1.2$ - $1.7$  mm, a small tendency of underestimating scar area with increasing variability for decreasing test data resolution was observed. However, changes in bias and variability were bound to -1.3 p.p. and 4.2 p.p., respectively. These results can be contextualized when comparing the errors to analyses of inter-center and inter-observer agreement of manual segmentations in e.g. the multi-center study by Klem et al. (331). In their work, the interobserver variability for manual scar segmentations ranged from  $\pm 3.5$  p.p. to  $\pm 6.4$ , respectively. Accordingly, the network predictions in this scenario yielded changes in variability similar to the variability introduced by multiple observers.

The PSF-dependent bias and variability demonstrated in our work indicates the importance of considering and reporting acquisition rather than reconstruction resolution as a crucial parameter when designing and evaluating segmentation networks. It is therefore suggested to always document acquisition resolution and PSF to estimate the effects.

While scar segmentation using post-mortem high-resolution data has previously been shown in studies with pigs ( $n=17$ ) and canines ( $n=11$ ) (231,333), the number of cases in these studies would have been too small for re-training of networks.

A limitation of the present work is that the impact of effective resolution on myocardial segmentation accuracy was only investigated for a standard CNN architecture. Other pipelines, e.g. multi-modality learning models for LGE LV segmentation incorporating LGE, cine and atlas data (339,340) were not investigated.

While no extensive hyperparameter tuning of the employed network architecture was conducted, for the test sets, the mean myocardial, total and dense scar Dice scores were on the order of 0.88, 0.85 and 0.5-



---

0.6, respectively. This is comparable with established work (38,252) and the network training was thus considered sufficient for the described analysis.

An aspect which has also not been investigated in this work is the through-plane resolution of the 3D image datasets. Future work should include this analysis, also regarding SNR, as this is of further interest when 3D LGE imaging is used and scar segmentation algorithms are applied (219,220).

Future work should also generate reference validation epi- and endocardial segmentations from multiple experienced observers to mitigate uncertainties in the current reference segmentation dataset. In addition, manual scar segmentation and/or thresholding using the FWHM method (232) should be considered to generate alternative reference segmentation as there is no consensus for the optimal method of quantitative scar assessment (31). Such data could then also serve as a better reference for interobserver variability and overall segmentation accuracy comparisons.

## 7.5 Conclusion

Image acquisition resolution variations can lead to misestimation of total and dense scar using convolutional neural networks. Networks, which are trained in lower-resolution training data and deployed on higher resolution test sets, tend to be more robust against variation in test image resolution. On the contrary, networks trained at higher resolution, when compared to the test data resolution, can lead to systematic overestimation of total and dense scar areas for decreasing test data resolution. It is therefore recommended to consider and report image acquisition resolution used in both training and testing.



# Chapter 8

## Summary

In this thesis, challenges in 3D CMR perfusion imaging and scar quantification have been addressed. Advances include a framework for tailored Cartesian acquisition strategies and motion-conditioned CS reconstruction for improved quantitative 3D free-breathing perfusion imaging with whole-heart coverage. The proposed framework was also employed to explore hypercapnia-induced stress in anaesthetized porcine models. To advance viability assessment using LGE imaging, a testing framework for current network-based automatic scar segmentation was implemented.

### 8.1 Discussion

In Chapter 5, a dual-stage approach for improved quantitative 3D free-breathing perfusion imaging using motion information from displacement fields was presented. A similar concept has been described for 2D imaging (i.e. BLOSM (191)), which was expanded to full 3D using pseudo-spiral in-out Cartesian data sampling (i.e. MI-LLR), herein. While the robustness of image reconstruction was shown in simulations with realistic physiological parameters, irregular breathing- and heart-motion patterns should be included in future experiments to corroborate current results. Along this line, the influence of registration on the final MBF quantification should be studied. To further benchmark the imaging performance of MI-LLR, comparisons with other frameworks such as STCR (149,161) and k-t PCA (18) reconstructions should also be included.

A limitation of all current iterative image reconstruction methods is the need to adjust the regularization weight without having ground truth in-vivo image information available. In consequence, the regularization weight is often not optimal, which may also impact the accuracy of MBF quantification. To this end, more sophisticated synthetic datasets are urgently needed to derive optimal regularization functions and corresponding weights.

Another open question remains in relation to the best k-t trajectory for free-breathing quantitative perfusion 3D imaging. While radial stack-of-stars acquisition schemes have been tried (20), the computational cost of gridding reconstruction presents a hurdle. Of note in this context, the Cartesian

---

pseudo-spiral in-out scheme proposed in the present work showed competitive image quality when compared to radial stack-of-stars. Recent work by Huang et al. (133) compared 2D simultaneous multi-slice imaging to a stack-of-stars dual-sequence scheme. Acquiring both schemes in alternating heart cycles allowed for a direct comparison of image quality and absolute perfusion quantification. Such an alternating heart cycle acquisition could also facilitate hyperparameter tuning if interleaved with e.g. conventional 2D sequences.

In terms of computational load, the main limitation of the dual stage MI-LLR framework is the computational cost of the required 3D image registration step. Although partially run on GPUs, it accounts for about 80% of the total reconstruction time. To speed up this step neural network-based image registration shall be implemented and tested.

In the second project an alternative approach to induce stress by hypercapnia was explored in this thesis. While the experiments could show that, with an optimized automatic gas blending setup, hypercapnic stimuli are applicable, hemodynamic response could not be detected. This finding links with an earlier study on the lack of effects of hypercapnia in a porcine model (316). At the same time, these findings differ from studies reporting responses in canine models in similar experimental setups (79,313,315). The fact that successful studies were almost exclusively conducted in canines raises suspicions that stress induction in porcine models is physiologically different.

In the third contribution of this thesis, automatic network-based segmentation of myocardium and scar was found to be susceptible to variations in image resolution between training and testing data. Our findings stress that image acquisition resolution used in both training and testing must be considered when applying network-based segmentation methods. A limitation of our high-resolution porcine infarction model dataset relates to the limited contrast-to-noise ratio when compared to clinical LGE imaging. To improve the comparability to 2D LGE imaging, re-slicing of the 3D images to the common slice thickness of 2D LGE images should thus be investigated. While our U-Net architecture used 2D images as input, a 3D architecture would presumably enhance segmentation accuracy as the extent of scar could then also be inferred from information of adjacent slices.

---

## 8.2 Outlook

While the MI-LLR acquisition and reconstruction framework has been tested in volunteers and in a small set of patients, larger patient cohorts with different diseases shall be studied to establish the diagnostic yield of the method. To speed up image reconstruction, CNN-based registration (341) shall be integrated. Further, motion-informed model-based reconstruction (342) may be attempted, potentially enabling reconstruction times of less than a minute.

In relation to streamlining quantitative perfusion analysis, approaches are well under way to automatize pixel-wise perfusion mapping (184). In particular, automatic MBF perfusion quantification using ML methods is a promising approach (343,344). As proposed by van Herten et al. (214), the lack of training data may be mitigated by physics-informed CNNs.

Robust ECG triggering remains a key challenge in cardiac acquisitions, especially in stress condition. Missed triggers during contrast uptake render absolute perfusion quantification problematic. While alternative triggering by e.g. ultrasonic or fiber-optic methods can be employed (345), continuous imaging methods for cardiac phase-resolved perfusion imaging should be kept in mind (135).

One aspect not covered in this thesis is the optimization of the k-space trajectory and sampling patterns for dynamic contrast-enhanced imaging. Undersampling mask optimization has been researched by means of learning and Bayesian inference in the context of model- and data-based image reconstruction (346,347). On-the-fly undersampling pattern generation would be ideal. Such sampling masks could be inferred using joint optimization of sampling and reconstruction as proposed by Vishnevskiy et al. (348).

To further enhance spatio-temporal resolution, a neural implicit k-space learning method for binning-free imaging should be considered (349). In such an approach, an implicit k-space representation of k-space coordinate intensity pairs is learned. From the acquired data, the learned k-space representation can be inferred.

Despite the inconclusive results of hypercapnia in our animal experiments, oxygenation-sensitive CMR has shown promising results previously (82). To verify hypercapnia-induced vasodilation, a pilot study in healthy young human volunteers comparable to the study by Pelletier et al. (312) should be conducted. The dose-dependent hypercapnic stress response should be investigated and compared to adenosine induced stress.

When using network-based scar segmentation, data consistency checks between training and clinical data need to be included to ensure reliable segmentation. In a study on multi-organ datasets (350) attempts to predict segmentation performance have been made. Automatic quality control has been included on largescale data (351) and in real-time (352).

---

As alternative to CNNs, multi-modality learning models for segmentation incorporating LGE, cine and atlas data (339,340) may be considered. Among alternative network topologies, especially transformer networks (353) could be of interest, which do not rely on convolution operations (354). Transformers have been successfully applied in the context of language processing and have gained momentum for medical image segmentation tasks (355–357). Most recent work by Ding et al. (358) proposes multi-scale transformer learning for myocardial scar segmentation achieving Dice scores of 0.84.

A general limitation of supervised learning-based methods is the dependence on labeled ground-truth training data. This poses a fundamental problem as there is no consensus on the optimal method for quantitative scar segmentation (31) (233). First, there is no clear consensus on how pathologies present in LGE imaging, especially in border regions of scar. Second, the image resolution has a large influence on the quantified scar mass (e.g. due to partial volume effects). An advanced simulation using a high-resolution synthetic model including realistic imperfections might help to compare image acquisition methods and parameters.

---

# Bibliography

1. WHO- Fact Sheets Cardiovascular Disease.

[https://www.who.int/news-room/fact-sheets/detail/cardiovascular-diseases-\(cvds\)](https://www.who.int/news-room/fact-sheets/detail/cardiovascular-diseases-(cvds)). Published 2021.

2. Schweizer Gesundheitsobservatorium. Statistik - Akuter Myokardinfarkt.

<https://ind.obsan.admin.ch/de/indicator/obsan/myokardinfarkt>.

3. Knuuti J, Wijns W, Saraste A, et al. 2019 ESC Guidelines for the diagnosis and management of chronic coronary syndromes: The Task Force for the diagnosis and management of chronic coronary syndromes of the European Society of Cardiology (ESC). *Eur. Heart J.* 2020;41:407–477 doi: 10.1093/eurheartj/ehz425.

4. Kramer CM, Barkhausen J, Bucciarelli-Ducci C, Flamm SD, Kim RJ, Nagel E. Standardized cardiovascular magnetic resonance imaging (CMR) protocols: 2020 update. *J. Cardiovasc. Magn. Reson.* 2020;22:1–18 doi: 10.1186/S12968-020-00607-1.

5. Atkinson DJ, Burstein D, Edelman RR. First-pass cardiac perfusion: evaluation with ultrafast MR imaging. *Radiology* 1990;174:757–62 doi: 10.1148/radiology.174.3.2305058.

6. Nagel E, Greenwood JP, McCann GP, et al. Magnetic Resonance Perfusion or Fractional Flow Reserve in Coronary Disease. *N. Engl. J. Med.* 2019;380:2418–2428 doi: 10.1056/NEJMOA1716734.

7. Greenwood JP, Maredia N, Younger JF, et al. Cardiovascular magnetic resonance and single-photon emission computed tomography for diagnosis of coronary heart disease (CE-MARC): A prospective trial. *Lancet* 2012;379:453–460 doi: 10.1016/S0140-6736(11)61335-4.

8. Schwitter J, Wacker CM, Wilke N, et al. MR-IMPACT II: Magnetic resonance imaging for myocardial perfusion assessment in coronary artery disease trial: Perfusion-cardiac magnetic resonance vs. single-photon emission computed tomography for the detection of coronary artery disease: A comparative . *Eur. Heart J.* 2013;34:775–781 doi: 10.1093/eurheartj/ehs022.

9. Arai AE, Schulz-Menger J, Berman D, et al. Gadobutrol-Enhanced Cardiac Magnetic Resonance Imaging for Detection of Coronary Artery Disease. *J. Am. Coll. Cardiol.* 2020;76:1536–1547 doi: 10.1016/J.JACC.2020.07.060.

10. Kim RJ, Chen EL, Lima JAC, Judd RM. Myocardial Gd-DTPA kinetics determine MRI contrast enhancement and reflect the extent and severity of myocardial injury after acute reperfused infarction. *Circulation* 1996;94:3318–3326 doi: 10.1161/01.CIR.94.12.3318.

11. Kellman P, Arai AE. Cardiac imaging techniques for physicians: Late enhancement. *J. Magn. Reson. Imaging* 2012;36:529–542 doi: 10.1002/JMRI.23605.
12. Puntmann VO, Valbuena S, Hinojar R, et al. Society for Cardiovascular Magnetic Resonance (SCMR) expert consensus for CMR imaging endpoints in clinical research: Part i - Analytical validation and clinical qualification. *J. Cardiovasc. Magn. Reson.* 2018;20:1–23 doi: 10.1186/S12968-018-0484-5.
13. Kramer CM, Barkhausen J, Flamm SD, Kim RJ, Nagel E. Standardized cardiovascular magnetic resonance (CMR) protocols 2013 update. *J. Cardiovasc. Magn. Reson.* 2013;15:1–10 doi: 10.1186/1532-429X-15-91.
14. Manka R, Jahnke C, Kozerke S, et al. Dynamic 3-dimensional stress cardiac magnetic resonance perfusion imaging: Detection of coronary artery disease and volumetry of myocardial hypoenhancement before and after coronary stenting. *J. Am. Coll. Cardiol.* 2011;57:437–444 doi: 10.1016/j.jacc.2010.05.067.
15. Jogiya R, Kozerke S, Morton G, et al. Validation of dynamic 3-dimensional whole heart magnetic resonance myocardial perfusion imaging against fractional flow reserve for the detection of significant coronary artery disease. *J. Am. Coll. Cardiol.* 2012;60:756–765 doi: 10.1016/j.jacc.2012.02.075.
16. Manka R, Paetsch I, Kozerke S, et al. Whole-heart dynamic three-dimensional magnetic resonance perfusion imaging for the detection of coronary artery disease defined by fractional flow reserve: Determination of volumetric myocardial ischaemic burden and coronary lesion location. *Eur. Heart J.* 2012;33:2016–2024 doi: 10.1093/eurheartj/ehs170.
17. Fair MJ, Gatehouse PD, DiBella EVR, Firmin DN. A review of 3D first-pass, whole-heart, myocardial perfusion cardiovascular magnetic resonance. *J. Cardiovasc. Magn. Reson.* 2015;17:1–25 doi: 10.1186/s12968-015-0162-9.
18. Schmidt JFM, Wissmann L, Manka R, Kozerke S. Iterative k-t principal component analysis with nonrigid motion correction for dynamic three-dimensional cardiac perfusion imaging. *Magn. Reson. Med.* 2014;72:68–79 doi: 10.1002/mrm.24894.
19. Fair MJ, Gatehouse PD, Reyes E, et al. Initial investigation of free-breathing 3D whole-heart stress myocardial perfusion MRI. *Glob. Cardiol. Sci. Pract.* 2020;2020:e202038 doi: 10.21542/gcsp.2020.38.
20. Mendes JK, Adluru G, Likhite D, et al. Quantitative 3D myocardial perfusion with an efficient arterial input function. *Magn. Reson. Med.* 2020;83:1949–1963 doi: 10.1002/mrm.28050.
21. Wang Y, Rossman PJ, Grimm RC, Riederer SJ, Ehman RL. Navigator-echo-based real-time respiratory gating and triggering for reduction of respiration effects in three-dimensional coronary MR angiography. *Radiology* 1996;198:55–60 doi: 10.1148/RADIOLOGY.198.1.8539406.



22. Sachs TS, Meyer CH, Hu BS, Kohli J, Nishimura DG, Macovski A. Real-time motion detection in spiral MRI using navigators. *Magn. Reson. Med.* 1994;32:639–645 doi: 10.1002/MRM.1910320513.
23. Adluru G, McGann C, Speier P, Kholmovski EG, Shaaban A, Dibella EVR. Acquisition and reconstruction of undersampled radial data for myocardial perfusion magnetic resonance imaging. *J. Magn. Reson. Imaging* 2009;29:466–473 doi: 10.1002/jmri.21585.
24. Uecker M, Zhang S, Frahm J. Nonlinear inverse reconstruction for real-time MRI of the human heart using undersampled radial FLASH. *Magn. Reson. Med.* 2010;63:1456–1462 doi: 10.1002/MRM.22453.
25. Scannell CM, Villa ADM, Lee J, Breeuwer M, Chiribiri A. Robust Non-Rigid Motion Compensation of Free-Breathing Myocardial Perfusion MRI Data. *IEEE Trans. Med. Imaging* 2019;38:1812–1820 doi: 10.1109/TMI.2019.2897044.
26. Wollny G, Kellman P, Santos A, Ledesma-Carbayo MJ. Automatic motion compensation of free breathing acquired myocardial perfusion data by using independent component analysis. *Med. Image Anal.* 2012;16:1015–1028 doi: 10.1016/J.MEDIA.2012.02.004.
27. Zhang T, Pauly JM, Levesque IR. Accelerating parameter mapping with a locally low rank constraint. *Magn. Reson. Med.* 2015;73:655–661 doi: 10.1002/mrm.25161.
28. Kotecha T, Martinez-Naharro A, Boldrini M, et al. Automated Pixel-Wise Quantitative Myocardial Perfusion Mapping by CMR to Detect Obstructive Coronary Artery Disease and Coronary Microvascular Dysfunction: Validation Against Invasive Coronary Physiology. *JACC Cardiovasc. Imaging* 2019 doi: 10.1016/J.JCMG.2018.12.022.
29. Kotecha T, Chacko L, Chehab O, et al. Assessment of Multivessel Coronary Artery Disease Using Cardiovascular Magnetic Resonance Pixelwise Quantitative Perfusion Mapping. *JACC. Cardiovasc. Imaging* 2020;13:2546–2557 doi: 10.1016/j.jcmg.2020.06.041.
30. Rahman H, Scannell CM, Demir OM, et al. High-Resolution Cardiac Magnetic Resonance Imaging Techniques for the Identification of Coronary Microvascular Dysfunction. *JACC. Cardiovasc. Imaging* 2021;14:978–986 doi: 10.1016/J.JCMG.2020.10.015.
31. Schulz-Menger J, Bluemke DA, Bremerich J, et al. Standardized image interpretation and post-processing in cardiovascular magnetic resonance - 2020 update: Society for Cardiovascular Magnetic Resonance (SCMR): Board of Trustees Task Force on Standardized Post-Processing. *J. Cardiovasc. Magn. Reson.* 2020;22:1–22 doi: 10.1186/s12968-020-00610-6.
32. Fredholm BB. Astra Award Lecture. Adenosine, adenosine receptors and the actions of caffeine. *Pharmacol. Toxicol.* 1995;76:93–101 doi: 10.1111/J.1600-0773.1995.TB00111.X.

- 
33. Kidambi A, Sourbron S, Maredia N, et al. Factors associated with false-negative cardiovascular magnetic resonance perfusion studies: A Clinical evaluation of magnetic resonance imaging in coronary artery disease (CE-MARC) substudy. *J. Magn. Reson. Imaging* 2016;43:566–573 doi: 10.1002/JMRI.25032.
34. Kwon DH, Asamoto L, Popovic ZB, et al. Infarct characterization and quantification by delayed enhancement cardiac magnetic resonance imaging is a powerful independent and incremental predictor of mortality in patients with advanced ischemic cardiomyopathy. *Circ. Cardiovasc. Imaging* 2014;7:796–804 doi: 10.1161/CIRCIMAGING.114.002077.
35. Catalano O, Moro G, Perotti M, et al. Late gadolinium enhancement by cardiovascular magnetic resonance is complementary to left ventricle ejection fraction in predicting prognosis of patients with stable coronary artery disease. *J. Cardiovasc. Magn. Reson.* 2012;14:29 doi: 10.1186/1532-429X-14-29.
36. Abbasi SA, Ertel A, Shah R V., et al. Impact of cardiovascular magnetic resonance on management and clinical decision-making in heart failure patients. *J. Cardiovasc. Magn. Reson.* 2013;15 doi: 10.1186/1532-429X-15-89.
37. Beek AM, Bondarenko O, Afsharzada F, Van Rossum AC. Quantification of late gadolinium enhanced CMR in viability assessment in chronic ischemic heart disease: A comparison to functional outcome. *J. Cardiovasc. Magn. Reson.* 2009;11:1–7 doi: 10.1186/1532-429X-11-6.
38. Chen C, Qin C, Qiu H, et al. Deep Learning for Cardiac Image Segmentation: A Review. *Front. Cardiovasc. Med.* 2020;7:25 doi: 10.3389/FCVM.2020.00025.
39. Shimron E, Tamir JI, Wang K, Lustig M. Implicit data crimes: Machine learning bias arising from misuse of public data. *Proc. Natl. Acad. Sci. U. S. A.* 2022;119:e2117203119 doi: 10.1073/PNAS.2117203119.
40. Dealgan12. The human heart - Original illustration is licensed under the Creative Commons Attribution-Share Alike 3.0 Unported license. [https://commons.wikimedia.org/wiki/File:Diagram\\_of\\_the\\_human\\_heart\\_\(cropped\).svg](https://commons.wikimedia.org/wiki/File:Diagram_of_the_human_heart_(cropped).svg). Accessed February 11, 2023.
41. Klinke R, Pape HC, Kurtz A, Silbernagl S. *Physiologie*. Georg Thieme Verlag; 2009.
42. Pijls NHJ, de Bruyne B, Peels K, et al. Measurement of Fractional Flow Reserve to Assess the Functional Severity of Coronary-Artery Stenoses. *N. Engl. J. Med.* 1996;334:1703–1708 doi: 10.1056/NEJM199606273342604.
43. Fox K, Alonso Garcia MA, Ardissino D, et al. Guidelines on the management of stable angina pectoris: Executive summary - The Task Force on the Management of Stable Angina Pectoris of the European Society of Cardiology. *Eur. Heart J.* 2006;27:1341–1381 doi: 10.1093/eurheartj/ehl001.

- 
44. Gould KL, Kirkeeide RL, Buchi M. Coronary flow reserve as a physiologic measure of stenosis severity. *J. Am. Coll. Cardiol.* 1990;15:459–474 doi: 10.1016/S0735-1097(10)80078-6.
  45. Qayyum AA, Kastrup J. Measuring myocardial perfusion: the role of PET, MRI and CT. *Clin. Radiol.* 2015;70:576–584 doi: 10.1016/J.CRAD.2014.12.017.
  46. Greenwood J, Motwani M, Maredia N, et al. The role of cardiovascular magnetic resonance in women with suspected CAD: a CE-MARC substudy. *J. Cardiovasc. Magn. Reson.* 2012;14:O94 doi: 10.1186/1532-429X-14-S1-O94.
  47. Danad I, Szymonifka J, Twisk JWR, et al. Diagnostic performance of cardiac imaging methods to diagnose ischaemia-causing coronary artery disease when directly compared with fractional flow reserve as a reference standard: a meta-analysis. *Eur. Heart J.* 2017;38:991–998 doi: 10.1093/EURHEARTJ/EHW095.
  48. Neumann F-J, Sousa-Uva M, Ahlsson A, et al. 2018 ESC/EACTS Guidelines on myocardial revascularization. *Eur. Heart J.* 2019;40:87–165 doi: 10.1093/eurheartj/ehy394.
  49. Sciagrà R, Lubberink M, Hyafil F, et al. EANM procedural guidelines for PET/CT quantitative myocardial perfusion imaging. *Eur. J. Nucl. Med. Mol. Imaging* 2021;48:1040–1069 doi: 10.1007/S00259-020-05046-9.
  50. Kellman P, Hansen MS, Nielles-Vallespin S, et al. Myocardial perfusion cardiovascular magnetic resonance: optimized dual sequence and reconstruction for quantification. *J. Cardiovasc. Magn. Reson.* 2017;19:1–14 doi: 10.1186/s12968-017-0355-5.
  51. Scott AD, Keegan J, Firmin DN. Motion in cardiovascular MR imaging. *Radiology* 2009;250:331–351 doi: 10.1148/RADIOL.2502071998.
  52. Motwani M, Fairbairn T, Larghat AM, et al. Systolic versus diastolic myocardial blood flow in patients with suspected coronary artery disease - A cardiovascular magnetic resonance study. *J. Cardiovasc. Magn. Reson.* 2012;14:P17 doi: 10.1186/1532-429X-14-S1-P17.
  53. Chung CS. Duration of diastole and its phases as a function of heart rate during supine bicycle exercise. *AJP Hear. Circ. Physiol.* 2004;287:H2003–H2008 doi: 10.1152/ajpheart.00404.2004.
  54. Gemignani V, Bianchini E, Faita F, et al. Assessment of cardiologic systole and diastole duration in exercise stress tests with a transcutaneous acceleromometer sensor. *Comput. Cardiol.* 2008;35:153–156 doi: 10.1109/CIC.2008.4749000.
  55. Benjelloun H, Itti R, Philippe L, Lorgeron JM, Brochier M. Beat-to-beat assessment of left ventricular ejection in atrial fibrillation. *Eur. J. Nucl. Med.* 1983;8:206–210 doi: 10.1007/BF00253767.

- 
56. Shin T, Pohost GM, Nayak KS. Systolic 3D first-pass myocardial perfusion MRI: Comparison with diastolic imaging in healthy subjects. *Magn. Reson. Med.* 2010;63:858–864 doi: 10.1002/mrm.22315.
57. Taylor AM, Jhooti P, Wiesmann F, Keegan J, Firmin DN, Pennell DJ. MR navigator-echo monitoring of temporal changes in diaphragm position: implications for MR coronary angiography. *J. Magn. Reson. Imaging* 1997;7:629–636 doi: 10.1002/JMRI.1880070404.
58. Wang Y, Riederer SJ, Ehman RL. Respiratory motion of the heart: kinematics and the implications for the spatial resolution in coronary imaging. *Magn. Reson. Med.* 1995;33:713–719 doi: 10.1002/MRM.1910330517.
59. Nehrke K, Börnert P, Manke D, Böck JC. Free-breathing Cardiac MR Imaging: Study of Implications of Respiratory Motion—Initial Results1. <https://doi.org/10.1148/radiol.2203010132> 2001;220:810–815 doi: 10.1148/RADIOL.2203010132.
60. McLeish K, Hill DLG, Atkinson D, Blackall JM, Razavi R. A study of the motion and deformation of the heart due to respiration. *IEEE Trans. Med. Imaging* 2002;21:1142–1150 doi: 10.1109/TMI.2002.804427.
61. McClelland JR, Hawkes DJ, Schaeffter T, King AP. Respiratory motion models: a review. *Med. Image Anal.* 2013;17:19–42 doi: 10.1016/J.MEDIA.2012.09.005.
62. Kober F, Jao T, Troalen T, Nayak KS. Myocardial arterial spin labeling. *J. Cardiovasc. Magn. Reson.* 2016;18:1–16 doi: 10.1186/s12968-016-0235-4.
63. Streif JUG, Hiller KH, Waller C, et al. In vivo assessment of absolute perfusion in the murine skeletal muscle with spin labeling MRI. *Magnetic resonance imaging. J. Magn. Reson. Imaging* 2003;17:147–152 doi: 10.1002/JMRI.10229.
64. Kampf T, Helluy X, Gutjahr FT, et al. Myocardial perfusion quantification using the T1 -based FAIR-ASL method: the influence of heart anatomy, cardiopulmonary blood flow and look-locker readout. *Magn. Reson. Med.* 2014;71:1784–1797 doi: 10.1002/MRM.24843.
65. Belle V, Kahler E, Waller C, et al. In vivo quantitative mapping of cardiac perfusion in rats using a noninvasive MR spin-labeling method. *J. Magn. Reson. Imaging* 1998;8:1240–1245 doi: 10.1002/JMRI.1880080610.
66. Epstein FH, Meyer CH. Myocardial Perfusion Using Arterial Spin Labeling CMR: Promise and Challenges. *JACC Cardiovasc. Imaging* 2011;4:1262–1264 doi: 10.1016/J.JCMG.2011.08.015.
67. Henningsson M, Carlhäll C-J, Kihlberg J. Myocardial arterial spin labeling in systole and diastole using flow-sensitive alternating inversion recovery with parallel imaging and compressed sensing. 2020 doi: 10.1002/nbm.4436.

- 
68. Kali A, Choi EY, Sharif B, et al. Native T1 Mapping by 3-T CMR Imaging for Characterization of Chronic Myocardial Infarctions. *JACC. Cardiovasc. Imaging* 2015;8:1019–1030 doi: 10.1016/J.JCMG.2015.04.018.
69. Kali A, Cokic I, Tang RLQ, et al. Determination of location, size, and transmuralty of chronic myocardial infarction without exogenous contrast media by using cardiac magnetic resonance imaging at 3 T. *Circ. Cardiovasc. Imaging* 2014;7:471–481 doi: 10.1161/CIRCIMAGING.113.001541.
70. Wacker CM, Fidler F, Dueren C, et al. Quantitative Assessment of Myocardial Perfusion With a Spin-Labeling Technique: Preliminary Results in Patients with Coronary Artery Disease. *J. Magn. Reson. Imaging* 2003;18:555–560 doi: 10.1002/jmri.10386.
71. Liu A, Wijesurendra RS, Francis JM, et al. Adenosine Stress and Rest T1 Mapping Can Differentiate between Ischemic, Infarcted, Remote, and Normal Myocardium Without the Need for Gadolinium Contrast Agents. *JACC Cardiovasc. Imaging* 2016;9:27–36 doi: 10.1016/j.jcmg.2015.08.018.
72. Bohnen S, Prüßner L, Vettorazzi E, et al. Stress T1-mapping cardiovascular magnetic resonance imaging and inducible myocardial ischemia. *Clin. Res. Cardiol.* 2019;108:909–920 doi: 10.1007/S00392-019-01421-1.
73. Nakamori S, Fahmy A, Jang J, et al. Changes in Myocardial Native T1 and T2 After Exercise Stress: A Noncontrast CMR Pilot Study. *JACC Cardiovasc. Imaging* 2020;13:667–680 doi: 10.1016/J.JCMG.2019.05.019.
74. Yimcharoen S, Zhang S, Kaolawanich Y, Tanapibunpon P, Krittayaphong R. Clinical assessment of adenosine stress and rest cardiac magnetic resonance T1 mapping for detecting ischemic and infarcted myocardium. *Sci. Rep.* 2020;10:14727 doi: 10.1038/S41598-020-71722-3.
75. Burrage MK, Shanmuganathan M, Masi A, et al. Cardiovascular magnetic resonance stress and rest T1-mapping using regadenoson for detection of ischemic heart disease compared to healthy controls. *Int. J. Cardiol.* 2021;333:239–245 doi: 10.1016/J.IJCARD.2021.03.010.
76. van Assen M, van Dijk R, Kuijpers D, Vliegenthart R, Oudkerk M. T1 reactivity as an imaging biomarker in myocardial tissue characterization discriminating normal, ischemic and infarcted myocardium. *Int. J. Cardiovasc. Imaging* 2019;35:1319–1325 doi: 10.1007/S10554-019-01554-4.
77. Ng MY, Chan KYE, Chan CWS. Cardiac magnetic resonance stress and rest perfusion with T1 mapping: Is it ready to assess for ischaemic heart disease? *Int. J. Cardiol.* 2021;335:137–138 doi: 10.1016/J.IJCARD.2021.04.014.
78. Bernhardt P, Manzke R, Bornstedt A, et al. Blood oxygen level-dependent magnetic resonance imaging using T2-prepared steady-state free-precession imaging in comparison to contrast-enhanced myocardial perfusion imaging. *Int. J. Cardiol.* 2011;147:416–419 doi: 10.1016/J.IJCARD.2009.09.547.

- 
79. Yang HJ, Yumul R, Tang R, et al. Assessment of myocardial reactivity to controlled hypercapnia with free-breathing T2-prepared cardiac blood oxygen level-dependent MR imaging. *Radiology* 2014;272:397–406 doi: 10.1148/RADIOL.14132549.
80. Hillier E, Covone J, Friedrich MG. Oxygenation-sensitive Cardiac MRI with Vasoactive Breathing Maneuvers for the Non-invasive Assessment of Coronary Microvascular Dysfunction. *J. Vis. Exp.* 2022 doi: 10.3791/64149.
81. Fischer K, Yamaji K, Luescher S, et al. Feasibility of cardiovascular magnetic resonance to detect oxygenation deficits in patients with multi-vessel coronary artery disease triggered by breathing maneuvers. *J. Cardiovasc. Magn. Reson.* 2018;20:1–11 doi: 10.1186/S12968-018-0446-Y.
82. Hillier E, Friedrich MG. The Potential of Oxygenation-Sensitive CMR in Heart Failure. *Curr. Heart Fail. Rep.* 2021;18:304–314 doi: 10.1007/S11897-021-00525-Y.
83. Weberling LD, Friedrich MG. Oxygenation-sensitive cardiac magnetic resonance imaging. *Radiologie* 2022 doi: 10.1007/S00117-022-01049-9.
84. Rohrer M, Bauer H, Mintorovitch J, Requardt M, Weinmann HJ. Comparison of magnetic properties of MRI contrast media solutions at different magnetic field strengths. *Invest Radiol* 2005;40:715–724 doi: 00004424-200511000-00005 [pii].
85. Bernstein MA, King KF, Zhou XJ. *Handbook of MRI Pulse Sequences*. Elsevier Science; 2004.
86. Kellman P, Hansen MS, Nielles-Vallespin S, et al. Myocardial perfusion cardiovascular magnetic resonance: optimized dual sequence and reconstruction for quantification. *J. Cardiovasc. Magn. Reson.* 2017;19 doi: 10.1186/s12968-017-0355-5.
87. Manning WJ, Atkinson DJ, Grossman W, Paulin S, Edelman RR. First-pass nuclear magnetic resonance imaging studies using gadolinium-DTPA in patients with coronary artery disease. *J. Am. Coll. Cardiol.* 1991;18:959–965.
88. Schwitter J, Nanz D, Kneifel S, et al. Assessment of myocardial perfusion in coronary artery disease by magnetic resonance: A comparison with positron emission tomography and coronary angiography. *Circulation* 2001;103:2230–2235 doi: 10.1161/01.CIR.103.18.2230.
89. Heitner JF, Kim RJ, Kim HW, et al. Prognostic Value of Vasodilator Stress Cardiac Magnetic Resonance Imaging: A Multicenter Study With 48 000 Patient-Years of Follow-up. *JAMA Cardiol.* 2019;4:256 doi: 10.1001/JAMACARDIO.2019.0035.
90. Nagel E, Greenwood JP, McCann GP, et al. Magnetic Resonance Perfusion or Fractional Flow Reserve in Coronary Disease. *N. Engl. J. Med.* 2019;380:2418–2428 doi: 10.1056/NEJMOA1716734.

- 
91. Pezel T, Hovasse T, Kinnel M, et al. Long-Term Prognostic Value of Stress Cardiovascular Magnetic Resonance in Patients with History of Percutaneous Coronary Intervention. *Circ. Cardiovasc. Imaging* 2021;14:E012374 doi: 10.1161/CIRCIMAGING.120.012374.
92. Weinmann HJ, Brasch RC, Press WR, Wesbey GE. Characteristics of gadolinium-DTPA complex: A potential NMR contrast agent. *Am. J. Roentgenol.* 1984;142:619–624 doi: 10.2214/ajr.142.3.619.
93. Grobner T. Erratum: Gadolinium - A specific trigger for the development of nephrogenic fibrosing dermopathy and nephrogenic systemic fibrosis? (*Nephrology Dialysis Transplantation* (2006) vol. 21 (1104-1108)). *Nephrol. Dial. Transplant.* 2006;21:1745 doi: 10.1093/ndt/gfl294.
94. Broome DR. Nephrogenic systemic fibrosis associated with gadolinium based contrast agents: A summary of the medical literature reporting. *Eur. J. Radiol.* 2008;66:230–234 doi: 10.1016/j.ejrad.2008.02.011.
95. Ramalho J, Semelka RC, Ramalho M, Nunes RH, AlObaidy M, Castillo M. Gadolinium-based contrast agent accumulation and toxicity: An update. *Am. J. Neuroradiol.* 2016;37:1192–1198 doi: 10.3174/ajnr.A4615.
96. Kanda T, Ishii K, Kawaguchi H, Kitajima K, Takenaka D. High Signal Intensity in the Dentate Nucleus and Globus Pallidus on Unenhanced T1-weighted MR Images: Relationship with Increasing Cumulative Dose of a Gadolinium-based Contrast Material. *Radiology* 2014;270:834–841 doi: 10.1148/radiol.13131669.
97. Kanda T, Osawa M, Oba H, et al. High Signal Intensity in Dentate Nucleus on Unenhanced T1-weighted MR Images: Association with Linear versus Macrocyclic Gadolinium Chelate Administration. *Radiology* 2015;275:803–809 doi: 10.1148/radiol.14140364.
98. McDonald RJ, McDonald JS, Kallmes DF, et al. Intracranial Gadolinium Deposition after Contrast-enhanced MR Imaging. *Radiology* 2015;275:772–782 doi: 10.1148/radiol.15150025.
99. Frenzel T, Lengsfeld P, Schirmer H, Hütter J, Weinmann HJ. Stability of gadolinium-based magnetic resonance imaging contrast agents in human serum at 37°C. *Invest. Radiol.* 2008;43:817–828 doi: 10.1097/RLI.0B013E3181852171.
100. Strzeminska I, Factor C, Robert P, et al. Long-Term Evaluation of Gadolinium Retention in Rat Brain After Single Injection of a Clinically Relevant Dose of Gadolinium-Based Contrast Agents. *Invest. Radiol.* 2020;55:138–143 doi: 10.1097/RLI.0000000000000623.
101. Agency EM. PRAC concludes assessment of gadolinium agents used in body scans and recommends regulatory actions, including suspension for some marketing authorisations. *Rentgenol. i Radiol.* 2017;56:10–12 doi: EMA/157486/2017.

- 
102. U.S. Food and Drug Administration. FDA warns that gadolinium-based contrast agents ( GBCAs ) are retained in the body ; requires new class warnings. <https://www.fda.gov/drugs/drug-safety-and-availability/fda-drug-safety-communication-fda-warns-gadolinium-based-contrast-agents-gbcas-are-retained-body>. Published 2017.
103. Harvey HB, Gowda V, Cheng G. Gadolinium Deposition Disease: A New Risk Management Threat. *J. Am. Coll. Radiol.* 2020;17:546–550 doi: 10.1016/J.JACR.2019.11.009.
104. McDonald RJ, Weinreb JC, Davenport MS. Symptoms Associated with Gadolinium Exposure (SAGE): A Suggested Term. *Radiology* 2022;302:270–273 doi: 10.1148/radiol.2021211349.
105. Paiman EHM, Lamb HJ. When should we use contrast material in cardiac MRI? *J. Magn. Reson. Imaging* 2017;46:1551–1572 doi: 10.1002/jmri.25754.
106. Kellman P, Arai AE. Imaging sequences for first pass perfusion - A review. *J. Cardiovasc. Magn. Reson.* 2007;9:525–537 doi: 10.1080/10976640601187604.
107. Cerqueira MD, Weissman NJ, Dilsizian V, et al. Standardized myocardial segmentation and nomenclature for tomographic imaging of the heart. *J. Cardiovasc. Magn. Reson.* 2002;4:203–210 doi: 10.1081/JCMR-120003946.
108. Jerosch-Herold M. Quantification of myocardial perfusion by cardiovascular magnetic resonance. *J. Cardiovasc. Magn. Reson.* 2010;12:57 doi: 10.1186/1532-429X-12-57.
109. Haase A. Snapshot flash mri. Applications to t1, t2, and chemical shift imaging. *Magn. Reson. Med.* 1990;13:77–89 doi: 10.1002/mrm.1910130109.
110. Jogiya R, Schuster A, Zaman A, et al. Three-dimensional balanced steady state free precession myocardial perfusion cardiovascular magnetic resonance at 3T using dual-source parallel RF transmission: initial experience. *J. Cardiovasc. Magn. Reson.* 2014;16:90 doi: 10.1186/s12968-014-0090-0.
111. Scheffler K, Lehnhardt S. Principles and applications of balanced SSFP techniques. *Eur. Radiol.* 2003;13:2409–2418 doi: 10.1007/s00330-003-1957-x.
112. Mansfield P, P BT and M, Becker E D FJA and FTC, et al. Multi-planar image formation using NMR spin echoes. *J. Phys. C Solid State Phys.* 1977;10:L55–L58 doi: 10.1088/0022-3719/10/3/004.
113. Gatehouse PD, Elkington AG, Ablitt NA, Yang G-Z, Pennell DJ, Firmin DN. Accurate assessment of the arterial input function during high-dose myocardial perfusion cardiovascular magnetic resonance. *J. Magn. Reson. Imaging* 2004;20:39–45 doi: 10.1002/jmri.20054.



- 
114. Vitanis V, Manka R, Giese D, et al. High resolution three-dimensional cardiac perfusion imaging using compartment-based k-t principal component analysis. *Magn. Reson. Med.* 2011;65:575–587 doi: 10.1002/mrm.22620.
115. Motwani M, Kidambi A, Sourbron S, et al. Quantitative three-dimensional cardiovascular magnetic resonance myocardial perfusion imaging in systole and diastole. *J. Cardiovasc. Magn. Reson.* 2014;16:1–11 doi: 10.1186/1532-429X-16-19.
116. Jogiya R, Morton G, De Silva K, et al. Ischemic burden by 3-dimensional myocardial perfusion cardiovascular magnetic resonance: Comparison with myocardial perfusion scintigraphy. *Circ. Cardiovasc. Imaging* 2014;7:647–654 doi: 10.1161/CIRCIMAGING.113.001620.
117. Manka R, Wissmann L, Gebker R, et al. Multicenter Evaluation of Dynamic Three-Dimensional Magnetic Resonance Myocardial Perfusion Imaging for the Detection of Coronary Artery Disease Defined by Fractional Flow Reserve. *Circ. Cardiovasc. Imaging* 2015;8:1–7 doi: 10.1161/CIRCIMAGING.114.003061.
118. Hamada S, Gotschy A, Wissmann L, et al. Multi-centre study of whole-heart dynamic 3D cardiac magnetic resonance perfusion imaging for the detection of coronary artery disease defined by fractional flow reserve: gender based analysis of diagnostic performance. *Eur. Hear. journal. Cardiovasc. Imaging* 2017;18:1099–1106 doi: 10.1093/ehjci/jex160.
119. Wissmann L, Niemann M, Gotschy A, Manka R, Kozerke S. Quantitative three-dimensional myocardial perfusion cardiovascular magnetic resonance with accurate two-dimensional arterial input function assessment. *J. Cardiovasc. Magn. Reson.* 2015;17:1–11 doi: 10.1186/s12968-015-0212-3.
120. Dibella EVR, Chen L, Schabel MC, Adluru G, McGann CJ. Myocardial perfusion acquisition without magnetization preparation or gating. *Magn. Reson. Med.* 2012;67:609–613 doi: 10.1002/MRM.23318.
121. Shin T, Nayak KS, Santos JM, Nishimura DG, Hu BS, McConnell M V. Three-dimensional first-pass myocardial perfusion MRI using a stack-of-spirals acquisition. *Magn. Reson. Med.* 2013;69:839–844 doi: 10.1002/mrm.24303.
122. Wang H, Bangerter NK, Park DJ, et al. Comparison of centric and reverse-centric trajectories for highly accelerated three-dimensional saturation recovery cardiac perfusion imaging. *Magn. Reson. Med.* 2015;74:1070–1076 doi: 10.1002/mrm.25478.
123. Pan JA, Robinson AA, Yang Y, et al. Diagnostic Accuracy of Spiral Whole-Heart Quantitative Adenosine Stress Cardiovascular Magnetic Resonance With Motion Compensated L1-SPIRIT. *J. Magn. Reson. Imaging* 2021 doi: 10.1002/jmri.27620.

- 
124. Sodickson DK, Manning WJ. Simultaneous acquisition of spatial harmonics (SMASH): Fast imaging with radiofrequency coil arrays. *Magn. Reson. Med.* 1997;38:591–603 doi: 10.1002/MRM.1910380414.
125. Larkman DJ, Hajnal J V, Herlihy AH, Coutts GA, Young IR, Sta Ehnholm G. Use of Multicoil Arrays for Separation of Signal from Multiple Slices Simultaneously Excited. 2001 doi: 10.1002/1522-2586.
126. Griswold MA, Jakob PM, Heidemann RM, et al. Generalized autocalibrating partially parallel acquisitions (GRAPPA). *Magn. Reson. Med.* 2002;47:1202–1210 doi: 10.1002/MRM.10171.
127. Breuer FA, Blaimer M, Heidemann RM, Mueller MF, Griswold MA, Jakob PM. Controlled aliasing in parallel imaging results in higher acceleration (CAIPIRINHA) for multi-slice imaging. *Magn. Reson. Med.* 2005;53:684–691 doi: 10.1002/MRM.20401.
128. Yutzy SR, Seiberlich N, Duerk JL, Griswold MA. Improvements in multislice parallel imaging using radial CAIPIRINHA. *Magn. Reson. Med.* 2011;65:1630–1637 doi: 10.1002/MRM.22752.
129. Nazir MS, Neji R, Speier P, et al. Simultaneous multi slice (SMS) balanced steady state free precession first-pass myocardial perfusion cardiovascular magnetic resonance with iterative reconstruction at 1.5 T. *J. Cardiovasc. Magn. Reson.* 2018;20:1–11 doi: 10.1186/S12968-018-0502-7.
130. Yang Y, Meyer CH, Epstein FH, Kramer CM, Salerno M. Whole-heart spiral simultaneous multi-slice first-pass myocardial perfusion imaging. *Magn. Reson. Med.* 2019;81:852–862 doi: 10.1002/MRM.27412.
131. Tian Y, Mendes J, Pedgaonkar A, et al. Feasibility of multiple-view myocardial perfusion MRI using radial simultaneous multi-slice acquisitions. *PLoS One* 2019;14 doi: 10.1371/JOURNAL.PONE.0211738.
132. Nazir MS, Neji R, Speier P, et al. Feasibility of absolute myocardial blood flow quantification using Simultaneous Multi Slice (SMS) SSFP first-pass myocardial perfusion imaging and iterative reconstruction at 1.5 Tesla. *Proc. Intern. Soc. Magn. Reson. Med.(ISMRM)* 2018.
133. Huang Q, Tian Y, Mendes J, Ranjan R, Adluru G, DiBella E. Quantitative myocardial perfusion with a hybrid 2D simultaneous multi-slice sequence. *Magn. Reson. Imaging* 2023;98:7–16 doi: 10.1016/J.MRI.2022.12.010.
134. Wang H, Adluru G, Chen L, Kholmovski EG, Bangerter NK, DiBella EVR. Radial simultaneous multi-slice CAIPI for ungated myocardial perfusion. *Magn. Reson. Imaging* 2016;34:1329–1336 doi: 10.1016/J.MRI.2016.07.015.
135. Tian Y, Mendes J, Wilson B, et al. Whole-heart, ungated, free-breathing, cardiac-phase-resolved myocardial perfusion MRI by using Continuous Radial Interleaved simultaneous Multi-slice acquisitions at sPoiled steady-state (CRIMP). *Magn. Reson. Med.* 2020;84:3071–3087 doi: 10.1002/mrm.28337.
136. Stäb D, Ritter CO, Breuer FA, Weng AM, Hahn D, Köstler H. CAIPIRINHA accelerated SSFP imaging. *Magn. Reson. Med.* 2011;65:157–164 doi: 10.1002/MRM.22600.

- 
137. Edelstein WA, Glover GH, Hardy CJ, Redington RW. The intrinsic signal-to-noise ratio in NMR imaging. *Magn. Reson. Med.* 1986;3:604–618 doi: 10.1002/MRM.1910030413.
138. Tsao J, Boesiger P, Pruessmann KP. k-t BLAST and k-t SENSE: Dynamic MRI With High Frame Rate Exploiting Spatiotemporal Correlations. *Magn. Reson. Med.* 2003;50:1031–1042 doi: 10.1002/mrm.10611.
139. Noll DC, Nishimura DG, Macovski A. Homodyne Detection in Magnetic Resonance Imaging. *IEEE Trans. Med. Imaging* 1991;10:154–163 doi: 10.1109/42.79473.
140. Küstner T, Würslin C, Gatidis S, et al. MR Image Reconstruction Using a Combination of Compressed Sensing and Partial Fourier Acquisition : ESPReSSo. 2016;35:2447–2458.
141. McGibney G, Smith MR, Nichols ST, Crawley A. Quantitative evaluation of several partial Fourier reconstruction algorithms used in MRI. *Magn. Reson. Med.* 1993;30:51–59 doi: 10.1002/MRM.1910300109.
142. Winkelmann S, Schaeffter T, Koehler T, Eggers H, Doessel O. An optimal radial profile order based on the golden ratio for time-resolved MRI. *IEEE Trans. Med. Imaging* 2007;26:68–76 doi: 10.1109/TMI.2006.885337.
143. Prieto C, Doneva M, Usman M, et al. Highly efficient respiratory motion compensated free-breathing coronary MRA using golden-step Cartesian acquisition. *J. Magn. Reson. Imaging* 2015;41:738–746 doi: 10.1002/jmri.24602.
144. Usman M, Ruijsink B, Nazir MS, Cruz G, Prieto C. Free breathing whole-heart 3D CINE MRI with self-gated Cartesian trajectory. *Magn. Reson. Imaging* 2017;38:129 doi: 10.1016/J.MRI.2016.12.021.
145. Yudilevich E, Stark H. Spiral Sampling in Magnetic Resonance Imaging-The Effect of Inhomogeneities. *IEEE Trans. Med. Imaging* 1987;6:337–345 doi: 10.1109/TMI.1987.4307852.
146. Salerno M, Sica C, Kramer CM, Meyer CH. Improved first-pass spiral myocardial perfusion imaging with variable density trajectories. *Magn. Reson. Med.* 2013;70:1369–1379 doi: 10.1002/mrm.24569.
147. Salerno M, Sica CT, Kramer CM, Meyer CH. Optimization of spiral-based pulse sequences for first-pass myocardial perfusion imaging. *Magn. Reson. Med.* 2011;65:1602–1610 doi: 10.1002/mrm.22746.
148. Wundrak S, Paul J, Ulrici J, et al. Golden ratio sparse MRI using tiny golden angles. *Magn. Reson. Med.* 2016;75:2372–2378 doi: 10.1002/mrm.25831.
149. Chen L, Adluru G, Schabel MC, McGann CJ, Dibella EVR. Myocardial perfusion MRI with an undersampled 3D stack-of-stars sequence. *Med. Phys.* 2012;39:5204–5211 doi: 10.1118/1.4738965.
150. Pruessmann KP, Weiger M, Scheidegger MB, Boesiger P. SENSE: Sensitivity Encoding for Fast MRI. doi: 10.1002/(SICI)1522-2594(199911)42:5.

- 
151. Pruessmann KP, Weiger M, Börnert P, Boesiger P. Advances in sensitivity encoding with arbitrary k-space trajectories. *Magn. Reson. Med.* 2001;46:638–651 doi: 10.1002/MRM.1241.
  152. Hansen PC, O’Leary DP. The Use of the L-Curve in the Regularization of Discrete Ill-Posed Problems. *SIAM J. Sci. Comput.* 1993;14:1487–1503 doi: 10.1137/0914086.
  153. Plein S, Ryf S, Schwitter J, Radjenovic A, Boesiger P, Kozerke S. Dynamic contrast-enhanced myocardial perfusion MRI accelerated with k-t SENSE. *Magn. Reson. Med.* 2007;58:777–785 doi: 10.1002/mrm.21381.
  154. Vitanis V, Manka R, Boesiger P, Kozerke S. Accelerated cardiac perfusion imaging using k-t SENSE with SENSE training. *Magn. Reson. Med.* 2009;62:955–965 doi: 10.1002/mrm.22078.
  155. Pedersen H, Kozerke S, Ringgaard S, Nehrke K, Won YK. K-t PCA: Temporally constrained k-t BLAST reconstruction using principal component analysis. *Magn. Reson. Med.* 2009;62:706–716 doi: 10.1002/mrm.22052.
  156. Hansen MS, Baltes C, Tsao J, Kozerke S, Pruessmann KP, Eggers H. k-t BLAST Reconstruction From Non-Cartesian k-t Space Sampling. 2006;91:85–91 doi: 10.1002/mrm.20734.
  157. Candes E, Romberg J, Tao T. Robust Uncertainty Principles : Exact Signal Reconstruction from Highly Incomplete Frequency Information. 2005:1–41 doi: 10.48550/arXiv.math/0409186.
  158. Donoho DL, Santos JM, Pauly JM, Lustig M, Donoho DL, Pauly JM. Sparse MRI: The application of compressed sensing for rapid MR imaging. *Magn. Reson. Med.* 2007;58:1182–1195 doi: 10.1002/mrm.21391.
  159. Lustig M, Donoho D, Pauly JM. Sparse MRI: The application of compressed sensing for rapid MR imaging. *Magn. Reson. Med.* 2007;58:1182–1195 doi: 10.1002/mrm.21391.
  160. Rudin LI, Osher S, Fatemi E. Nonlinear total variation based noise removal algorithms. *Phys. D Nonlinear Phenom.* 1992;60:259–268 doi: 10.1016/0167-2789(92)90242-F.
  161. Adluru G, Awate SP, Tasdizen T, Whitaker RT, DiBella EVR. Temporally constrained reconstruction of dynamic cardiac perfusion MRI. *Magn. Reson. Med.* 2007;57:1027–1036 doi: 10.1002/MRM.21248.
  162. Motwani M, Fairbairn TA, Larghat A, et al. Systolic versus Diastolic Acquisition in Myocardial Perfusion MR Imaging. *Radiology* 2012;262:816–823 doi: 10.1148/radiol.11111549.
  163. Lustig M, Santos JM, Donoho D, Pauly JM. k-t SPARSE: high frame rate dynamic MRI exploiting spatio-temporal sparsity. *Proc. ISMRM, Seattle* 2006;50:2420.
  164. Otazo R, Kim D, Axel L, Sodickson DK. Combination of compressed sensing and parallel imaging for highly accelerated first-pass cardiac perfusion MRI. *Magn. Reson. Med.* 2010;64:767–776 doi: 10.1002/mrm.22463.

- 
165. Jung H, Sung K, Nayak KS, Kim EY, Ye JC. k-t FOCUSS : A General Compressed Sensing Framework for High Resolution Dynamic MRI. 2009;116:103–116 doi: 10.1002/mrm.21757.
166. Wissmann L, Gotschy A, Santelli C, et al. Analysis of spatiotemporal fidelity in quantitative 3D first-pass perfusion cardiovascular magnetic resonance. *J. Cardiovasc. Magn. Reson.* 2017;19:0–15 doi: 10.1186/s12968-017-0324-z.
167. Lingala SG, Hu Y, Dibella E, Jacob M. Accelerated dynamic MRI exploiting sparsity and low-rank structure: K-t SLR. *IEEE Trans. Med. Imaging* 2011;30:1042–1054 doi: 10.1109/TMI.2010.2100850.
168. Lingala SG, Hu Y, Dibella E, Jacob M. Accelerated first pass cardiac perfusion MRI using improved k - T SLR. *Proc. - Int. Symp. Biomed. Imaging* 2011;2:1280–1283 doi: 10.1109/ISBI.2011.5872635.
169. Lefkimmiatis S, Ward JP, Unser M. Hessian Schatten-Norm Regularization for Linear Inverse Problems. *IEEE Trans. Image Process.* 2013;22:1873–1888 doi: 10.1109/TIP.2013.2237919.
170. Otazo R, Cande E, Sodickson DK. Low-Rank Plus Sparse Matrix Decomposition for Accelerated Dynamic MRI with Separation of Background and Dynamic Components. *Magn. Reson. Med.* 2015;73:1125–1136 doi: 10.1002/mrm.25240.
171. Cand EJ, Recht B. Exact Matrix Completion via Convex Optimization. 2008:1–49 doi: 10.48550/arXiv.0805.4471.
172. Otazo R, Candès E, Sodickson DK. Low-Rank and Sparse Matrix Decomposition for Accelerated DCE-MRI with Background and Contrast Separation. *Proc. Intl. Soc. Mag. Reson. Med.* 2012;218:4248.
173. Fessler JA. Optimization methods for MR image reconstruction (long version). 2019 doi: 10.48550/ARXIV.1903.03510.
174. Daubechies I, Defrise M, De Mol C. An iterative thresholding algorithm for linear inverse problems with a sparsity constraint. *Commun. Pure Appl. Math.* 2004;57:1413–1457 doi: 10.1002/cpa.20042.
175. Boyd S, Parikh N, Chu E, Peleato B, Eckstein J. Distributed optimization and statistical learning via the alternating direction method of multipliers. *Found. Trends Mach. Learn.* 2010;3:1–122 doi: 10.1561/22000000016.
176. Afonso M V, Bioucas-Dias JM, Figueiredo MAT. Fast Image Recovery Using Variable Splitting and Constrained Optimization. *IEEE Trans. Image Process.* 2010;19:2345–2356 doi: 10.1109/TIP.2010.2047910.
177. Liu J, Hyder R, Asif MS, Kamilov US. Chapter 3 - Optimization Algorithms for MR Reconstruction. In: Akçakaya M, Doneva M, Prieto C, editors. *Magnetic Resonance Image Reconstruction. Vol. 7. Advances in Magnetic Resonance Technology and Applications.* Academic Press; 2022. pp. 59–72. doi: 10.1016/B978-0-12-822726-8.00012-9.

- 
178. NESTEROV YE. A method for solving the convex programming problem with convergence rate  $O(1/k^2)$ . Dokl. Akad. Nauk SSSR 1983;269:543–547.
179. Sotiras A, Davatzikos C, Paragios N. Deformable medical image registration: a survey. *IEEE Trans. Med. Imaging* 2013;32:1153–1190 doi: 10.1109/TMI.2013.2265603.
180. Bidaut LM, Vallée JP. Automated registration of dynamic MR images for the quantification of myocardial perfusion. *J. Magn. Reson. Imaging* 2001;13:648–655 doi: 10.1002/JMRI.1092.
181. Gupta SN, Solaiyappan M, Beache GM, Arai AE, Foo TKF. Fast method for correcting image misregistration due to organ motion in time-series MRI data. *Magn. Reson. Med.* 2003;49:506–514 doi: 10.1002/MRM.10394.
182. Zhou R, Huang W, Yang Y, et al. Simple motion correction strategy reduces respiratory-induced motion artifacts for k-t accelerated and compressed-sensing cardiovascular magnetic resonance perfusion imaging. *J. Cardiovasc. Magn. Reson.* 2018;20:1–13 doi: 10.1186/s12968-018-0427-1.
183. Pontre B, Cowan BR, DiBella E, et al. An Open Benchmark Challenge for Motion Correction of Myocardial Perfusion MRI. *IEEE J. Biomed. Heal. Informatics* 2017;21 doi: 10.1109/JBHI.2016.2597145.
184. Xue H, Brown LAE, Nielles-Vallespin S, Plein S, Kellman P. Automatic in-line quantitative myocardial perfusion mapping: Processing algorithm and implementation. *Magn. Reson. Med.* 2020;83:712–730 doi: 10.1002/mrm.27954.
185. Vishnevskiy V, Gass T, Szekely G, Tanner C, Goksel O. Isotropic Total Variation Regularization of Displacements in Parametric Image Registration. *IEEE Trans. Med. Imaging* 2017;36:385–395 doi: 10.1109/TMI.2016.2610583.
186. Huizinga W, Poot DHJ, Guyader J-M, et al. PCA-based groupwise image registration for quantitative MRI. *Med. Image Anal.* 2016;29:65–78 doi: 10.1016/j.media.2015.12.004.
187. Blomgren P, Chan TF. Color TV: total variation methods for restoration of vector-valued images. *IEEE Trans. Image Process.* 1998;7:304–309 doi: 10.1109/83.661180.
188. Likhite D, Adluru G, Hu N, McGann C, Dibella E. Quantification of myocardial perfusion with self-gated cardiovascular magnetic resonance. *J. Cardiovasc. Magn. Reson.* 2015;17:1–15 doi: 10.1186/s12968-015-0109-1.
189. Feng L, Axel L, Chandarana H, Block KT, Sodickson DK, Otazo R. XD-GRASP: Golden-angle radial MRI with reconstruction of extra motion-state dimensions using compressed sensing. *Magn. Reson. Med.* 2016;75:775–788 doi: 10.1002/mrm.25665.

- 
190. Haji-Valizadeh H, Guo R, Kucukseymen S, et al. Artifact reduction in free-breathing, free-running myocardial perfusion imaging with interleaved non-selective RF excitations. *Magn. Reson. Med.* 2021;86:954–963 doi: 10.1002/mrm.28765.
191. Chen X, Salerno M, Yang Y, Epstein FH. Motion-compensated compressed sensing for dynamic contrast-enhanced MRI using regional spatiotemporal sparsity and region tracking: block low-rank sparsity with motion-guidance (BLOSM). *Magn. Reson. Med.* 2014;72:1028–1038 doi: 10.1002/mrm.25018.
192. Nagel E, Klein C, Paetsch I, et al. Magnetic resonance perfusion measurements for the noninvasive detection of coronary artery disease. *Circulation* 2003;108:432–437 doi: 10.1161/01.CIR.0000080915.35024.A9.
193. Klocke FJ, Simonetti OP, Judd RM, et al. Limits of detection of regional differences in vasodilated flow in viable myocardium by first-pass magnetic resonance perfusion imaging. *Circulation* 2001;104:2412–2416 doi: 10.1161/hc4501.099306.
194. Zierler K. Indicator dilution methods for measuring blood flow, volume, and other properties of biological systems: a brief history and memoir. *Ann. Biomed. Eng.* 2000;28:836–848 doi: 10.1114/1.1308496.
195. Christian TF, Rettmann DW, Aletras AH, et al. Absolute myocardial perfusion in canines measured by using dual-bolus first-pass MR imaging. *Radiology* 2004;232:677–684 doi: 10.1148/RADIOL.2323030573.
196. Zierler KL. Theoretical basis of indicator dilution methods for measuring flow and volume. *Circ Res* 1962;10:393–407 doi: 10.1161/01.RES.10.3.393.
197. Jerosch-herold M, Wilke N, Stillman AE, et al. Magnetic resonance quantification of the myocardial perfusion reserve with a Fermi function model for constrained deconvolution Magnetic resonance quantification of the myocardial perfusion reserve with a Fermi function model for constrained deconvolution. *Med. Physiol.* 1998;25:73–84 doi: 10.1118/1.598163.
198. Kellman P, Hansen MS, Nielles-Vallespin S, et al. Myocardial perfusion cardiovascular magnetic resonance: optimized dual sequence and reconstruction for quantification. *J. Cardiovasc. Magn. Reson.* 2017;19:1–14 doi: 10.1186/s12968-017-0355-5.
199. Sánchez-González J, Fernandez-Jiménez R, Nothnagel ND, López-Martín G, Fuster V, Ibañez B. Optimization of dual-saturation single bolus acquisition for quantitative cardiac perfusion and myocardial blood flow maps. *J. Cardiovasc. Magn. Reson.* 2015;17:21 doi: 10.1186/s12968-015-0116-2.
200. Brix G, Schad LR, Deimling M, Lorenz WJ. Fast and precise T1 imaging using a TOMROP sequence. *Magn. Reson. Imaging* 1990;8:351–356 doi: 10.1016/0730-725X(90)90041-Y.

- 
201. Messroghli DR, Radjenovic A, Kozerke S, Higgins DM, Sivananthan MU, Ridgway JP. Modified look-locker inversion recovery (MOLLI) for high-resolution T<sub>1</sub> mapping of the heart. *Magn. Reson. Med.* 2004;52:141–146 doi: 10.1002/mrm.20110.
202. Hsu LY, Kellman P, Arai AE. Nonlinear myocardial signal intensity correction improves quantification of contrast-enhanced first-pass MR perfusion in humans. *J. Magn. Reson. Imaging* 2008;27:793–801 doi: 10.1002/jmri.21286.
203. Cernicanu A, Axel L. Theory-Based Signal Calibration with Single-Point T<sub>1</sub> Measurements for First-Pass Quantitative Perfusion MRI Studies. *Acad. Radiol.* 2006;13:686–693 doi: 10.1016/j.acra.2006.02.040.
204. Zierler KL. Theoretical Basis of Indicator-Dilution Methods For Measuring Flow and Volume. *Circ. Res.* 1962;10:393–407 doi: 10.1161/01.RES.10.3.393.
205. Pack NA, DiBella EVR. Comparison of myocardial perfusion estimates from dynamic contrast-enhanced magnetic resonance imaging with four quantitative analysis methods. *Magn. Reson. Med.* 2010;64:125–137 doi: 10.1002/mrm.22282.
206. Pelgrim GJ, Handayani A, Dijkstra H, et al. Quantitative Myocardial Perfusion with Dynamic Contrast-Enhanced Imaging in MRI and CT: Theoretical Models and Current Implementation. *Biomed Res. Int.* 2016;2016:1–12 doi: 10.1155/2016/1734190.
207. Schwab F, Ingrisich M, Marcus R, et al. Tracer kinetic modeling in myocardial perfusion quantification using MRI. *Magn. Reson. Med.* 2015;73:1206–1215 doi: 10.1002/mrm.25212.
208. Wissmann L. Quantitative 3D cardiac first-pass perfusion magnetic resonance imaging. PhD Thesis 2016;23813:193 doi: 10.3929/ETHZ-A-010863816.
209. Bassingthwaighe JB, Wang CY, Chan IS. Blood-tissue exchange via transport and transformation by capillary endothelial cells. *Circ. Res.* 1989;65:997–1020 doi: 10.1161/01.RES.65.4.997.
210. Sourbron SP, Buckley DL. Tracer kinetic modelling in MRI: Estimating perfusion and capillary permeability. *Phys. Med. Biol.* 2012;57 doi: 10.1088/0031-9155/57/2/R1.
211. Bassingthwaighe JB, Chan ISJ, Wang CY. Computationally efficient algorithms for convection-permeation-diffusion models for blood-tissue exchange. *Ann. Biomed. Eng.* 1992;20:687–725 doi: 10.1007/BF02368613.
212. Lingwood R. Absolute Quantification of Myocardial Perfusion Using Machine Learning - Semester Thesis. ETH Zürich; 2018.



- 
213. Hoh T, Spiczak J, Joyce T, Lingwood R, Dillinger H, Kozerke S. Rapid cardiac MR myocardial perfusion quantification using machine learning trained with synthetically generated sample data. In: Proc. Int. Symp. ESMRMB. ; 2019.
214. van Herten RLM, Chiribiri A, Breeuwer M, Veta M, Scannell CM. Physics-informed neural networks for myocardial perfusion MRI quantification. *Med. Image Anal.* 2022;78 doi: 10.1016/J.MEDIA.2022.102399.
215. Nijveldt R, Hofman MBM, Hirsch A, et al. Assessment of microvascular obstruction and prediction of short-term remodeling after acute myocardial infarction: Cardiac MR imaging study. *Radiology* 2009;250:363–370 doi: 10.1148/radiol.2502080739.
216. Klein C, Schmal TR, Nekolla SG, Schnackenburg B, Fleck E, Nagel E. Mechanism of late gadolinium enhancement in patients with acute myocardial infarction. *J. Cardiovasc. Magn. Reson.* 2007;9:653–658 doi: 10.1080/10976640601105614.
217. Bayer (Schweiz) AG. Swissmedic-genehmigte Fachinformation: Gadovist 1,0 Injektionslösung. <https://compendium.ch/product/121134-gadovist-1-0-inj-los/mpro>. Published 2022. Accessed February 16, 2023.
218. Look DC, Locker DR. Time Saving in Measurement of NMR and EPR Relaxation Times. *Rev. Sci. Instrum.* 2003;41:250 doi: 10.1063/1.1684482.
219. Peters DC, Appelbaum EA, Nezafat R, et al. Left ventricular infarct size, peri-infarct zone, and papillary scar measurements: A comparison of high-resolution 3D and conventional 2D late gadolinium enhancement cardiac MR. *J. Magn. Reson. Imaging* 2009;30:794–800 doi: 10.1002/JMRI.21897.
220. Goetti R, Kozerke S, Donati OF, et al. Acute, subacute, and chronic myocardial infarction: quantitative comparison of 2D and 3D late gadolinium enhancement MR imaging. *Radiology* 2011;259:704–711 doi: 10.1148/RADIOL.11102216.
221. Kühl HP, Papavasiliu TS, Beek AM, Hofman MBM, Heusen NS, Van Rossum AC. Myocardial viability: rapid assessment with delayed contrast-enhanced MR imaging with three-dimensional inversion-recovery prepared pulse sequence. *Radiology* 2004;230:576–582 doi: 10.1148/RADIOL.2302021120.
222. Foo TKF, Stanley DW, Castillo E, et al. Myocardial viability: breath-hold 3D MR imaging of delayed hyperenhancement with variable sampling in time. *Radiology* 2004;230:845–851 doi: 10.1148/RADIOL.2303021411.
223. Menon RG, Miller GW, Jeudy J, Rajagopalan S, Shin T. Free breathing three-dimensional late gadolinium enhancement cardiovascular magnetic resonance using outer volume suppressed projection navigators. *Magn. Reson. Med.* 2017;77:1533–1543 doi: 10.1002/MRM.26234.

- 
224. Bratis K, Henningsson M, Grigoratos C, et al. Image-navigated 3-dimensional late gadolinium enhancement cardiovascular magnetic resonance imaging: Feasibility and initial clinical results. *J. Cardiovasc. Magn. Reson.* 2017;19:1–9 doi: 10.1186/S12968-017-0418-7.
225. Kino A, Zuehlsdorff S, Sheehan JJ, et al. Three-dimensional phase-sensitive inversion-recovery turbo FLASH sequence for the evaluation of left ventricular myocardial scar. *AJR. Am. J. Roentgenol.* 2009;193 doi: 10.2214/AJR.08.1952.
226. Nguyen TD, Spincemaille P, Weinsaft JW, et al. A fast navigator-gated 3D sequence for delayed enhancement MRI of the myocardium: Comparison with breathhold 2D imaging. *J. Magn. Reson. Imaging* 2008;27:802–808 doi: 10.1002/JMRI.21296.
227. Toupin S, Pezel T, Bustin A, Cochet H. Whole-Heart High-Resolution Late Gadolinium Enhancement: Techniques and Clinical Applications. *J. Magn. Reson. Imaging* 2022;55:967–987 doi: 10.1002/JMRI.27732.
228. Bustin A, Sridi S, Gravinay P, et al. High-resolution Free-breathing late gadolinium enhancement Cardiovascular magnetic resonance to diagnose myocardial injuries following COVID-19 infection. *Eur. J. Radiol.* 2021;144:109960 doi: 10.1016/J.EJRAD.2021.109960.
229. Klem I, Heitner JF, Shah DJ, et al. Improved Detection of Coronary Artery Disease by Stress Perfusion Cardiovascular Magnetic Resonance With the Use of Delayed Enhancement Infarction Imaging. *J. Am. Coll. Cardiol.* 2006;47:1630–1638 doi: 10.1016/j.jacc.2005.10.074.
230. Amado LC, Gerber BL, Gupta SN, et al. Accurate and objective infarct sizing by contrast-enhanced magnetic resonance imaging in a canine myocardial infarction model. *J. Am. Coll. Cardiol.* 2004;44:2383–2389 doi: 10.1016/J.JACC.2004.09.020.
231. Hsu LY, Natanzon A, Kellman P, Hirsch GA, Aletras AH, Arai AE. Quantitative myocardial infarction on delayed enhancement MRI. Part I: Animal validation of an automated feature analysis and combined thresholding infarct sizing algorithm. *J. Magn. Reson. Imaging* 2006;23:298–308 doi: 10.1002/jmri.20496.
232. Schulz-Menger J, Bluemke DA, Bremerich J, et al. Standardized image interpretation and post processing in cardiovascular magnetic resonance: Society for Cardiovascular Magnetic Resonance (SCMR) board of trustees task force on standardized post processing. *J. Cardiovasc. Magn. Reson.* 2013;15 doi: 10.1186/1532-429X-15-35.
233. Heiberg E, Engblom H, Carlsson M, et al. Infarct quantification with cardiovascular magnetic resonance using “standard deviation from remote” is unreliable: validation in multi-centre multi-vendor data. *J. Cardiovasc. Magn. Reson.* 2022;24:1–12 doi: 10.1186/S12968-022-00888-8/.

- 
234. Flett AS, Hasleton J, Cook C, et al. Evaluation of techniques for the quantification of myocardial scar of differing etiology using cardiac magnetic resonance. *JACC. Cardiovasc. Imaging* 2011;4:150–156 doi: 10.1016/J.JCMG.2010.11.015.
235. Karim R, Bhagirath P, Claus P, et al. Evaluation of state-of-the-art segmentation algorithms for left ventricle infarct from late Gadolinium enhancement MR images. *Med. Image Anal.* 2016;30:95–107 doi: 10.1016/j.media.2016.01.004.
236. Mikami Y, Kolman L, Joncas SX, et al. Accuracy and reproducibility of semi-automated late gadolinium enhancement quantification techniques in patients with hypertrophic cardiomyopathy. *J. Cardiovasc. Magn. Reson.* 2014;16 doi: 10.1186/s12968-014-0085-x.
237. Carminati MC, Boniotti C, Fusini L, et al. Comparison of Image Processing Techniques for Nonviable Tissue Quantification in Late Gadolinium Enhancement Cardiac Magnetic Resonance Images. *J. Thorac. Imaging* 2016;31:168–176 doi: 10.1097/RTI.0000000000000206.
238. Ibanez B, Aletras AH, Arai AE, et al. Cardiac MRI Endpoints in Myocardial Infarction Experimental and Clinical Trials: JACC Scientific Expert Panel. *J. Am. Coll. Cardiol.* 2019;74:238 doi: 10.1016/J.JACC.2019.05.024.
239. Zenger B, Cates J, Morris A, et al. A Practical Algorithm for Improving Localization and Quantification of Left Ventricular Scar. *Comput. Cardiol. (2010)*. 2014;2014:105–108.
240. Engblom H, Tufvesson J, Jablonowski R, et al. A new automatic algorithm for quantification of myocardial infarction imaged by late gadolinium enhancement cardiovascular magnetic resonance: experimental validation and comparison to expert delineations in multi-center, multi-vendor patient data. *J. Cardiovasc. Magn. Reson.* 2016;18 doi: 10.1186/S12968-016-0242-5.
241. Tao Q, Piers SRD, Lamb HJ, Van Der Geest RJ. Automated left ventricle segmentation in late gadolinium-enhanced MRI for objective myocardial scar assessment. *J. Magn. Reson. Imaging* 2015;42:390–399 doi: 10.1002/JMRI.24804.
242. Leong CO, Lim E, Tan LK, et al. Segmentation of left ventricle in late gadolinium enhanced MRI through 2D-4D registration for infarct localization in 3D patient-specific left ventricular model. *Magn. Reson. Med.* 2019;81:1385–1398 doi: 10.1002/MRM.27486.
243. Kurzendorfer T, Forman C, Schmidt M, Tillmanns C, Maier A, Brost A. Fully automatic segmentation of left ventricular anatomy in 3-D LGE-MRI. *Comput. Med. Imaging Graph.* 2017;59:13–27 doi: 10.1016/J.COMPMEDIMAG.2017.05.001.
244. Long J, Shelhamer E, Darrell T. Fully convolutional networks for semantic segmentation. In: 2015 IEEE Conference on Computer Vision and Pattern Recognition (CVPR). ; 2015. pp. 3431–3440. doi: 10.1109/CVPR.2015.7298965.

- 
245. Ronneberger O, Fischer P, Brox T. U-Net: Convolutional Networks for Biomedical Image Segmentation. In: Navab N, Hornegger J, Wells WM, Frangi AF, editors. Medical Image Computing and Computer-Assisted Intervention -- MICCAI 2015. Cham: Springer International Publishing; 2015. pp. 234–241. doi: 10.1007/978-3-319-24574-4\_28.
246. He K, Zhang X, Ren S, Sun J. Deep Residual Learning for Image Recognition. ArXiv e-prints 2015 doi: 10.48550/arXiv.1512.03385.
247. Lin T-Y, Goyal P, Girshick RB, He K, Dollár P. Focal Loss for Dense Object Detection. CoRR 2017;abs/1708.0 doi: 10.48550/arXiv.1708.02002.
248. Srivastava N, Hinton G, Krizhevsky A, Sutskever I, Salakhutdinov R. Dropout: A Simple Way to Prevent Neural Networks from Overfitting. J. Mach. Learn. Res. 2014;15:1929–1958.
249. Wang G, Li W, Aertsen M, Deprest J, Ourselin S, Vercauteren T. Aleatoric uncertainty estimation with test-time augmentation for medical image segmentation with convolutional neural networks. Neurocomputing 2019;338:34–45 doi: 10.1016/J.NEUCOM.2019.01.103.
250. Peng P, Lekadir K, Gooya A, Shao L, Petersen SE, Frangi AF. A review of heart chamber segmentation for structural and functional analysis using cardiac magnetic resonance imaging. Magn. Reson. Mater. Physics, Biol. Med. 2016 292 2016;29:155–195 doi: 10.1007/S10334-015-0521-4.
251. Huttenlocher DP, Klanderman GA, Rucklidge WJ. Comparing images using the Hausdorff distance. IEEE Trans. Pattern Anal. Mach. Intell. 1993;15:850–863 doi: 10.1109/34.232073.
252. Lalande A, Chen Z, Pommier T, et al. Deep learning methods for automatic evaluation of delayed enhancement-MRI. The results of the EMIDEC challenge. Med. Image Anal. 2022;79 doi: 10.1016/J.MEDIA.2022.102428.
253. Fahmy AS, Rowin EJ, Chan RH, Manning WJ, Maron MS, Nezafat R. Improved Quantification of Myocardium Scar in Late Gadolinium Enhancement Images: Deep Learning Based Image Fusion Approach. J. Magn. Reson. Imaging 2021;54:303–312 doi: 10.1002/JMRI.27555.
254. Moccia S, Banali R, Martini C, et al. Development and testing of a deep learning-based strategy for scar segmentation on CMR-LGE images. Magn. Reson. Mater. Physics, Biol. Med. 2019;32:187–195 doi: 10.1007/s10334-018-0718-4.
255. Fahmy AS, Neisius U, Chan RH, et al. Three-dimensional deep convolutional neural networks for automated myocardial scar quantification in hypertrophic cardiomyopathy: A multicenter multivendor study. Radiology 2020;294:52–60 doi: 10.1148/radiol.2019190737.

- 
256. Zabihollahy F, Rajchl M, White JA, Ukwatta E. Fully automated segmentation of left ventricular scar from 3D late gadolinium enhancement magnetic resonance imaging using a cascaded multi-planar U-Net (CMPU-Net). *Med. Phys.* 2020;47:1645–1655 doi: 10.1002/MP.14022.
257. Brahim K, Arega TW, Boucher A, Bricq S, Sakly A, Meriaudeau F. An Improved 3D Deep Learning-Based Segmentation of Left Ventricular Myocardial Diseases from Delayed-Enhancement MRI with Inclusion and Classification Prior Information U-Net (ICPIU-Net). *Sensors* 2022;22:2084 doi: 10.3390/S22062084.
258. Popescu DM, Abramson HG, Yu R, et al. Anatomically informed deep learning on contrast-enhanced cardiac magnetic resonance imaging for scar segmentation and clinical feature extraction. *Cardiovasc. Digit. Heal. J.* 2022;3:2–13 doi: 10.1016/J.CVDHJ.2021.11.007.
259. Nagel E, Greenwood JP, McCann GP, et al. Magnetic Resonance Perfusion or Fractional Flow Reserve in Coronary Disease. *N. Engl. J. Med.* 2019;380:2418–2428 doi: 10.1056/NEJMoa1716734.
260. Jerosch-Herold M, Seethamraju RT, Swingen CM, Wilke NM, Stillman AE. Analysis of myocardial perfusion MRI. *J. Magn. Reson. Imaging* 2004;19:758–770 doi: 10.1002/jmri.20065.
261. Wilke N, Jerosch-Herold M, Stillman AE, et al. Concepts of myocardial perfusion imaging in magnetic resonance imaging. *Magn. Reson. Q.* 1994;10:249–286.
262. Biglands JD, Ibraheem M, Magee DR, Radjenovic A, Plein S, Greenwood JP. Quantitative Myocardial Perfusion Imaging Versus Visual Analysis in Diagnosing Myocardial Ischemia: A CE-MARC Substudy. *JACC. Cardiovasc. Imaging* 2018;11:711–718 doi: 10.1016/j.jcmg.2018.02.019.
263. Hsu LY, Jacobs M, Benovoy M, et al. Diagnostic Performance of Fully Automated Pixel-Wise Quantitative Myocardial Perfusion Imaging by Cardiovascular Magnetic Resonance. *JACC Cardiovasc. Imaging* 2018;11:697–707 doi: 10.1016/j.jcmg.2018.01.005.
264. Patel AR, Antkowiak PF, Nandalur KR, et al. Assessment of advanced coronary artery disease: advantages of quantitative cardiac magnetic resonance perfusion analysis. *J. Am. Coll. Cardiol.* 2010;56:561–569 doi: 10.1016/j.jacc.2010.02.061.
265. Zorach B, Shaw PW, Bourque J, et al. Quantitative cardiovascular magnetic resonance perfusion imaging identifies reduced flow reserve in microvascular coronary artery disease. *J. Cardiovasc. Magn. Reson. Off. J. Soc. Cardiovasc. Magn. Reson.* 2018;20:14 doi: 10.1186/s12968-018-0435-1.
266. Camaioni C, Knott KD, Augusto JB, et al. Inline perfusion mapping provides insights into the disease mechanism in hypertrophic cardiomyopathy. *Heart* 2020;106:824–829 doi: 10.1136/heartjnl-2019-315848.

- 
267. Kozerke S, Tsao J, Razavi R, Boesiger P. Accelerating cardiac cine 3D imaging using k-t BLAST. *Magn. Reson. Med.* 2004;52:19–26 doi: 10.1002/mrm.20145.
268. Tsao J, Kozerke S. MRI temporal acceleration techniques. *J. Magn. Reson. Imaging* 2012;36:543–560 doi: 10.1002/jmri.23640.
269. Vitanis V, Manka R, Boesiger P, Pedersen H, Kozerke S. High resolution 3D cardiac perfusion imaging using compartment based k-t PCA. *J. Cardiovasc. Magn. Reson.* 2010;12:174–176 doi: 10.1186/1532-429X-12-S1-P107.
270. Naresh NK, Haji-Valizadeh H, Aouad PJ, et al. Accelerated, first-pass cardiac perfusion pulse sequence with radial k-space sampling, compressed sensing, and k-space weighted image contrast reconstruction tailored for visual analysis and quantification of myocardial blood flow. *Magn. Reson. Med.* 2019;81:2632–2643 doi: 10.1002/mrm.27573.
271. Pflugi S, Roujol S, Akçakaya M, et al. Accelerated cardiac MR stress perfusion with radial sampling after physical exercise with an MR-compatible supine bicycle ergometer. *Magn. Reson. Med.* 2015;74:384–395 doi: 10.1002/mrm.25405.
272. Neimatallah MA, Chenevert TL, Carlos RC, et al. Subclavian MR Arteriography: Reduction of Susceptibility Artifact with Short Echo Time and Dilute Gadopentetate Dimeglumine. *Radiology* 2000;217:581–586 doi: 10.1148/radiology.217.2.r00oc37581.
273. Kholmovski EG, DiBella EVR. Perfusion MRI with radial acquisition for arterial input function assessment. *Magn. Reson. Med.* 2007;57:821–827 doi: 10.1002/mrm.21210.
274. Batchelor PG, Atkinson D, Irrazaval P, Hill DLG, Hajnal J, Larkman D. Matrix description of general motion correction applied to multishot images. *Magn. Reson. Med.* 2005;54:1273–1280 doi: 10.1002/mrm.20656.
275. Akçakaya M, Basha TA, Pflugi S, et al. Localized spatio-temporal constraints for accelerated CMR perfusion. *Magn. Reson. Med.* 2014;72:629–639 doi: 10.1002/mrm.24963.
276. Liu J, Jin S, Li Q, et al. Motion compensation combining with local low rank regularization for low dose dynamic CT myocardial perfusion reconstruction. *Phys. Med. Biol.* 2021;66 doi: 10.1088/1361-6560/ac0f2f.
277. Cruz G, Qi H, Jaubert O, et al. Generalized low-rank nonrigid motion-corrected reconstruction for MR fingerprinting. *Magn. Reson. Med.* 2022;87:746–763 doi: 10.1002/mrm.29027.
278. Milidonis X, Franks R, Schneider T, et al. Influence of the arterial input sampling location on the diagnostic accuracy of cardiovascular magnetic resonance stress myocardial perfusion quantification. *J. Cardiovasc. Magn. Reson.* 2021;23:35 doi: 10.1186/s12968-021-00733-4.

- 
279. Liu B, Zou YM, Ying L. Sparsesense: Application of compressed sensing in parallel MRI. In: 2008 International Conference on Information Technology and Applications in Biomedicine. ; 2008. pp. 127–130. doi: 10.1109/ITAB.2008.4570588.
280. Liang D, Liu B, Wang J, Ying L. Accelerating SENSE using compressed sensing. *Magn. Reson. Med.* 2009;62:1574–1584 doi: <https://doi.org/10.1002/mrm.22161>.
281. Ogg RJ, Kingsley PB, Taylor JS. WET, a T1- and B1-Insensitive Water-Suppression Method for in Vivo Localized<sup>1</sup>H NMR Spectroscopy. *J. Magn. Reson. Ser. B* 1994;104:1–10 doi: 10.1006/jmrb.1994.1048.
282. Ravishankar S, Ye JC, Fessler JA. Image Reconstruction: From Sparsity to Data-Adaptive Methods and Machine Learning. *Proc. IEEE* 2020;108:86–109 doi: 10.1109/JPROC.2019.2936204.
283. Uecker M, Lai P, Murphy MJ, et al. ESPIRiT - An eigenvalue approach to autocalibrating parallel MRI: Where SENSE meets GRAPPA. *Magn. Reson. Med.* 2014;71:990–1001 doi: 10.1002/mrm.24751.
284. Otazo R, Kim D, Axel L, Sodickson DK. Combination of compressed sensing and parallel imaging for highly accelerated first-pass cardiac perfusion MRI. *Magn. Reson. Med.* 2010;64:767–776 doi: <https://doi.org/10.1002/mrm.22463>.
285. Hollingsworth KG. Reducing acquisition time in clinical MRI by data undersampling and compressed sensing reconstruction. *Phys. Med. Biol.* 2015;60:R297–R322 doi: 10.1088/0031-9155/60/21/r297.
286. Tamir JI, F O, Cheng JY Uecker M, and Lustig M. Generalized magnetic resonance image reconstruction using the Berkeley advanced reconstruction toolbox. In: Proceedings of the ISMRM 2016 data sampling and image reconstruction workshop. ; 2016. p. 9660006.
287. Wissmann L, Santelli C, Segars WP, Kozerke S. MRXCAT: Realistic numerical phantoms for cardiovascular magnetic resonance. *J. Cardiovasc. Magn. Reson.* 2014;16 doi: 10.1186/s12968-014-0063-3.
288. Ferrazzi G, McElroy S, Neji R, et al. All-systolic first-pass myocardial rest perfusion at a long saturation time using simultaneous multi-slice imaging and compressed sensing acceleration. *Magn. Reson. Med.* 2021;86:663–676 doi: 10.1002/mrm.28712.
289. Akbudak E, Norberg RE, Conturo TE. Contrast-agent phase effects: An experimental system for analysis of susceptibility, concentration, and bolus input function kinetics. *Magn. Reson. Med.* 1997;38:990–1002 doi: 10.1002/mrm.1910380619.
290. Di Bella EVR, Parker DL, Sinusas AJ. On the dark rim artifact in dynamic contrast-enhanced MRI myocardial perfusion studies. *Magn. Reson. Med.* 2005;54:1295–1299 doi: 10.1002/mrm.20666.

- 
291. Kellman P, Hansen MS, Nielles-Vallespin S, et al. Myocardial perfusion cardiovascular magnetic resonance: optimized dual sequence and reconstruction for quantification. *J. Cardiovasc. Magn. Reson.* 2017;19:43 doi: 10.1186/s12968-017-0355-5.
292. Walheim J, Dillinger H, Kozerke S. Multipoint 5D flow cardiovascular magnetic resonance - Accelerated cardiac- and respiratory-motion resolved mapping of mean and turbulent velocities. *J. Cardiovasc. Magn. Reson.* 2019;21:1–13 doi: 10.1186/s12968-019-0549-0.
293. Buehrer M, Pruessmann KP, Boesiger P, Kozerke S. Array compression for MRI with large coil arrays. *Magn. Reson. Med.* 2007;57:1131–1139 doi: 10.1002/mrm.21237.
294. Siebes M. Coronary flow and physiology beyond the stenosis. *Hear. Metabol.* 2013;58:4–9.
295. Glover DK, Ruiz M, Takehana K, et al. Pharmacological stress myocardial perfusion imaging with the potent and selective A(2A) adenosine receptor agonists ATL193 and ATL146e administered by either intravenous infusion or bolus injection. *Circulation* 2001;104:1181–1187 doi: 10.1161/HC3601.093983.
296. Crystal GJ. Carbon Dioxide and the Heart: Physiology and Clinical Implications. *Anesth. Analg.* 2015;121:610–623 doi: 10.1213/ANE.0000000000000820.
297. Feigl EO. Coronary physiology. *Physiol. Rev.* 1983;63:1–205 doi: 10.1152/PHYSREV.1983.63.1.1.
298. Barcroft J, Dixon WE. The gaseous metabolism of the mammalian heart. *J. Physiol.* 1907;35:182–204 doi: 10.1113/JPHYSIOL.1907.SP001189.
299. Hoffman WE, Albrecht RF, Ripper R, Jonjev ZS. Brain compared to heart tissue oxygen pressure during changes in arterial carbon dioxide in the dog. *J. Neurosurg. Anesthesiol.* 2001;13:303–309 doi: 10.1097/00008506-200110000-00004.
300. Ledingham IMA, McBride TI, Parratt JR, Vance JP. The effect of hypercapnia on myocardial blood flow and metabolism. *J. Physiol.* 1970;210:87 doi: 10.1113/JPHYSIOL.1970.SP009197.
301. Alexander CS, Liu SM. Effect of hypercapnia and hypocapnia on myocardial blood flow and performance in anaesthetized dogs. *Cardiovasc. Res.* 1976;10:341–348 doi: 10.1093/CVR/10.3.341.
302. Kwiatkowski G, Kozerke S. Quantitative myocardial first-pass perfusion imaging of CO<sub>2</sub>-induced vasodilation in rats. *NMR Biomed.* 2021;34:e4593 doi: 10.1002/NBM.4593.
303. Powers ER, Bannerman KS, Fitz-James I, Cannon PJ. Effect of elevations of coronary artery partial pressure of carbon dioxide (PCO<sub>2</sub>) on coronary blood flow. *J. Am. Coll. Cardiol.* 1986;8:1175–1181 doi: 10.1016/S0735-1097(86)80398-9.
304. Case RB, Greenberg H. The response of canine coronary vascular resistance to local alterations in coronary arterial P CO<sub>2</sub>. *Circ. Res.* 1976;39:558–566 doi: 10.1161/01.RES.39.4.558.



- 
305. Eckenhoff J, Hafkenschiel J, Landmesser C. The coronary circulation in the dog. *Am. J. Physiol.* 1947;148:582–596 doi: 10.1152/AJPLEGACY.1947.148.3.582.
306. Green HD, Wégria R. Effects of asphyxia, anoxia and myocardial ischemia on the coronary blood flow. *Am. J. Physiol.* Content 1941;135:271–280 doi: 10.1152/AJPLEGACY.1941.135.2.271.
307. Beaudin AE, Brugniaux J V., Vöhringer M, et al. Cerebral and myocardial blood flow responses to hypercapnia and hypoxia in humans. *Am. J. Physiol. - Hear. Circ. Physiol.* 2011;301:1678–1686 doi: 10.1152/AJPHEART.00281.2011.
308. Tzou WS, Korcarz CE, Aeschlimann SE, Morgan BJ, Skatrud JB, Stein JH. Coronary Flow Velocity Changes in Response to Hypercapnia: Assessment by Transthoracic Doppler Echocardiography. *J. Am. Soc. Echocardiogr.* 2007;20:421 doi: 10.1016/J.ECHO.2006.10.002.
309. Kazmaier S, Weyland A, Buhre W, et al. Effects of Respiratory Alkalosis and Acidosis on Myocardial Blood Flow and Metabolism in Patients with Coronary Artery Disease. *Anesthesiology* 1998;89:831–837 doi: 10.1097/00000542-199810000-00006.
310. Yokoyama I, Inoue Y, Kinoshita T, Itoh H, Kanno I, Iida H. Heart and brain circulation and CO<sub>2</sub> in healthy men. *Acta Physiol.* 2008;193:303–308 doi: 10.1111/J.1748-1716.2008.01846.X.
311. Momen A, Mascarenhas V, Gahremanpour A, et al. Coronary blood flow responses to physiological stress in humans. *Am. J. Physiol. Heart Circ. Physiol.* 2009;296 doi: 10.1152/AJPHEART.01075.2007.
312. Pelletier-Galarneau M, DeKemp RA, Hunter CRRN, et al. Effects of Hypercapnia on Myocardial Blood Flow in Healthy Human Subjects. *J. Nucl. Med.* 2018;59:100–106 doi: 10.2967/JNUMED.117.194308.
313. Yang HJ, Oksuz I, Dey D, et al. Accurate needle-free assessment of myocardial oxygenation for ischemic heart disease in canines using magnetic resonance imaging. *Sci. Transl. Med.* 2019;11:4407 doi: 10.1126/SCITRANSLMED.AAT4407/.
314. Fischer K, Guensch DP, Friedrich MG. Response of myocardial oxygenation to breathing manoeuvres and adenosine infusion. *Eur. Hear. J. - Cardiovasc. Imaging* 2015;16:395–401 doi: 10.1093/EHJCI/JEU202.
315. Yang HJ, Dey D, Sykes J, et al. Arterial CO<sub>2</sub> as a Potent Coronary Vasodilator: A Preclinical PET/MR Validation Study with Implications for Cardiac Stress Testing. *J. Nucl. Med.* 2017;58:953–960 doi: 10.2967/JNUMED.116.185991.
316. Elias AN, Wesley RC, Gordon IL, Pandian MR, Vaziri ND. Effects of adenosine infusion on renal function, plasma ANP and ADH concentrations and central hemodynamics in anesthetized pigs. *Gen. Pharmacol. Vasc. Syst.* 1997;28:429–433 doi: 10.1016/S0306-3623(96)00242-X.

- 
317. Husso M, Nissi MJ, Kuivanen A, et al. Quantification of porcine myocardial perfusion with modified dual bolus MRI-A prospective study with a PET reference. *BMC Med. Imaging* 2019;19:1–11 doi: 10.1186/S12880-019-0359-8.
318. Slessarev M, Han J, Mardimae A, et al. Prospective targeting and control of end-tidal CO<sub>2</sub> and O<sub>2</sub> concentrations. *J. Physiol.* 2007;581:1207 doi: 10.1113/JPHYSIOL.2007.129395.
319. Fierstra J, Sobczyk O, Battisti-Charbonney A, et al. Measuring cerebrovascular reactivity: what stimulus to use? *J. Physiol.* 2013;591:5809 doi: 10.1113/JPHYSIOL.2013.259150.
320. Ito S, Mardimae A, Han J, et al. Non-invasive prospective targeting of arterial P in subjects at rest. *J. Physiol.* 2008;586:3675–3682 doi: 10.1113/JPHYSIOL.2008.154716.
321. Hoh T, Vishnevskiy V, Polacin M, Manka R, Fuetterer M, Kozerke S. Free-breathing motion-informed locally low-rank quantitative 3D myocardial perfusion imaging. *Magn. Reson. Med.* 2022;88:1575–1591 doi: 10.1002/mrm.29295.
322. Kassam SI, Lu C, Buckley N, Lee RMKW. The mechanisms of propofol-induced vascular relaxation and modulation by perivascular adipose tissue and endothelium. *Anesth. Analg.* 2011;112:1339–1345 doi: 10.1213/ANE.0B013E318215E094.
323. Schöffmann G, Winter P, Palme R, Pollak A, Trittenwein G, Golej J. Haemodynamic changes and stress responses of piglets to surgery during total intravenous anaesthesia with propofol and fentanyl. *Lab. Anim.* 2009;43:243–248 doi: 10.1258/LA.2008.0080026.
324. Liu P, De Vis JB, Lu H. Cerebrovascular reactivity (CVR) MRI with CO<sub>2</sub> challenge: A technical review. *Neuroimage* 2019;187:104–115 doi: 10.1016/J.NEUROIMAGE.2018.03.047.
325. Phillis JW, Song D, O'Regan MH. Mechanisms involved in coronary artery dilatation during respiratory acidosis in the isolated perfused rat heart. *Basic Res. Cardiol.* 2000;95:93–97 doi: 10.1007/S003950050169.
326. Kim RJ, Wu E, Rafael A, et al. The use of contrast-enhanced magnetic resonance imaging to identify reversible myocardial dysfunction. *N. Engl. J. Med.* 2000;343:1445–1453 doi: 10.1056/NEJM200011163432003.
327. Pi SH, Kim SM, Choi JO, et al. Prognostic value of myocardial strain and late gadolinium enhancement on cardiovascular magnetic resonance imaging in patients with idiopathic dilated cardiomyopathy with moderate to severely reduced ejection fraction. *J. Cardiovasc. Magn. Reson.* 2018;20 doi: 10.1186/s12968-018-0466-7.

- 
328. Chan RH, Maron BJ, Olivotto I, et al. Prognostic value of quantitative contrast-enhanced cardiovascular magnetic resonance for the evaluation of sudden death risk in patients with hypertrophic cardiomyopathy. *Circulation* 2014;130:484–495 doi: 10.1161/CIRCULATIONAHA.113.007094.
329. Spiewak M, Malek LA, Misko J, et al. Comparison of different quantification methods of late gadolinium enhancement in patients with hypertrophic cardiomyopathy. *Eur. J. Radiol.* 2010;74 doi: 10.1016/J.EJRAD.2009.05.035.
330. Liu D, Ma X, Liu J, et al. Quantitative analysis of late gadolinium enhancement in hypertrophic cardiomyopathy: comparison of diagnostic performance in myocardial fibrosis between gadobutrol and gadopentetate dimeglumine. *Int. J. Cardiovasc. Imaging* 2017;33:1191–1200 doi: 10.1007/s10554-017-1101-7.
331. Klem I, Heiberg E, Van Assche L, et al. Sources of variability in quantification of cardiovascular magnetic resonance infarct size - reproducibility among three core laboratories. *J. Cardiovasc. Magn. Reson.* 2017;19:62 doi: 10.1186/s12968-017-0378-y.
332. Block KT. Subtle pitfalls in the search for faster medical imaging. *Proc. Natl. Acad. Sci.* 2022;119:e2203040119 doi: 10.1073/PNAS.2203040119.
333. Nies HMJM, Gommers S, Bijvoet GP, et al. Histopathological validation of semi-automated myocardial scar quantification techniques for dark-blood late gadolinium enhancement magnetic resonance imaging. *Eur. Hear. journal. Cardiovasc. Imaging* 2022 doi: 10.1093/ehjci/jeac107.
334. Iglovikov V, Shvets A. TerausNet: U-Net with VGG11 Encoder Pre-Trained on ImageNet for Image Segmentation. *ArXiv e-prints* 2018 doi: 10.48550/arXiv.1801.05746.
335. Iakubovskii P. Segmentation Models Pytorch. GitHub repository. [https://github.com/qubvel/segmentation\\_models.pytorch](https://github.com/qubvel/segmentation_models.pytorch). Published 2019. Accessed September 15, 2022.
336. Bian C, Yang X, Ma J, et al. Pyramid Network with Online Hard Example Mining for Accurate Left Atrium Segmentation. doi: 10.48550/arXiv.1812.05802.
337. Shvets A, Rakhlin A, Kalinin AA, Iglovikov V. Automatic Instrument Segmentation in Robot-Assisted Surgery Using Deep Learning. *Proc. - 17th IEEE Int. Conf. Mach. Learn. Appl. ICMLA 2018* 2018:624–628 doi: 10.1109/ICMLA.2018.00100.
338. Dice LR. Measures of the Amount of Ecologic Association Between Species. *Ecology* 1945;26:297–302 doi: 10.2307/1932409.
339. Wang Y, Zhang J. CMMCSegNet: Cross-Modality Multicascade Indirect LGE Segmentation on Multimodal Cardiac MR. *Comput. Math. Methods Med.* 2021;2021 doi: 10.1155/2021/9942149.

- 
340. Zhuang X. Multivariate Mixture Model for Myocardial Segmentation Combining Multi-Source Images. *IEEE Trans. Pattern Anal. Mach. Intell.* 2019;41:2933–2946 doi: 10.1109/TPAMI.2018.2869576.
341. Munoz C, Qi H, Cruz G, Küstner T, Botnar RM, Prieto C. Self-supervised learning-based diffeomorphic non-rigid motion estimation for fast motion-compensated coronary MR angiography. *Magn. Reson. Imaging* 2022;85:10–18 doi: 10.1016/J.MRI.2021.10.004.
342. Qi H, Hajhosseiny R, Cruz G, et al. End-to-end deep learning nonrigid motion-corrected reconstruction for highly accelerated free-breathing coronary MRA. *Magn. Reson. Med.* 2021;86:1983–1996 doi: 10.1002/MRM.28851.
343. Xue H, Davies RH, Brown LAE, et al. Automated inline analysis of myocardial perfusion mri with deep learning. *Radiol. Artif. Intell.* 2020;2:1–8 doi: 10.1148/RYAI.2020200009.
344. Correia T, Schneider T, Chiribiri A. Model-Based Reconstruction for Highly Accelerated First-Pass Perfusion Cardiac MRI. *Lect. Notes Comput. Sci.* 2019;11765 LNCS:514–522 doi: 10.1007/978-3-030-32245-8\_57.
345. Ladrova M, Martinek R, Nedoma J, et al. Monitoring and Synchronization of Cardiac and Respiratory Traces in Magnetic Resonance Imaging: A Review. *IEEE Rev. Biomed. Eng.* 2022;15:200–221 doi: 10.1109/RBME.2021.3055550.
346. Bahadir CD, Dalca A V, Sabuncu MR. Learning-based Optimization of the Under-sampling Pattern in MRI. 2019 doi: 10.48550/ARXIV.1901.01960.
347. Seeger M, Nickisch H, Pohmann R, Schölkopf B. Optimization of k-space trajectories for compressed sensing by Bayesian experimental design. *Magn. Reson. Med.* 2010;63:116–126 doi: 10.1002/MRM.22180.
348. Vishnevskiy V, Hoh T, Kozerke S. Learning Time-Adaptive Data-Driven Sampling Pattern for Accelerated 3D Myocardial Perfusion Imaging. In: *Proc. Int. Symp. Magn. Reson. Med.* ; 2022.
349. Huang W, Li H, Pan J, Cruz G, Rueckert D, Hammernik K. Neural Implicit k-Space for Binning-free Non-Cartesian Cardiac MR Imaging. 2022 doi: 10.48550/ARXIV.2212.08479.
350. Valindria V, Lavdas I, Bai W, Kamnitsas K, Aboagye EO, Rockall AG, Rueckert D, Glocker B. Reverse Classification Accuracy: Predicting Segmentation Performance in the Absence of Ground Truth. *Trans Med Imaging IEEE.* 2017;1. doi:10.1109/TMI.2017.
351. Robinson R, Valindria V, Bai W, et al. Automatic quality control of cardiac mri segmentation in large-scale population imaging BT - *Medical Image Computing and Computer Assisted Intervention - MICCAI 2017*. In: Cham: Springer; 2017. doi: 10.1007/978-3-319-66182-7\_82.

- 
352. Robinson R, Oktay O, Bai W, et al. Real-time Prediction of Segmentation Quality. 2018 doi: 10.48550/ARXIV.1806.06244.
353. Vaswani A, Shazeer N, Parmar N, et al. Attention Is All You Need. *Adv. Neural Inf. Process. Syst.* 2017:5999–6009 doi: 10.48550/ARXIV.1706.03762.
354. Phuong M, Hutter M. Formal Algorithms for Transformers. 2022 doi: 10.48550/ARXIV.2207.09238.
355. Gao Y, Zhou M, Metaxas D. UTNet: A Hybrid Transformer Architecture for Medical Image Segmentation. 2021 doi: 10.48550/ARXIV.2107.00781.
356. Hatamizadeh A, Nath V, Tang Y, Yang D, Roth H, Xu D. Swin UNETR: Swin Transformers for Semantic Segmentation of Brain Tumors in MRI Images. 2022 doi: 10.48550/ARXIV.2201.01266.
357. Karimi D, Vasylechko SD, Gholipour A. Convolution-Free Medical Image Segmentation Using Transformers. In: de Bruijne M, Cattin PC, Cotin S, et al., editors. *Medical Image Computing and Computer Assisted Intervention -- MICCAI 2021*. Cham: Springer International Publishing; 2021. pp. 78–88. doi: 10.48550/arXiv.2102.13645.
358. Ding Y, Xie W, Wong KKL, Liao Z. DE-MRI myocardial fibrosis segmentation and classification model based on multi-scale self-supervision and transformer. 2022;226:107049 doi: 10.1016/J.CMPB.2022.107049.

# Acknowledgements

A PhD thesis is not a journey that is embarked on lightheartedly and could not have been successful without the generous support and countless contributions from various people in- and outside the Institute for Biomedical Engineering at ETH Zurich.

First and foremost, I would like to thank Prof. Sebastian Kozerke, who made this thesis possible by providing guidance, exceptional infrastructure and the necessary trust in my abilities. I am deeply grateful for his everlasting support especially during challenging times - his availability was unparalleled.

Furthermore, I would like to thank Prof. Dominik von Elverfeldt for being the co-examiner of this thesis.

Additionally, I want to express my deep gratitude to Maximilian Fütterer for taking me under his wing, sharing his knowledge about pulse programming, cardiac perfusion and in vivo MRI imaging. His opinion was not only highly valued and appreciated but also always available outside regular working hours. Thank you for helping me to navigate through shallow waters, many scientific as well as casual conversations.

I also want to thank Valeriy Vishnevskiy for sharing his vast insights into image reconstruction theory that sometimes seem to be from a different planet. His kind and generous support in image reconstruction and implementation was motivating and dearly appreciated.

Further, I especially want to thank...

...Jonathan Weine for leading by example in coding matters, his kind and altruistic willingness to provide help when needed.

...Thomas Joyce for sharing his knowledge on machine learning and his wit that kept spirits high at all times.

...the clinical CMR team, led by Robert Manka: Jochen von Spiczak, Mareike Cramer, Rabea Schlenker and Verena Wilzeck along with the entire staff at MR Zentrum Süd for their guidance and necessary hands-on support. Alexander Gotschy deserves a special mentioning for holding my hand during my first contrast enhanced CMR scan and for sharing his knowledge on cardiology. I'm especially grateful to Mex Polacin for her help with volunteer scans.

...the entire Corflow/Minoca team: Nikola Cesarovic, Miriam Weisskopf, Oliver Bludau, Marko Canic, Mareike Kron, Mareike Cramer, Conny Waschkies, Melanie Hierweger, Nina Trimmel, Andrea Leuthardt and Thorald Stolte for long but always entertaining hours behind the scanner. In this context, I want to thank Christian Stoeck for sharing his tremendous experience in experimental and in-vivo MR imaging as well as his great camaraderie on and off the water.

I want to specially mention and thank Jorn Fierstra and Bart Thompson for not only granting access to their precious Respiract device but also for their outstanding personal support and advice during the hypercapnia experiments.

...the CMR Predict team: Maximilian Fütterer, Julia Trächtler, Andreas Dounas, Jonas Steinhauser, Mex Polacin and Jochen von Spiczak for showing great teamwork and letting me take part in it.

...Roger Lüchinger for his always joyful and pragmatic support in and around the scanner room.

...Gérard Crelier and Martin Bühner for sharing their knowledge about the pulse programming environment and quick support with their valuable software tools.

...Isabel Spiess for her entrusted administrative groundwork that always allowed us to sail in clear air.

...Stephen Wheeler for his manufacturing skillset.

...Bruno Willi for his IT support.

...my first office mates: Christian Günthner, Jonas Wahlheim, Robbert van Gorkum, Mareike Cramer, Alexander Gotschy, Ezgi Berberoglu, Johanna Stimm and Hannes Dillinger for warmly welcoming me at the IBT and offering help and guidance during the early stages.

...the crew aboard F71: Jonas Steinhauser, Sophie Peereboom, Julia Trächtler, Maximilian Fütterer, Andreas Dounas, Jochen von Spiczak, Rabea Schlenker and Alexander Gotschy for their companionship and for keeping the morale high.

...past and ongoing members of the CMR Team: Johannes Schmidt, Lukas Wissmann, Julia Busch, Constantin von Deuster, Patrick Wespi, Georg Spinner, Greg Kwiatkowski, Patrick Bosshard, Stefano Buoso, Christian Federeau, Gevin v. Witte, Eva Peper, Felix Kreis, Moritz Platscher, Mohammed Albannay, Pietro Dirix, Charles McGrath, Gloria Wolkerstorfer, Manuel Christanell, Sébastien Emery, Vencel Somai and Isabel Margolis for joyful times, fruitful discussions, granting a supportive environment and simply for being a great bunch of people.

...the entire MR Tech team for the nice atmosphere and kind interactions over many years.

...Andreas Port for countless coffee breaks with genuinely great conversations about all aspects of life – thank you for your supportive attitude when the seas got rough.

...my sailing friends from Zurich for providing physical and equally joyful distraction and making me feel at home.

At last, I want to cordially thank my closest family and friends for their continuous guidance and motivation as well as their generous support in every matter.

I am utmost grateful to my parents and Roni for their perpetual patience and love – without, I would still be at sea.

---

# List of Publications

## Journal articles:

- 2023 **T. Hoh**, J. Weine, T. Joyce, R. Manka, M. Weisskopf, N. Cesarovic, M. Fuetterer and S. Kozerke  
Impact of Late Gadolinium Enhancement Image Resolution on Neural Network-based Automatic Scar Segmentation in Cardiovascular Magnetic Resonance Imaging.  
(submitted)
- 2022 **T. Hoh**, V. Vishnevskiy, M. Polacin, R. Manka, M. Fuetterer and S. Kozerke  
Free-breathing Motion-informed Locally Low-rank Quantitative 3D Myocardial Perfusion Imaging, *Magn Reson Med*, 2022, 1-17
- 2023 N. Cesarovic, M. Weisskopf, T. Stolte, N. Trimmel, M. Hierweger, **T. Hoh**, J. Iske, C. Waschkies, J. Chen, E. van Gelder, A. Leuthardt, L. Glaus, Y. Rösch, C. Stoeck, P. Wolint, D. Obrist, S. Kozerke, V. Falk, and M. Emmert  
Development of a Translational Autologous Microthrombi-Induced MINOCA Pig Model, *Circ Res*, 2023, 133:291-293
- 2023 J. Traechtler, M. Fuetterer, M. Albannay, **T. Hoh** and S. Kozerke  
Considerations for Hyperpolarized  $^{13}\text{C}$  MR at Reduced Field: Comparing 1.5T versus 3T, *Magn Reson Med*, 2023, 1-16
- 2020 D. Zimmermann, K. Seufert, L. Dordevic, **T. Hoh**, S. Joshi, T. Marangoni, D. Bonifazi and W. Auwärter  
Self-assembly and Spectroscopic Fingerprints of Photoactive Pyrenyl Tectons on h- BN/CU(111), *Beilstein J Nanotechnol*, 2020, 11, pp 1470–1483
- 2016 T. Kaposi, S. Joshi, **T. Hoh**, A. Wiengarten, K. Seufert, M. Paszkiewicz, F. Klappenberger, D. Écija, W. Auwärter, L. Dordevic, T. Marangoni, D. Bonifazi and J. Barth  
Supramolecular Spangling, Crocheting and Knitting of Functionalized Pyrene Molecules on a Silver Surface, *ACS Nano*, 2016, 10 (8), pp 7665–7674
- 2015 S. Joshi, C. Palma, **T. Hoh**, D. Écija, J. V. Barth and W. Auwärter  
Two-level Spatial Modulation of Vibronic Conductance in Conjugated Oligophenylenes on Boron Nitride, *Nano Lett*, 2015, 15 (4), pp 2242–2248



---

**Conference contributions:**

- 2022 **T. Hoh**, V. Vishnevskiy, C. Stoeck, C. Waschkies, N. Cesarovic, M. Weisskopf, M. Fuetterer and S. Kozerke  
Performance of Quantitative, Free-Breathing 3D Perfusion CMR using Motion-Informed LLR Reconstruction in a Porcine Infarction Model, In: Proceedings of the 31<sup>th</sup> Annual Meeting of ISMRM, London, UK, 2022
- 2022 V. Vishnevskiy, **T. Hoh** and S. Kozerke  
Learning Time-Adaptive Data-Driven Sampling Pattern for Accelerated 3D Myocardial Perfusion Imaging, In: Proceedings of the 31<sup>th</sup> Annual Meeting of ISMRM, London, UK, 2022
- 2022 J. Traechtler, M. Fuetterer, **T. Hoh**, M. Albannay, A. Dounas and S. Kozerke  
On the Impact of Heart Rate and Relaxation on SNR of Hyperpolarized <sup>13</sup>C Pyruvate Metabolic Imaging of the Human Heart, In: Proceedings of the 31<sup>th</sup> Annual Meeting of ISMRM, London, UK, 2022
- 2022 M. Fuetterer, J. Traechtler, A. Dounas, **T. Hoh**, M. Albannay and S. Kozerke  
Hyperpolarized <sup>13</sup>C Imaging at Moderate Field Strengths: SNR Considerations and In-vivo Feasibility at 1.5T, In: Proceedings of the 31<sup>th</sup> Annual Meeting of ISMRM, London, UK, 2022
- 2021 **T. Hoh**, V. Vishnevskiy, M. Fuetterer and S. Kozerke  
Free-Breathing Motion-Informed Quantitative 3D Myocardial Perfusion Imaging, In: Proceedings of the 30<sup>th</sup> Annual Meeting of ISMRM, 2021
- 2020 N. Cesarovic, M. Lipiski, **T. Hoh**, C. Waschkies, M. Joner, R. Schwartz, J. Hoem, E. Gertheis, O. Bludau and M. Rothman  
Dynamic Microvascular Flow Resistance (dMVR) Measurement Using the Controlled Flow Infusion (CoFI) Method in a Porcine STEMI model with Reduced TIMI Flow Outcome Post-stenting and Subsequent Microvascular Obstruction by Injecting Endogenous Microthrombi, In: Abstracts of PCR eCourse, 2020
- 2019 **T. Hoh**, J. von Spiczak, T. Joyce, R. Lingwood, H. Dillinger and S. Kozerke  
Rapid Cardiac Myocardial Perfusion Quantification Using Machine Learning Trained with Synthetically Generated Sample Data, In: Proceedings of the 36<sup>th</sup> Annual Scientific Meeting of ESMRMB, Rotterdam, Netherlands, 2019
- 2018 **T. Hoh**, J. Walheim, M. Gastl, A. Gotschy and S. Kozerke  
Partial Fourier Acquisitions in Myocardial First Pass Perfusion Revisited, In: Proceedings of the 26<sup>th</sup> Annual Meeting of ISMRM, Paris, France, 2018
- 2017 **T. Hoh**, E. Coello, J. Carretero Benignos, A. Haase and R. Schulte  
Temperature Mapping of Fluorinated (<sup>19</sup>F) Gas in a Cool Down Experiment, In: Proceedings of the 25<sup>th</sup> Annual Meeting of ISMRM, Honolulu, USA, 2017